

OPTIMIZATION AND FABRICATION OF HEAT EXCHANGERS FOR HIGH –DENSITY POWER CONTROL UNIT APPLICATIONS

Pritish Ranjan Parida

Dissertation submitted to the faculty of the Virginia Polytechnic Institute and State
University in partial fulfillment of the requirements for the degree of

Doctor of Philosophy

In

Mechanical Engineering

Dr. Srinath V. Ekkad
Dr. Khai D. T. Ngo
Dr. Danesh K. Tafti
Dr. Mark R. Paul
Dr. Scott T. Huxtable

August 5, 2010
Blacksburg, Virginia

*Keywords: Jet Impingement, Swirl-impingement-Fin, Ribbed Mini-channel, Electronic
cooling, Automotive Application, Power Converters for HEV, Thermal Management,
Turbine Blade Internal Cooling*

Copyright 2010, Pritish Ranjan Parida

OPTIMIZATION AND FABRICATION OF HEAT EXCHANGERS FOR HIGH –DENSITY POWER CONTROL UNIT APPLICATIONS

Pritish Ranjan Parida

ABSTRACT

The demand for more power and performance from electronic equipment has constantly been growing resulting in an increased amount of heat dissipation from these devices. Thermal management of high-density power control units for hybrid electric vehicles is one such application. Over the last few years, the performance of this power control unit has been improved and size has been reduced to attain higher efficiency and performance causing the heat dissipation as well as heat density to increase significantly. However, the overall cooling system has remained unchanged and only the heat exchanger corresponding to the power control unit (PCU) has been improved. This has allowed the manufacturing costs to go down. Efforts are constantly being made to reduce the PCU size even further and also to reduce manufacturing costs. As a consequence, heat density will go up ($\sim 200 - 250 \text{ W/cm}^2$) and thus, a better high performance cooler/heat exchanger is required that can operate under the existing cooling system design and at the same time, maintain active devices temperature within optimum range ($<120 - 125 \text{ }^\circ\text{C}$) for higher reliability.

The aim of this dissertation was to study the various cooling options based on jet impingement, mini-channel, ribbed mini-channel, phase change material and double sided cooling configurations for application in hybrid electric vehicle and other similar consumer products and perform parametric and optimization study on selected designs. Detailed experimental and computational analysis was performed on different cooling designs to evaluate overall performance. Severe constraints such as choice of coolant,

coolant flow-rate, pressure drop, minimum geometrical size and operating temperature were required for the overall design. High performance jet impingement based cooler design with incorporated fin-like structures induced swirl and provided enhanced local heat transfer compared to traditional cooling designs. However, the cooling scheme could manage only 97.4% of the target effectiveness. Tapered/nozzle-shaped jets based designs showed promising results (~40% reduction in overall pressure drop) but were not sufficient to meet the overall operating temperature requirement. Various schemes of mini-channel arrangement, which were based on utilizing conduction and convection heat transfer in a conjugate mode, demonstrated improved performance over that of impingement cooling schemes. Impingement and mini-channel based designs were combined to show high heat transfer rates but at the expense of higher pressure drops (~5 times). As an alternate, mini-channel based coolers with ~1.5 mm size channels having trip strips or ribs were studied to accommodate the design constraints and to enhance local as well as overall heat transfer rates and achieve the target operating temperature.

A step by step approach to the development of the heat exchanger is provided with an emphasis on system level design. The computational based optimization methodology is confirmed by a fabricated test bed to evaluate overall performance and compare the predicted results with actual performance.

Additionally, one of the impingement based configuration (Swirl-Impingement-Fin) developed during the course of this work was applied to the internal cooling of a turbine blade trailing edge and was shown to enhance the thermal performance by at least a factor of 2 in comparison to the existing pin-fin technology for the conditions studied in this work.

ACKNOWLEDGEMENTS

It gives me immense pleasure to express my most sincere feelings of gratitude to Dr. Srinath Ekkad and Dr. Khai Ngo for their benevolent guidance and worthy suggestions during the course of this thesis. The valuable research experience gained during this dissertation would not have been possible without their encouragement and, technical and financial support. I would also like to thank my Committee members, Dr. Danesh Tafti, Dr. Mark Paul and Dr. Scott Huxtable, for their continued support and guidance.

I am extremely grateful to the faculty and staff of Mechanical Engineering Department, Virginia Tech, for helping me form a strong theoretical background and develop inclination towards research. I am also grateful to the machinists, especially Bill Songer and James Dowdy, at the Virginia Tech ME workshop for fabricating the heat exchanger test samples. I would also like to acknowledge my colleagues and friends Xiao Cao, Li Jiang, Tao Wang, Satoru Sasaki, Dan Huff, Kapil Panchal, Santosh Abraham, Justin Lamont, Chris LeBlanc and Preston Stoakes, for extending their help and sharing their experience in the field. I am thankful to Dan Huff for helping me with the liquid-based thermal test bed and Xiao Cao for fabricating the power modules for heat exchanger sample testing.

I would also like to extend my special acknowledgements to my parents and brother and to Devdutta Deb for constantly supporting and helping me. Finally, I express my sincere gratitude to all my classmates for all their support and their presence at time when I needed it the most.

TABLE OF CONTENTS

ABSTRACT.....	ii
ACKNOWLEDGEMENTS.....	iv
LIST OF FIGURES.....	vii
LIST OF TABLES.....	xx
NOMENCLATURE.....	xxii
ABBREVIATIONS.....	xxiii
CHAPTER 1: INTRODUCTION.....	1
1.1 Hybrid Electric Vehicle.....	2
1.2 Power Control Unit.....	3
1.3 Problem Statement.....	6
CHAPTER 2: LITERATURE REVIEW.....	8
CHAPTER 3: APPLICABLE COOLING SCHEMES AND OVERALL HEAT EXCHANGER DESIGNS.....	19
3.1 Applicable and Selected Cooling Schemes.....	21
3.2 Overall Heat Exchanger Structures.....	25
3.3 Flow Distribution.....	30
3.4 Summary.....	36
CHAPTER 4: CONCEPT TESTING.....	37
4.1 Thermo-chromic Liquid Crystal Test Setup.....	37
4.2 Numerical Validation and Analysis.....	46
4.3 Comparison of Experimental and Numerical Results.....	51
4.4 Summary.....	63
CHAPTER 5: LIQUID BASED THERMAL TEST BED AND SIMULATION STRATEGY.....	65
5.1 Thermal Test Bed.....	65
5.1.1 Pumping Section.....	68
5.1.2 Control Panel.....	72
5.1.3 Test Section.....	81
5.2 Thermal Test Bed Experiment.....	86
5.3 Simulation Strategy.....	88
5.4 Model Verification.....	90
5.5 Simulation Validation.....	94
5.6 Partial Module Simulations.....	101
5.7 Summary.....	103
CHAPTER 6: IMPINGEMENT BASED DESIGNS.....	104
6.1 Parametric Study and Optimization.....	104

6.2 Impingement-Based Partial Module Simulation.....	110
6.3 Cooling Performance.....	112
6.4 Summary.....	119
CHAPTER 7: MINI-CHANNEL, RIBBED MINI-CHANNEL AND DOUBLE SIDED COOLING BASED DESIGNS.....	121
7.1 Mini-channels Based Cooler.....	122
7.2 Ribbed Mini-channels.....	126
7.3 Parametric Study & Optimization.....	130
7.4 Conjugate Analysis for Ribbed Mini-Channels Based Cooler Optimization.....	133
7.5 Ribbed Mini-Channels Based Cooler Prototype.....	146
7.6 Etching Ribs/Channels on DBA Substrate and Al 6063 Block.....	150
7.7 Test Assembly and Cooler Performance.....	155
7.8 Double Sided Cooling.....	159
7.9 Summary.....	162
CHAPTER 8: PHASE CHANGE MATERIAL (PCM) BASED AND ALTERNATE DESIGNS.....	164
8.1 Phase Change Materials (PCM) as Heat Spreader Option.....	164
8.2 Tapered Jets.....	172
8.3 Combined Impingement and Mini-Channel Based Coolers.....	174
8.4 Summary.....	177
CHAPTER 9: BEYOND ELECTRONIC COOLING.....	178
9.1 Geometry and Simulation Model.....	179
9.2 Data Reduction.....	183
9.3 Boundary Conditions.....	184
9.4 Results and Discussion.....	184
9.5 Conclusion and Future Work.....	194
CHAPTER 10: CONCLUSION AND RECOMMENDATIONS.....	195
REFERENCES.....	203
APPENDIX A.....	208
A.1 Measurement From the Experiment.....	209
A.2 Simulation Prediction.....	210
A.3 Conclusion.....	211
APPENDIX B: PUBLICATIONS.....	215
VITA.....	217

LIST OF FIGURES

Figure 1.1.	Schematic of the various components of a hybrid electric vehicle [5].....	2
Figure 1.2.	Typical power control unit of a hybrid electric vehicle. (Source: 2007 Annual Progress Report, Vehicle Technologies Program, US DOE).....	3
Figure 1.3.	Schematics of typical (a) Single-sided and (b) Double-sided Power Module.	4
Figure 1.4.	Typical heat exchanger used for cooling power control unit of hybrid vehicle.	5
Figure 2.1.	Schematics showing (a) Heat-piped DBC based power module concept and (b) working principle of a heat-piped DBC [15].....	10
Figure 2.2.	Schematic of a direct-cooled power module substrate [19].....	11
Figure 3.1.	Schematic showing the placement of the heat exchanger with respect to the active components of the high-density power control unit. Figure also shows a cross-sectional view of the heat exchanger based on SIF cooling scheme.....	20
Figure 3.2.	Impingement based heat exchanger designs for a conventional power module package. (a) Conventional normally impinging jet based design (b) Inclined impinging jet based design (c) Conventional jet impingement on a finned base-plate based design (d) Inclined jet impingement on a finned base-plate based design (Swirl-Impingement-Fin based design) (e) Conventional jet impingement on an angled base-plate based design.....	22
Figure. 3.3.	Direct-cooled mini-channel based cooling configuration.....	24
Figure 3.4.	Schematic of the overall heat exchanger structure which allows 0.025 L/s flow rate and ~2.5 kPa pressure drop across the simulation model.	25
Figure 3.5.	Schematic of the overall heat exchanger structure which allows 0.0125 L/s flow rate and ~5 kPa pressure drop across the simulation model.	26
Figure 3.6.	Schematic of the overall heat exchanger structure which allows for 0.0185 L/s flow rate and ~5 kPa pressure drop across the simulation model.	27

Figure 3.7.	Schematic of the overall heat exchanger structure which allows for 0.00925 L/s flow rate and ~10 kPa pressure drop across the simulation model.	27
Figure 3.8.	Schematic of the overall heat exchanger structure which allows for 0.0416 L/s flow rate and ~1 kPa pressure drop across the simulation model.	28
Figure 3.9.	Schematic of the overall heat exchanger structure which allows for 0.0208 L/s flow rate and ~2 kPa pressure drop across the simulation model.	29
Figure 3.10.	Overview of an impingement cooler based on the overall heat exchanger structure 1.	30
Figure 3.11.	Sectional views of impingement cooler with the arrows indicating the flow direction.....	31
Figure 3.12.	Fluid domain for a portion of the impingement cooler. White arrows indicate the inlet; yellow arrows indicate the outlet and the pink arrows represent the plane of symmetry.....	32
Figure 3.13.	Wall heat transfer coefficients at the target surface for a smaller section of the second preliminary design. A coarse mesh was used near the walls. Angle of the jet holes = 90° from the horizontal (i.e., normally impinging jets).....	32
Figure 3.14.	Fluid velocity vectors at the target surface for a smaller section of the second preliminary design. A coarse mesh was used near the walls. Angle of the jet holes = 90° from the horizontal (i.e., normally impinging jets).....	33
Figure 3.15.	Fluid domain for a portion of the modified impingement based heat exchanger design with normally impinging jet holes with the red circles highlighting the modifications. White arrows indicate the inlet; yellow arrows indicate the outlet and the pink arrows represent the plane of symmetry.....	33
Figure 3.16.	Fluid domain for another portion of the impingement-based heat exchanger design with normally impinging jet holes. White arrows indicate the inlet; yellow arrows indicate the outlet.....	34
Figure 3.17.	Wall heat transfer coefficients at the target surface for a smaller section of the modified design. A medially refined mesh was used near the walls. Angle of the jet holes = 90° from the horizontal	

	(i.e., normally impinging jets).....	35
Figure 3.18.	Fluid velocity vectors at the target surface for a smaller section of the modified design. A medially refined mesh was used near the walls. Angle of the jet holes = 90° from the horizontal (i.e., normally impinging jets).....	35
Figure 4.1.	Schematic of the test-bed.....	38
Figure 4.2.	Liquid crystal images at different instances of time. A) Heater switched on (frame # 54) b) Frame # 66 @ 30 fps c) Frame # 100 @ 30 fps d) Frame # 150 @ 30 fps.....	39
Figure 4.3.	Transient temperature measurements at different locations.....	40
Figure. 4.4.	Thermal images of the outside surface of the target plate at different instances of time.....	43
Figure 4.5.	Nusselt number contours for (a) normally (90°) impinging jets at $Re = 8526$, and (b) 70° impinging jets at $Re = 8192$	44
Figure 4.6.	Nusselt number contours for 70° impinging jets at $Re = 7800$ evaluated using infrared thermography and lumped capacitance method.....	45
Figure 4.7.	Schematic of the test chamber [72].....	46
Figure 4.8.	2-D Axis-symmetry configuration for simulation.....	47
Figure 4.9.	Four different levels of grid with the incorporated boundary layers used for the second configuration. (a) Coarse mesh (b) Medium mesh (c) Fine mesh (d) Finer mesh.....	48
Figure 4.10.	Comparison of the heat transfer coefficient for (a) $k-\varepsilon$, (b) standard $k-\omega$, (c) Shear Stress Transport $k-\omega$ and (d) Reynolds Stress turbulence models with the experimental data for $Re=5000$ (Air jet).....	49
Figure 4.11.	Comparison of the heat transfer coefficient for standard $k-\omega$ turbulence model with the experimental data for $Re=10000$ (Water jet).....	50
Figure 4.12.	ANSYS-CFX model used for simulating the liquid crystal experiments for normally impinging jets with a Reynolds number of 8500.....	51

Figure 4.13.	Heat transfer coefficient predicted for the liquid crystal experiments for (a) normally impinging jets with a Reynolds number of 8200. Max $Nu = 33$. Average $Nu = 18.67$, and (b) 70° impinging jets with a Reynolds number of 8200. Max $Nu = 35.17$. Average $Nu = 19.3$	52
Figure 4.14.	Velocity vectors at the cross-sectional planes passing through the jet centers for (A) 90° and (B) 70° impinging jets.....	53
Figure 4.15.	Velocity contours at the cross-sectional planes passing through the jet centers for (A) 90° and (B) 70° impinging jets.....	56
Figure 4.16.	Vorticity contours at the cross-sectional planes passing through the jet centers for (A) 90° and (B) 70° impinging jets.....	57
Figure 4.17.	Small single impinging jet configurations for the flow and heat transfer study of wall-integrated (a) normal and (b) 70° inclined impingement cases.....	58
Figure 4.18.	Nusselt number predictions at the target surfaces for the three configurations (a) 90° impinging jet with inlet flow normal to the inlet face, (b) 70° impinging jet with inlet flow normal to the inlet face, and (c) 70° impinging jet with inlet flow along the jet axis.....	60
Figure 4.19.	Velocity streamlines inside the flow domain for the three configurations (a) 90° impinging jet with inlet flow normal to the inlet face, (b) 70° impinging jet with inlet flow normal to the inlet face, and (c) 70° impinging jet with inlet flow along the jet axis.....	61
Figure 4.20.	Vorticity (velocity curl component along the cross-flow direction) contours at different cross-sectional planes for the three configurations (a) 90° impinging jet with inlet flow normal to the inlet face, (b) 70° impinging jet with inlet flow normal to the inlet face, and (c) 70° impinging jet with inlet flow along the jet axis.....	62
Figure 5.1.	Schematic of the Thermal Test Bed.....	66
Figure 5.2.	Schematic representation of the liquid-based thermal test bed.....	67
Figure 5.3.	Overall view of the functional liquid-based thermal test bed.....	67
Figure 5.4.	Various components of the thermal test bed before assembly.....	68
Figure 5.5.	(a) Image of the coolant reservoir (Photo by author) (b) and (c) schematic representation of the coolant reservoir (Source: www.mcmaster.com).....	69

Figure 5.6.	Schematic of the immersion heater with temperature control (Source: www.mcmaster.com).....	70
Figure 5.7.	(a) Centrifugal pump with attached electric motor and filter. (b) 1/12 HP electric motor (c) Motor specifications.....	71
Figure 5.8.	Image of the tube-fin type heat exchanger used to dissipate the thermal energy gained at the test-section to the ambient.....	71
Figure 5.9.	(a) Image of the 20W fan used with the tube-fin type heat exchanger. (b) Tube-fin type heat exchanger performance when the above fan is used.....	72
Figure 5.10.	Overall view of the control panel.....	73
Figure 5.11.	Series 490 Wet/Wet Dwyer digital manometer.....	74
Figure 5.12.	Image of the pressure regulator with gauge ports (Source: www.mcmaster.com).....	75
Figure 5.13.	Image of the pressure transmitter.....	76
Figure 5.14.	Image of the pressure indicator.....	77
Figure 5.15.	Image of the ten point temperature indicator.....	77
Figure 5.16.	Image of the remote flow rate indicator.....	78
Figure 5.17.	Image of the flow rate monitor.....	79
Figure 5.18.	36 gauge K-type Thermocouple with molded subminiature connector and 1 mm diameter transition joint thermocouple probe.....	79
Figure 5.19.	OMB-DAQ-54 Data Acquisition System.....	81
Figure 5.20.	Overall view of the assembled test section for the first heat exchanger sample.....	82
Figure 5.21.	Exploded view of the different components of the test section for the first heat exchanger sample.....	83
Figure 5.22.	Schematic representation of the thermocouple probing locations on the target plate.....	83

Figure 5.23.	Different views of the simulation model corresponding to the test section of the thermal test bed. Red and Blue dots represent the location of high and low pressure taps respectively.....	85
Figure 5.24.	Streamlines showing the flow path in the impingement based cooler. (a) Isometric View (b) Side View.....	86
Figure 5.25.	Concentrated heat source made from copper block and 2 cartridge heaters. Foot-print area of each rectangular heater leg is 1.61 cm^2 (1.27 cm X 1.27 cm).....	88
Figure 5.26.	Flow chart summarizing the present simulation strategy.....	89
Figure 5.27.	Conjugate heat transfer model. (a) ANSYS-CFX model with black arrows showing the in-flow and out-flow directions and red arrows indicating the symmetry boundary conditions. (b) Cross-sectional view of the model.....	90
Figure 5.28.	Temperature contours on the symmetry planes showing the flow is thermally fully developed much before the outlet.....	91
Figure 5.29.	Velocity contours on the symmetry planes showing the flow is hydro-dynamically fully developed much before the outlet.....	92
Figure 5.30.	(a) Wall adjacent temperature and center line temperature profile (b) Wall heat flux profile for the conjugate heat transfer problem subject to constant temperature boundary condition.....	92
Figure 5.31.	(a) Conjugate simulation model for validation against the literature. (b) Conjugate model used in the literature [73]. Black dots show the location of the thermocouples [73].....	93
Figure 5.32.	Comparison of the simulation data with the data provided in the literature. (a) Experimental and numerical data in the literature [73] (b) ANSYS-CFX simulation data for the inlet temperature of $20 \text{ }^\circ\text{C}$. (c). Temperature and velocity contours on the symmetry plane. Velocity contours in the fluid region and temperature contours in the solid region.....	95
Figure 5.33.	Cross-sectional view of the meshed domain with fine meshing at all the interfaces.....	96
Figure 5.34.	Simulation model for comparison with experimental data. Yellow cross-hairs represent the temperature and pressure measurement locations. (HP: High Pressure) (LP: Low Pressure).....	97

Figure 5.35.	Temperature measurement at different measurement locations indicated in Figure 5.34 for low power experiment and its comparison with the simulation predictions (k-ε) for different mesh sizes.....	98
Figure 5.36.	Temperature prediction at measurement locations indicated in Figure 5.34 by k-ε and SST models and its comparison with the experimental data for low power experiments.....	99
Figure 5.37.	Different views of the conjugate simulation model of a typical partial power module package.....	102
Figure 6.1.	Conjugate heat transfer models for the study of wall/fin and impingement angle effects on the effective heat transfer coefficient and solid bulk temperature. (a) Simulation model with no center wall/fin. (b) Simulation model with center wall/fin (half domain).....	104
Figure 6.2.	Velocity streamlines showing the vortices for different impingement angles and wall locations. (a) 90° (b) 70°, (c) 45°.....	105
Figure 6.3.	Wall heat transfer coefficient and temperature predictions using k-ε model for the 90° impinging jets (a), (c) With no center wall/fin (b), (d) with center wall/fin (half domain). No change in wall heat transfer coefficient. 7.1K reduction in maximum surface temperature due to center wall/fin.....	106
Figure 6.4.	Wall heat transfer coefficient and temperature predictions using k-ε model for the 70° impinging jets (a), (c) With no center wall/fin (b), (d) with center wall/fin (half domain). Peak heat transfer coefficient increases with the placement of a wall. 12.8 K reduction in the maximum surface temperature as compared to 90° impinging jets.....	107
Figure 6.5.	Wall heat transfer coefficient and temperature predictions using k-ε model for the 45° impinging jets (a), (c) With no center wall/fin (b), (d) with center wall/fin (half domain). Peak heat transfer coefficient increases with the placement of a wall. 23 K reduction in the maximum surface temperature as compared to 90° impinging jets.....	109
Figure 6.6.	Variation of the maximum IGBT temperature with respect to the coolant inlet temperature with pumping power for water as well as ethylene glycol as the coolant.....	111
Figure 6.7.	IGBT and Diode temperature prediction and velocity streamlines	

	for the partial module shown in Figure 5.37.....	112
Figure 6.8.	Different views and dimensions of the cooler designed for single-sided single channel multi chip power module.....	115
Figure 6.9.	Assembled power module package with the active devices as heat sources and inlet and outlet locations.....	115
Figure 6.10.	Thermal Test Bed set-up for cooler performance evaluation. (a) Overall set-up for cooler evaluation. (b) Zoomed-in image of the test section.....	116
Figure 6.11.	Thermal resistances corresponding to the IGBTs for various heat dissipation rates through each device.....	116
Figure 6.12.	Simulation model for the packaged single-sided power module configuration that was fabricated and tested. (a) Side View (b) Top View (c) Wall heat transfer coefficient at the bottom surface of the DBA substrate emphasizing the even coolant distribution inside the cooler.....	117
Figure 6.13.	Variation of the thermal resistance with pressure drop for the present impingement based configuration and its comparison with existing high performance technology.....	118
Figure 6.14.	Double-sided single channel multi chip power module configuration.....	119
Figure 7.1.	Different views of the conjugate heat transfer simulation model for double-sided single channel multi chip power module.....	121
Figure 7.2.	Preliminary mini-channel single channel power module packaging design.....	122
Figure 7.3.	Temperature contours at the central plane for the preliminary mini-channel based design.....	123
Figure 7.4.	Temperature contours at the central plane for the mini-channel based design having a slightly larger coolant to power module separation.....	124
Figure 7.5.	Modified mini-channel based configuration.....	124
Figure 7.6.	Cross-section of a 4-pass mini-channels based cooler with different pressure measurement locations.....	125

Figure 7.7.	Flow domain in a (a) straight channel, (b) 90° ribbed channel and (c) 45° ribbed channel.....	126
Figure 7.8.	Four different faces of a ribbed channel.....	127
Figure 7.9.	Temperature contours at the (a) packaging central plane and at the (b) cross-sectional plane at the IGBT 1 center for a cooler based on ribbed mini-channel configuration.....	128
Figure 7.10.	Temperature contours at the packaging central plane for models based on ribbed mini-channels (a) Model 33, (b) Model 41 and (c) Model 42.....	130
Figure 7.11.	Fluid model for rib based parametric study.....	131
Figure 7.12.	Variation of Output parameters (channel average HTC and pressure drop) with input parameters (rib angle, rib height and rib spacing).....	132
Figure 7.13.	Sensitivity of the output parameters to the input parameters.....	133
Figure 7.14.	Smaller conjugate model for ribbed mini-channel based cooler optimization.....	134
Figure 7.15.	Comparison between the various ribbed mini-channels models.....	137
Figure 7.16.	Conjugate mini-channel model.....	139
Figure 7.17.	(a) Inline multi-layer mini-channel arrangement with green arrow indicating the flow direction. (b) Staggered multi-layer mini-channel arrangement with green arrow indicating the flow direction.....	139
Figure 7.18.	Effect of number of layers on the effective heat transfer coefficient for inline and staggered arrangement for two different horizontal offsets (0.25 mm and 1 mm).....	140
Figure 7.19.	Double-sided single channel multi-chip power module packaging model based on optimum 2 layers mini-channel configuration. Flow direction based on overall structure 6.....	141
Figure 7.20.	Variation of IGBT temperature as a function of effective heat transfer coefficient under the IGBTs.....	142
Figure 7.21.	Conjugate mini-channel model with one ribbed wall.....	143

Figure 7.22.	Double-sided single channel multi-chip power module packaging model based on optimum 2 layers 1 ribbed wall mini-channel configuration. Flow direction based on overall structure 3.....	144
Figure 7.23.	Double-sided single channel multi-chip power module packaging model based on optimum 2 layers 1 ribbed wall mini-channel configuration. Flow direction based on overall structure 6.....	144
Figure 7.24.	Conjugate mini-channel model with 3 ribbed walls.....	145
Figure 7.25.	Schematic showing the cooler bulk and the bottom cover plate with the arrow heads showing the flow direction.....	147
Figure 7.26.	Schematic representation of the etched ribs on the bottom copper of the DBC substrate.....	148
Figure 7.27.	Different views of the cooler bulk and the bottom cover plate. (a) Top view of the cooler bulk (b) Bottom view of the cooler bulk (c) Bottom cover plate.....	149
Figure 7.28.	Process flow for etching ribbed channels on the DBA substrate.....	151
Figure 7.29.	Final etched ribbed channels (2) with 4 measurement rows.....	151
Figure 7.30.	Dimensions of the grooves and ribs along four different rows for the two channels after etching.....	152
Figure 7.31.	Process flow for etching channel on the Al 6063 block.....	152
Figure 7.32.	Top view of the channel before and after etching.....	153
Figure 7.33.	Digitized image with pink line showing the digital scale and blue cross-hairs as the curve points used for channel dimension measurement.....	153
Figure 7.34.	Dimensions of the channel before and after etching. The bottom left corner of the channel was used as the reference (0,0).....	154
Figure 7.35.	Process flow for etching ribbed channels on the DBC substrate.....	154
Figure 7.36.	Ribbed mini-channel cooler and cover plate assembly.....	155
Figure 7.37.	Assembled power module – ribbed mini-channel cooler test sample.....	156

Figure 7.38.	Different view of the simulation model corresponding to the ribbed mini-channel based heat exchanger test sample. (a) Top view (b) Side view (c) View from the inlet.....	157
Figure 7.39.	Thermal resistances corresponding to the IGBTs for various heat dissipation rates through each device.....	158
Figure 7.40.	Variation of the thermal resistance with pumping power for the present ribbed mini-channel based configuration with that of the impingement based configuration studied earlier.....	159
Figure 7.41.	Variation of IGBT temperature as a function of effective heat transfer coefficient under the IGBTs for single-sided and double-sided cooling configurations.....	161
Figure 7.42.	Mini-channel based double-sided cooler configuration.....	161
Figure 8.1.	Different views of the simulation model corresponding to the test section of the thermal test bed. Red and Blue dots represent the location of high and low pressure taps respectively.....	165
Figure 8.2.	Different views of the PCM plate. The rectangular cavity will be filled with paraffin wax having a melting point of 130 F. The cylindrical holes are for temperature measurements. All Dimensions in mm.....	166
Figure 8.3.	Simulation model of PCM based heat exchanger for comparison with experimental data. Yellow cross-hairs represent the temperature and pressure measurement locations. (HP: High Pressure) (LP: Low Pressure).....	168
Figure 8.4.	Temperature measurement at different measurement locations indicated by Figure 8.3 for low power experiment with PCM and its comparison with the simulation predictions (k- ϵ).....	169
Figure 8.5.	Temperature measurement at different locations indicated by Figure 8.3 for medium power experiment with PCM and its comparison with the simulation predictions (k- ϵ).....	170
Figure 8.6.	Transient temperature profile for different experimental cases of with and without PCM.....	171
Figure 8.7.	Wall heat transfer predictions at the fluid-solid interface on the back side of the power module for (a) cylindrical jets, (b) tapered jets and, (c) 60° angled tapered jets with the same exit diameter as the cylindrical jets.....	173

Figure 8.8.	Temperature contours on the central plane for a combined slot impingement and mini-channels based cooler.....	175
Figure 8.9.	Combined tapered angled impingement and mini-channel configuration.....	175
Figure 8.10.	Wall heat transfer coefficient on the target surface for the design shown in Figure 8.9.....	176
Figure 9.1.	Typical first stage stator trailing edge ejection configuration [76-78]. (a) Gill slot (b) Covered (c) Letter-box.....	178
Figure 9.2.	Different views of the model of the flow domain in the trailing edge with the inlet and outlet plenums. (a) Orthographic view. (b) Top view. (c) Side view.....	180
Figure 9.3.	(a) Sectional view of the typical meshed geometry. (b) Zoomed-in image of the mesh.....	182
Figure 9.4.	Side view of the impingement based trailing edge geometry with regions of interest as named faces. Faces <i>A</i> , <i>B</i> , <i>C</i> and <i>D</i> are the regions of interest in first passage. Faces <i>E</i> , <i>F</i> , <i>G</i> and <i>H</i> are the regions of interest in second passage. Faces <i>I</i> , <i>J</i> and <i>K</i> are the regions of interest in third passage. The outlet pressure was measured at face <i>M</i>	184
Figure 9.5.	Streamlines in the third model for the cases of one inlet and two inlets at an inlet Reynolds number of 7240. (a) One inlet (b) Two inlets.....	185
Figure 9.6.	Variation of overall pressure drop across the trailing edge with Reynolds number.....	186
Figure 9.7.	Variation of channel wise loss coefficient as well as entrance losses with Reynolds number.....	188
Figure 9.8.	Typical heat transfer coefficient distribution obtained at the internal faces of the trailing edge for a first passage Reynolds number of 1360°. (a) faces <i>A</i> , <i>E</i> and <i>I</i> (left to right) (b) faces <i>C</i> , <i>G</i> and <i>K</i>	190
Figure 9.9.	Variation of area averaged Nusselt number with first passage inlet Reynolds number.....	191
Figure 9.10.	Variation of channel wise averaged Nusselt number with channel	

	specific Reynolds number.....	191
Figure 9.11.	Variation of ratio of overall averaged heat transfer coefficient to overall pressure drop with the total mass flow rate.....	192
Figure 9.12.	Different views of the model of the flow domain in the trailing edge for a pin-fin based scheme with the inlet and outlet plenums. (a) Orthographic view. (b) Top view. (c) Side view.....	193
Figure 10.1.	Comparison among various cooler configurations for the same pumping power. (a) Effective Single-Sided Heat Transfer Coefficient (b) Minimum Heat Exchanger Volume (c) Junction Temperature with respect to the Coolant Temperature (d) Cost-effectiveness in terms of cooler machining time.....	198
Figure 10.2.	Comparison of the variation of R_{th} (thermal resistance) values with pumping power for few of the cooler configurations studied.....	199
Figure A.1.	Overall geometry and the CFX model for the conjugate heat transfer simulations of test section of the thermal test bed. (a) Overall geometry without the gasket (b) overall geometry with the rubber gasket. (c) CFX model for the geometry without the gasket.....	212
Figure A.2.	(a) Local wall heat transfer coefficient on the fluid-solid interface computed based on the average coolant temperature. (b) Temperature at the fluid-solid interface.....	213
Figure A.3.	Velocity streamlines showing the alternate fluid path (red circle) generated due to the placement of a gasket.....	214

LIST OF TABLES

Table 4.1.	Summary of Mesh Statistics.....	48
Table 4.2.	Maximum as well as the average Nusselt number predictions at the target surfaces (faces A, B and C).....	59
Table 5.1.	Dimensions of the coolant reservoir.....	69
Table 5.2.	Dimensions of the conjugate geometry used Sung and Mudawar [73].....	93
Table 5.3.	Mesh details for the simulation validation experiments.....	98
Table 5.4.	Pressure prediction by k- ϵ and SST k- ω models for different mesh sizes and its comparison with the experimental data for low power experiments.....	100
Table 6.1.	Heat transfer coefficient (W/m^2K) predictions for 90° impingement.....	107
Table 6.2.	Heat transfer coefficient (W/m^2K) predictions for 70° impingement.....	108
Table 6.3.	Heat transfer coefficient (W/m^2K) predictions for 45° impingement.....	110
Table 6.4.	Comparison of the thermal resistances predicted by simulations with those obtained experimentally.....	117
Table 7.1.	Pressure drop and temperature predictions for various mini-channel based configurations.....	125
Table 7.2.	Channel and rib dimensions with associated thermal performance and pressure drop.....	127
Table 7.3.	Pressure drop and temperature predictions for ribbed mini-channels based configurations.....	129
Table 7.4.	Dimensions and thermal performance of few of the conjugate ribbed mini-channel models.....	136
Table 7.5.	Comparison of the thermal resistances predicted by simulations with those obtained experimentally.....	157

Table 8.1.	Pressure drop and temperature predictions for single channel power module packaging using k- ϵ model for different cases of tapered jets.....	173
Table 8.2.	Pressure drop and temperature predictions for combined impingement and mini-channel based configurations.....	176
Table 9.1.	Geometrical parameters of the jets in the three trailing edge models.....	181
Table 9.2.	Variation in Reynolds number across the trailing edge for three models at a given total mass flow rate.....	186
Table A.1.	Experimental data from the first set of experiments (without the gasket).....	209
Table A.2.	Experimental data from the second set of experiments (with the gasket).....	209

NOMENCLATURE

c_p	-	Specific heat capacity at constant pressure, J/kg-K
D	-	Jet diameter, m
D_h	-	Hydraulic diameter, m
\dot{E}	-	Rate of heat transfer, W
G	-	Mass Flux, kg/m ² s
H	-	Height, m
h	-	Heat transfer coefficient, W/m ² -K
K_L	-	Loss coefficient
k	-	Thermal conductivity, W/m-K
l	-	Target plate thickness, m
\dot{m}	-	Mass flow rate, kg/s
Nu	-	Nusselt number
Pr	-	Prandtl number
p	-	Pressure, kPa
Q	-	Volumetric flow rate, L/min
q''	-	Heat flux, W/m ²
Re	-	Reynolds number
S	-	Jet to target plate spacing, m
T	-	Temperature, K
t	-	Time, s or Thickness, m
<i>Greek Symbols</i>		
α	-	Thermal diffusivity, m ² /s
μ	-	Dynamic viscosity, kg/m-s
θ	-	Jet angle, degrees
ρ	-	Density, kg/m ³
<i>Subscripts</i>		
eff	-	Effective
f	-	Fin
fs	-	Spacing between fins
f,avg	-	Fluid average
i	-	Initial
j	-	Jet Plate
M	-	Mainstream
W	-	Wall

ABBREVIATIONS

AC	-	Alternating Current
CFD	-	Computational Fluid Dynamics
CNG	-	Compressed Natural Gas
CPU	-	Central Processing Unit
CTE	-	Coefficient of Thermal Expansion
DC	-	Direct Current
DBA	-	Direct Bonded Aluminum
DBC	-	Direct Bonded Copper
FET	-	Field Effect Transistor
HEV	-	Hybrid Electric Vehicle
IGBT	-	Insulated Gate Bipolar Transistor
MG	-	Motor Generator
MOSFET	-	Metal-Oxide Semiconductor Field Effect Transistor
PCM	-	Phase Change Material
PCU	-	Power Control Unit
SST	-	Shear Stress Transport
scfm	-	Standard cubic feet per minute

CHAPTER 1: INTRODUCTION

Science and technology related to new and more environmentally-friendly ways of producing and distributing energy are being intensely investigated. New technologies capable of increasing the energy efficiency of transportation, housing, and appliance systems, if successfully commercialized, will reduce energy consumption and positively impact the global environment [1]. Moreover, necessitated by the dwindling supply of petroleum resources, various new automotive technologies have been actively developed from the perspective of achieving energy security and diversifying energy sources.

Conventional internal combustion engines have been continuously improved to attain higher efficiency and higher fuel economy. Additionally, engines have also been modified so that vehicles can run on alternate fuels such as fuel cells, electricity and compressed natural gas (CNG). Such diversification, over the years, has necessitated the use of electronic equipment, especially semiconductor based devices, for efficient power control and manipulation.

The demand for more power and performance from such electronic equipment has constantly been growing causing an increased amount of heat dissipation. While conventional cooling solutions have performed the task of heat removal, no straightforward extension has been possible for significantly high heat fluxes dissipated by smaller and more efficient electronic devices. For example, air-based pin-fin cooling schemes cannot be used for dissipating heat in excess of 60 W/cm^2 while maintaining proper device operating temperatures [2]. Micro-channel and impingement-based cooling have been used as a recent solution to this problem. High heat transfer rates obtained by impingement and micro-channel cooling with water can help dissipate up to 1800 W/cm^2 [3] and 790 W/cm^2 [4]. However, there are many application specific complications involved such as size limitation, limited choice of coolants, limited pumping

power and other such limitations that determine the highest heat transfer rates that can be attained. Thermal management of a high-density power control unit for hybrid electric vehicles is one such challenging application. The power control unit of a hybrid electric vehicle is essentially the brain of the hybrid system as it manages the power flow between the electric motor generator, battery and gas engine.

1.1. Hybrid Electric Vehicle

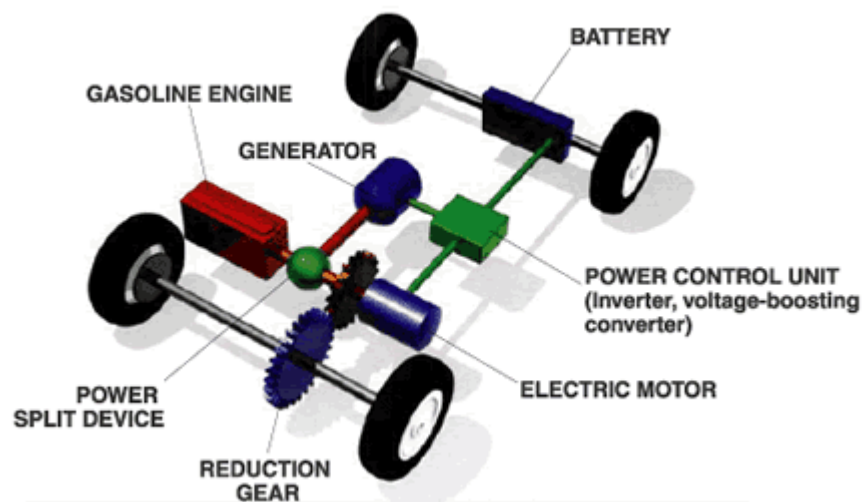


Figure 1.1. Schematic of the various components of a hybrid electric vehicle [5].

Figure 1.1 schematically shows the various components of a hybrid electric vehicle. The system consists of two kinds of motive power sources – a high-efficiency gasoline engine and a permanent magnet AC synchronous motor with 60kW output, a generator, high-performance nickel-metal hydride (Ni-MH) battery and a power control unit [5]. This power control unit contains a high-voltage power circuit for raising the voltage of the power supply system for the motor and the generator to a high voltage (~ 500 V), in addition to an AC-DC inverter for converting between the AC from the motor and the generator and the DC from the hybrid battery [5]. Other key components include a power split device, which transmits the mechanical motive forces from the engine, the motor and the generator by allocating and combining them. The

power control unit precisely controls these components at high speeds to enable them to cooperatively work at high efficiency [5].

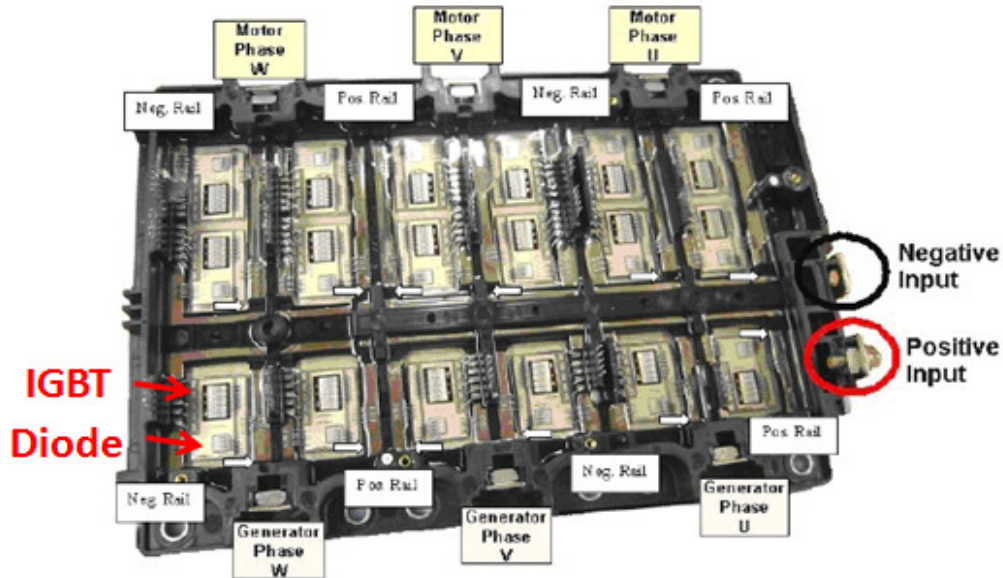


Figure 1.2. Typical power control unit of a hybrid electric vehicle. (Source: 2007 Annual Progress Report, Vehicle Technologies Program, US DOE).

1.2. Power Control Unit

Figure 1.2 shows a typical power control unit of a hybrid electric vehicle and it consists of 18 pairs of IGBTs and diodes. Each of these IGBTs and diodes are capable of dissipating 60 W/cm^2 and 20 W/cm^2 , respectively [6]. Over the last few years, the performance of this power control unit has been improved and the size has been reduced to attain higher efficiency and performance causing the heat dissipation as well as heat density to increase significantly. The overall cooling system has, however, remained unchanged and only the heat exchanger corresponding to the power control unit (PCU) has been improved. This has allowed the manufacturing costs to go down. Efforts are constantly being made to reduce the PCU size even further and also to reduce the manufacturing costs. As a consequence, the heat density will go up ($\sim 200 - 250 \text{ W/cm}^2$) with a total dissipation of approximately 6.5 kW from the localized silicon based heat sources (18 IGBTs and 18 Diodes) and other auxiliary electronic circuits and thus, a

better high performance cooler/heat exchanger is required which can operate under the existing cooling system design and at the same time, maintain active devices temperature within optimum range ($120 - 125\text{ }^\circ\text{C}$) for higher reliability [6].

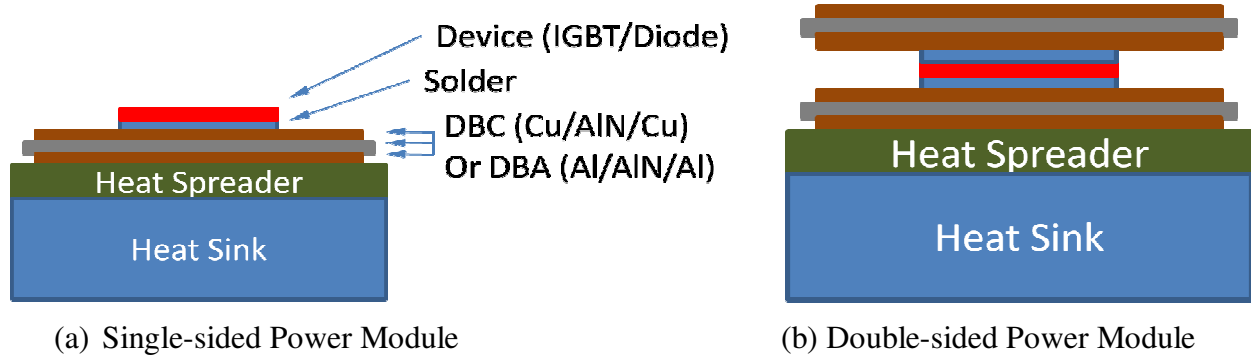


Figure 1.3. Schematics of typical (a) Single-sided and (b) Double-sided Power Module.

Achieving the aforementioned high heat flux dissipation and active devices temperature is greatly dependent on the electronic packaging. Figure 1.3 shows schematics of single sided and double sided power module packaging existing in the power control units of hybrid vehicles, DC-DC converters, DC-AC converters and other such devices. Each of these power modules consist of field-effect transistors (FETs) and metal-oxide semiconductor field effect transistors (MOSFETs) such as IGBTs (Insulated Gate Bipolar Transistors) and Diodes. IGBTs are the main source of heat dissipation and usually dissipate 3-4 times more power than the diodes in a given packaging [6-7]. With the advancement in technology, the size of these FETs has been significantly reduced and thereby allowing them to run at 90 – 95 % efficiency resulting in high heat fluxes of $200 - 250\text{ W/cm}^2$ [6]. These FETs are usually soldered to a base substrate made up of either direct bonded copper (DBC) or direct bonded aluminum (DBA).

Traditionally, a power module is cooled using an indirect liquid cooling scheme wherein a copper or aluminum based heat sink is attached to the electronic packaging and more often, water/ethylene glycol or a 50% vol./vol. mix of water and ethylene glycol (LLC 50% v/v) at

either 65 °C or 105 °C having a volumetric flow rate of 10 - 20 lpm is used as the coolant [6]. The typical pressure drop across the heat sink is of the order of 10 kPa [6]. The Figure 1.4 shows a typical heat sink for a power module. In this structure, the base-plate of the power module is usually bolted to a liquid coolant plate/heat sink. These heat sinks usually contain multiple fins or serpentine channels as their underlying cooling scheme and are attached to the electronic packaging using thermal adhesives. An intermediate layer of thermal paste is used to compensate for surface roughness and to make good thermal contact. As the heat is carried through the material of the coolant-plate, this material has to offer a low thermal resistance. This is why metals (especially copper or aluminum) are usually employed. This results in a heavy structure (the base-plate is 2 to 5-mm thick, and the coolant plate is more than 1-cm thick), with most of the material used only to carry the heat. However, because of the resistances of different layers of materials separating the chip from the liquid coolant, a relatively large temperature gradient is incurred when dissipating high heat fluxes. In such cases, lower active devices temperature can essentially be maintained by reducing such thermal resistances or by increasing the effective heat transfer rates of the heat exchanger.



Figure 1.4. Typical heat exchanger used for cooling power control unit of hybrid vehicle.

Currently, several high performance heat exchangers essentially based on micro-channels and pin-fin cooling scheme are available in the market. However, application of such heat exchangers to hybrid electric vehicles would require the replacement of the existing cooling system and hence, production costs will go up. On the other hand, if the efficiency of existing heat exchanger can be improved, then the production cost will not change much. Thus, the latter is a better solution from a consumer point of view.

The aim of the dissertation was therefore to study the various cost-effective cooling options based on jet impingement, mini-channel, ribbed mini-channel, phase change material and double sided cooling configurations for application in hybrid electric vehicles and other similar consumer products and to perform parametric and optimization studies on the selected designs. Finally, the optimized cooler/heat exchanger was fabricated and tested under actual running conditions. One of the near-term applications would be to implement this design in a future generation hybrid electric vehicle.

1.3. Problem Statement

The goal of this study was to design and analyze a heat exchanger capable of carrying away approximately 7kW of heat dissipated by localized silicon based heat sources (18 IGBTs and 18 Diodes) and other auxiliary electronic circuits while maintaining their optimum operating conditions (120 °C – 125 °C). Each of these localized heat sources can dissipate as much as 220 W/cm² under steady operating conditions.

The following limitations make the problem selective and more challenging:

- *Pumping Power limitation:* The coolant mass flow rate 10 lpm and allowed pressure drop 10 kPa across the heat exchanger are fixed.
- *Coolant limitation:* Only engine coolant (LLC 50% v/v) is to be used at prescribed flow

rate and temperature (65 °C). Due to its low thermal properties, LLC 50% v/v is only 66% as effective in cooling as water for any given heat exchanger configuration.

- *Channel size limitation:* Due to impurities in the coolant, minimum channel size has to be greater than or equal to 1 mm. This limits the use of cooling options such as micro-channel heat sinks and micro-jet impingement options.
- *Compatibility limitation:* Due to compatibility issues, materials like copper cannot be used.
- *Reliability limitation:* This limitation mostly relates to the temperature cycling issues in the whole power module packaging.
- *Cost limitation:* Being designed for consumer application, the end product should be economically justifiable to the average customers.
- *Environment limitation:* Due to consumer product norms, “green” materials have to be used. For example, lead-free solder has to be used in the packaging.

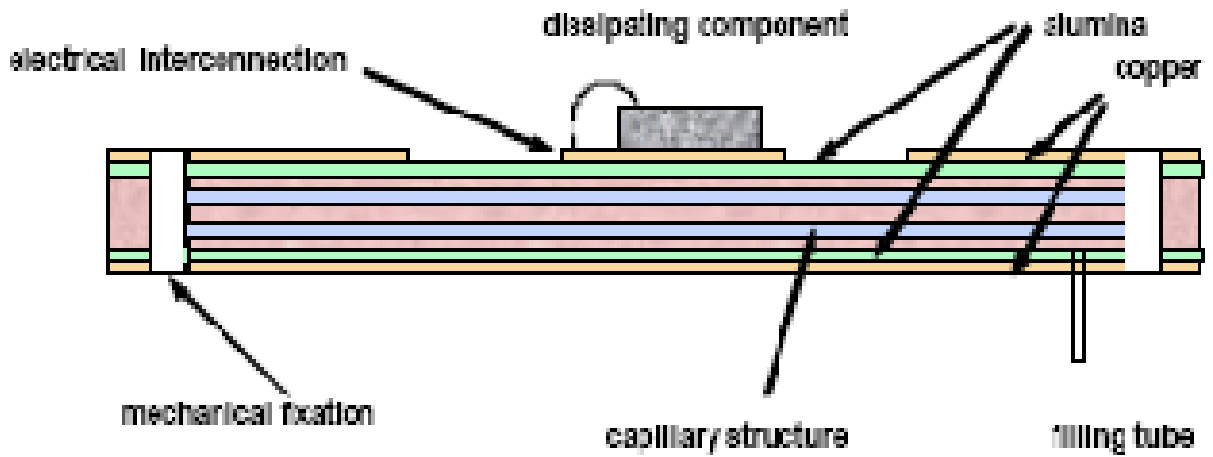
CHAPTER 2: LITERATURE REVIEW

Breakthroughs in the recent cutting-edge technologies have become increasingly dependent on the ability to safely dissipate a large amount of heat from small areas. The power dissipation of electronic equipment grows continually, but their volumes are gradually reduced. The rapid development of semiconductor devices such as IGBTs, MOSFETS and computer processors has led to power loss densities of about 100 W/cm^2 , and are still showing a rapidly increasing tendency [8]. Excessive temperature has a strong effect on device lifetime and can eventually lead to thermal failure. It is reported that about 55% of microcircuit failures occur due to thermal reasons [9]. Besides, most electronic chips generate much more heat at runtime than at standby time, and the transient temperature rise is fast accordingly. Therefore, resisting high heat flux shock has become the bottleneck in the silicon device technology's development [10]. Electric drive systems (which include power converters and electric machines) of a hybrid electric vehicle are another such rapidly developing technology that requires challenging thermal management solutions. Electric drive systems technology is being developed so as to significantly reduce the dependence on petroleum as well as to enable hybrid vehicle solutions to be economically viable. As critical components of the electric drive system are made smaller, lighter, and more cost effective, heat removal becomes an increasing challenge [7]. Improvements in cooling techniques are therefore, required to avoid unacceptable temperature rise and at the same time maintain a high efficiency.

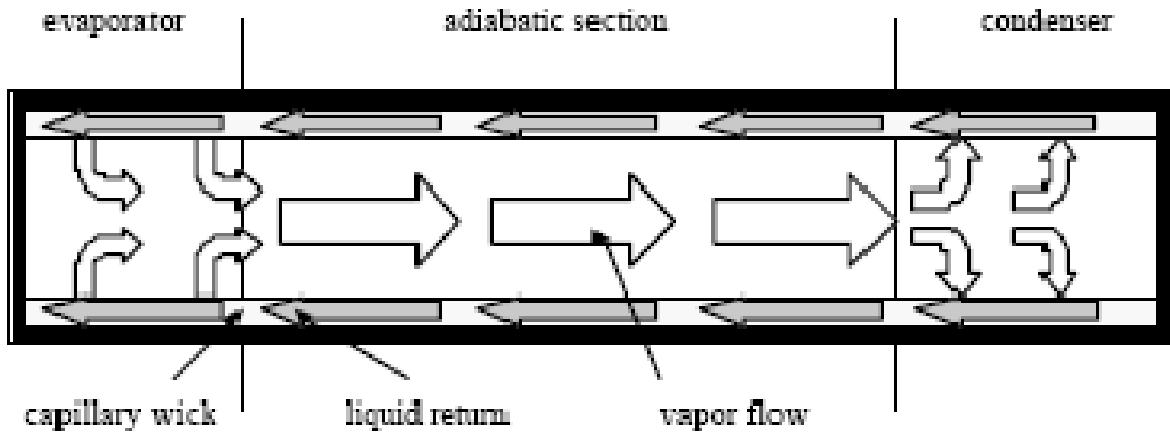
As presented in the earlier chapter, conventionally, a power module is cooled by using an indirect liquid cooling scheme wherein a copper or aluminum based heat sink is attached to the electronic packaging and more often, water/ethylene glycol is used as the coolant. Also, the heat is extracted from the silicon device through a stack of many layers of different materials. As the

heat density for such structures is increased, the structure shows poor reliability to thermal cycling, as each layer expands differently with temperature. It has been shown that the interfaces, especially the DBC to baseplate and the die to wirebond are very sensitive to this phenomenon [11, 12]. Moreover, because of the resistances of the different layers of materials separating the chip from the liquid coolant, a relatively large temperature gradient is incurred when dissipating high heat fluxes. In such cases, lower active device temperatures can essentially be maintained by reducing thermal resistance or by increasing the effective heat transfer rate of the heat exchanger.

Looking at the lower thermal resistance options, direct cooling using impinging jets, droplets and sprays, heat-piped substrate and directly cooled ceramic are a few promising schemes [13-18]. Direct cooling schemes use impinging jets, droplets or sprays of a dielectric coolant such as FC-72 and FC-87 directly on to the active devices. Clearly, such a scheme offers the lowest possible thermal resistance. However, the thermal and physical properties of dielectric coolants are inferior to that of water/ethylene glycol to offer any significant advantage in terms of total thermal resistance. Moreover, for the current application direct cooling scheme would require an auxiliary coolant loop. To counter this, devices are sometimes coated with a thin (3 – 5 μm) layer of dielectric material (parylene) and the coolant (water) impinges on the coating [17]. Although the coolant is in very close proximity of the devices, a large temperature drop can take place even across the thin parylene coating due to the poor thermal conductivity ($\sim 0.06\text{--}0.12\text{ W/mK}$) of the material. Moreover, such direct cooling schemes raise a few practical concerns such as mechanical stability of the device and reliability of the wire-bonds under the impacting liquid and degradation of electrical performance at high frequency operation due to the presence of liquid [17].



(a) Heat-piped DBC based power module concept



(b) Working principle of a heat-piped DBC.

Figure 2.1. Schematics showing (a) Heat-piped DBC based power module concept and (b) working principle of a heat-piped DBC [15].

Heat-piped substrate and directly cooled ceramic schemes, on the other hand, are very effective in taking advantage of reduced thermal resistance. In heat-piped substrate (Figure 2.1), miniature heat pipes are embedded in a Direct Bonded Copper/Aluminum structure. The advantage of this kind of heat pipe is the integration of the electronic component layout directly on the heat pipe itself, which eliminates the existence of a thermal interface between the device and the cooling system [15]. Currently, this scheme has more drawbacks than positives. First of all, the active devices have to be on one side to allow for proper heat removal from the other end.

Thus, the overall power module size will increase. Also, larger substrate cannot be used due to reliability issues. Directly cooled ceramic scheme shown in Figure 2.2 is another such low thermal resistance scheme and is still at the conceptual level. In this scheme, coolant flow paths are generated in a thick ceramic layer so as to reduce the thermal resistance. Biggest challenges in this concept are to meet the increased stresses due to greater coefficient of thermal expansion (CTE) mismatch resulting from thicker ceramic layer.

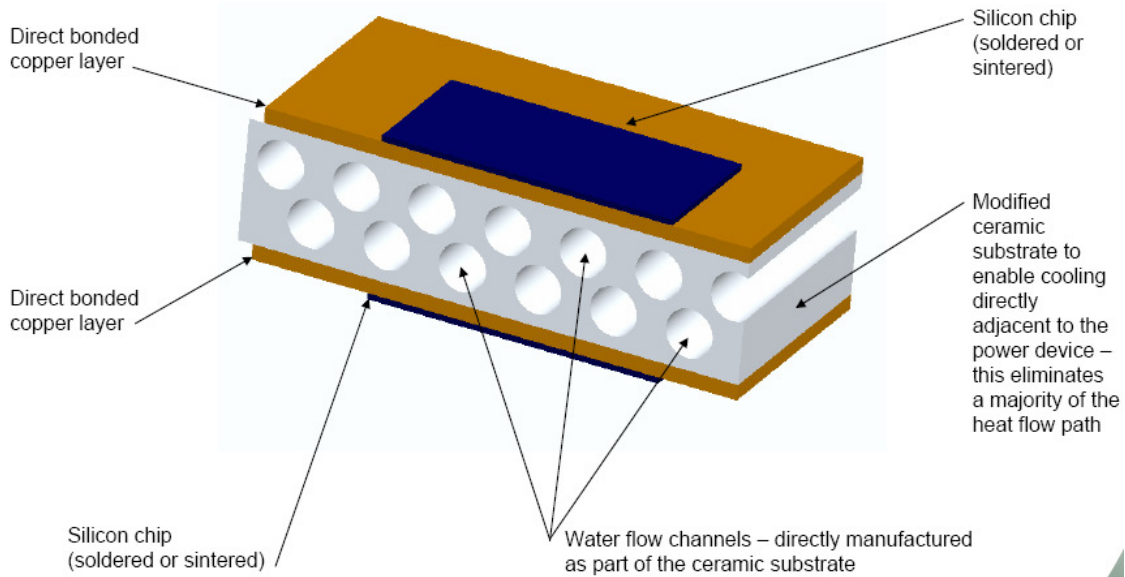


Figure 2.2. Schematic of a direct-cooled power module substrate [19].

Looking at the heat exchanger part, conventional cooling schemes such as jet-impingement cooling, micro pin fin cooling and micro-channel cooling are few promising schemes that have been known to provide high heat transfer performance. However, for the current application micro-channel cooling cannot be applied due to size limitations. In any case, the positives of micro-channel cooling such as enhanced contact surface area and heat spreading through the base material, can be applied to the present application. These three conventional schemes can also be combined and modified to come-up with new schemes and designs to enhance heat transfer performance with reduced pressure drop. But before making any

modification, it is very important to understand which basic scheme is desirable for a given high heat flux application. In jet impingement cooling scheme, thin hydrodynamic and thermal boundary layers forming in the impingement region result in high heat transfer coefficients. On the other hand, micro pin fins and micro-channels provide a large area of contact between the solid and coolant as well as a huge temperature gradient in the coolant near the channel wall due to the extremely small channel width. In other words, a heat exchanger can be designed so as to either have localized high heat transfer coefficients or have large solid – fluid (coolant) contact surface area or have both.

Currently, several high performance heat exchangers essentially based on micro-channels and pin-fin cooling scheme are available in the market. However, application of such heat exchangers to hybrid electric vehicles would require the replacement of the existing cooling system and hence, production costs will go up. On the other hand, if the efficiency of existing heat exchanger can be improved, then the production cost will not change much. Thus, the latter is a better solution from a consumer point of view.

Jet impingement is one such cooling scheme which has been widely used to dissipate transient and steady concentrated heat loads and can be applied to existing cooling system with minor modifications. Some of its conventional applications are in cooling turbine blades and electrical equipment, drying of paper and textiles, and annealing of metals. Jet impingement has also been widely used to maintain relatively low, steady temperatures in devices which dissipate enormous heat fluxes such as lasers and x-ray anodes. Jet impingement can be implemented in three basic forms: free jet in which a fluid jet is issued in a less dense ambient, submerged jet in which fluid jet is issued in a similar or same fluid ambient and confined jet in which a fluid jet is confined between the orifice plate and a heated wall. Over the last decade, jet impingement has

also become a viable candidate for high-powered electronic and photonic thermal management solutions and numerous jet impingement studies have been aimed directly at cooling of electronics [20-25].

Womac et al. [26, 27] have shown that higher heat transfer coefficients result from submerged jet conditions than from free-surface jet conditions for $Re \geq 4000$. The presence of a confining top wall in jet impingement causes lower heat transfer coefficients, thought to be caused by the recirculation of fluid heated by the target plate [28, 29]. Huang et al. [30] suggest that confinement promotes a more uniform heat transfer distribution for the area enclosed by a non-dimensional radial distance from the stagnation point (r/D) of 5. The key parameters determining the heat transfer characteristics of a single impinging jet are the Reynolds number, Prandtl number, jet diameter and jet-to-target spacing. Nozzle geometry can also have a significant influence on heat transfer. Numerous studies have been conducted to investigate the influence of each of these parameters. Martin [31] presented extensively to the literature on submerged jet impingement and its heat transfer characteristics by compiling experimental data. Chou and Hung [32] conducted an analytical study for cooling of an isothermal heated surface with a confined slot jet. Chou and Hung [33] performed a numerical study for the fluid flow and heat transfer of slot jet impingement with an extended nozzle.

Besides providing high heat transfer coefficients, impingement cooling has the advantage of eliminating the presence of all thermal interface resistances between the power module and the cooling fluid. Heat flux levels of 250 W/cm^2 for water and 40 W/cm^2 for dielectric liquid; have been reported for single-phase impingement [22, 34-36]. With phase change, power densities up to 1000 W/cm^2 can be achieved [37]. Compelling evidence of thermal and electrical (power) performance improvement of a power module by liquid impingement cooling has also

been demonstrated [38, 39]. In one of the most recent works, Olesen et al. [39] presented a new impingement based liquid cooling configuration, which they called *ShowerPower*, for automotive power module cooling application. The design has been shown to have a high thermal performance at a much reduced pressure drop. The data reported by Olesen et al. [39] has been used as a benchmark to compare the present impingement based heat exchanger performance.

All these research have normal orientation of the impinging jets with respect to the target surface in common. Several other researchers investigated the heat transfer distribution and flow characteristics of tilted jets impinging on plane surfaces. In one of the early works, Perry [40] showed the dependency of the heat transfer characteristics on incident angle. He reported that Nusselt number decreases with incident angle and found a correlation $Nu \propto Re^{0.7} Pr^{0.33}$, where the proportional factor depends on incident angle. Sparrow and Lovell [41] as well as Yan and Saniei [42] studied experimental heat transfer results of a circular inclined impingement jet. Both showed the shift of the point of maximum heat transfer from the geometrical impingement point. The displacement increases with higher Reynolds numbers and decreasing incident angles. Furthermore, they presented dependencies of averaged and maximum transfer coefficients on the jet-to-plate distance, the jet Reynolds number and the inclination angle. Goldstein and Franchett [43] showed that the local ratio of Nusselt number divided by $Re^{0.7}$ is independent of the Reynolds number. They proposed a correlation with 4 constants for the local distribution of $Nu/Re^{0.7}$. The correlation accounts for jet-to-plate distance, tilt angle, shift of the stagnation point, and for the local offset from the symmetry line. Most of these studies aimed at looking at the effect of stagnation region on the local heat transfer rates as well as shift of stagnation region and change in the local heat transfer rates due to the changes in jet angles. In all these studies, the

flow is assumed to enter the jets along the axial direction. In other words, the effect of how the flow enters the jet is neglected. Moreover, none of these studies have focused on the effect of heat transfer characteristics of wall-integrated inclined impinging jets. Thus, as a part of the present study, the effect of how the flow enters the inclined jet as well as the effect of wall-integrated inclined impinging jets on heat transfer characteristics is studied.

Inclined jets in wall corners were investigated and analyzed for future high heat flux cooling applications. One of the configuration examined in the present study aims at wall-integrated inclined impinging jets in a confined environment wherein the coolant outlet is perpendicular to the plane of the impinging jets and is along the cross-flow direction. Another objective of the present work was to understand the physics and mechanisms of the jet structure and its interactions with the walls to help in designing a jet impinging cooling scheme for high heat density applications systems such as micro- and meso-scale electronic systems and internal cooling of trailing edge of a turbine blade.

In addition to the impingement based heat exchanger configurations, a combined cooling scheme based on jet impingement and phase change materials (PCMs) has also been presented as one alternative to existing heat exchangers. A high heat storage capability of PCMs in combination with a high heat transfer rates of impingement cooling was believed to help overcome the existing heat distribution and transient cooling problem in high heat flux dissipating devices.

While phase change energy storage has been extensively studied for solar energy applications [44, 45], its use in the thermal management of electronics is being investigated only more recently [46]. Ishizuka and Fukuoka [47] investigated a low melting point metallic PCM (Bi/Pb/Sn/In) and found experimentally that the operating temperature rise of the substrate could

be suppressed for a significant amount of time. Baker et al. [48] performed a conduction-only analysis of the thermal performance of a heterogeneous package. Periodic heating was considered and two nonmetallic PCMs (octadecane and pentacosane) were used for heat storage with metal fins to enhance the effective thermal conductivity. Peak operating temperatures, energy storage rates in the package and the PCM were reported.

Pal and Joshi [49] performed a numerical analysis of the melting of an organic PCM under a constant power input for passive thermal control of a plastic quad flat package. Pal and Joshi [50], also considered transient variations in the power input for passive thermal control of electronic modules. Alawadhi and Amon [51] used a conduction analysis to compare the performance of a PCM thermal control unit, with and without a thermal conductivity enhancer (TCE) included in the domain. More recent PCM applications explored for in electronics thermal management include handsets, portables, and power electronics [46–56]. These materials are particularly attractive for transient applications where the heat loads are pulsed [46, 51]. Commonly used organic and non-metallic PCMs (e.g. Paraffin) have very low thermal conductivity and could potentially increase the thermal resistance. In order to improve the effective thermal conductivity and enhance heat transfer rates, internal fins and metal foams have been introduced into the PCM [57–60]. However, a combined PCM-jet impingement cooling scheme for such high heat density applications has not been explored before. In the present study, a combined PCM-jet impingement based heat exchanger has also been proposed and its thermal performance has been evaluated both experimentally as well as numerically using readily available commercial codes.

In addition to jet impingement-based cooling configurations, pin fin cooling schemes in the form of micro-fins and mini-channels (~ 1 mm) are also a few options. Although micro-

channel cooling cannot be applied to hybrid vehicles but the advancement in micro-channel technology can surely be applied in the form of mini-channels. Inspired by the fractal pattern of mammalian circulatory and respiratory systems, a new design of fractal branching micro-channel net for cooling of electronic chips was studied [61, 62]. Their analysis shows that the new fractal branching channel net has a stronger heat transfer capability with a lower pumping power than that of the traditional parallel micro-channels. In other words, the fractal branching micro-channel net has a higher thermal efficiency than that of the parallel micro-channel net. Subsequently, Pence [63] also made some comparisons on a fractal-like branching channel network heat sink with a parallel channel array heat sink. It was pointed out that with identical total convective surface areas for both configurations and maintaining a heat sink surface area equal to that of the convective surface area, the fractal-like channel network yielded a 60% lower pressure drop for the same total flow rate and a 30 °C lower wall temperature under identical pumping power conditions. A similar concept was applied by Lei et al. [64] to reduce thermal resistances and overall pressure drop by stacking multiple layers of low aspect ratio (circular or square cross-section) channels together to create multiple layer mini-channel heat sinks. They studied copper and SiC based multilayer mini-channel heat sinks and showed that these heat sinks have significant advantages over single-layer equivalents in terms of reductions in thermal resistance and overall pressure drop. Most of these mini-channel cooling schemes are based on enhancing the effective fluid-solid contact surface area and reducing the overall pressure drop by distributing the flow among a number of channels. By doing this, each individual channel gets a small share of the total flow rate and thus, the flow inside usually gets developed hydrodynamically as well as thermally over a very small length. As a consequence, the heat transfer rate for each individual channel is constant for almost the entire length and is not able to utilize

the high heat transfer rates associated with the development region. For very high flow rates, that is not the case as the flow is turbulent for most of the channel length. In the present study, rib-turbulated mini-channel configurations are studied as possible alternatives to further enhance the heat transfer rates in mini-channels operating at low pumping powers.

Over the last few years, CFD using Reynolds-averaged Navier–Stokes equations, coupled with turbulence modeling, has become a standard practical simulation tool for the design and analysis of engineering systems. In the present work, similar approach has been taken for the designing and analysis of jet impingement cooling schemes for high performance micro scale electronic systems. Simulations validated with theory and experiments were used to study various cooling options based on impingement for application in hybrid electric vehicle and other similar consumer products and to perform parametric and optimization study on the selected designs. The optimized design was then applied to generate specific heat exchanger designs for cooling of automotive power converters and simulated to meet the required temperature and pumping power constraints. The high performance design was then fabricated and tested under conditions similar to the actual running environment.

CHAPTER 3: APPLICABLE COOLING SCHEMES AND OVERALL HEAT EXCHANGER DESIGNS

The main objective of the present study was to design, simulate, test and fabricate a high performance heat exchanger capable of maintaining the maximum operating temperatures of the silicon chips (18 pairs of IGBTs and Diodes) in the High-Density Power Control Unit below 120 °C under extreme running conditions. The objective (presented in Section 1.3) was to be achieved under certain constraints. The heat exchanger should be capable of cooling 220 W/cm² dissipated by active devices under normal operating conditions. LLC30 (50% vol./vol. mix of water and ethylene glycol) with an overall volumetric flow rate (Q) of 10 L/min should be used as the coolant and the coolant temperature at the heat-exchanger inlet will be around 65 °C. The maximum pressure allowed across the heat exchanger was around 10 kPa. Additionally, due to reliability and coolant compatibility issues, the heat exchanger should be fabricated from Aluminum or an Aluminum alloy.

Based on these requirements and constraints, a conservative analysis (Eq. (3.1)) was performed using an overall energy balance to estimate the required heat transfer coefficient.

$$\dot{E}_{in} = \dot{E}_{out} \quad (3.1)$$

where, \dot{E}_{in} is the rate of energy flowing into the heat exchanger (that is, heat dissipated by the active Silicon devices) and \dot{E}_{out} is the rate of energy flowing out of the heat exchanger (that is, heat taken away by the coolant). Hence,

$$\begin{aligned} \dot{E}_{out} &= \dot{m}c_p\Delta T \\ \Delta T &= T_{out,avg} - T_{in,avg} \end{aligned} \quad (3.2)$$

where T is the temperature and $\dot{m} = \rho Q$ is the mass flow rate with ρ being the coolant density and Q being the volumetric flow rate. Subscripts ‘ in,avg ’ and ‘ out,avg ’ stand for average inlet and outlet temperatures, respectively.

For coolant inlet temperature of 65 °C and heat dissipation rate of 7 kW, the above relation gives $\Delta T \sim 11$ °C resulting in 76 °C average coolant temperature at the heat exchanger exit. Hence, the average coolant temperature ($T_{c,avg} = (T_{out,avg} + T_{in,avg})/2$) could be estimated to be ~ 70.5 °C. Maintaining a 45° heat spreading angle, the heat flux at the cooling system surface (wall, Figure 3.1) would be around 120 W/cm². Thus, in order to maintain the active devices temperature less than 115 °C (5 °C as a safety factor), an effective heat transfer coefficient (h_{eff}) of about 60,000 W/m²K was required.

$$h_{eff} = \frac{q''_{wall}}{(T_{wall,avg} - T_{c,avg})} \quad (3.3)$$

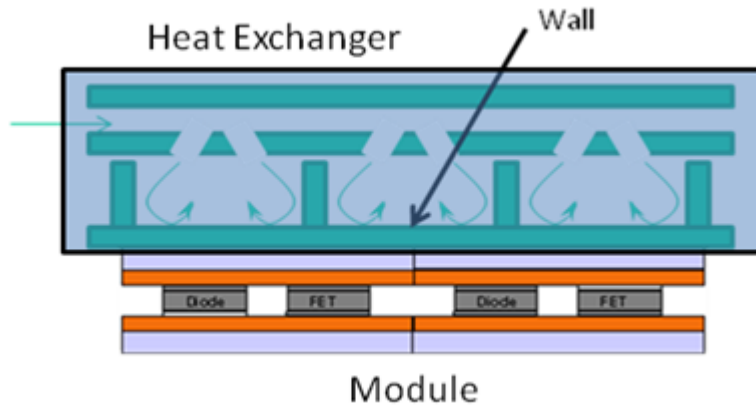


Figure 3.1. Schematic showing the placement of the heat exchanger with respect to the active components of the high-density power control unit. Figure also shows a cross-sectional view of the heat exchanger based on SIF cooling scheme.

This high heat transfer coefficient is based on the effective heat flux under the active IGBT device and not under the diode. Hence, this high average heat transfer coefficient was required for smaller regions under the IGBT locations. Following a similar analysis, the average

heat transfer coefficient at the heat exchanger base plate under the diode was required to be around $15000 \text{ W/m}^2\text{K}$. This is based on the fact that power dissipated by the diode is about one quarter of that dissipated by the IGBT unit. In other words, the overall heat transfer coefficient at the heat exchanger base plate should be somewhere in between $15000 - 60^{\circ}00 \text{ W/m}^2\text{K}$ and not $60^{\circ}00 \text{ W/m}^2\text{K}$ for the whole heat exchanger base area. Also, having an overall heat transfer coefficient of $60^{\circ}00 \text{ W/m}^2\text{K}$ would have been an over-design and moreover, a very difficult requirement to meet. The value is also beyond the attainable limits within the constraints of flow rate and pressure drop.

3.1. Applicable and Selected Cooling Schemes

The aforementioned design parameters and constraints necessitated the use of high performance cooling schemes such as direct-cooled impingement and mini-channel based structures. In the direct-cooled impingement based structures (Figure 3.2), the coolant is in direct contact with the back of the power module substrate. Using this method, the heat-exchanger can be made out of any material (even plastics), as it is only used to guide the coolant, not for heat transport. Also, as there is no need to compensate for surface roughness, the substrate can be mounted onto the heat-exchanger with little clamping force (just enough to seal properly). In this case, DBC or DBA substrates can have enough mechanical strength to be used without a base-plate. Additionally, modifications can be made for example, when the heat exchanger is made out of materials like Copper and Aluminum, separating walls can be placed between the jets, so as to significantly enhance the effective surface area for heat transport. Also, neighboring jets can be angled towards the center of the MOSFETs so as to attain a much higher heat transfer rate. Based on such modifications, heat exchanger designs as shown in Figure 3.2 can be generated.

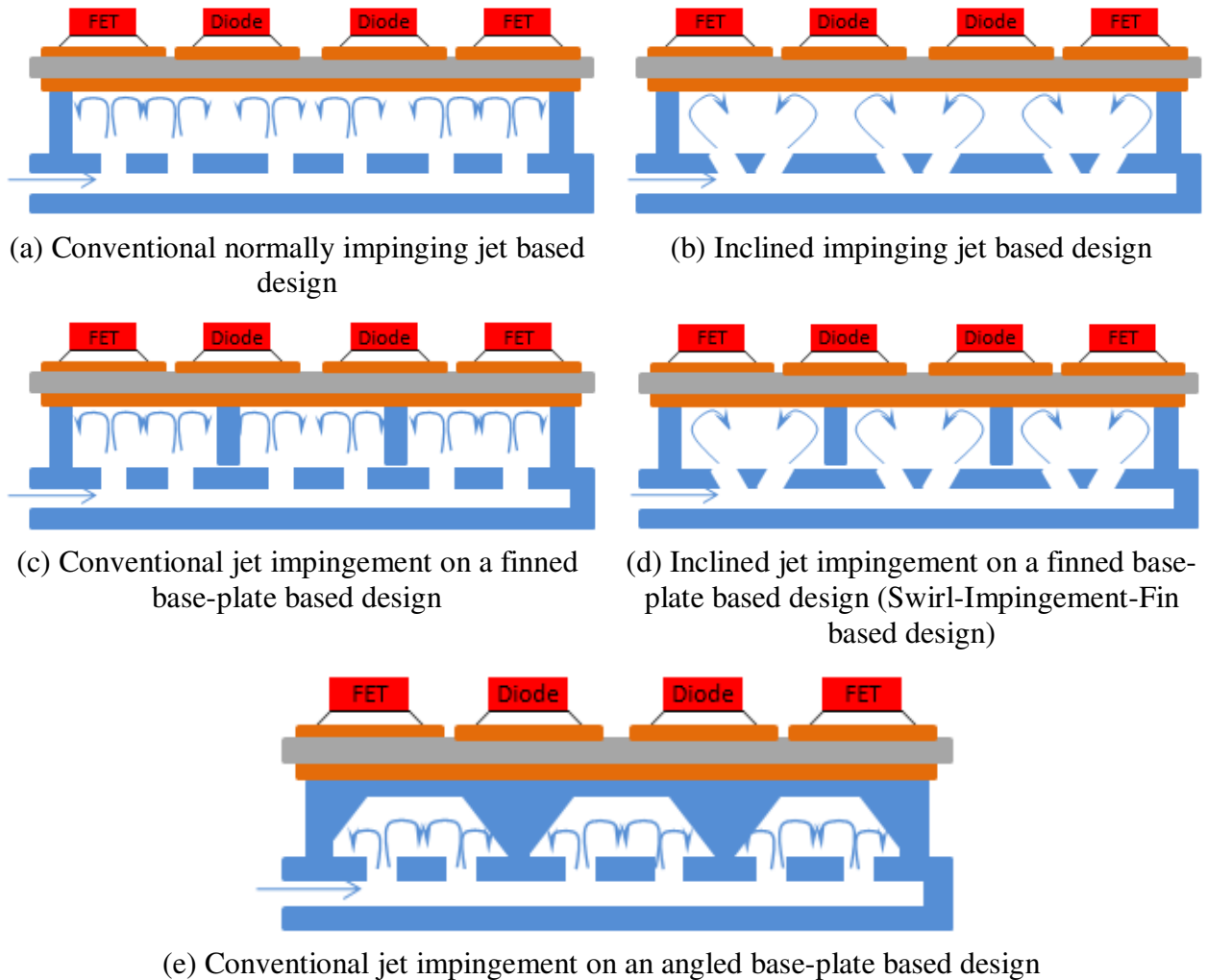


Figure 3.2. Impingement based heat exchanger designs for a conventional power module package.

Figure 3.2(a) shows the cross-sectional view of a heat exchanger design based on conventional jet impingement cooling. This approach uses coolant, which is directed normal/perpendicular to the heat transfer surface (wall) as an impinging jet. This method has proven to produce very high, localized convection coefficients that can be arranged in a pattern to cool the active areas of the chips. Figure 3.2(b) shows the cross-sectional view of a heat exchanger design based on conventional inclined jet impingement cooling. This approach uses coolant, which is directed at an angle to the heat transfer surface (wall) as an impinging jet. The orientation of the jets induce natural swirl in the flow after impingement which reduces the

stagnant boundary layer similar to an impinging jet but over a larger area. This method has been proven to produce higher localized convection coefficients than the corresponding normally impinging configuration [65, 66] and can also be arranged in a pattern to cool the active areas of the chips. Figure 3.2(c) shows the cross-sectional view of a conventional jet impingement approach in combination with conventional finned cooling. In this cooling scheme, rectangular or circular fins are present on the base plate and the coolant jets impinge normally onto this base plate. The fins enhance the heat transfer by extending the surface area and reducing the jet-jet interactions. However, they have a potential to increase the overall pressure drop significantly. This scheme can be optimized to attain a high heat transfer coefficient with a nominal increase in pressure drop as compared to the conventional jet impingement cooling.

Figure 3.2(d) shows the cross-sectional view of a swirl-impingement-fin (SIF) cooling configuration. This new impingement cooling design takes the advantage of key principles of both impinging jet and conventional fin cooling. In SIF cooling an angled jet is directed against a wall perpendicular to the base plate. The jet is deflected by the wall and directed against the base plate, then continues along the base plate to the drain. This swirling action reduces the stagnant boundary layer similar to an impinging jet, but over a larger area, which is believed to result in a higher convection coefficient. This advanced design has several parametric variations that may be used to match the required hot surface geometry. Figure 3.2(e) shows the cross-sectional view of another heat exchanger design based on SIF concept. The earlier proposed swirling-impingement scheme involved angled impingement (angled jet) onto a normal target plate. However, the new scheme uses normal impingement on angled walls. Both the schemes induce a swirling motion into the flow stream. Conceptually, both the designs are similar but look different. Owing to the simplicity of this design, it can be manufactured much easily as

compared to the earlier design. However, the overall pressure drop and the overall average heat transfer coefficient might be lower.

All the earlier designs discussed were based on impingement cooling which aimed at attaining a very high local heat transfer coefficient. However as we go away from the impingement region, the heat transfer coefficients can be relatively low and hence, a low averaged heat transfer coefficient. Thus, it becomes essential to remove the heat from these low heat transfer coefficient regions by utilizing the conduction effect through the cooler body (that is, by using fins, center walls etc.). Moreover, by using angled impingement on finned walls, a higher local and overall heat transfer coefficients can be obtained as well as the high heat transfer regions can be extended.

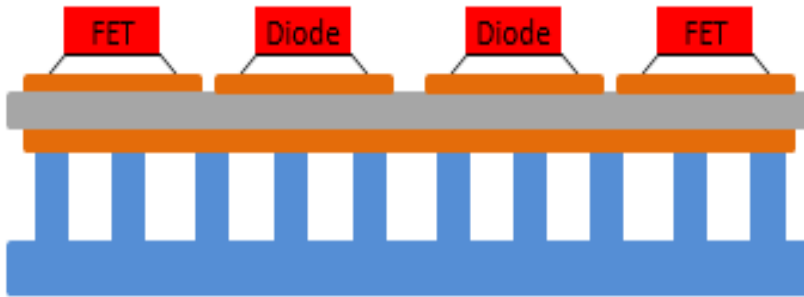


Figure. 3.3. Direct-cooled mini-channel based cooling configuration.

On the other hand, pin-fin or micro-fin or mini-channel based cooling schemes can also be employed in a direct-cooled (Figure 3.3) as well as indirect-cooled configurations. The essential feature of such extended surface cooling is that it takes the advantage of both convection heat transfer at the fluid-solid interface as well as conduction heat transfer through the cooler bulk material. Also, it can help reduce the effective heat transfer coefficients required at the fluid-solid interfaces. This feature, as a consequence, requires the heat sink to be fabricated from highly conductive materials like Aluminum and Copper. Figure 3.3 shows a direct-cooled

mini-channel based cooling configuration where the channel walls are attached to the bottom surface of the power module substrate. The attachment could be a direct metal-to-metal bonding or a solder bond which enables a larger heat spreading through the cooler bulk by reducing interface thermal resistances [67].

3.2. Overall Heat Exchanger Structures

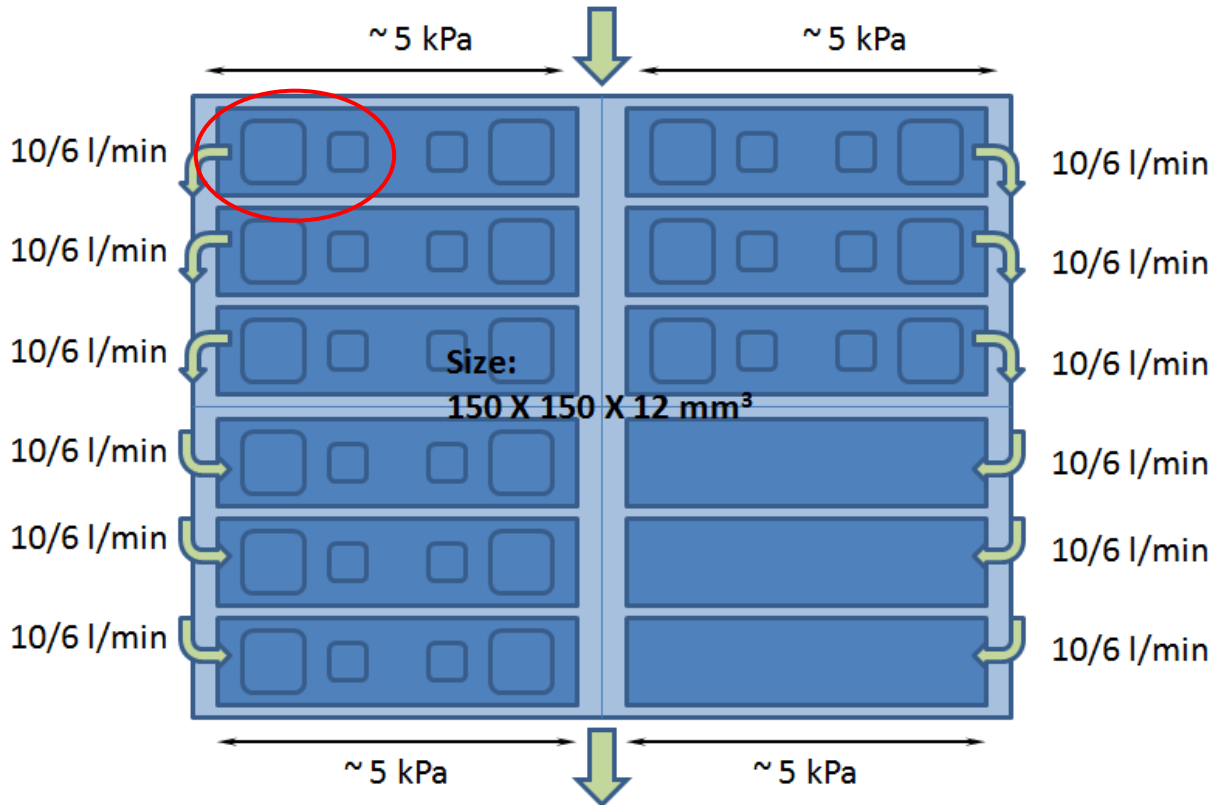


Figure 3.4. Schematic of the overall heat exchanger structure which allows 0.025 L/s flow rate and ~2.5 kPa pressure drop across the simulation model.

Before applying any of the above proposed schemes, it was important to analyze the possible overall heat exchanger structures for an approximate active-devices location and allowed pumping power through a small repetitive structure. Six major overall heat exchanger structures were considered either to maximize the flow rate through each individual channel or to maximize the allowed pressure drop through each channel. Based on the overall structures, the allowable pressure drop across the simulated model (marked by red circle in Figure 3.4) was

required to be ~ 2.5 kPa for a flow rate ~ 0.025 L/s through this section, or ~ 5 kPa for a flow rate ~ 0.0125 L/s through this section, or ~ 5 kPa for a flow rate ~ 0.0185 L/s through this section, or ~ 10 kPa for a flow rate ~ 0.00925 L/s through this section, or ~ 1 kPa for a flow rate ~ 0.0416 L/s through this section, or ~ 2 kPa for a flow rate ~ 0.0208 L/s through this section.

Figure 3.4 shows a schematic of the overall heat exchanger structure that allows 0.025 L/s flow rate and ~ 2.5 kPa drop across the simulation model. This structure allows for higher flow rate through each channel and hence, is good for large number of jets in parallel or pin-fin/mini-channels cooling scheme. However, this design does not allow for higher-pressure drop and thus, high-speed jets cannot be used.

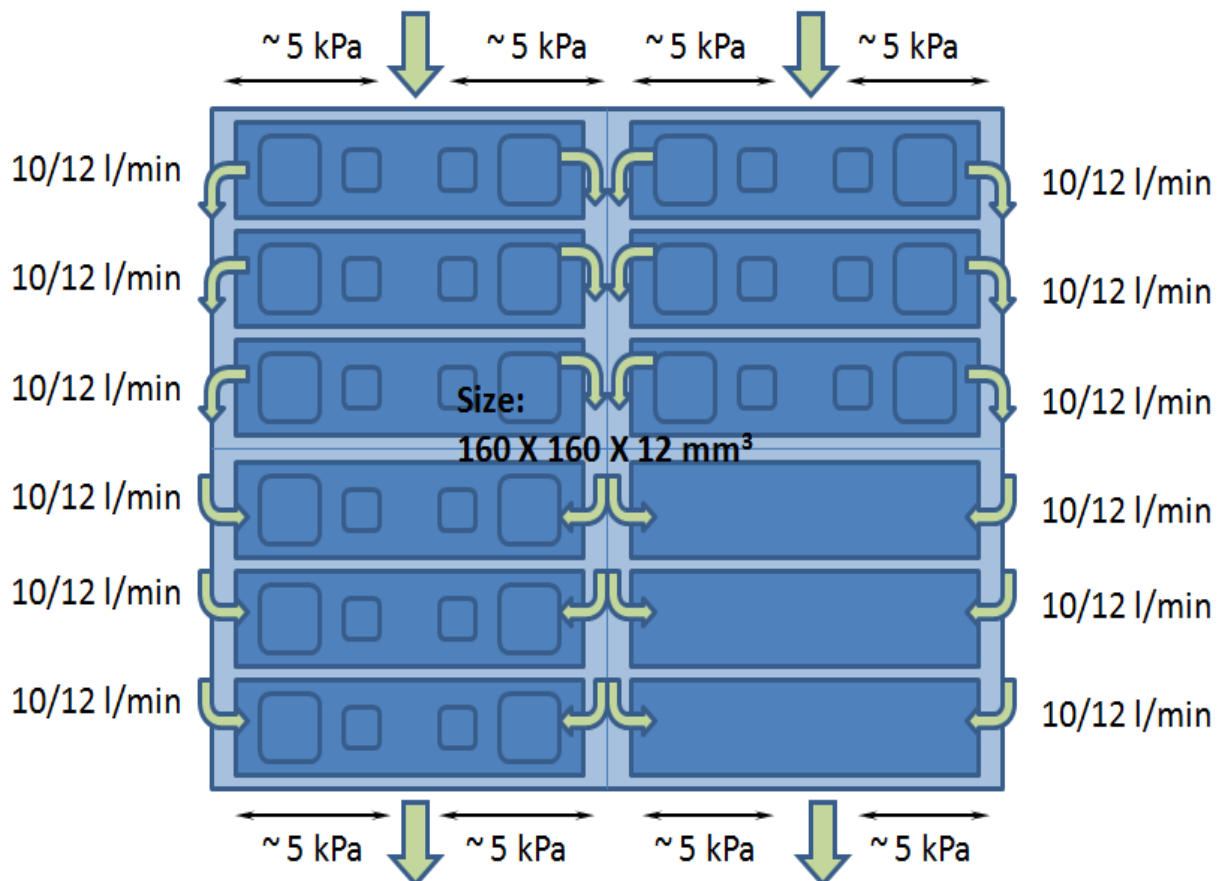


Figure 3.5. Schematic of the overall heat exchanger structure which allows 0.0125 L/s flow rate and ~ 5 kPa pressure drop across the simulation model.

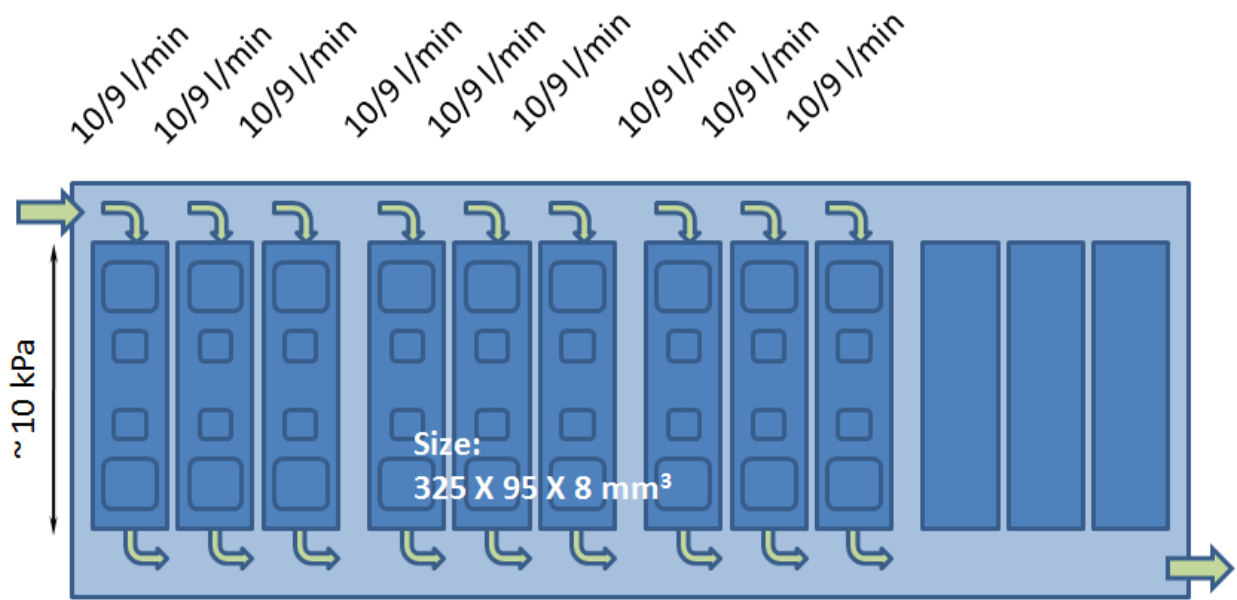


Figure 3.6 Schematic of the overall heat exchanger structure which allows for 0.0185 L/s flow rate and ~5 kPa pressure drop across the simulation model.

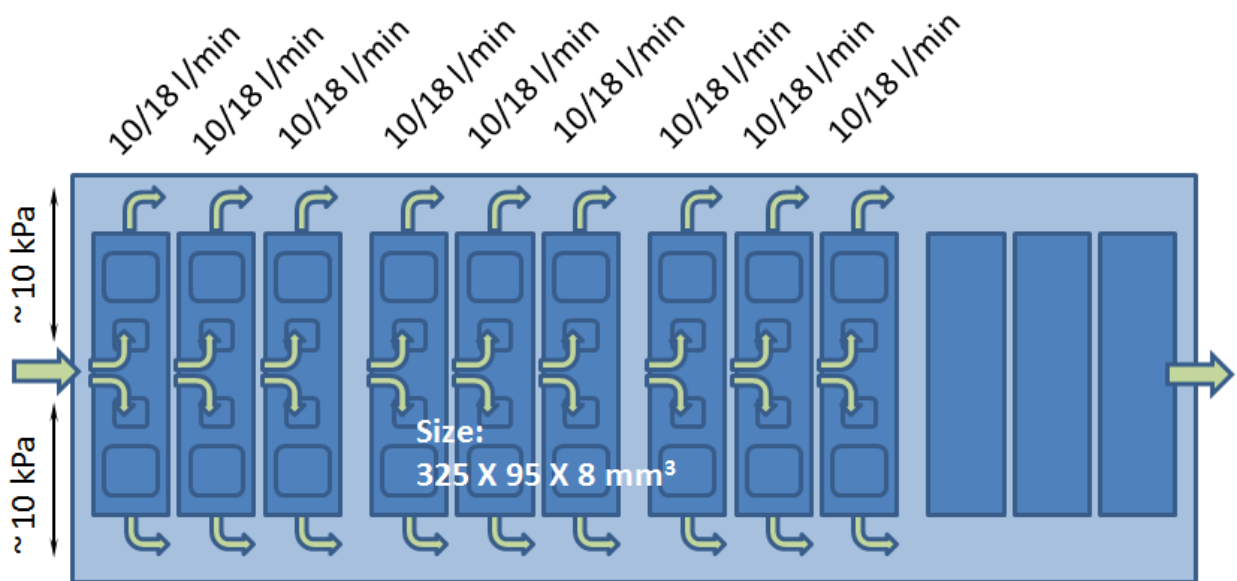


Figure 3.7. Schematic of the overall heat exchanger structure which allows for 0.00925 L/s flow rate and ~10 kPa pressure drop across the simulation model.

Figure 3.5 shows a schematic of the overall heat exchanger structure that allows for 0.0125 L/s flow rate and ~ 5 kPa pressure drop across the simulation model. This structure

allows for slightly reduced flow rate as well as increased allowable pressure drop. It is good for slightly high speed jets as well as combined impingement/pin-fin/mini-channels cooling schemes. Figure 3.6 shows a schematic of the overall heat exchanger structure that allows for 0.0185 L/s flow rate and ~5 kPa pressure drop across the simulation model. This structure allows for a higher flow rate at the same allowable pressure drop as compared to the previous structure. This structure is very good for pin-fin/mini-channel cooling schemes. *One of the best ribbed mini-channel models from this study was based on this overall design.*

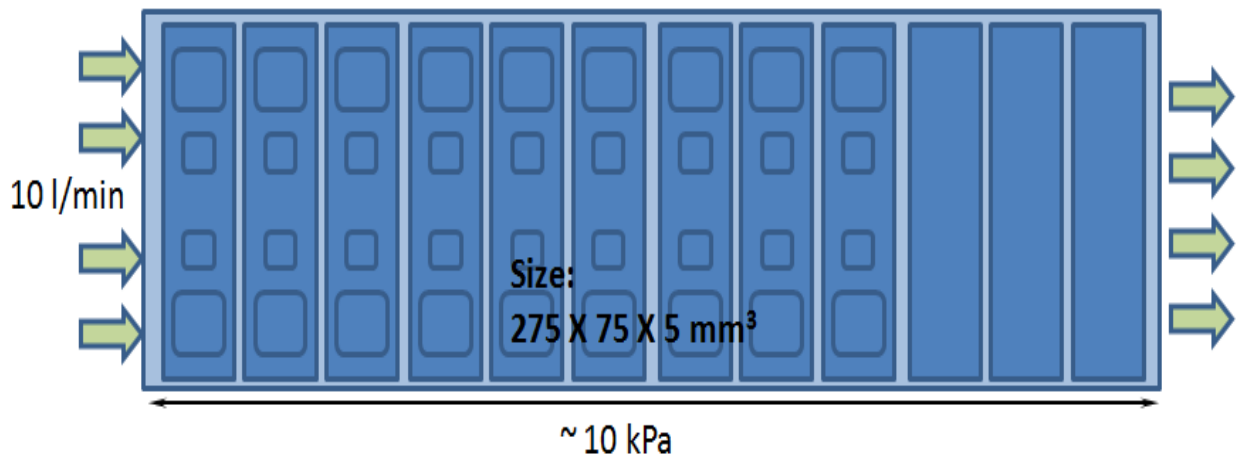


Figure 3.8 Schematic of the overall heat exchanger structure which allows for 0.0416 L/s flow rate and ~1 kPa pressure drop across the simulation model.

Figure 3.7 shows a schematic of the overall heat exchanger structure that allows for 0.00925 L/s flow rate and ~10 kPa pressure drop across the simulation model. This structure allows for highest allowable pressure drop at the expense of reduced flow rate through each channel. This model is very good for impingement as it can allow high-speed jets in series. However, as the flow rate is very low, it is not well suited to mini-channel/pin-fin cooling scheme. It might work well for micro-channel cooling, but then we will not be able to meet the minimum channel size constraints. *The best impingement cooler model was based on this overall design.*

Figure 3.8 shows a schematic of the overall heat exchanger structure that allows for 0.0416 L/s flow rate and ~ 1 kPa pressure drop across the simulation model. This structure allows for a much higher flow rate at much reduced allowable pressure drop as compared to the previous structures. This structure is very good for pin-fin/mini-channel cooling schemes.

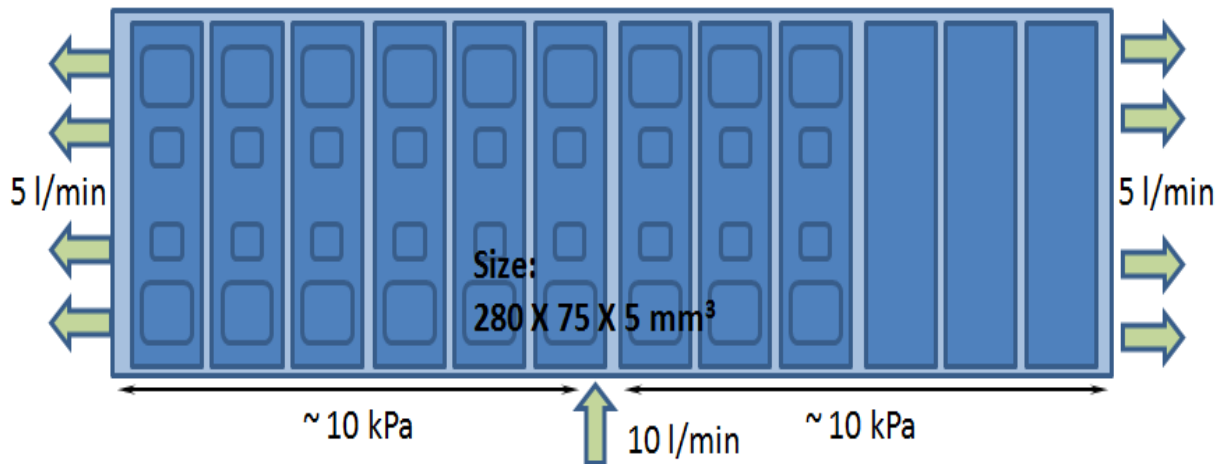


Figure 3.9. Schematic of the overall heat exchanger structure which allows for 0.0208 L/s flow rate and ~ 2 kPa pressure drop across the simulation model.

Figure 3.9 shows another schematic of the overall heat exchanger structure that allows for 0.0208 L/s flow rate and ~ 2 kPa pressure drop across the simulation model. This structure allows for a higher allowable pressure drop at the expense of reduced flow rate through each channel. This model is also very good for mini-channel/pin-fin based schemes. However, as the allowed pressure drop is very low, it is not well suited to impingement based cooling schemes. It might also work well for micro-channel cooling but then we will not be able to meet the minimum channel size constraints. *One the best mini-channel cooler models so far is based on this overall design.* It should be noted here that the flow direction, with respect to the IGBT and Diode locations, in overall heat exchanger structures 5 and 6 is perpendicular to the flow direction compared to previous four overall structures. It is therefore simpler to have a more uniform coolant distribution in these structures.

3.3. Flow Distribution

In addition to the overall heat exchanger designs, it was also important to check the feasibility of even flow distribution through each of the unit structures. Figure 3.10 shows an impingement cooler based on the overall heat exchanger structure 1 that was studied. It had overall dimensions of about 199 mm X 188 mm X 10 mm and consisted of one inlet and one outlet ports and 1024 jet holes with 1 mm diameter each. Figure 3.11 shows the sectional views of this model with the arrows indicating the flow directions. This model is symmetric only about the YZ-plane passing through the center of the inlet and outlet ports.

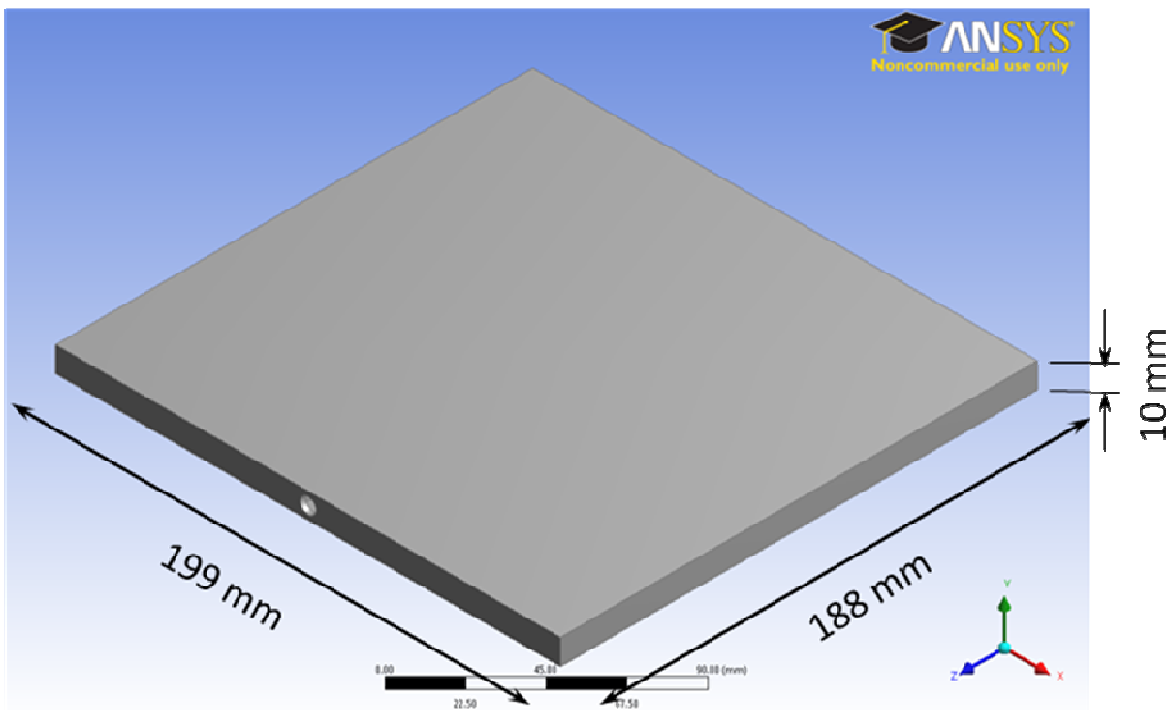


Figure 3.10. Overview of an impingement cooler based on the overall heat exchanger structure 1.

Figure 3.12 shows the fluid domain for a smaller portion of the model under consideration. The pink arrows show the plane of symmetry and the other colored arrows show the in- and out- flow directions. A constant heat flux was applied at the bottom surface while all the other surfaces were taken to be adiabatic walls.

Figure 3.13 shows the wall heat transfer coefficients at the target surface for the model shown in Figure 3.12. Normally impinging jets were considered in this design. It can clearly be seen that the heat transfer or rather the flow distribution are not uniform. The main aim of this simulation was to identify the flow distribution and to use as stepping stone for future modifications. Therefore, a coarse mesh was used and the reported values are much different from the actual values. Figure 3.14 shows the fluid velocity vectors and highlights the reason for the non-uniformity of the heat transfer coefficient at the target surface. Clearly, most of the fluid goes toward the end of the inlet plenum and thereby causing an uneven distribution.

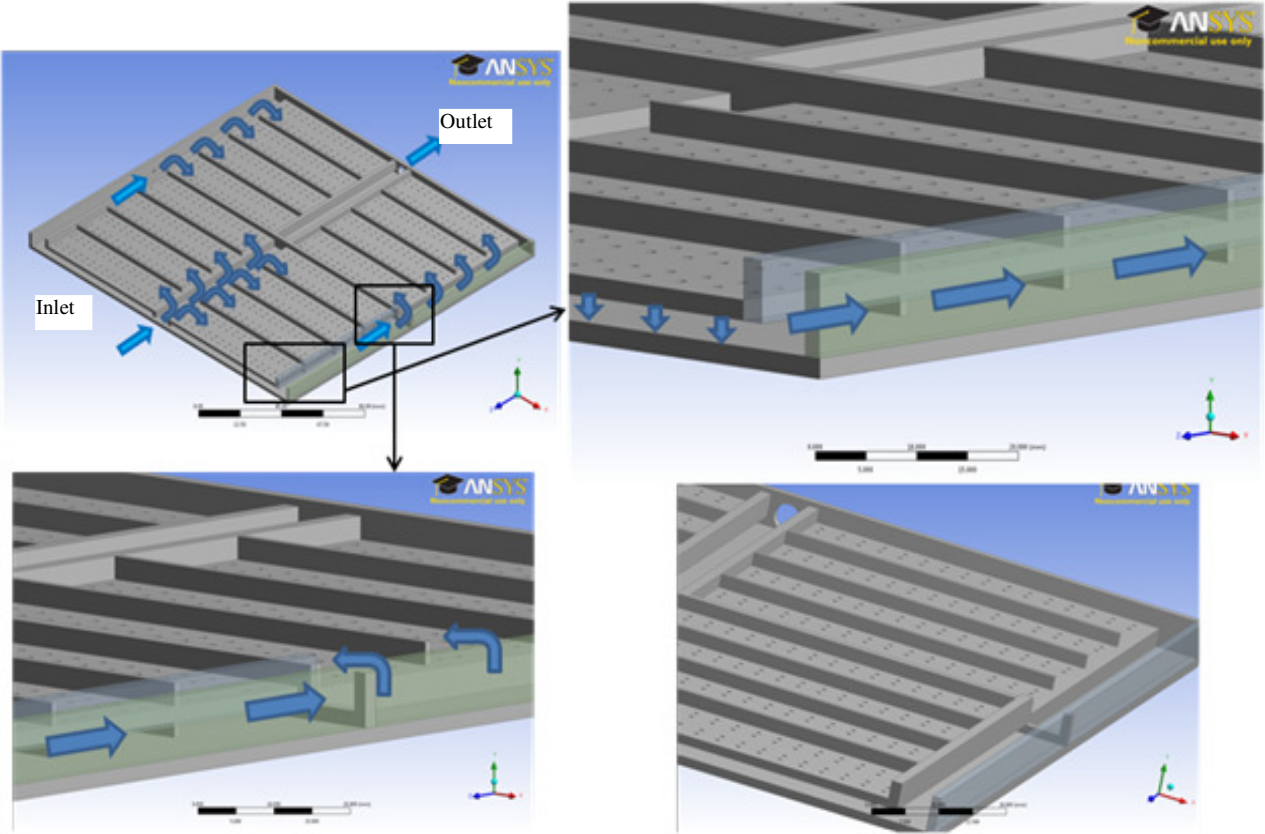


Figure 3.11. Sectional views of impingement cooler with the arrows indicating the flow direction.

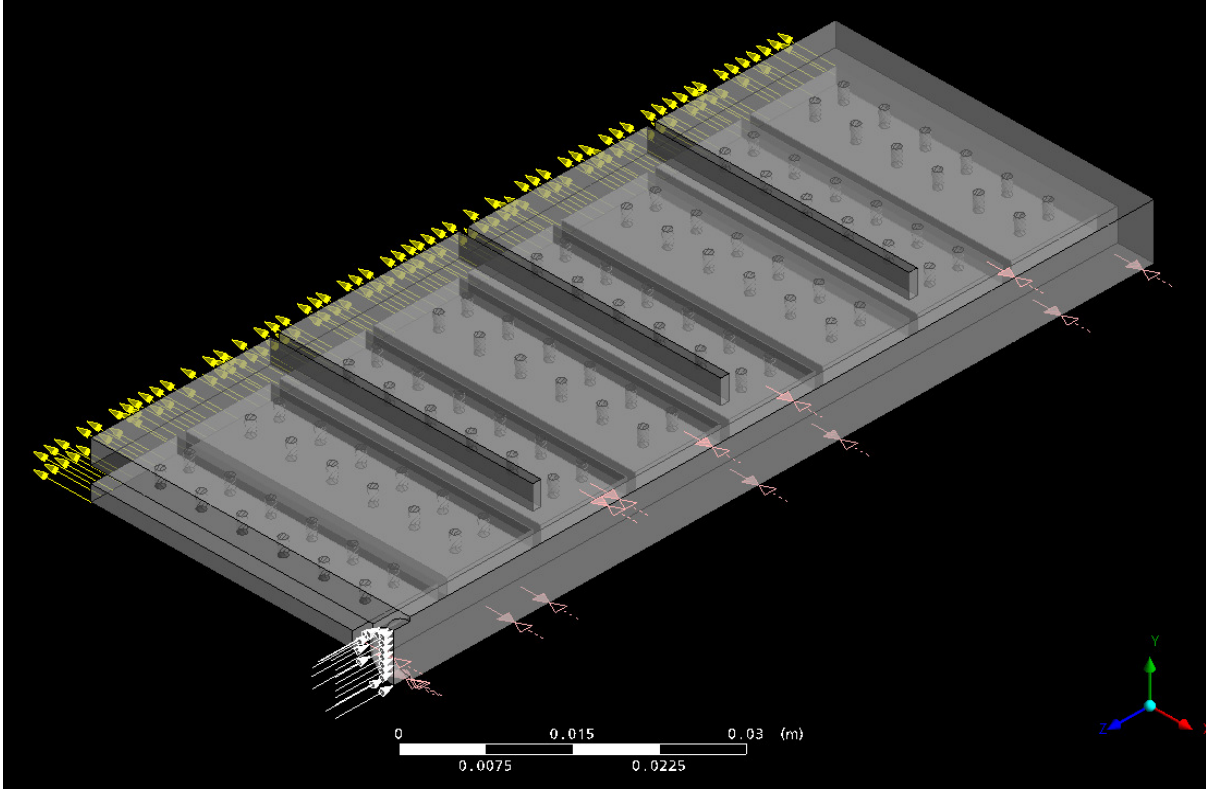


Figure 3.12. Fluid domain for a portion of the impingement cooler. White arrows indicate the inlet; yellow arrows indicate the outlet and the pink arrows represent the plane of symmetry.

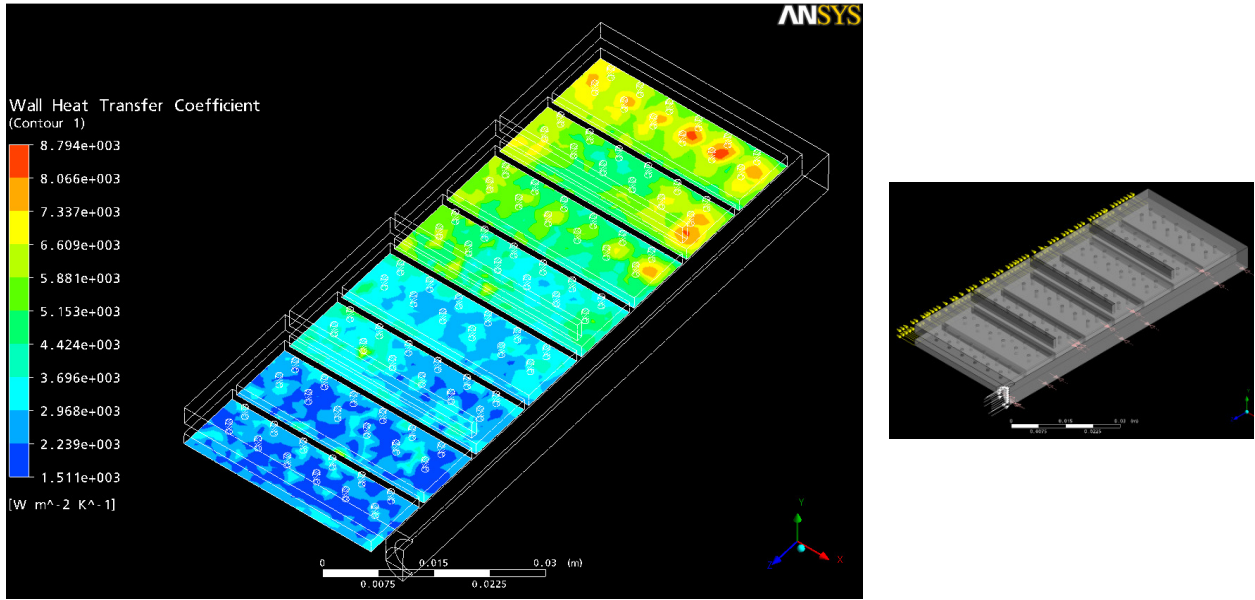


Figure 3.13. Wall heat transfer coefficients at the target surface for a smaller section of the second preliminary design. A coarse mesh was used near the walls. Angle of the jet holes = 90° from the horizontal (i.e., normally impinging jets).

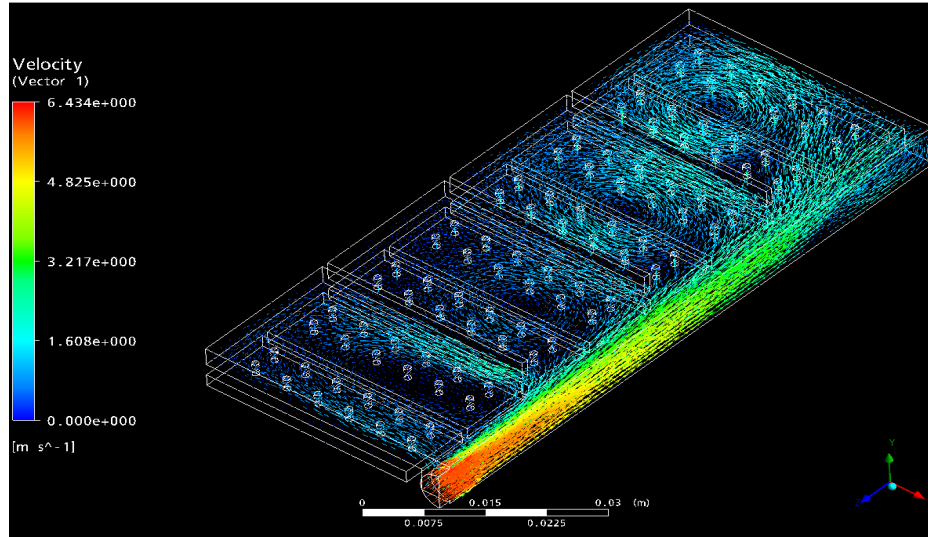


Figure 3.14. Fluid velocity vectors at the target surface for a smaller section of the second preliminary design. A coarse mesh was used near the walls. Angle of the jet holes = 90° from the horizontal (i.e., normally impinging jets).

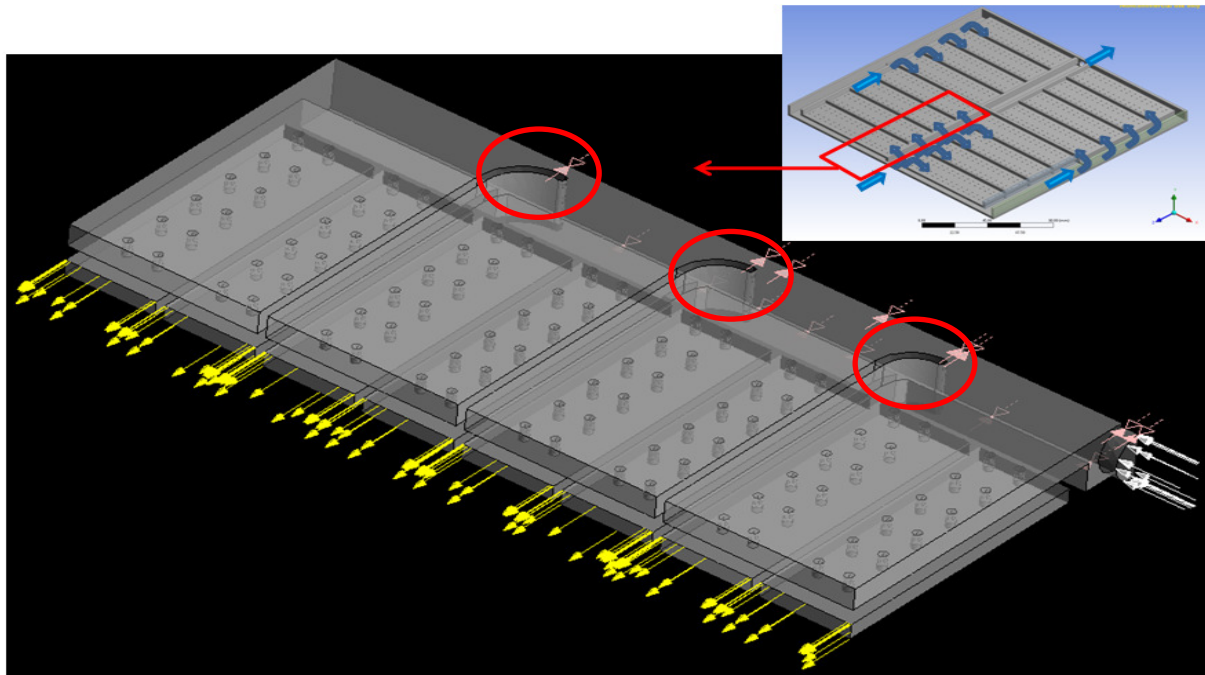


Figure 3.15. Fluid domain for a portion of the modified impingement based heat exchanger design with normally impinging jet holes with the red circles highlighting the modifications. White arrows indicate the inlet; yellow arrows indicate the outlet and the pink arrows represent the plane of symmetry.

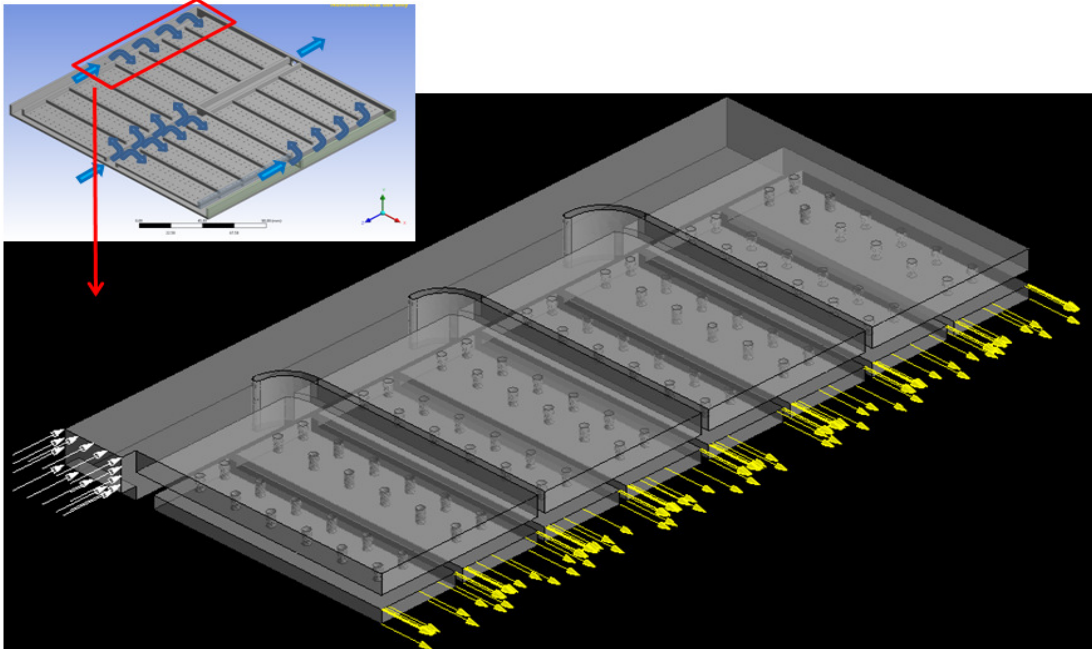


Figure 3.16. Fluid domain for another portion of the impingement-based heat exchanger design with normally impinging jet holes. White arrows indicate the inlet; yellow arrows indicate the outlet.

After observing this non-uniform flow and thermal behavior of the above model, few modifications were made to have a more uniform distribution of the flow field. Figure 3.15 shows the modified model. The modification is marked by the red circles and can be interpreted as curved extension of the larger fins. Figure 3.15 also shows the fluid domain for a small portion (marked by red quadrilateral) of the heat exchanger with normally impinging jet holes. This simulated portion was closer to the inlet of the heat exchanger. The pink arrows show the plane of symmetry while the other colored arrows show the inlet and outlet flow directions. Except for the bottom surface where a constant heat flux was applied, all other outer surfaces were considered to be adiabatic walls.

Figure 3.16 shows the fluid domain for another small portion (marked by red quadrilateral) of the heat exchanger with normally impinging jet holes. This portion is far away from the inlet. Here again, the white and yellow arrows show the in- and out-flow directions, respectively. There is no plane of symmetry as this portion is closer to the side wall of the heat

exchanger. A constant heat flux was applied at the bottom surface while all other surfaces were taken to be adiabatic walls.

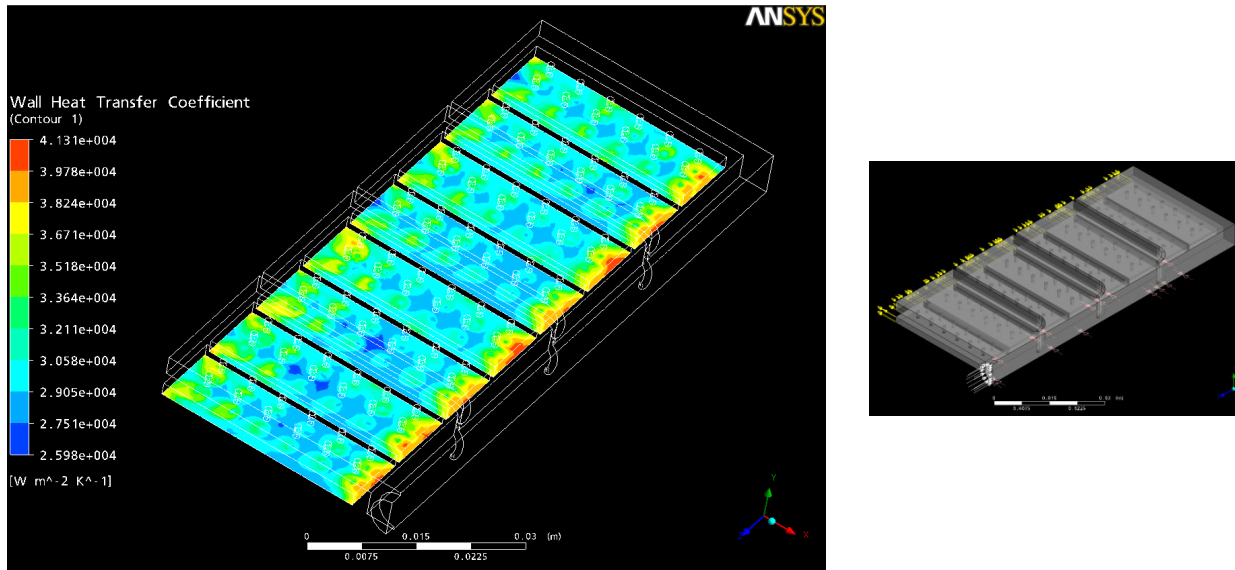


Figure 3.17. Wall heat transfer coefficients at the target surface for a smaller section of the modified design. A medially refined mesh was used near the walls. Angle of the jet holes = 90° from the horizontal (i.e., normally impinging jets).

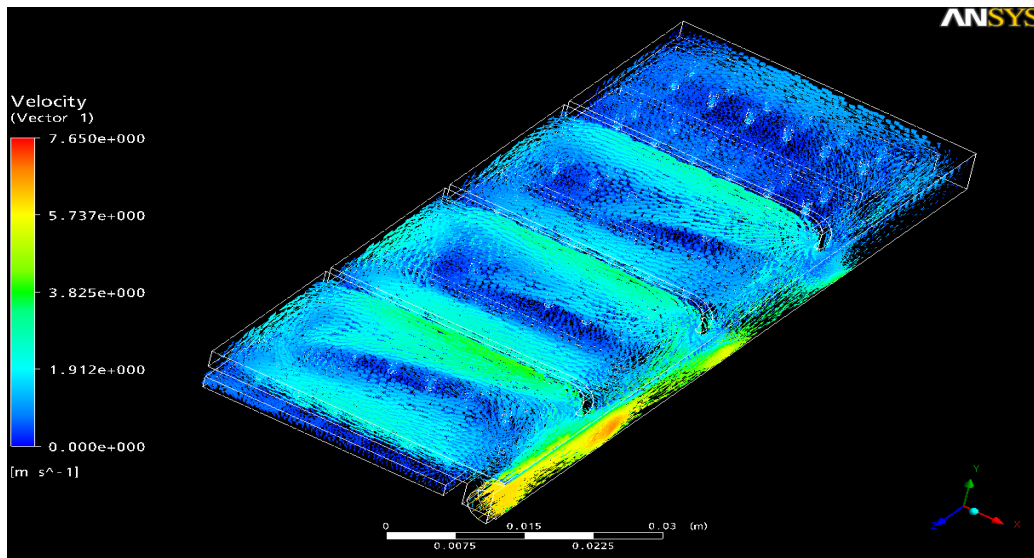


Figure 3.18. Fluid velocity vectors at the target surface for a smaller section of the modified design. A medially refined mesh was used near the walls. Angle of the jet holes = 90° from the horizontal (i.e., normally impinging jets).

The above mentioned non-uniformity was countered by incorporating a small modification as shown in Figure 3.15. The simulation results for this model are reported in

Figure 3.17. Clearly, the distribution of the heat transfer coefficient at the target surface was much more uniform. A medially refined mesh was used and hence the reported values were closer to the actual values. Figure 3.18 shows the fluid velocity vectors and justifies the uniformity of the fluid and thermal behavior. Moreover, the presence of curved fin extensions helped in the even distribution of the incoming fluid. In short, it was possible to have uniform flow distribution across multiple channels by incorporating few features such as the curved fin extensions.

3.4. Summary

Based on the heat exchanger design objectives and constraints, a conservative analysis was performed using an overall energy balance to estimate the required heat transfer coefficient. The effective heat transfer coefficient required locally under the IGBTs and diodes was estimated to be $60000 \text{ W/m}^2\text{-K}$ and $15000 \text{ W/m}^2\text{-K}$, respectively. This requirement necessitated the use of high performance cooling schemes such as direct-cooled impingement and mini-channel based structures. However, before applying any of these schemes, it was important to analyze the possible overall heat exchanger structures for an approximate active-devices location and allowed pumping power through a small repetitive structure. Six major overall heat exchanger structures were considered either to maximize the flow rate through each individual channel or to maximize the allowed pressure drop through each channel. Additionally, flow through these overall heat exchanger structures was simulated to check the feasibility of even coolant distribution through each of the unit structures. It was shown that uniform flow distribution across multiple channels can be achieved by incorporating certain features such as the curved fin extensions.

CHAPTER 4: CONCEPT TESTING

Concepts for pin-fin and channel cooling schemes is well developed and many correlations for the heat transfer coefficient estimation can be found in heat transfer books and thus, rough estimate of wall heat transfer coefficient for any given flow rate can be made. Even for single impinging jet cooling scheme, correlations are well developed. However, for multiple-jet array impingement, multiple inclined-jets array impingement and flow through fractal-like channels, there are no available correlations. Thus, it was very important to characterize their performance against conventional cooling schemes before implementing the designs based on these new schemes. Owing to the localized nature of the active heat sources and high local heat transfer rates offered by impingement, only impinging jets based cooling schemes presented earlier were selected for concept testing. Preliminary simulations showed that inclined/angled impingement having a configuration similar to Figure 3.2(b) and Figure 3.2(d), showed a higher local heat transfer coefficient resulting in lower devices temperature. Configuration similar to Figure 3.2(e) was not found out to be useful as the local as well as the average wall heat transfer coefficients were lower than the convention jet impingement scheme for a fixed jet-target-plate spacing. This observation was validated experimentally as well.

4.1. Thermo-chromic Liquid Crystal Test Setup

A thermo-chromic liquid crystal based test bed was used to study the thermal behavior of the impinging air jets for different jet angles and jet-to-target plate spacing. Figure 4.1 shows a schematic of this test-bed. Compressed air from the storage tank was used as the coolant and was regulated down to required flow rate using a pressure regulator and flow control valves. The regulated air was then fed through a diffuser and a rectangular plenum which allowed the flow to decelerate and expand before the jet plate to ensure even flow distribution across the jets array.

The test bed was designed to provide improved heater response by reducing the thermal capacitance of the heater and placing it close to the test section. The heater was placed at the exit of the plenum and a spacer separated it from the jet plate. The mesh heater used has the capability of providing an instantaneous temperature step to the mainstream air (Esposito et al., [68]).

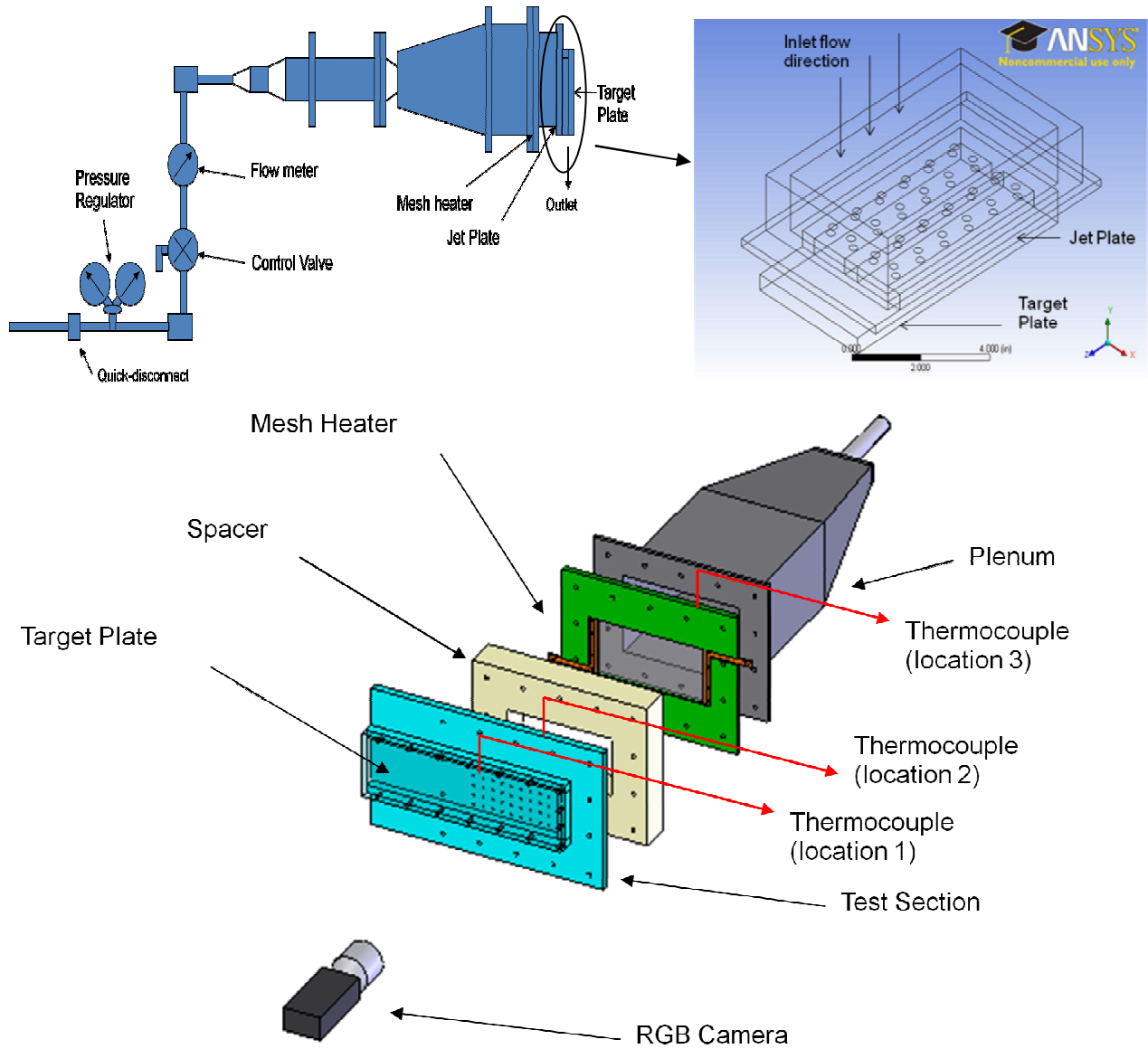
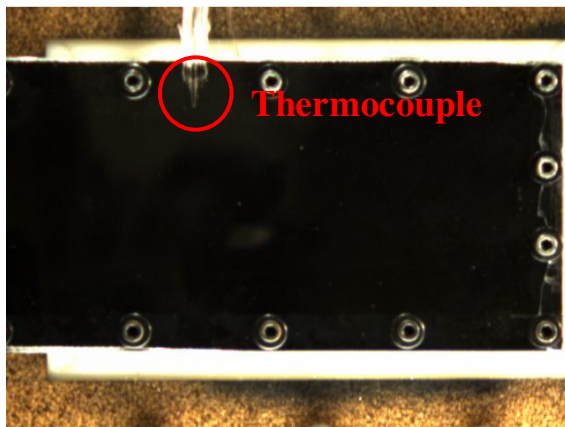
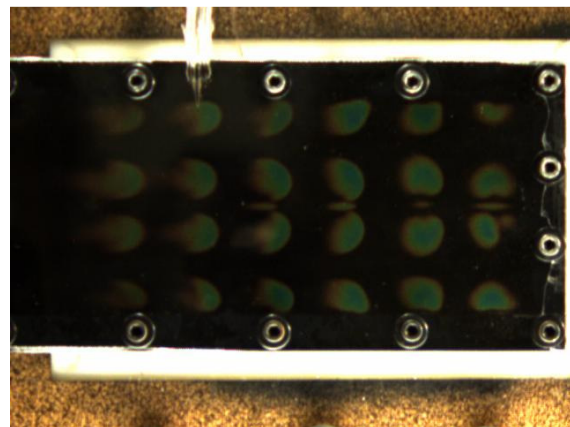


Figure 4.1. Schematic of the test-bed.

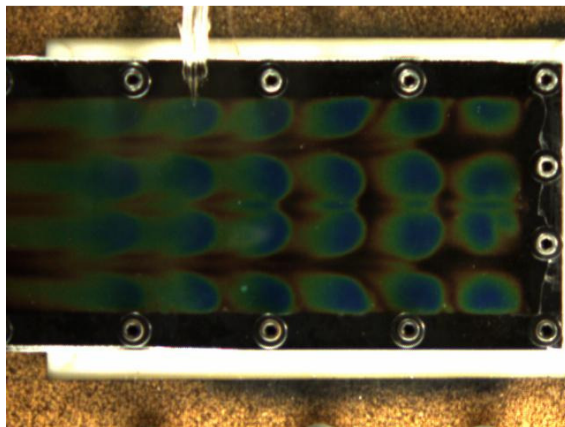
The test sections were manufactured out of acrylic and ABS plastics to reduce any thermal losses to the jet plate. The target plate was manufactured from clear acrylic to allow the camera to view the liquid crystal paint on the inner wall. Two jet array configurations were studied – 90° impinging jets and 70° impinging jets. The angle was measured with respect to the target surface. The jet plate consisted of 24 6.35-mm diameter jets arranged in 6 rows and 4 columns. For both the configurations, the location of the center of the jets inlet was kept constant. The jet plate to target plate separation was taken to be 9.525 mm. (that is, 1.5 jet diameter).



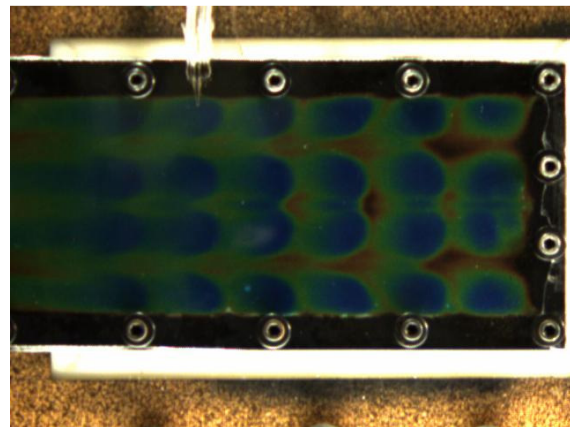
a) Heater switched on (frame # 54)



b) Frame # 66 @ 30 fps



c) Frame # 100 @ 30 fps



d) Frame # 150 @ 30 fps

Figure 4.2. Liquid crystal images at different instances of time.

Figure 4.1 also shows the locations of the thermocouples. Location 1 corresponds to the wall temperature of the target plate and was used to calibrate the liquid crystal colors. Thermocouple at location 2 measured the fluid temperature just before the jet plate while the thermocouple at location 3 measured the fluid temperature before the mesh heater. Figure 4.2 shows the change in liquid crystal colors with time for a sample experiment as heated air impinges on the target surface. The thermocouple placed on the target surface (Figure 4.2) was used to calibrate the liquid crystal colors with temperature which was recorded simultaneously. Figure 4.3 shows the transient temperature measurements at the three locations for the same experiment. It can clearly be seen that within three seconds of switching on the heater, the inlet fluid temperature (location 2) becomes constant.

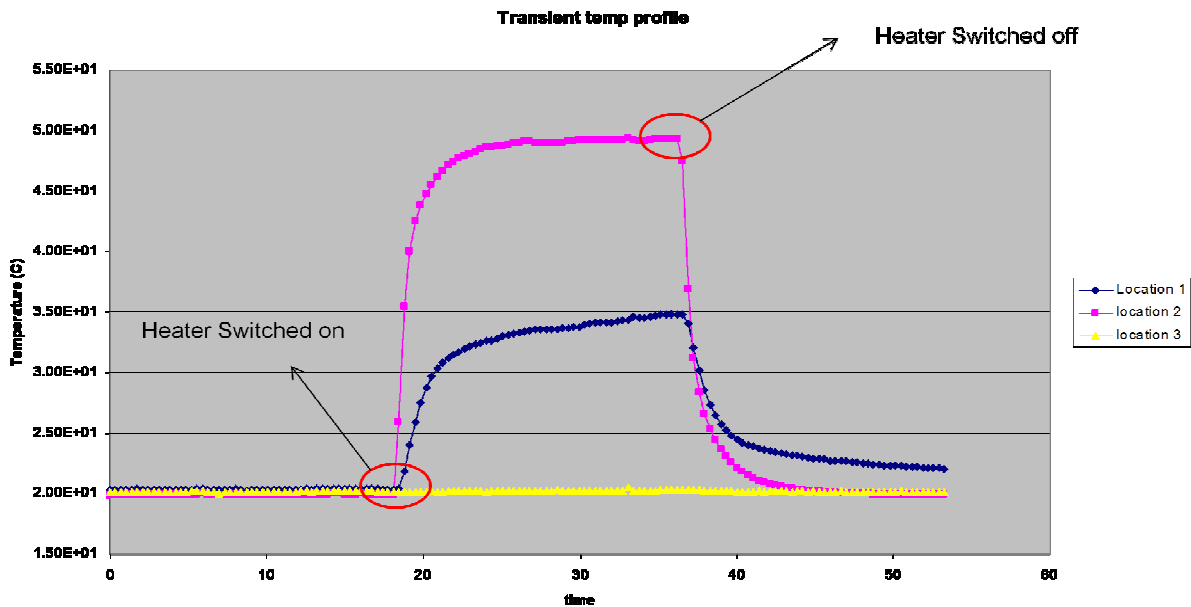


Figure 4.3. Transient temperature measurements at different locations.

For each experiment, the air flow rate through the set-up was activated and then the data acquisition system and the CCD camera were switched on to record the temperature and color data. The CCD camera recorded the images in a RGB color format and saved the video in .avi file format which was post-processed in Matlab© to select the region of interest. The

thermocouple placed on the target surface (location 1) was then used to calibrate the liquid crystal colors with temperature which was recorded simultaneously. Once the temperature at each pixel was known, the following 1-D transient semi-infinite heat conduction equation was solved using a regression analysis method to get the heat transfer coefficient, h :

$$\frac{T_w - T_i}{T_M - T_i} = 1 - \exp\left(\frac{h^2 \alpha t}{k^2}\right) \operatorname{erfc}\left(\frac{h \sqrt{\alpha t}}{k}\right) \quad (4.1)$$

where, T_w is the wall temperature (from calibration of video frames), T_M is the main stream temperature (location 2), T_i is the initial temperature (location 3), k is the thermal conductivity of the fluid (air), t is time with $t=0$ when the heater was switched on and α is the thermal diffusivity of the target plate material (plexi-glass). This technique has been used extensively and documented for detailed surface heat transfer coefficient measurements [68].

For each pixel, Eq. (1) was solved over the usable length of frames using a regression analysis method to obtain corresponding heat transfer coefficient. The regression analysis method was used to eliminate random errors in recorded local wall temperatures. The regression analysis put all terms of the conduction equation to the right hand side of the equation and was solved for all usable points of data for each pixel. This resulted in a residual error for each time-temperature data pair. The residual error was minimized in a least squares sense solving for the heat transfer coefficient that best fit all data. This reduced the random camera read errors of the liquid crystal paint and also relaxed the dependence of the initial temperature of the target plate on the results. The results were then converted to a meaningful non-dimensional parameter called the Nusselt number, Nu .

$$Nu = hD / k \quad (4.2)$$

where D is the jet diameter and k is the thermal conductivity of the working fluid (air).

In addition to the thermo-chromic liquid crystal analysis, infrared thermography was also used to observe similar trends. For the infrared thermography technique, the plexi-glass target plate was replaced with a plate made of thin Aluminum sheet and the CCD camera was replaced with an infrared camera. The back side of this plate, facing the infrared camera, was painted black with a flat-black paint to increase the emissivity of the surface to ~0.95. The experiments for this case were carried out in a dark room and the set-up was covered with a black cloth so as to mitigate the effects of surrounding light. FLIR SC640 Infrared camera was used for the thermal imaging on the back side of the target plate. The camera has a maximum resolution of 640 X 480 pixels at an imaging frequency of up to 60 Hz and a wide measurement range of -40 °C to + 1500 °C, in three ranges. Moreover, the camera allows for precise calibration of the target surface emissivity with an emissivity adjustment from 0.1 to 1.

For each infrared experiment, first the location of the calibrated thermocouple on the backside of the target plate was located and then its reading was used to adjust the emissivity of the target surface. The air flow through the experimental set-up was then started and allowed to stabilize. The data acquisition system for temperature recording and the infrared camera recording were then initiated. Mesh heater was then switched on to provide an instantaneous rise in the air temperature. The time when the heater was switched-on was used as the reference time for data analysis. To analyze the transient data and to convert the temperature information from the thermal images into local heat transfer coefficients, the lumped capacitance model derived by Lander et al. [69] was used:

$$\frac{\left(T_{W (SteadyState)} - T_W (t)\right)}{\left(T_{W (SteadyState)} - T_W (initial)\right)} = e^{-at} \quad (4.3)$$

$$a = \frac{h}{\rho l c_p} \quad (4.4)$$

where T_W is the target wall temperature obtained from thermal imaging, h is the local heat transfer coefficient, ρ is the density of the target plate, c_p is the specific heat capacity of the target plate and l is the target plate thickness. The infrared video provided the temperature value for each pixel over the entire duration of the experiment. Figure 4.4 shows the infrared images of the outside surface of the target plate at different instances of time for a sample experiment as heated air impinges on the inside surface of the target plate. The above equation was then solved to obtain the local heat transfer coefficients which were then converted to Nusselt number values using Eq. (2).

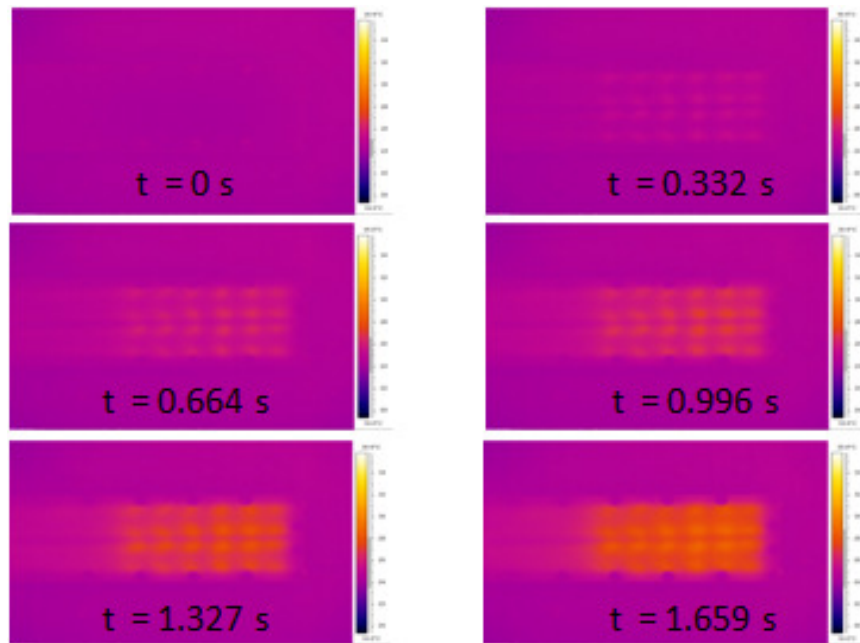


Figure. 4.4. Thermal images of the outside surface of the target plate at different instances of time.

Uncertainty Analysis:

The experimental uncertainty for each measured parameter was estimated using the method outlined by Moffat [70]. The uncertainty for each thermocouple reading was 0.25°C or

less. This uncertainty in temperature measurements was used to estimate uncertainties of quantities such as $T_M - T_i$, and ρ , μ , c_p and k through their known dependence on temperature [71]. For the flow rate measurements, the uncertainty of reading was less than 4%, for the pressure drop measurement, it was about 3% and for the jet diameter measurement, it was less than 1% resulting in about 4.5% uncertainty in the Reynolds number. Their effect on the results was minimized by the use of regression analysis and a maximum of $\pm 8\%$ uncertainty was found out in the Nusselt number [68].

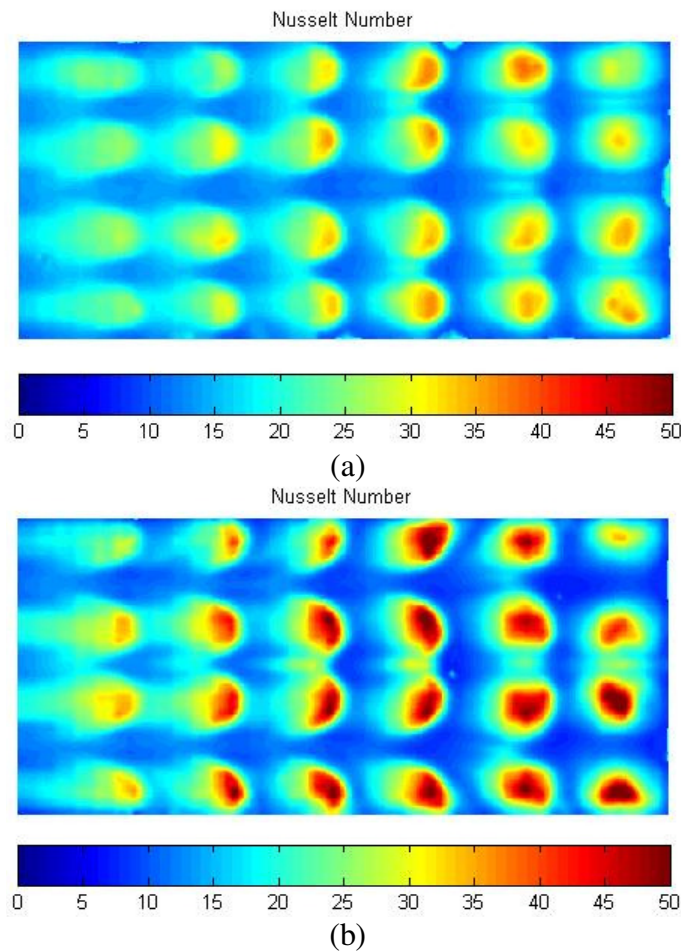


Figure 4.5. Nusselt number contours for (a) normally (90°) impinging jets at $Re = 8526$, and (b) 70° impinging jets at $Re = 8192$.

Figure 4.5 shows the Nusselt number contour for both the impingement configurations tested. Figure 4.5a shows the Nusselt number contours for normally (90°) impinging jets at a

Reynolds number, $Re \sim 8500$. The average Nu over the entire region was computed to be 18.4 with a maximum value of 44.57. Figure 4.5b shows the Nusselt number contours for 70° impinging jets at a slightly lower Re (~ 8200). The average Nu over the entire region was computed to be 19.67 with a maximum value of 64.55. It is to be noted that there is no separation/wall between the second and the third row of jets. Moreover, these experiments were observed to be repeatable, that is, for different experiments at a given flow rate the Nu contours obtained were similar. The same case was also evaluated using the Infrared thermography and lumped capacitance technique. Figure 4.6 shows the Nusselt number contours obtained using this method. Clearly, similar trends were observed. In the light of these results, it was concluded that the confined angled impingement scheme worked better than the conventional normally impinging jets. Thus, for the same geometry and flow rate, higher local heat transfer coefficients can be obtained by just changing the jet angle in a confined environment.

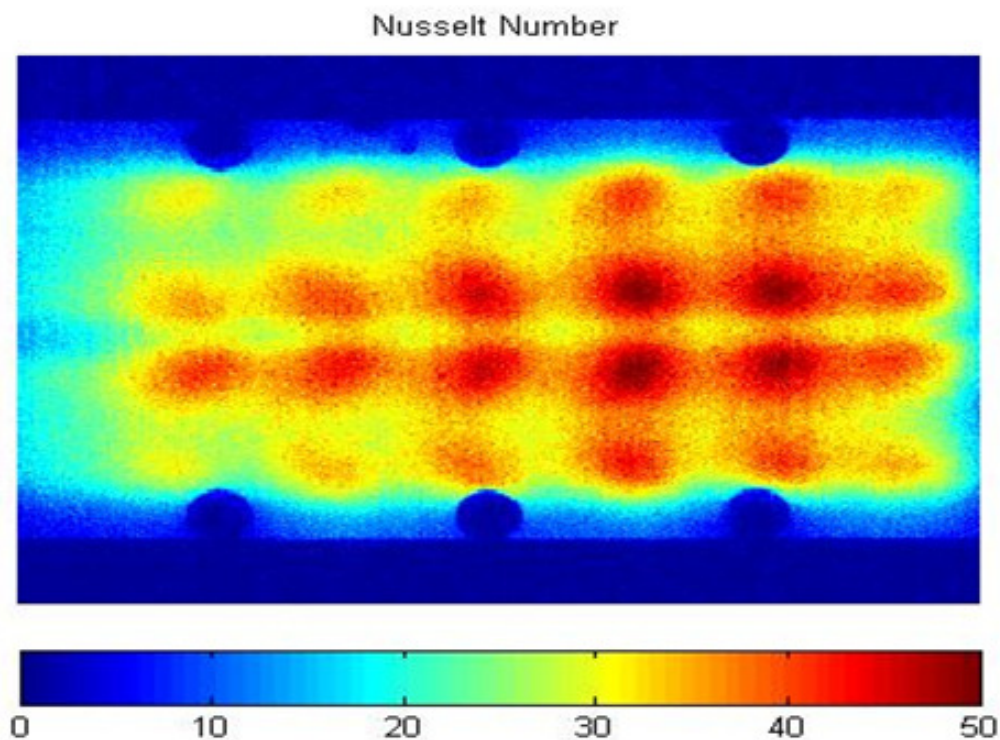


Figure 4.6. Nusselt number contours for 70° impinging jets at $Re = 7800$ evaluated using infrared thermography and lumped capacitance method.

4.2. Numerical Validation and Analysis

It is important to select an efficient turbulence model for the study of jet impingement cooling. For this purpose, heat transfer characteristics of a single normal impinging jet were studied and compared with the experimental data reported by Glynn *et al.* [72]. The experimental set-up of Glynn *et al.* considered for the validation case consisted of a 5mm thick orifice plate with non-dimensional jet-to-target plate spacing (H/D) of 2 and the jet diameter of $D=1.5\text{mm}$.

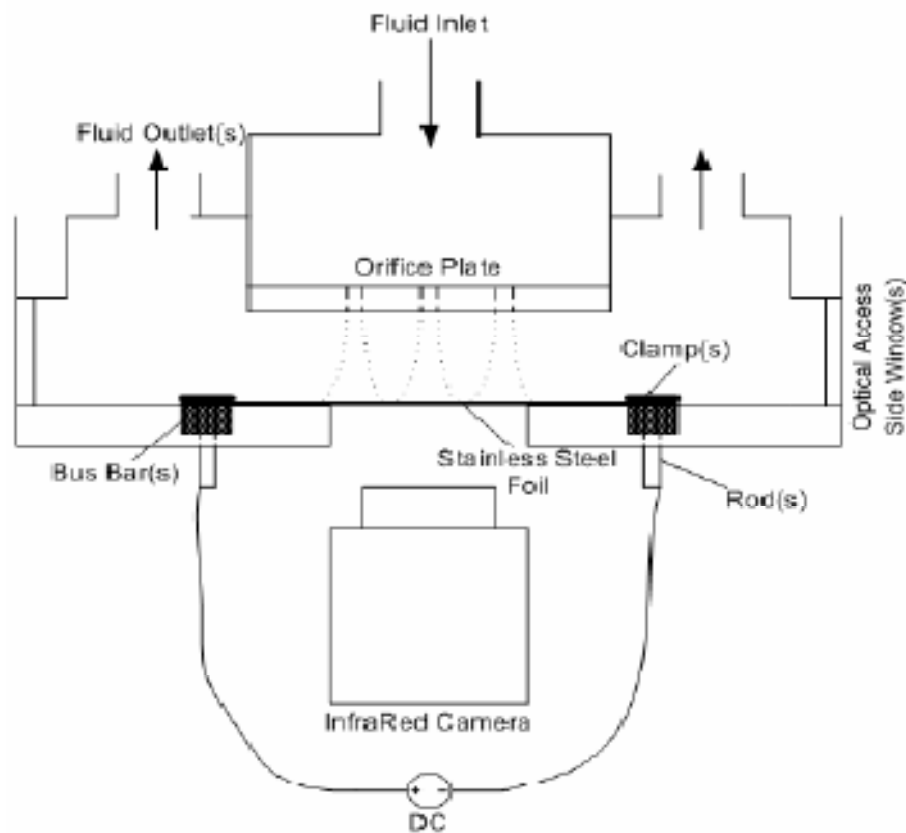


Figure 4.7. Schematic of the test chamber [72].

The impinging fluid considered was compressed air coming from the shop. The temperature of the air at orifice inlet was about $22\text{ }^{\circ}\text{C}$ (295 K). The flow Reynolds number based on orifice diameter was 5000 giving an average inlet velocity of 51.4 m/s . The orifice plate consisted of only one jet of diameter. The target plate was a thin ($25\text{ }\mu\text{m}$) Stainless Steel foil which was connected to a D.C. power supply so as to give an input heat flux of about 2 W/cm^2 .

They had four fluid exits of 10mm diameter positioned in the four corners of the test chamber ceiling. Full-field temperature measurements on the underside of the foil were made using a FLIR ThermaCAM™ A40 infrared camera. Figure 4.7 shows a schematic of the test chamber [72]. Due to the symmetry of the problem, the above defined experiment was modeled by considering an axis-symmetry about the jet center (Figure 4.8).

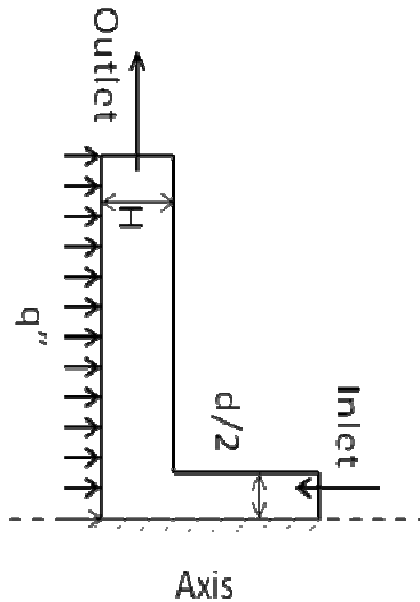
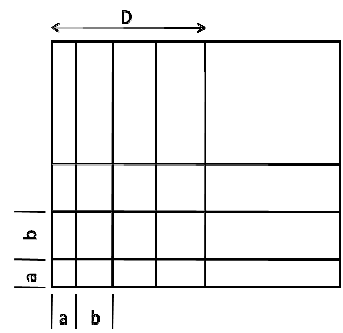
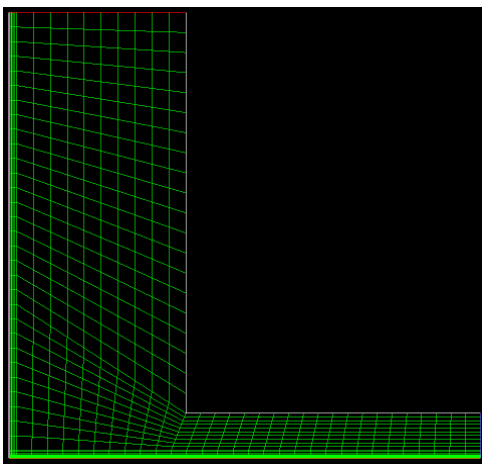


Figure 4.8. 2-D Axis-symmetry configuration for simulation.

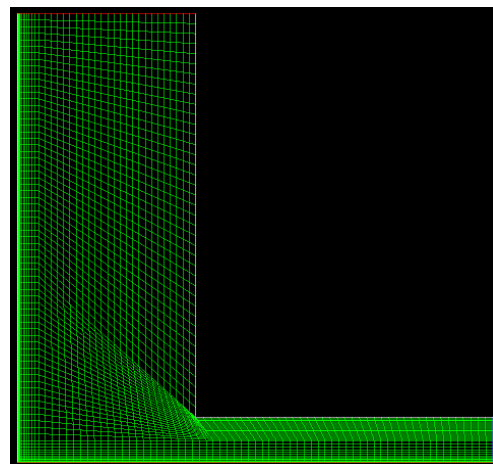
Four different turbulence models, namely $k-\varepsilon$, standard $k-\omega$, Shear Stress Transport $k-\omega$ and Reynolds Stress models, were studied. The solution algorithm used was SIMPLEC with standard discretization for pressure and second order upwind for all the other equations such as x (or z) -momentum, y (or r) -momentum, energy etc. Four different levels of meshes (Figure 4.9) – coarse, medium, fine and finer, were used for the simulation of flow field and heat transfer phenomena involved in the problem. It should be noted here that the classification of the meshes into the four categories is based on the near wall resolution of the grids. Table 4.1 summarizes the mesh statistics. Root mean square values of the residues were required to be less than 10^{-4} for convergence. For the energy equation, the convergence criterion was less than 10^{-6} .

Table 4.1. Summary of Mesh Statistics.

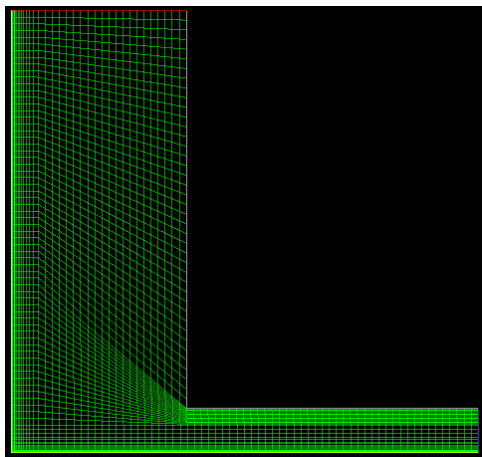
		Mesh	a (mm)	b/a	D	# of Layers	Cells	Faces	Nodes
		Coarse	0.005	1.2	0.129793	10	1200	2480	1281
		Medium	0.005	1.2	0.360176	15	4800	9760	4961
		Fine	0.0025	1.2	0.46672	20	5043	10250	5208
		Finer	0.00125	1.2	0.407796	23	5043	10250	5208



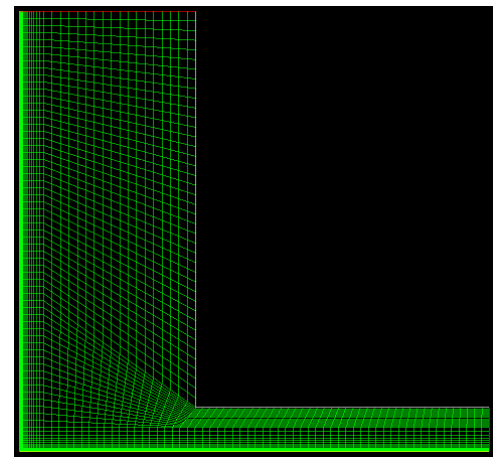
(a) Coarse mesh



(b) Medium mesh

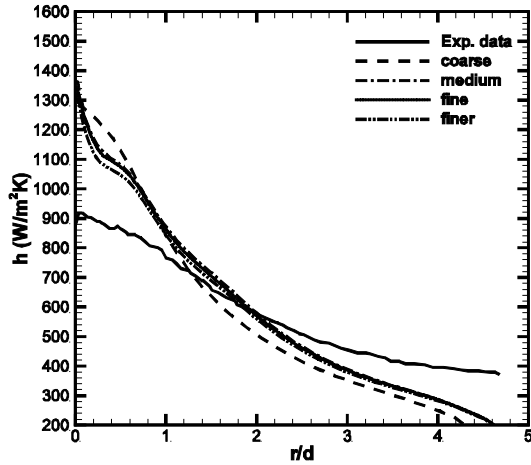


(c) Fine mesh

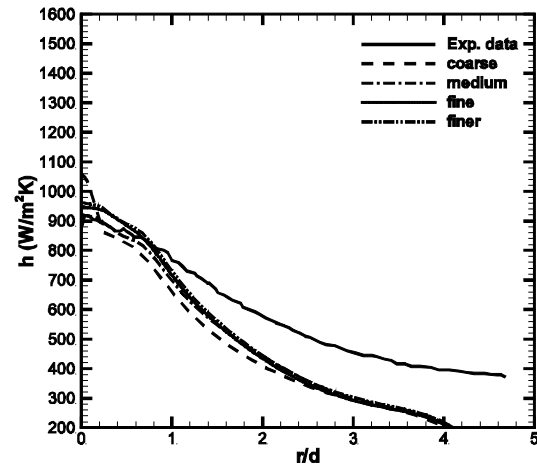


(d) Finer mesh

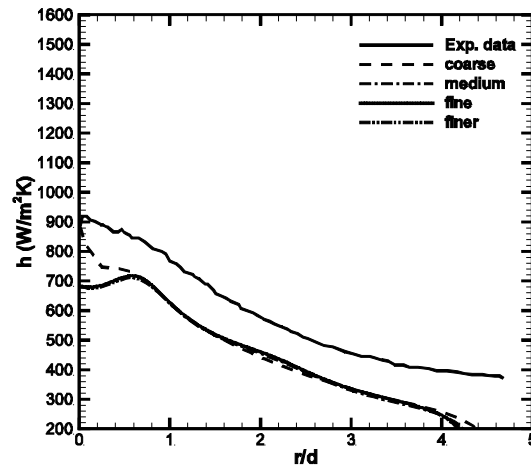
Figure 4.9. Four different levels of grid with the incorporated boundary layers used for the second configuration.



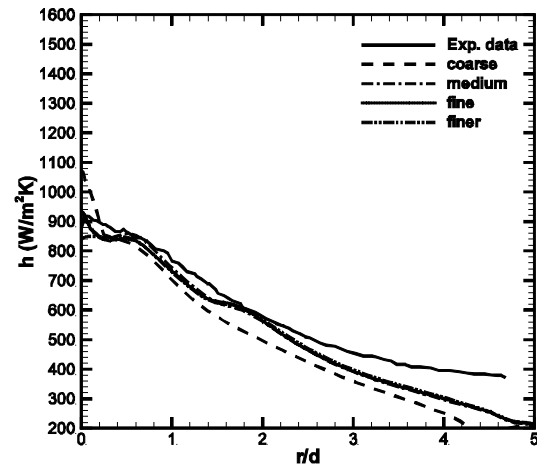
(a) $k-\varepsilon$



(b) standard $k-\omega$



(c) Shear Stress Transport $k-\omega$



(d) Reynolds Stress Model

Figure 4.10. Comparison of the heat transfer coefficient for (a) $k-\varepsilon$, (b) standard $k-\omega$, (c) Shear Stress Transport $k-\omega$ and (d) Reynolds Stress turbulence models with the experimental data for $Re=5000$ (Air jet).

Figure 4.10 compares the simulation data of the (a) $k-\varepsilon$, (b) standard $k-\omega$, (c) Shear Stress Transport (SST) $k-\omega$ and (d) Reynolds Stress turbulence models with the experimental data. It can clearly be seen that most the simulations predicted the local heat transfer coefficients fairly well. The $k-\varepsilon$ model predictions were much higher than the experimental data. The predictions of the standard $k-\omega$ model were in very good agreement with the experimental data near in the stagnation region. Away from stagnation region, the local heat transfer coefficients were quite

under-predicted. The variation of the local heat transfer coefficient with the non-dimensional distance was captured fairly well by the SST $k-\omega$ turbulence model. However, the magnitude was under-predicted. The predictions of the local heat transfer coefficients by the Reynolds Stress model were in excellent agreement with the experimental data. Moreover, all the predictions were more or less grid independent.

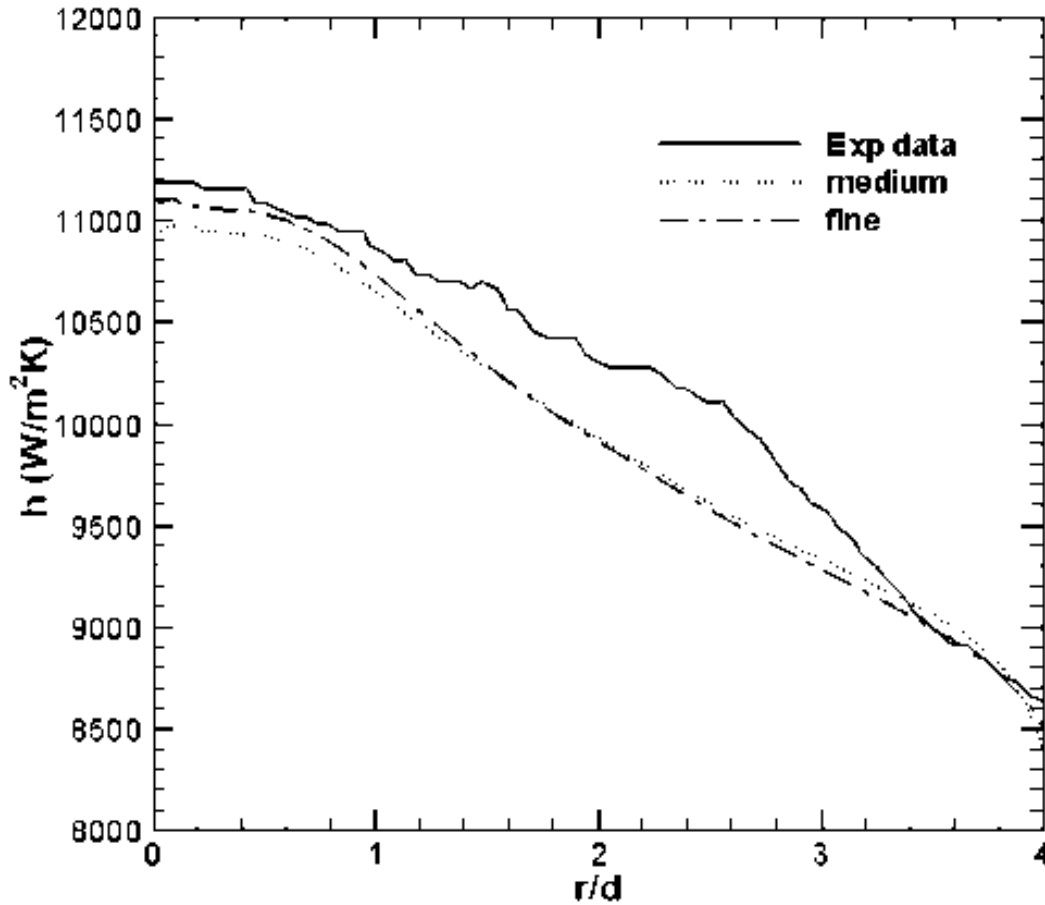


Figure 4.11. Comparison of the heat transfer coefficient for standard $k-\omega$ turbulence model with the experimental data for $Re=10000$ (Water jet).

Overall, numerical simulations were able to predict the local heat transfer coefficients with a very good accuracy. The Reynolds Stress model was the best out of the four models studied. The accuracy of the Reynolds Stress model can be in a way attributed to the fact that this model solves for five scalar equations in addition to the conventional fluid flow and heat transfer equations. On the other hand, the other three models solved for two additional scalar equations

and accounted for about half the computational time. Thus, in terms of accuracy and computational effort, the standard $k-\omega$ model was found out to be the most efficient model.

In the light of the above observations, standard $k-\omega$ turbulence model was selected and used to compute the local heat transfer coefficients for a water jet. The predictions for two different mesh sizes are compared with the available experimental data as shown in Figure 4.11. It can clearly be seen that the predictions are in very good agreement with the experimental data especially near the stagnation region. Thus, all future simulation studies were performed using the standard $k-\omega$ turbulence model.

4.3. Comparison of Experimental and Numerical Results

In an attempt to validate the simulation results for the current configuration and to get an insight into the flow field inside the test section, a small portion of the liquid crystal test section was modeled and simulated in ANSYS-CFX. Both the cases presented in the previous section were simulated.

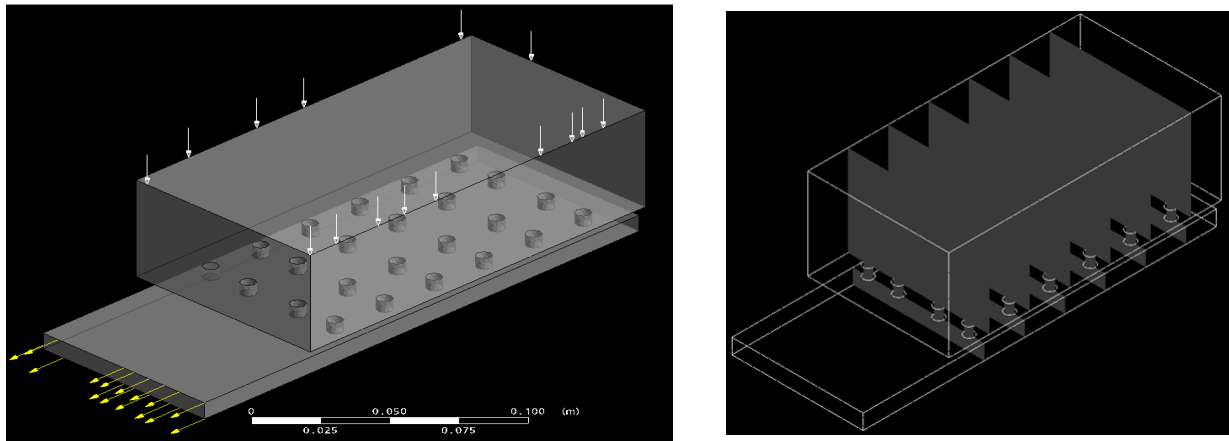
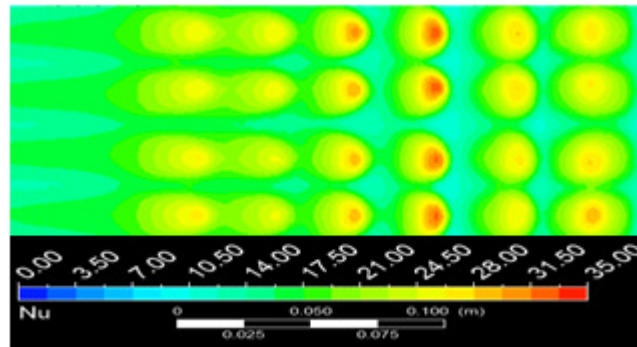


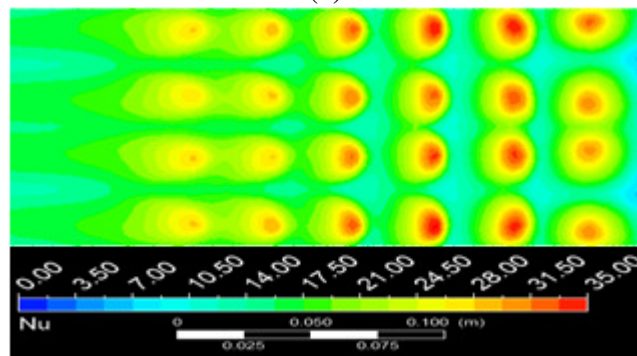
Figure 4.12. ANSYS-CFX model used for simulating the liquid crystal experiments for normally impinging jets with a Reynolds number of 8500.

Figure 4.12 shows the CFX model used for simulating the normally (90°) impinging jets configuration. It also shows the planes passing through the jet centers for each row. The white arrows represent the air inflow direction along with the inlet face while the yellow arrows

represent the outflow direction along with the outlet face. An air mass flow rate of 18.869 g/s at 25 °C was applied at the inlet with 10% inlet turbulence. 24 jets with a jet-hole diameter of 0.25 in. (0.00635 m) were considered. These numbers were selected based on the experimental conditions. At the target surface a constant heat flux was applied while all the other surfaces were considered to be adiabatic. A very fine mesh similar to the one described in the previous section was used only near the significant walls (target surface, jet-hole surfaces, etc.) and a relatively coarser mesh was used in the bulk. A similar CFX model was used for 70° impinging jet configuration. Similar to the previous model, a very fine mesh was used only near the significant walls (target surface, jet-hole surfaces, etc.) and a relatively coarser mesh was used in the bulk. All the other simulation parameters were adjusted based on the experimental conditions.

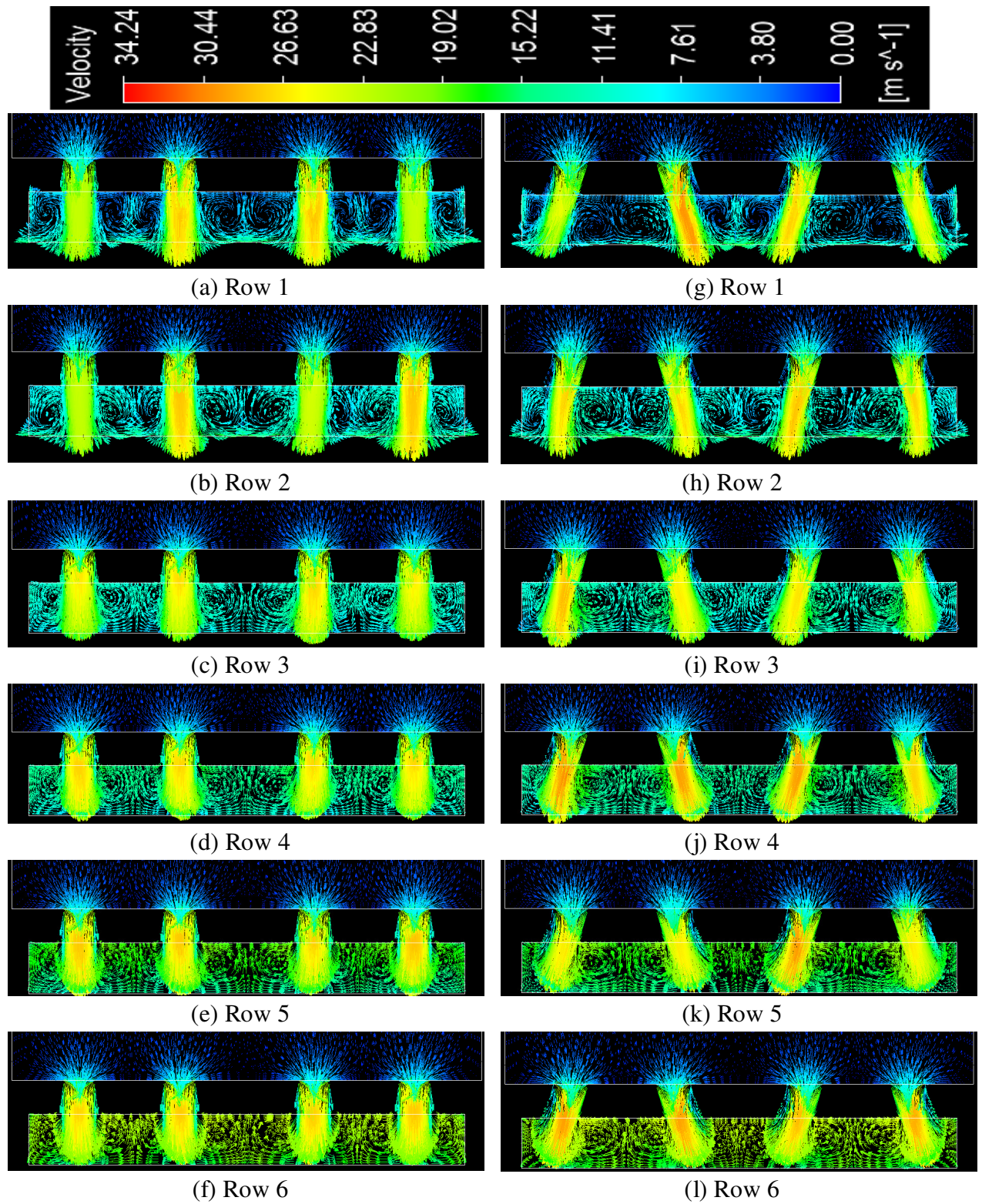


(a)



(b)

Figure 4.13. Heat transfer coefficient predicted for the liquid crystal experiments for (a) normally impinging jets with a Reynolds number of 8200. Max $Nu = 33$. Average $Nu = 18.67$, and (b) 70° impinging jets with a Reynolds number of 8200. Max $Nu = 35.17$. Avg $Nu = 19.3$.



(A) 90° impinging jets

(B) 70° impinging jets

Figure 4.14. Velocity vectors at the cross-sectional planes passing through the jet centers for (A) 90° and (B) 70° impinging jets.

Figure 4.13 shows the Nusselt number predicted for both the impingement cases simulated. Figure 4.13a shows the Nusselt number contours for normally impinging jets. The maximum value of the heat transfer coefficient obtained was $140.3 \text{ W/m}^2\text{K}$ which corresponds to a Nusselt number (Eq. (2)) of about 33 based on the geometry simulated. The Nusselt number relation is given by Eq. (2). Jet diameter, ($D = 0.25 \text{ in.}$ or 0.00635 m) and k is the thermal conductivity of the fluid (air, 0.0271 W/m-K) were used for the calculation. The average heat transfer coefficient obtained for this case was $79.4 \text{ W/m}^2\text{K}$ (i.e. $Nu = 18.19$). However, the peak values were not obtained where they were supposed to occur. This may be due to the fact that the mesh was not properly refined in the key regions such as the jets centre and jet-impact regions. Figure 4.13b shows the Nusselt number predicted for 70° impinging jets with a maximum value of $150 \text{ W/m}^2\text{K}$ ($Nu = 35.2$). The average value obtained was about $82.1 \text{ W/m}^2\text{K}$ ($Nu = 19.3$). The location of the peak heat transfer coefficient values and the heat transfer trend matched fairly well with the experimental data.

The CFD calculations were also used to understand the flow field in the test section and to help interpret the experimentally obtained heat transfer results. Figure 4.14 shows the velocity vectors at the cross-sectional planes passing through the jet centers for both 90° and 70° impinging jets. Figure 4.12 shows these planes in an isometric view of the simulation model. From these plots it can be seen that the first row is free from any cross-flow effects and the jets are able to impact the target plate with a high velocity. It can also be seen that for the 70° impinging jets, the velocity of the jets as it comes out from the jet holes is slightly higher than that for the 90° impinging jets. The reason for this will be clearer from the velocity contours shown in Figure 4.15. As a consequence, the jets hit the target plate at slightly higher velocity to create a relatively higher local heat transfer rate. It can also be observed that for the 90° jets, after

impingement the flow forms two symmetric vortices, while for the 70° jets, two non-symmetric vortices – one large and one small, are formed which are then convected downstream towards the outlet. As the flow moves downstream towards the outlet, the vortices formed by 90° jets are not able to retain their swirl strength due to increased cross flow effects. However, that is not the case with 70° jets, as the large vortices are able to retain most of their strength even until the last set of jets and beyond.

Figure 4.15 compares the velocity contours for the 90° and 70° impinging jets. For the 90° jets, the flow enters normally to the jet inlet and then starts to develop slightly before impinging on to the target surface. As a result, there are two symmetric secondary flow regions/velocity boundary layers are formed near the jet walls. For the 70° impinging jets, we expect it to be the same but it is not due to the way the flow enters the 70° jets. The flow enters normally to the inlet face which is elliptical in shape and then it has to turn and adjust to the cylindrical jet before starting to develop. This causes the formation of two non-symmetrical secondary flow regions – one large which is closer to the bend and one small which is away from the bend. Especially due to this large secondary flow region, the jets get accelerated and flow out at relatively higher velocity causing the heat transfer rate to increase locally. This trend will be much clearer from the vorticity plots compared in Figure 4.16.

Figure 4.16 compares the vorticity component along the cross flow direction for the 90° and 70° impinging jets. Clearly, the vortex strengths formed after impingement from all jets are much higher for the inclined impingement. These plots also highlight the large secondary flow regions formed inside the 70° inclined cylindrical jets. Clearly, these regions are large enough to cause localized acceleration of the jets and thereby, cause an increased local heat transfer rate.

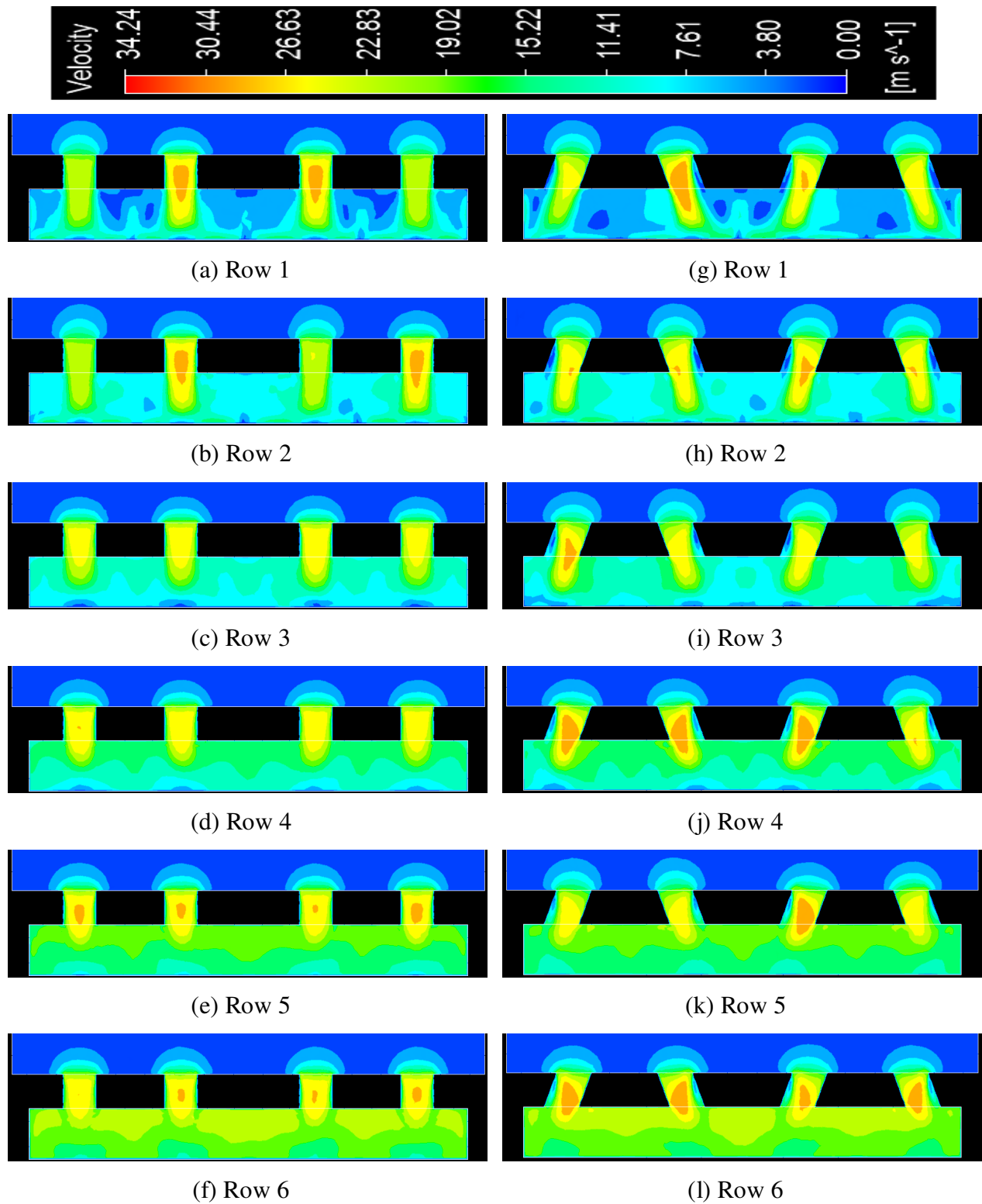


Figure 4.15. Velocity contours at the cross-sectional planes passing through the jet centers for (A) 90° and (B) 70° impinging jets

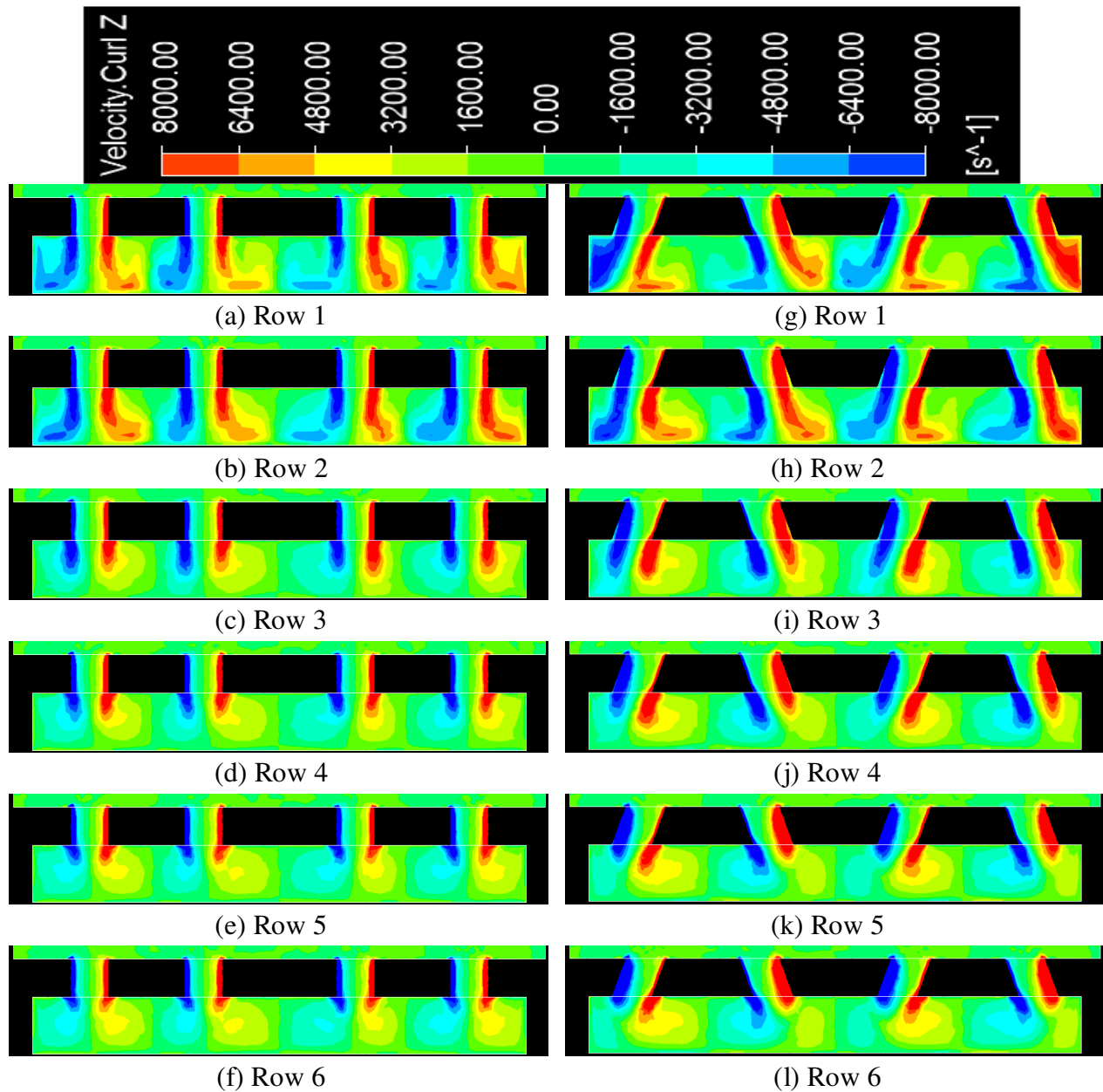


Figure 4.16. Vorticity contours at the cross-sectional planes passing through the jet centers for (A) 90° and (B) 70° impinging jets

In the light of these results and to further analyze the flow and heat transfer characteristics of the proposed configuration, small simple configurations, as shown in Figure 4.17, of wall-integrated normal and 70° inclined impingement were studied. In these configurations, the jet diameter and the jet plate thickness were taken to be 1.5 mm. The jet to

target plate spacing was taken to be 3 mm. The faces A, B and C were at an offset of 0.25 D from the jet circumference. The outlet was placed far away from the jet so as to observe the swirl/swirl strength after impingement. A symmetry boundary condition was used at the face D and a constant heat flux boundary condition was applied at the other wall faces. A total mass flow rate of 0.105 g/s of air at 25 °C (corresponding to $Re = 5000$) was applied normal to the inlet face for both the configurations. For the 70° inclined jets, the case of inlet flow along the jet axis was also studied so as to characterize the effect of flow inside the jets on the local heat transfer rates at the target surfaces.

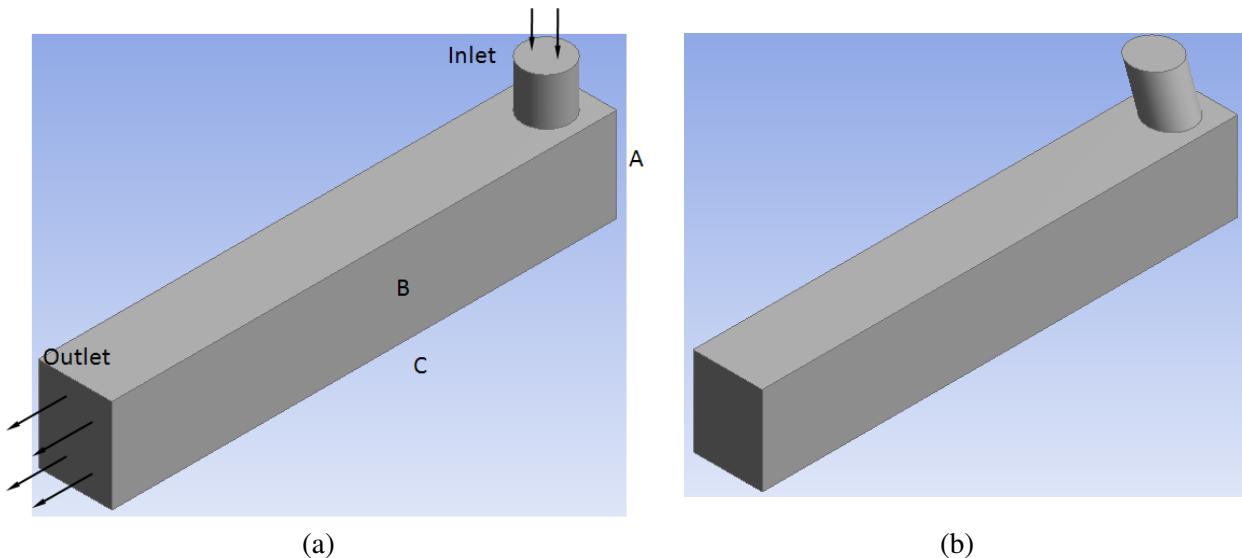


Figure 4.17. Small single impinging jet configurations for the flow and heat transfer study of wall-integrated (a) normal and (b) 70° inclined impingement cases.

Figure 4.18 compares the Nusselt number at the target surfaces for the three configurations stated above. It can be clearly seen that for the 70° inclined impingement case with the inlet flow normal to the inlet face, the maximum local heat transfer rates in the impingement region as well as the overall heat transfer rates are much higher than the other two cases and is in agreement with experimental observations made earlier. Table 4.2 compares the maximum as well as the average Nusselt number values at faces A, B and C. Clearly, for the

angled impingement with normal flow at inlet face case, the local as well as average heat transfer rates are much higher. However, when the inlet flow is along the jet axis for the same configuration, the local heat transfer rates are much lower than the normal impingement case as well. In other words, this configuration is worse than the normal impingement case in terms of local heat transfer rates. The overall average heat transfer rates for this configuration are however better than the normal impingement case. Reasons for such trends would be clearer from the flow distribution study.

Table 4.2. Maximum as well as the average Nusselt number predictions at the target surfaces (faces A, B and C).

Case	Nusselt number predictions						Area Avg Nu at Target surfaces
	Face A		Face B		Face C		
	Max.	Area Avg	Max.	Area Avg	Max.	Area Avg	
90⁰ impingement	34.3	25.6	41.4	16.9	43.8	19.7	18.7
70⁰ impingement with inlet flow along jet axis	35.7	27.5	34.4	18.9	37.9	19.7	19.8
70⁰ impingement with inlet flow normal to inlet face	47.2	34	48.9	17.2	59.6	21.8	20.4

Figure 4.19 compares the streamlines for the three configurations stated above. It can be clearly seen that for the normal impingement case, after impingement, the flow breaks down into two more or less even vortices which dies down after sufficient distance from the jet center. However for the angled impingement cases, the flow essentially breaks down into one large vortex and one small vortex. Moreover, the larger vortex seems to sustain itself almost till the outlet, keeping the flow turbulent all along the fluid domain, thereby, increasing the overall heat transfer rate. From these plots, it can also be seen that for the case of inclined impingement with inlet flow normal to the inlet face, the maximum jet velocity is significantly higher than the other

two cases due to the larger recirculation region towards the bend. This local acceleration of the impinging jet is thus responsible for an increased heat transfer rate.

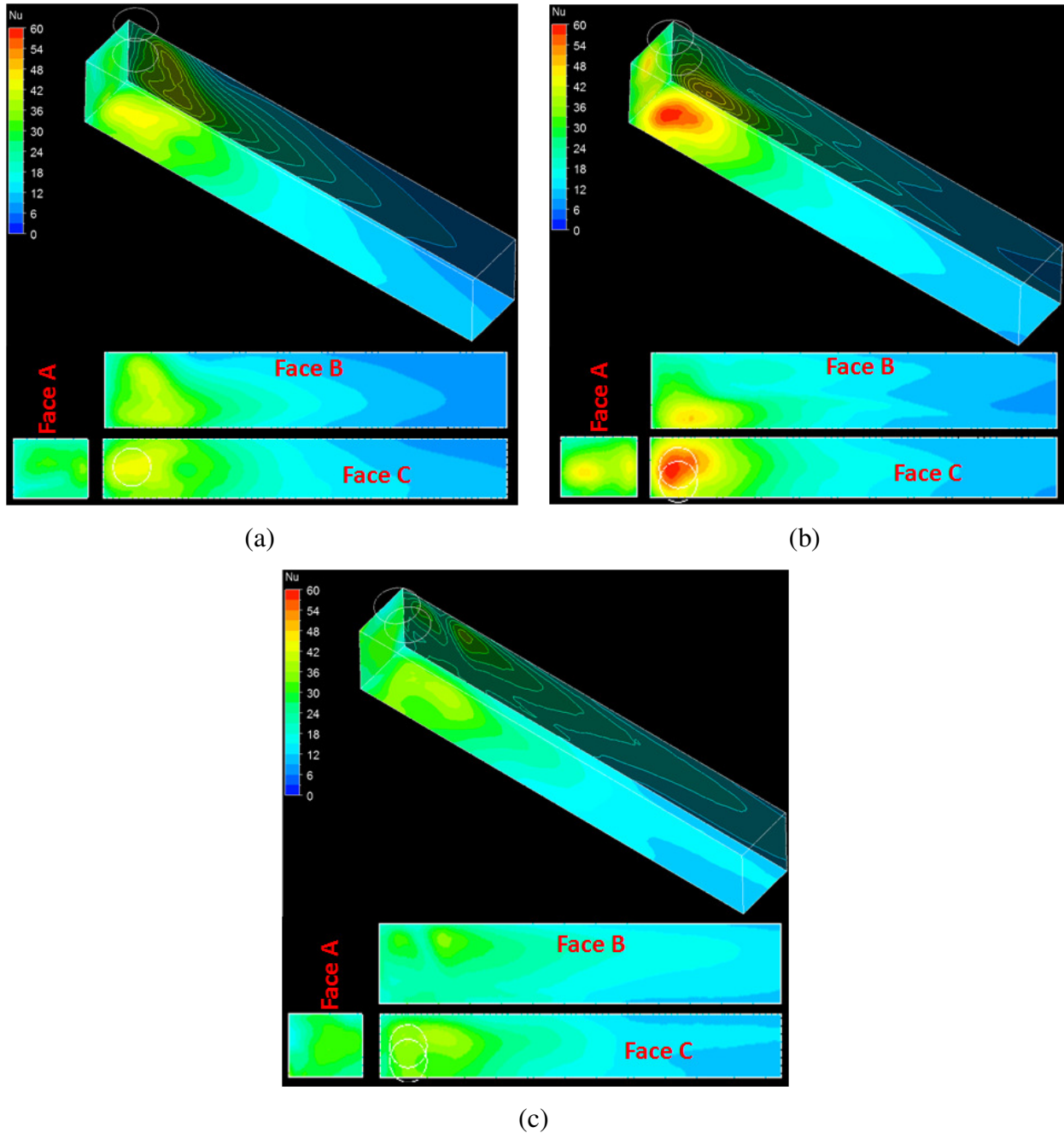


Figure 4.18. Nusselt number predictions at the target surfaces for the three configurations (a) 90° impinging jet with inlet flow normal to the inlet face, (b) 70° impinging jet with inlet flow normal to the inlet face, and (c) 70° impinging jet with inlet flow along the jet axis.

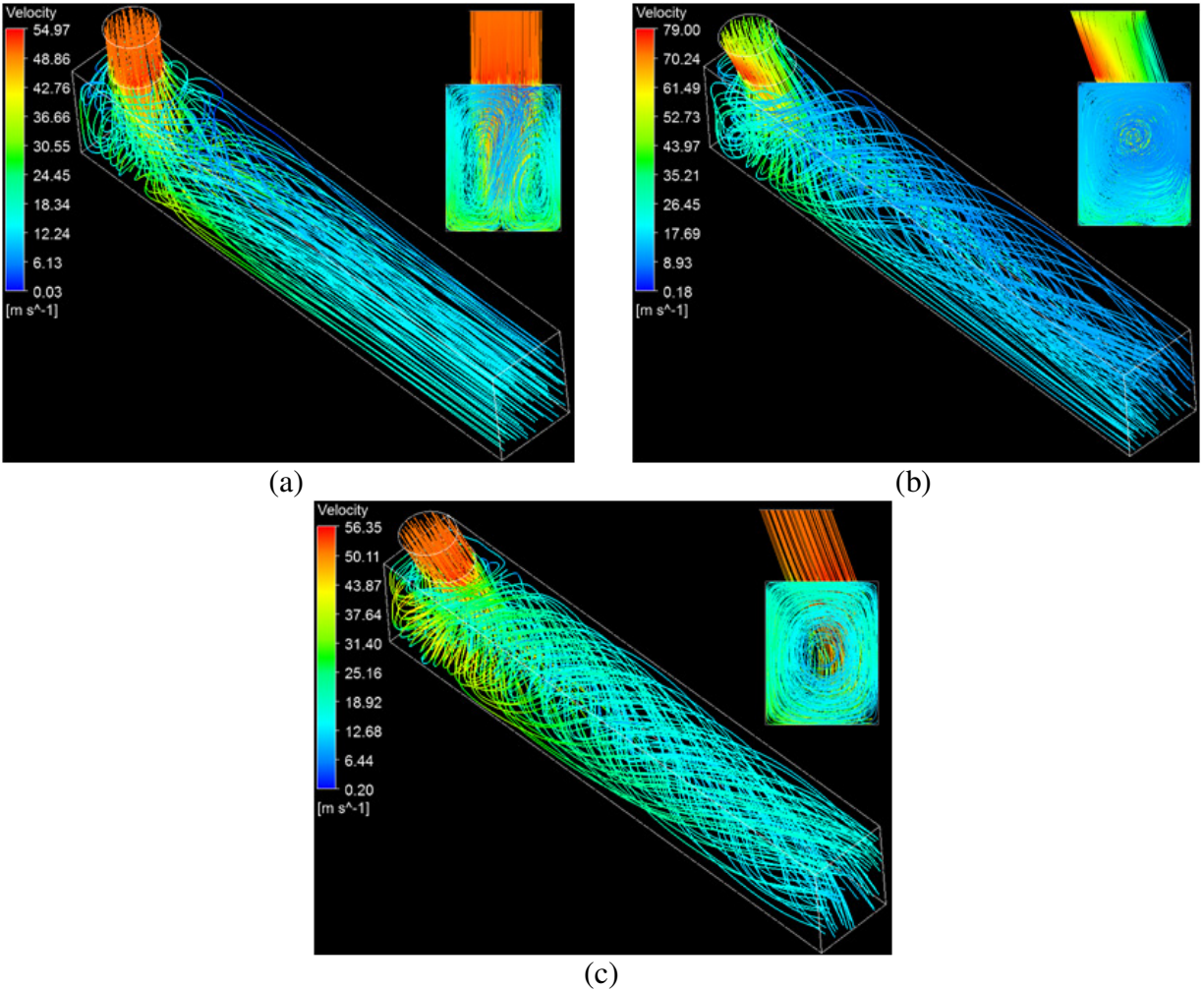


Figure 4.19. Velocity streamlines inside the flow domain for the three configurations (a) 90° impinging jet with inlet flow normal to the inlet face, (b) 70° impinging jet with inlet flow normal to the inlet face, and (c) 70° impinging jet with inlet flow along the jet axis.

Figure 4.20 compares the vorticity (or rather, velocity curl along the cross-flow direction) plots for the three configurations at different cross-sectional planes along the cross-flow direction. The cross-sectional planes are separated by a distance of one jet diameter. It can be clearly seen that for the normal impingement case, two vortices of similar strength are generated after impingement which die down within five jet diameter distance from the jet center. However, for the 70° impingement case with inlet flow normal to the inlet face, the flow breaks down into one large and one small vortex which are able to sustain much beyond the impingement region. The smaller vortex, however, dies down much faster than the large vortex.

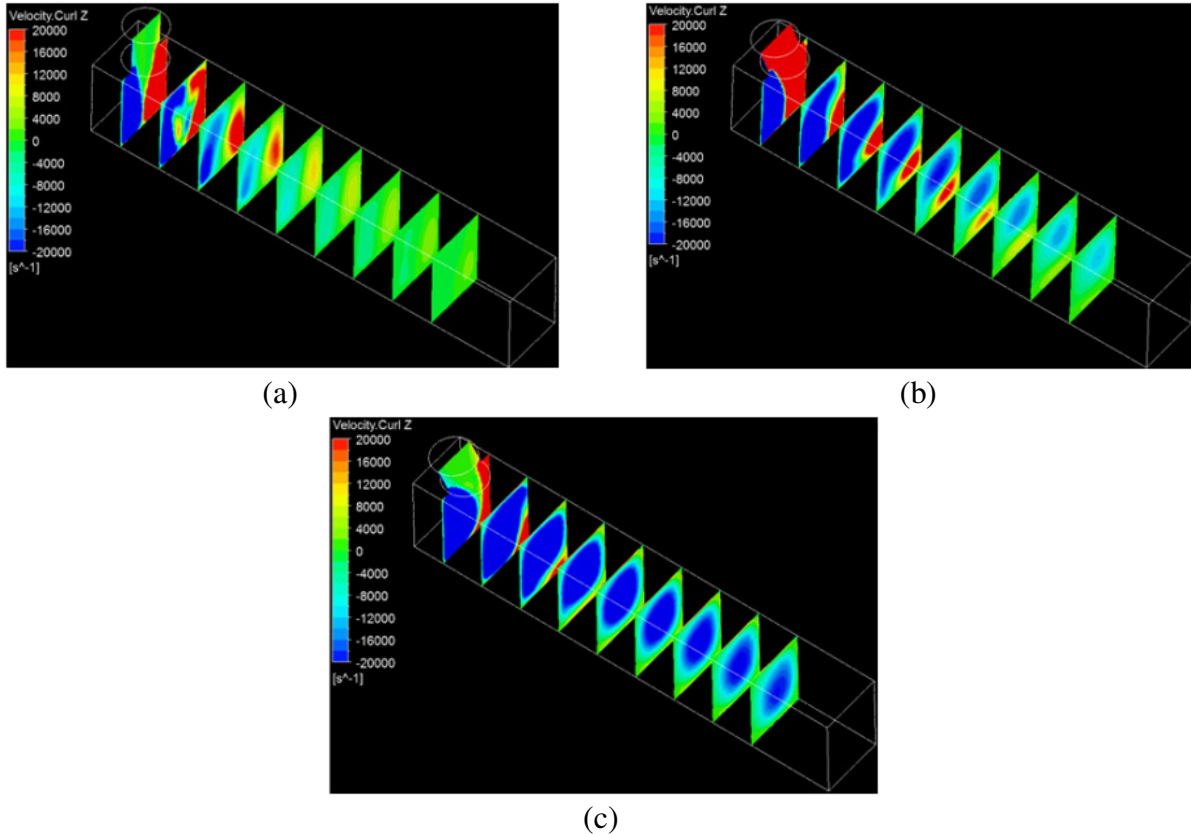


Figure 4.20. Vorticity (velocity curl component along the cross-flow direction) contours at different cross-sectional planes for the three configurations (a) 90° impinging jet with inlet flow normal to the inlet face, (b) 70° impinging jet with inlet flow normal to the inlet face, and (c) 70° impinging jet with inlet flow along the jet axis.

Also, the smaller vortex moves closer to the bottom target surface and expands to cover a larger area as we go away from the impingement region. The larger vortex, on the other hand, shrinks and dies down further downstream. Similar to the previous case, for the 70° impingement case with inlet flow along the jet axis, the jet breaks down into one large and one small vortex. However, the small vortex is relatively smaller and dies down with 3 jet diameters from the jet center. This feature can help mitigate the effects of cross-flow on the subsequent downstream jets. The larger vortex, on the other hand has a much higher strength and remains sustained all the way up to the outlet. This keeps the flow highly turbulated much beyond the impingement region and causes an increased heat transfer rate over a much larger area. Thus, the face average heat transfer rates for this configuration are higher. So, in order to benefit by using this

configuration, sufficient spacing between the downstream jets is required. This can result in less number of jets on a large area making it less useful than the other two configurations. An important consequence is that, thermal resistance in present impingement based high heat flux dissipating electronic packages can be reduced significantly just by changing the jet angle and generating swirl.

4.4. Summary

Thermo-chromic liquid crystal based test bed was used to study the thermal behavior of the impinging jets for different jet angles. At a similar flow rate, higher average Nusselt number (19.67 with a maximum value of 64.55) was obtained for 70° impinging jets than the 90° normally impinging jets (18.4 with a maximum value of 44.57). These experimental cases were simulated using ANSYS-CFX which predicted the average Nusselt number for the 70° impinging jets fairly well. These experiments and simulations were also performed for other angles. Significant improvements in the maximum local heat transfer coefficients were observed both experimentally and numerically. Similar heat transfer trends were observed, when the same case was evaluated using the Infrared thermography and lumped capacitance technique. The CFD calculations were also used to understand the flow field in the test section and to help interpret the experimentally obtained heat transfer results. It was observed that for inclined impingement case with the flow entering normally to the inlet face which is elliptical in shape, the flow has to turn and adjust to the cylindrical jet before starting to develop inside the jet holes. This causes the formation of two non-symmetrical secondary flow regions – one large which is closer to the bend and one small which is away from the bend. Especially due to this large secondary flow region, the jets get accelerated and flow out at relatively higher velocity causing the heat transfer rates to increase locally. Moreover, the swirl generated after impingement sustains itself for a

longer distance, thereby increasing the overall heat transfer rates. Thus, for the same geometry and flow rate, higher local heat transfer coefficients can be obtained.

Based on the above experimental as well as simulation predictions, if properly oriented, wall-integrated inclined impingement can help attain much higher local as well as overall heat transfer rates than the normal impingement case. Thus, the present swirl-impingement-fin configuration was selected as a viable candidate for high heat density applications such as thermal management of power converters. Other applications of this cooling scheme include liquid cooling of computer CPU's, data center cooling and internal cooling of turbine trailing edge.

CHAPTER 5: LIQUID BASED THERMAL TEST BED AND SIMULATION STRATEGY

In this chapter, the liquid-based experimental set-up and the details of the apparatus used for the investigation of the overall heat transfer rate and of cooling performance of heat exchangers developed during the course of this work, is presented in detail. Additionally, the simulation strategy employed is also discussed in detail.

5.1. Thermal Test Bed

A thermal test bed was designed to test the performance of heat exchangers developed during the course of this work, under a load from either a powered module or a calibrated heat source. This test bed is also capable of simulating the actual running conditions of a hybrid vehicle cooling system. Monitors were installed to measure the temperature increase of the coolant as well as the pressure drop through the heat exchanger. The system is capable of varying the in-coming fluid temperature, pressure, and flow rate, in order to evaluate the heat exchanger performance over a range of parameters. Figure 5.1 shows a detailed schematic of this test bed.

The following is a detailed description of how the system was operated, referring to the circled numbers shown in Figure 5.1. To start, the coolant was heated to a set temperature in the reservoir at point 1. The flow was regulated at point 2 and monitored at point 3. The pressure of the flow was controlled and monitored at point 4. The coolant flows through the heat exchanger at point 5. Universal connectors were used to permit the testing of a variety of heat exchangers and scaled prototype designs. This test bed can accommodate various prototype module designs and also calibrated, variable heat sources to accurately characterize heat exchangers performance. The pressure drop across the heat exchanger was measured at point 6. A ten-

channel temperature monitor at point 7 was used to display the fluid temperature at the points shown as well as the surface temperatures of the exchanger and devices under test (DUT). The fluid cooler at point 8 was used to remove the heat added to the system by the heat exchanger. The pump at point 9 was positioned after the exchanger, prior to the coolant's return to the reservoir. This position was intended to dampen any pressure pulsations from the pump, thus smoothing the flow. However, this configuration increased the pumping effort and thus, the pump was not able to push enough flow. Therefore, the location of the pump and reservoir were switched and the pump was placed after the reservoir. An additional data acquisition unit was also connected to collect and record the data from the monitors.

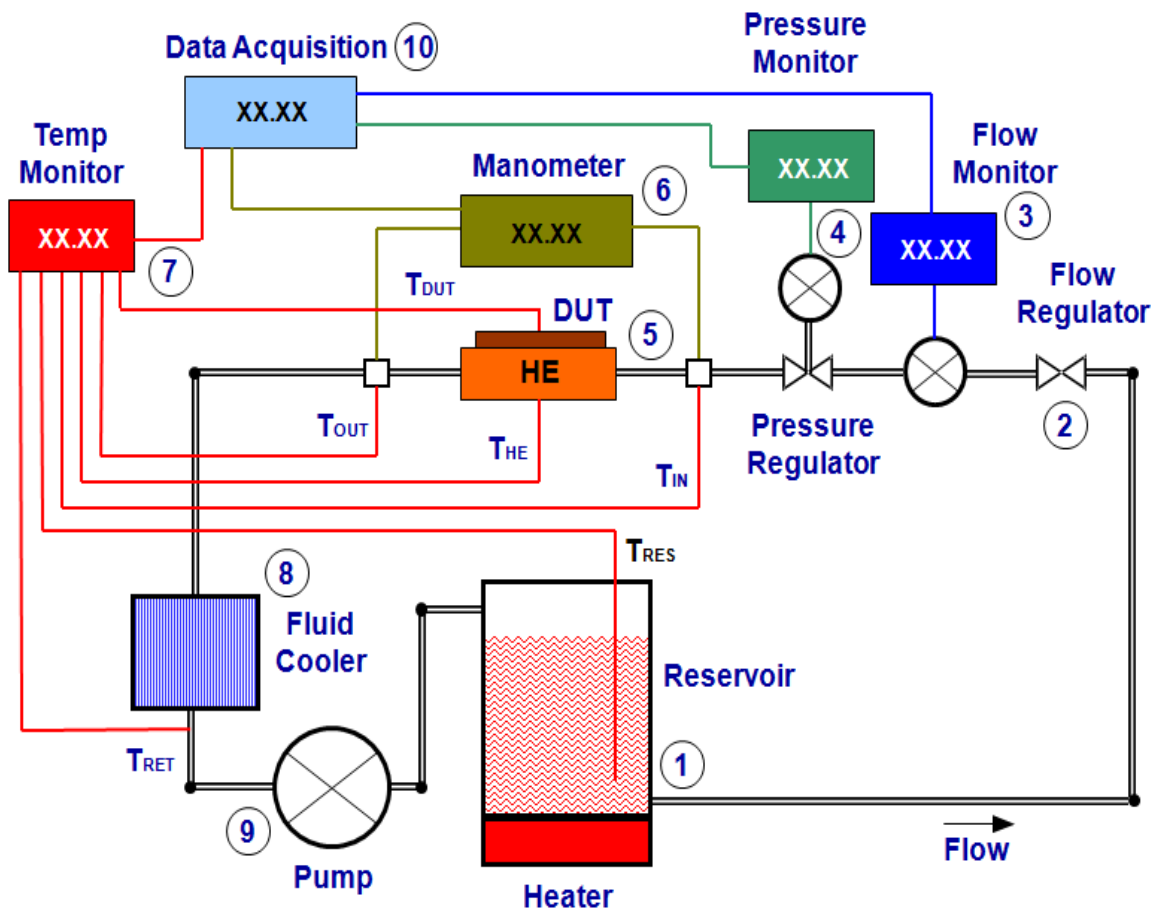


Figure 5.1. Schematic of the Thermal Test Bed

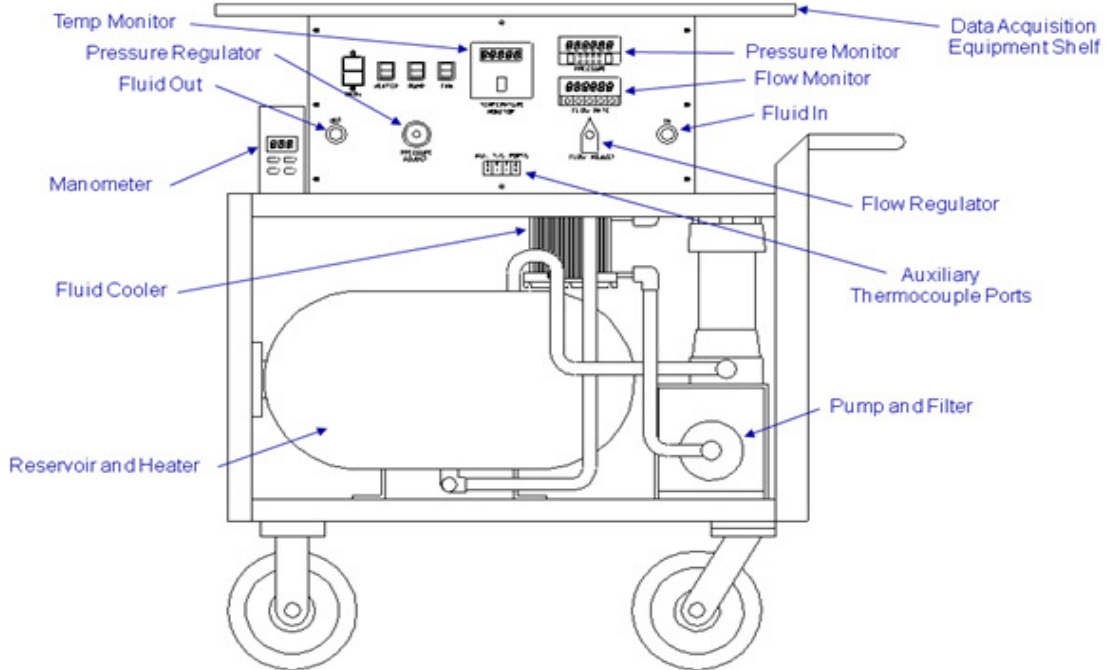


Figure 5.2 Schematic representation of the liquid-based thermal test bed.

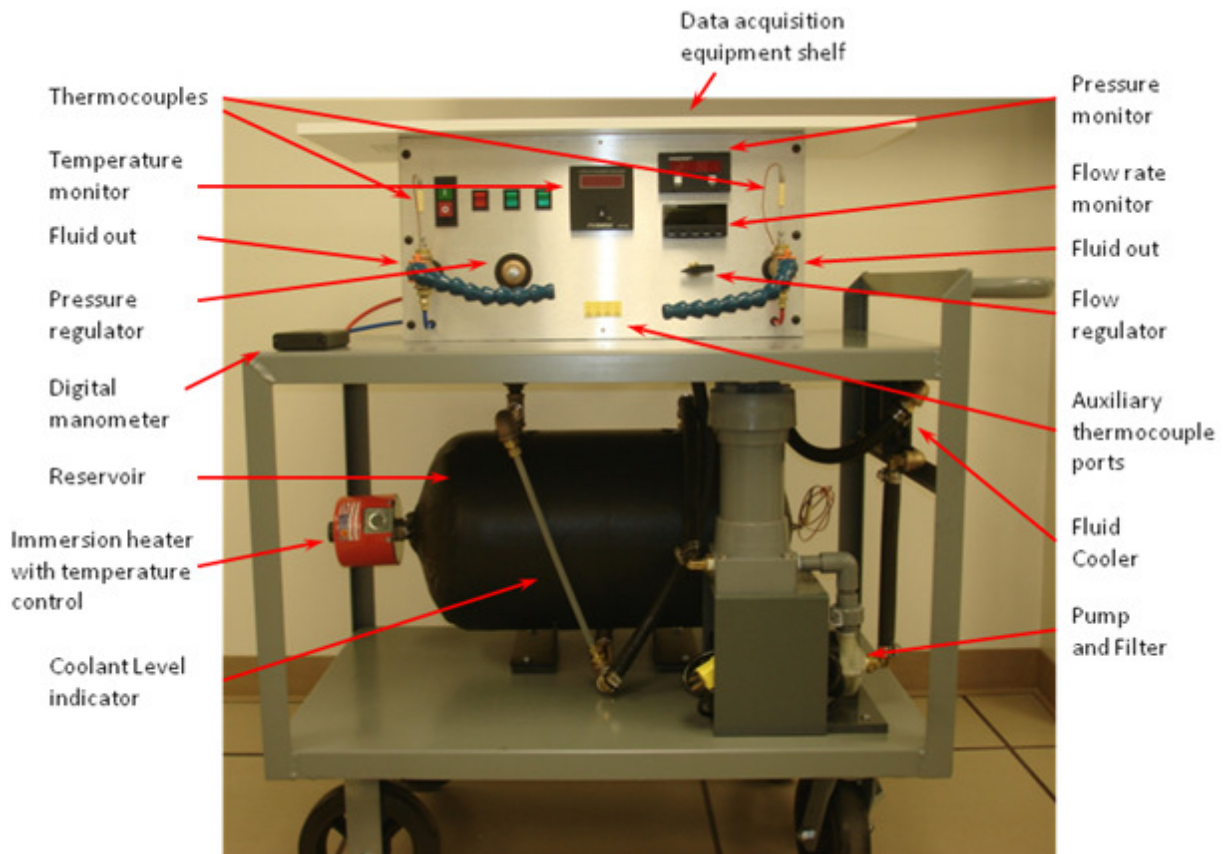


Figure 5.3. Overall view of the functional liquid-based thermal test bed.

Figure 5.2 schematically represents the overall view of the thermal test bed with the locations of various components. Figure 5.3 shows an overall view of the assembled test set-up. The test bed consisted of three sections – pumping section, control panel and the test section. Figure 5.4 shows the various components of the pumping and control panel section along with the fittings, tubing and connectors.



Figure 5.4. Various components of the thermal test bed before assembly.

5.1.1. Pumping Section:

The pumping section consisted of a large reservoir, an immersion heater with a thermostat, a centrifugal pump with filter, and an air-cooled cross-flow based radiator type fluid cooler to dissipate the thermal energy gained during the experiments to the ambient so as to maintain a constant inlet temperature. Following is a detailed description of the various components of the pumping section.

Reservoir:

An ASME-Code horizontal pressure tank having a capacity of slightly over 10 gallons was used as a coolant reservoir. The tank was purchased from McMaster-CARR (part # 9908K14). The tank has two mounting feet; pressure-rated plugs; and a welded plate that lists ASME approval and maximum pressure, which is 200 psi. Tank is rated for 29.9" Hg vacuum, but is not ASME rated for vacuum. The tank has a temperature range of -20° to +650° F. All openings in the tank have NPT female threads and all plugs are steel. The tank is black powder-coated finish and also has an epoxy lining that prevents the internal surface of the tank from rusting. Figure 5.5 shows an image and schematic of this reservoir. Table 5.1 lists the various dimensions of this reservoir.

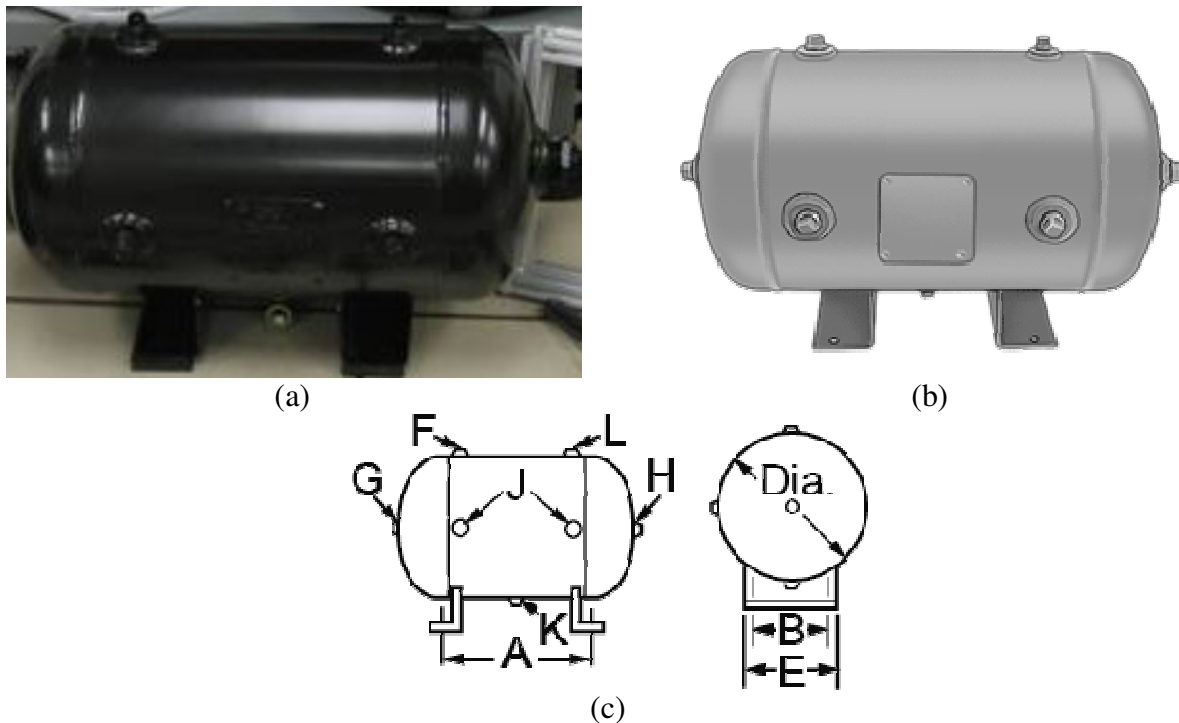


Figure 5.5. (a) Image of the coolant reservoir (Photo by author) (b) and (c) schematic representation of the coolant reservoir (Source: www.mcmaster.com).

Table 5.1. Dimensions of the coolant reservoir.

Diameter	Length	Overall Height	A	B	E	F	G	H	J	K	L	Mounting Hole Size
12"	23"	14"	10"	6½"	8"	¾"	¾"	1½"	¾"	½"	½"	7/16"

Immersion Heater:

A single phase 1500 W immersion heater having an Incoloy heating element as well as having a temperature control was used for heating the coolant temperature to a set temperature and to maintain a fixed coolant inlet temperature. The Incoloy element enables its use with tap water, light weight oils, heat-transfer oils, degreasing solutions, fuel oils and mineral oils. This heater was purchased from McMaster-CARR (part # 3656K132) and comes with brass screw plugs that have NPT threads and thus, it was easy to insert into the coolant reservoir. The temperature control on this heater was adjustable from 60° F to 250° F. Figure 5.6 shows an image of this immersion heater. The length of the heating element (A) was 11”.

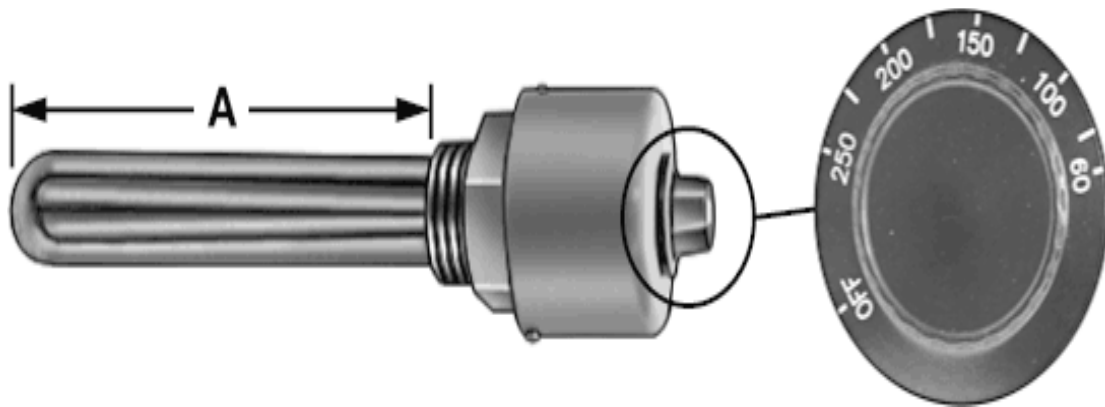


Figure 5.6. Schematic of the immersion heater with temperature control (Source: www.mcmaster.com).

Centrifugal Pump:

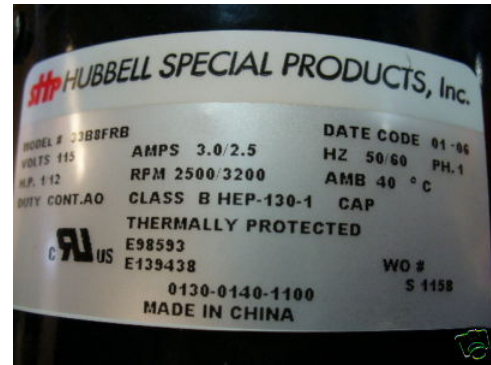
A centrifugal pump with attached filter and driven by a 1/12 horsepower electric motor (Manufacturer: Hubbell, Model # 33B8FRB) was used for pumping the required flow rate through the thermal test bed. The motor has a voltage and amperage rating of 115 V and 3.0/2.4 A respectively and is capable of operating at up to 3200 rpm. The motor has a shaft of 5/16” and is 1/2” long. Figure 5.7 shows the centrifugal pump attached to the electric motor and filter as well as the electric motor and its specifications.



(a)



(b)



(c)

Figure 5.7. (a) Centrifugal pump with attached electric motor and filter. (b) 1/12 HP electric motor (c) Motor specifications

Tube-Fin Heat Exchanger:

A tube-fin type heat exchanger manufactured by Lytron (part # 6110G1AN) was used to dissipate the thermal energy gained at the test-section to the ambient. Figure 5.8 shows an image of this heat exchanger. This heat exchanger has copper tubing that expands into copper fins for enhanced heat transfer rates. The recommended coolant for this copper heat exchanger is water or ethylene glycol with water. This heat exchanger is electro-static dip painted for hostile environments (corrosion resistance) and is supplied with built-in, fan-ready mounting hardware.

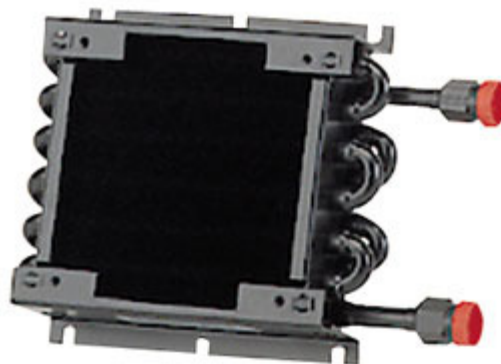


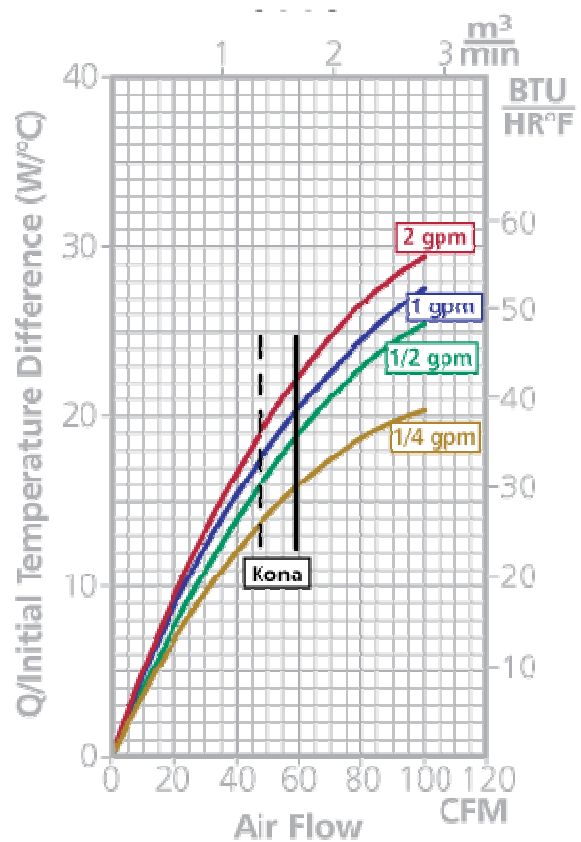
Figure 5.8. Image of the tube-fin type heat exchanger used to dissipate the thermal energy gained at the test-section to the ambient.

Fan for the Tube-Fin Heat Exchanger:

To increase the dissipation from the tube-fin heat exchanger to the ambient air, a fan was required. A 20 W axial fan manufactured by PAPST (Model # TYP 460°X) and recommended by Lytron was used. Figure 5.9(a) shows an image of this fan. The size of the fan is 119 mm X 119 mm X 38 mm and can produce up to 60 cfm of air flow. Figure 5.9(b) summarizes the performance of the tube-fin heat exchanger when it is operated with this fan.



(a)



(b)

Figure 5.9. (a) Image of the 20W fan used with the tube-fin type heat exchanger. (b) Tube-fin type heat exchanger performance when the above fan is used.

5.1.2. Control Panel:

The control panel section of the thermal test bed essentially consisted of the main power switches and data monitoring systems. Figure 5.10 shows a zoomed in view of the control panel for a sample experimental condition. The main power switches included the power switch for the

entire test bed, for the immersion heater, for the pump and for the fluid cooler fan. The data monitoring system included K-type thermocouples, ten channels thermocouple readout, thermocouple ports, a digital manometer, a pressure transducer, a pressure regulator, a flow control valve, a line pressure monitor, a flow-rate monitor and auxiliary data acquisition systems for data recording. Following is a detailed description of the various components.

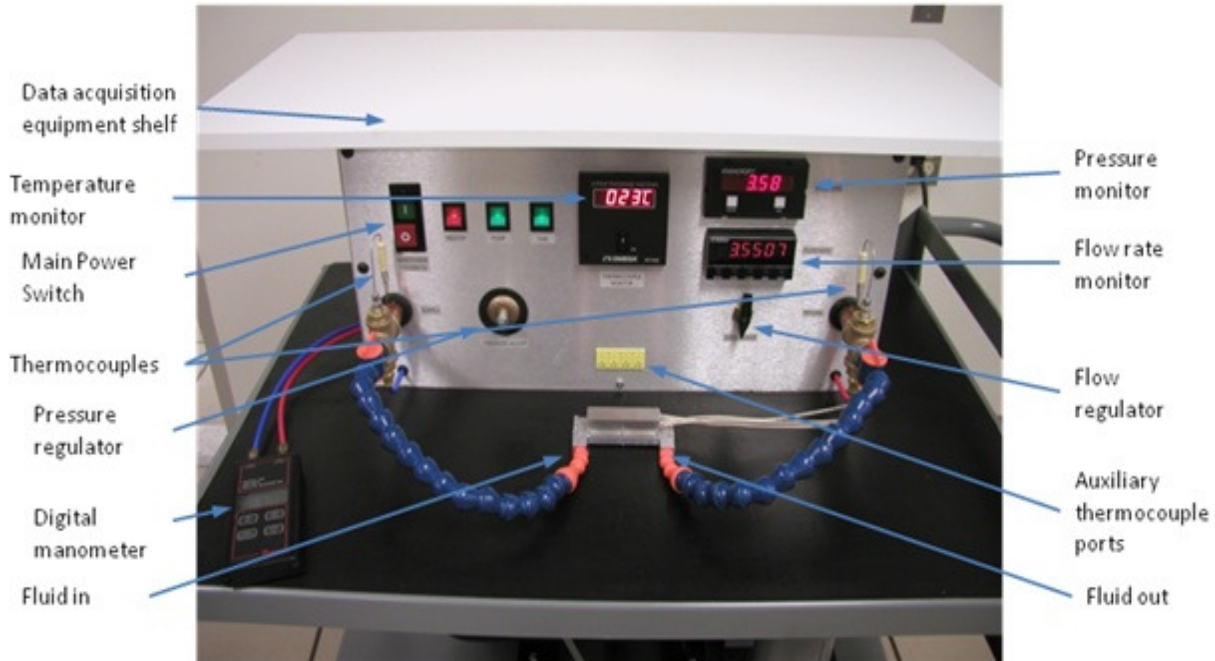


Figure 5.10. Overall view of the control panel.

Digital Manometer

The differential pressure across the sample coolers was measured using a wet/wet Dwyer digital manometer shown in Figure 5.11. It is a versatile, hand-held and battery operator series 490 digital manometer having a range of 0 - 100 psi (0 - 690 kPa). Units are highly accurate ($\pm 0.5\%$ Full Scale) for positive or positive differential pressure measurement and can tolerate most liquid media compatible with 316L stainless steel. Other features include a selection from up to seven common English and metric pressure units (psi, in. H₂O, in. Hg, mm Hg, kPa, bar or

mbar), a memory function that allows up to 40 readings for later recall and a backlight for providing auxiliary lighting at hard-to-see locations.



Figure 5.11. Series 490 Wet/Wet Dwyer digital manometer.

The following are its technical specifications:

- Service: Compatible gases & liquids.
- Wetted Materials: Type 316L SS.
- Accuracy: $\pm 0.5\%$ F.S., 60 to 78°F (15.6 to 25.6°C); $\pm 1.5\%$ F.S. from 32 to 60°F and 78 to 104°F (0 to 15.6°C and 25.6 to 40°C).
- Pressure Hysteresis: $\pm 0.1\%$ of full scale.
- Temperature Limits: 32 to 104°F (0 to 40°C).
- Pressure Limits:

6.895 bar

100.0 bar

203.6 in Hg

689.5 kPa

2768 in w.c.

5171 mm Hg

6895 mbar

- Storage Temperature Limits: -4 to 176°F (-20 to 80°C).
- Display: 0.42" (10.6 mm) 4 digit LCD.
- Power Requirements: 9 volt alkaline battery.
- Weight: 14.1 oz (400 g).
- Connections: Two 1/8" (3.18 mm) female NPT.



Figure 5.12. Image of the pressure regulator with gauge ports (Source: www.mcmaster.com).

Pressure Regulator:

A high capacity brass pressure regulator was used to regulate the pressure and high flow rates of the warranted application. The pressure regulator has a Buna-N seal and a neoprene diaphragm and is compatible with air, water, oil (up to 300 SSU) and gases. This regulator can handle up to a maximum inlet pressure of 400 psi. Its operational temperature range is -20⁰ F to

+180⁰ F. It comes with two 1/4" NPT female side gauge ports and plugs to close off one port. The outlet pressure range was 0 to 5 psi and it comes with a factory setting of 3 psi outlet pressure. Figure 5.12 shows an image of the pressure regulator.

Pressure Transducer/Transmitter:

A poly-silicon thin film pressure transmitter manufactured by Ashcroft (Model # K17M0242F2100) was used to measure the line pressure. The transmitter has an operational pressure range of up to 100psig and temperature range of -20⁰ F to +180⁰ F. The transmitter uses a metal diaphragm and a poly-silicon strain gage bridge to convert the pressure data to electrical data (either current or voltage). The integral metal diaphragm and the poly-silicon bridge are very robust and are virtually unaffected by shock, vibration or mounting. The accuracy of the system is 1% ± 0.04 %/⁰F and provides an output signal within 4 mA to 20 mA. This unit comes with 1/4" NPT-Male threads and 36" shielded cable with PVC sheathing. Figure 5.13 shows an image of this unit.



Figure 5.13. Image of the pressure transmitter.

Pressure Indicator:

A pressure indicator manufactured by Ashcroft (Model # 2269A) and compatible with the above pressure transmitter was used for monitoring the line pressure. It accepts all the standard process signals: 4-20mA, 1-5V, 0-5V and 0-10V from transmitters and transducers, and displays these signals in engineering units on a 4½ digit display. The display includes an extra zero which

may be used to handle numbers up to 199,990. It has a jumper 3, at the rear of the instrument, to restrict the modifications of calibration values and it has an accuracy of $\pm 0.05\%$ of calibrated span. The instrument has an operational temperature range of $-10\text{ }^{\circ}\text{C}$ to $+75\text{ }^{\circ}\text{C}$. Figure 5.14 shows an image of this instrument.



Figure 5.14. Image of the pressure indicator.



Figure 5.15. Image of the ten point temperature indicator.

Ten Point Temperature Indicator:

A temperature scanner manufactured by Omega (Model # DP1096) capable of monitoring up to 10 Type K thermocouples was used to monitor the temperature at various

locations in the test section. The instrument has a measurement range of $-50\text{ }^{\circ}\text{C}$ to $+1350\text{ }^{\circ}\text{C}$ with a resolution of $1.0\text{ }^{\circ}\text{C}$ and an accuracy of $\pm 0.25\%$. Figure 5.15 shows an image of this instrument.

Flow Meter/Transducer:

A pulse output water meter manufactured by omega (part # FTB-4605) was used for remote flow rate indication. This instrument is also capable of flow totalization. It has an operational range of 0.15 GPM to 13 GPM with a maximum allowable pressure of 150 psig. It has an accuracy of $\pm 1.5\%$ of flow rate for flow rates greater than 6.6 GPM and an accuracy of 2% of flow rate for flow rates below 6.6 GPM. It has a rated pressure drop of 2.9 psid across the unit at 6.6 GPM. It comes with 1/2" NPT-Male threads and has an operational temperature range of $0\text{ }^{\circ}\text{C}$ to $88\text{ }^{\circ}\text{C}$. Figure 5.16 shows an image of this flow meter.

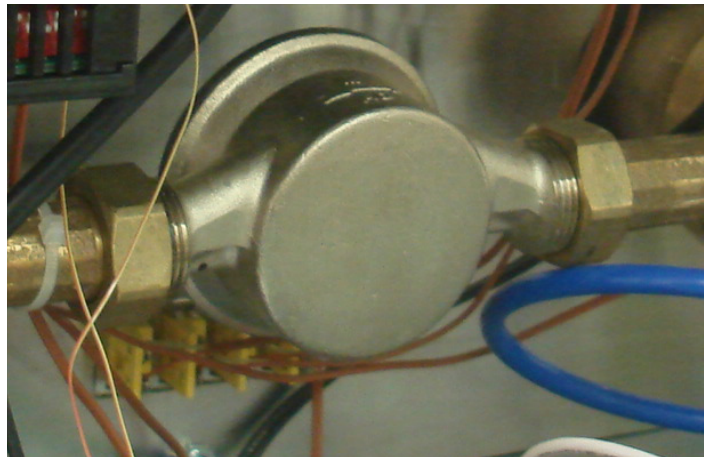


Figure 5.16. Image of the remote flow rate indicator.

Flow Rate Monitor:

A flow rate monitor manufactured by omega (part # DPF 701) and compatible with the above flow sensor was used to monitor the flow rate. This ratemeter/totalizer offers user programming options via 5 front-panel keys. Scale factor in this unit may be programmed from -99,999 to 999,999 (any decimal point, multiply or divide), while offset may be programmed from -99,999 to 999,999 (any decimal point). Programs are stored in non-volatile memory, with

three levels of program lockout for security. Optional features of this unit include Hi or Lo setpoints for control or alarm, plus RS-232 communication. It also provides for fixed decimal point as well as auto-ranging. This unit has an operational frequency range of 0.5 Hz to 30 kHz.

Figure 5.17 shows an image of this instrument.



Figure 5.17. Image of the flow rate monitor.

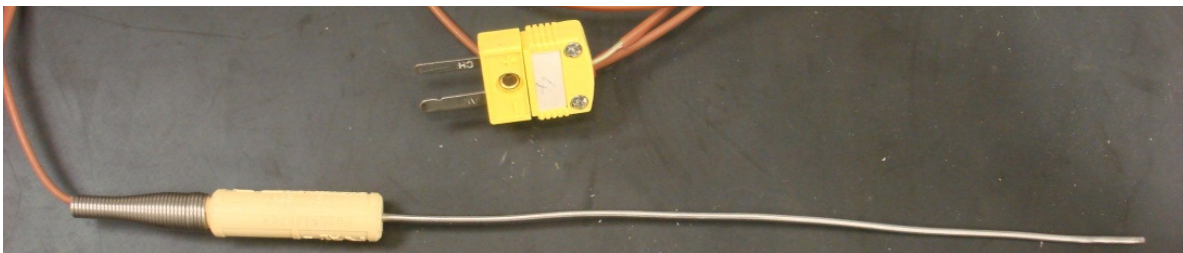
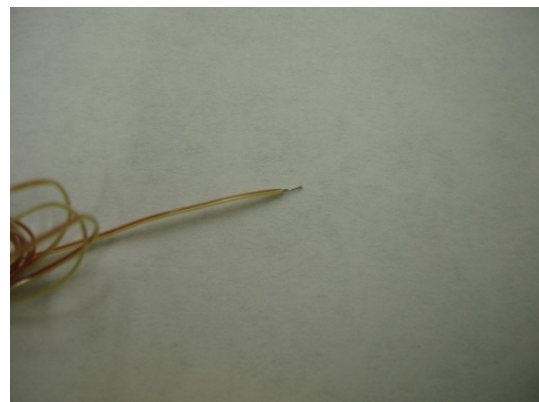
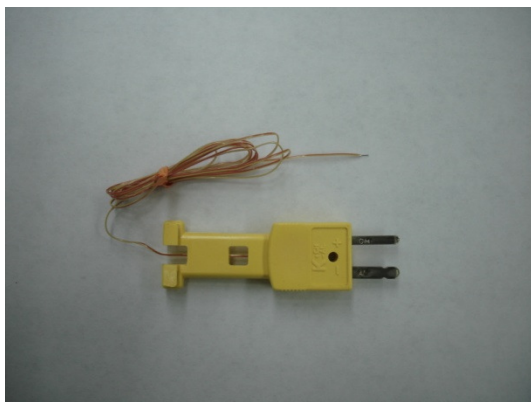


Figure 5.18. 36 gauge K-type Thermocouple with molded subminiature connector and 1 mm diameter transition joint thermocouple probe.

Type K Thermocouples:

36-gauge K-type thermocouples (5SC-TT-K-36-36) and 1 mm diameter transition joint thermocouple probes (TJ36-CASS-040U-6) as shown in Figure 5.18 were used for the temperature measurements. Transition joint thermocouples provide durability and fast, accurate temperature measurements as well as allow "pin-point" accuracy of measured values while protecting the measurement junction inside the metal sheathing and mineral insulation. The technical specifications of the K-type thermocouples used are as follows:

- K-type calibration
- 36 AWG Wires with PFA Insulation. Max. Service Temp 260°C (500°F)
- Made from Special Limits of Error Wire
- 36" Lengths Standard
- Molded Subminiature Connector with Integral Strain Relief/Spool
- Max Service Temp for Connector Body 220°C (425°F)

Data Acquisition System:

In addition to the ten-point temperature indicator, the OMB-DAQ-54 Personal Daq (Figure 5.19) connected to a PC was used for temperature readout and recording. It is a full-featured data acquisition product that uses the Universal Serial Bus (USB) built into almost every new PC. Designed for high accuracy and resolution, the OMB-DAQ-54 data acquisition systems directly measure multiple channels of voltage, thermocouple, pulse, frequency, and digital I/O. A single cable to the PC provides high-speed operation and power to the OMB-DAQ-54. The OMB-DAQ-54 data acquisition system offers 10 single-ended or 5 differential analog (up to ± 20

V full scale) or thermocouple input channels with 16 programmable ranges and 500 V optical isolation.



Figure 5.19. OMB-DAQ-54 Data Acquisition System.

5.1.3. Test Section

The test section essentially consisted of the heat exchanger samples to be tested and the concentrated heat sources. The heat sources used were either thin foil heaters readily available in the market or copper block heaters made by inserting super watt cartridge heaters into the copper block or regulated real active devices (that is, IGBTs and Diodes). In all 4 different heat exchanger samples were tested.

Heat Exchanger Sample1:

Figure 5.20 shows the overall view of the assembled test section for the first heat exchanger sample and Figure 5.21 shows the exploded view of its various components. Eleven thermocouples were placed inside the target plate alone to monitor the axial and lateral heat conduction in the target plate. A couple others were located at the coolant inlet and outlet and few others on the heater surface. Small holes were drilled into the target plate and the thermocouples placed into those holes and sealed. Figure 5.22 schematically shows the location of the

thermo-couples in the target plate. Few experiments were conducted on the thermal test bed using water as the coolant. For each experiment, inlet and outlet water temperature and temperatures at different locations on the target plate and on the surface of the heater block were recorded. The cartridge heaters placed inside the copper heater block were connected to a DC power supply to provide the input power. Line pressure, pressure drop across the heat exchanger and flow rate were also measured. The experimental results and simulation predictions for this heat exchanger sample are presented in Appendix I.

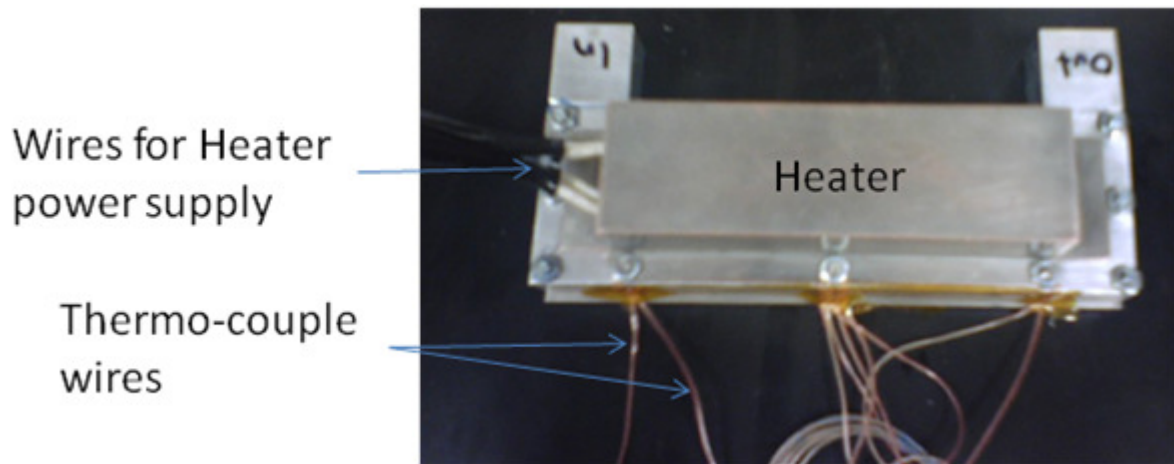


Figure 5.20. Overall view of the assembled test section for the first heat exchanger sample.

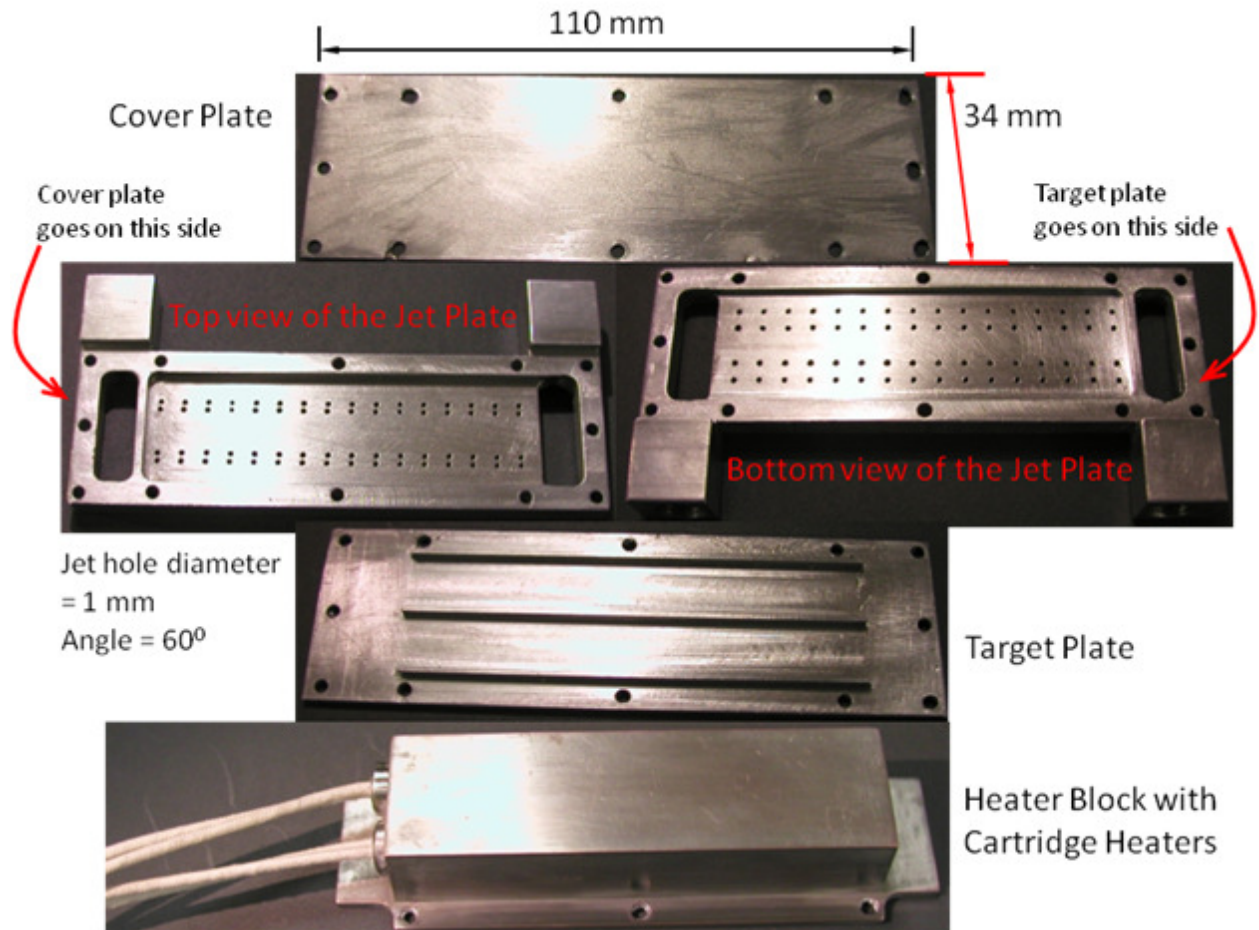


Figure 5.21. Exploded view of the different components of the test section for the first heat exchanger sample.

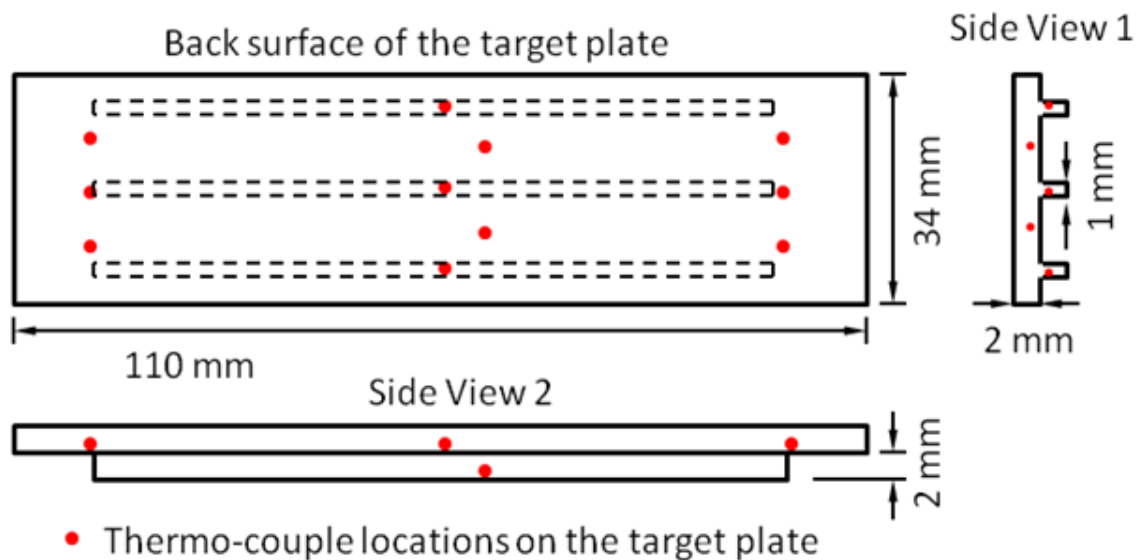


Figure 5.22. Schematic representation of the thermocouple probing locations on the target plate.

Heat Exchanger Sample 2:

Figure 5.23 schematically shows the assembled test section for the second heat exchanger sample. For this case, concentrated heating was provided with the help of two different types of heater. In one case, thin foil polyimide heaters from MINCO were used and in the other case, a copper block heater with rectangular legs was used. Details of this sample are presented in the section 5.2. This heat exchanger sample was also modified to work in conjunction with phase change material. The details of this set-up are presented in Chapter 8.

Heat Exchanger Sample 3:

This heat exchanger sample was one of the prototype coolers that was based on the best performing impingement cooler and was designed and fabricated to test under real thermal loads from IGBTs and Diodes. The details of this sample are presented in Chapter 6.

Heat Exchanger Sample 4:

This heat exchanger sample was one of the prototype coolers that was based on one of the high performance ribbed mini-channel cooler configuration and was designed and fabricated to test under real thermal loads from IGBTs and Diodes. The details of this sample are presented in Chapter 7.

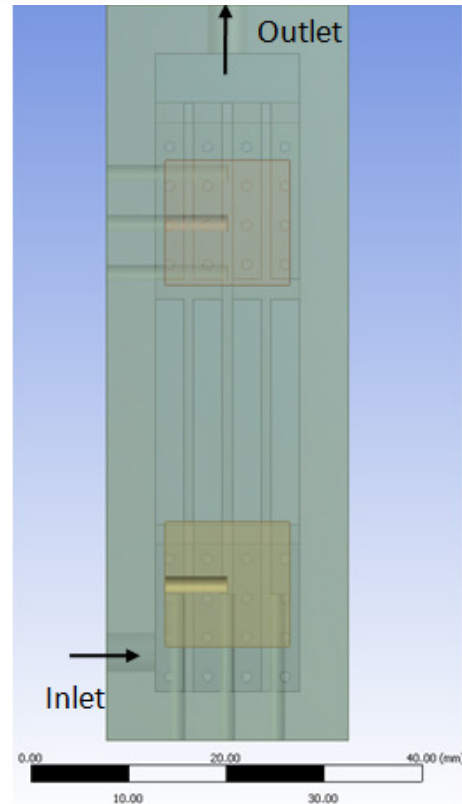
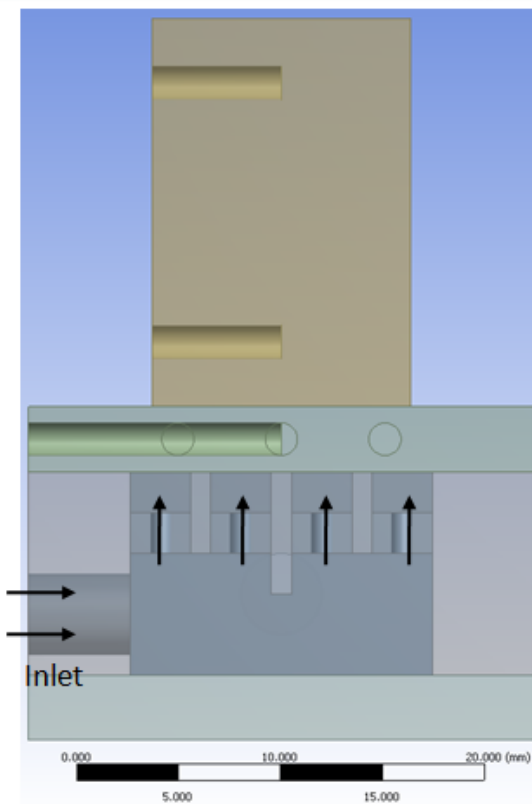
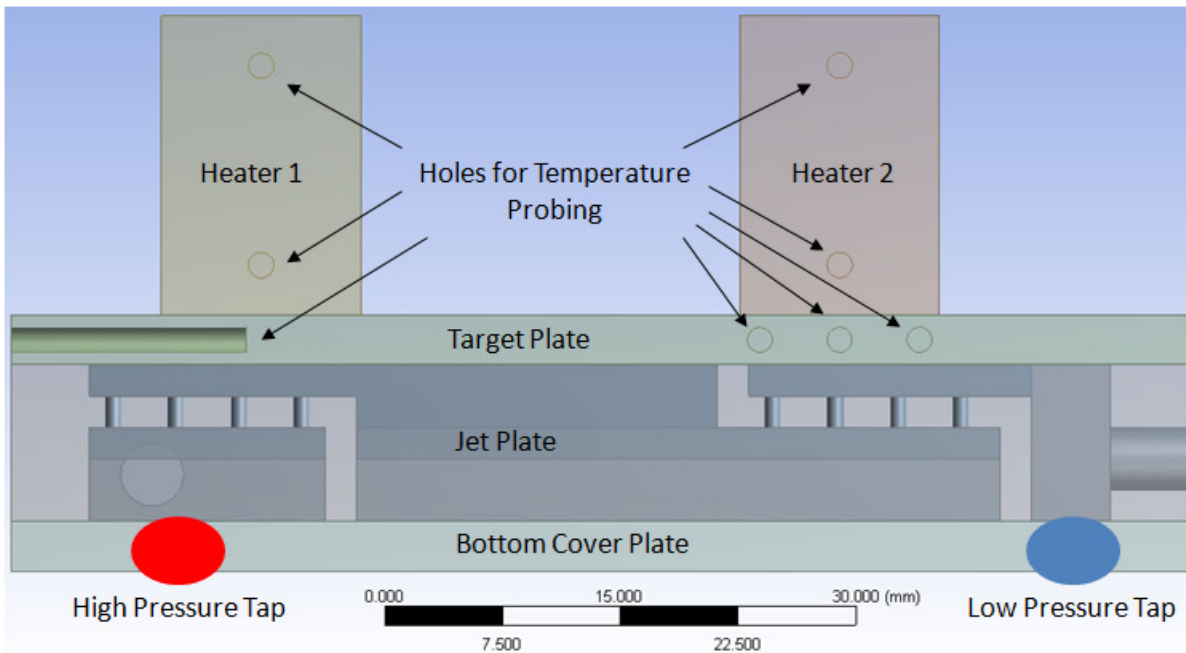


Figure 5.23. Different views of the simulation model corresponding to the test section of the thermal test bed. Red and Blue dots represent the location of high and low pressure taps respectively

5.2. Thermal Test Bed Experiment

A normally impinging jets based heat exchanger, schematically shown in Figure 5.23 was one of the heat exchangers that were fabricated and tested for its performance under concentrated heat sources and also tested for conjugate simulation validation. The flow enters the impingement based cooler from one side and impinges onto the foot print of one of the heat sources and is then collected into a plenum and then re-impinges on the target plate under the second heat source. The heat is conducted to the target plate from the heaters and accounts for some spreading. The heat is then dissipated by the impinging jets cooling the target plate.

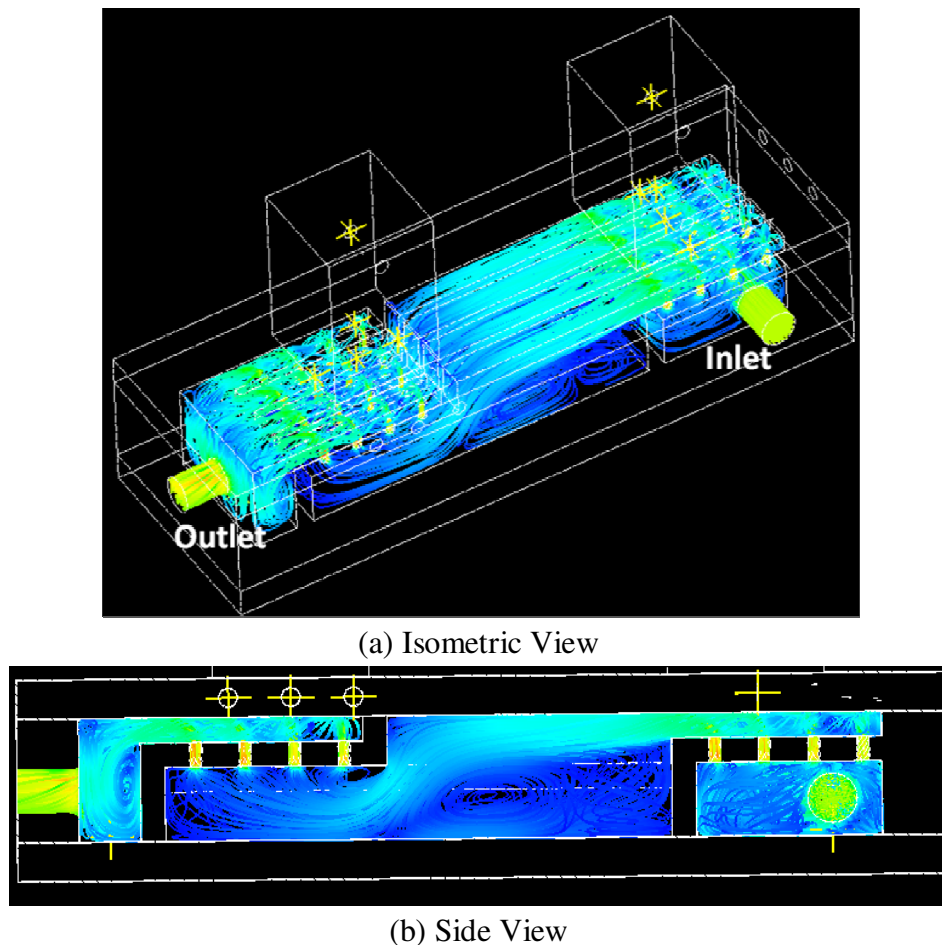


Figure 5.24. Streamlines showing the flow path in the impingement based cooler.

Figure 5.24 shows the isometric view and side view of the flow path within the cooler from the inlet on the right to the outlet on the left. The target plate, the cover plate and the jet

plate were attached in the desired orientation by means of a thermal adhesive (thermal conductivity: 1.8 W/m-K). Two pressure taps were drilled on the cover plate for pressure drop measurements and six cylindrical holes were drilled into the target plate for temperature measurements. The cover plate and the target plate were fabricated from Al 6061 while the jet plate was fabricated from Al 6063.

Initially, two thin foil Polyimide heater from Minco (Part # HK5573R15.7L12F) having a foot-print area of 1.94 cm² and powered by a DC power source were used as the heat source. Few of the experiments were conducted with 2 MINCO heaters and few others were conducted with one MINCO heater. For the case of one MINCO heater, the adhesive layer underneath the heater was removed and a thermal adhesive having $k = 1.8$ W/m-K was applied. This enabled as to achieve higher heat flux (~ 28.5 W/cm²). Although, a high input power of 55 W was safely supplied by a single MINCO heater, it was not sufficient to provide a larger change in the coolant temperature. Thus, the uncertainty in the inlet and outlet temperature comparison with the simulations was very high. To reduce such errors and improve the input power, a copper block with two hot-watt heaters (part # HS37-3) as shown in Figure 5.25 was used to mimic high density concentrated heat sources. It was designed in such a way so that each rectangular leg acts as a heat source. In the simulation model shown in Figure 5.23, only these two rectangular legs were modeled. The foot-print area of each leg was 1.61 cm² (1.27 cm X 1.27 cm). This enabled as to achieve over 300 W of input power with heat fluxes as high as 116 W/cm². The chosen heat flux is relatively low for the warranted applications. Two holes were drilled in each legs/heaters to measure the thermal energy/flux through each heater. The heater was attached to the cooler by using a thermal adhesive ($k = 1.8$ W/m-K) and also, the set-up was well covered with the insulation material but even then the heat losses from the bulky heater were high ($\sim 18\%$). This

loss was measured as the difference between the power (voltage X current) supplied to the cartridge heaters and the thermal energy flowing into the cooler through the rectangular legs. The heat losses in rest of the test-section were very low (~ 1-2%) and was measured as the difference between the heat flowing into the cooler and the heat carrier away by the coolant.

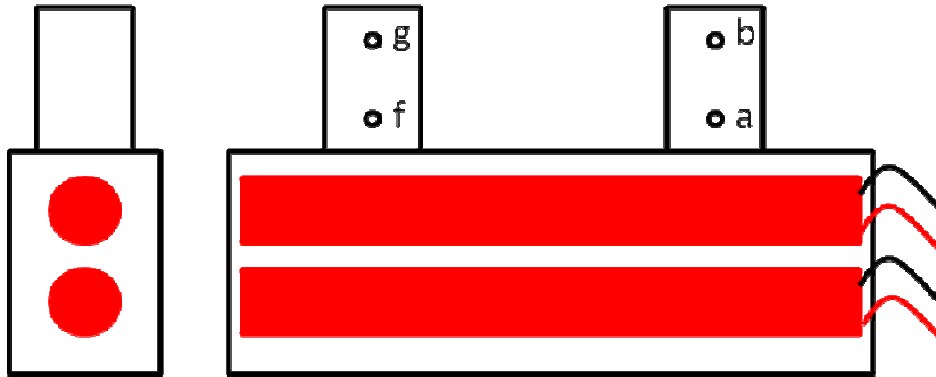


Figure 5.25. Concentrated heat source made from copper block and 2 cartridge heaters. Foot-print area of each rectangular heater leg is 1.61 cm^2 (1.27 cm X 1.27 cm).

In all the experiments, temperature errors were minimized by using a data acquisition system for temperature recording and also, the entire test section was well insulated. The temperature difference readings had a maximum error of $\pm 0.2 \text{ }^\circ\text{C}$. For each experiment, the cooling system was switch-on and adjusted to the required flow rate and then allowed to run for about 15-20 minutes to reach steady state. The heater was then switched-on and the system was allowed to reach steady state. Throughout the course of each experiment, the pressure drop across the test section showed a maximum fluctuation of about 0.2 kPa. Such slight fluctuation in the flow caused an average temperature variation of $0.1 \text{ }^\circ\text{C}$ with a maximum variation of $0.2 \text{ }^\circ\text{C}$. This same experimental set-up was also used for the testing of the final optimized impingement based heat exchanger design.

5.3. Simulation Strategy

Most of the earlier simulations were based on the strategy of simulating for the flow field (that is, convection) inside the heat exchanger to obtain the heat transfer coefficient at the inside

walls of the heat exchanger and then use that value to simulate for the heat transfer (that is, conduction) in the module under steady continuous operation. This process was however, a bit too cumbersome. Hence, it was worth an effort to simulate for the heat transfer behavior in the module and heat exchanger unit simultaneously. In other words, a new simulation strategy of solving conjugate heat transfer (that is, solving conduction and convection simultaneously) was used. With this strategy, the heat transfer coefficient definition can be by-passed and, also potential hot spots on the power module can be better identified. Figure 5.26 shows a flow chart to summarize this simulation strategy.

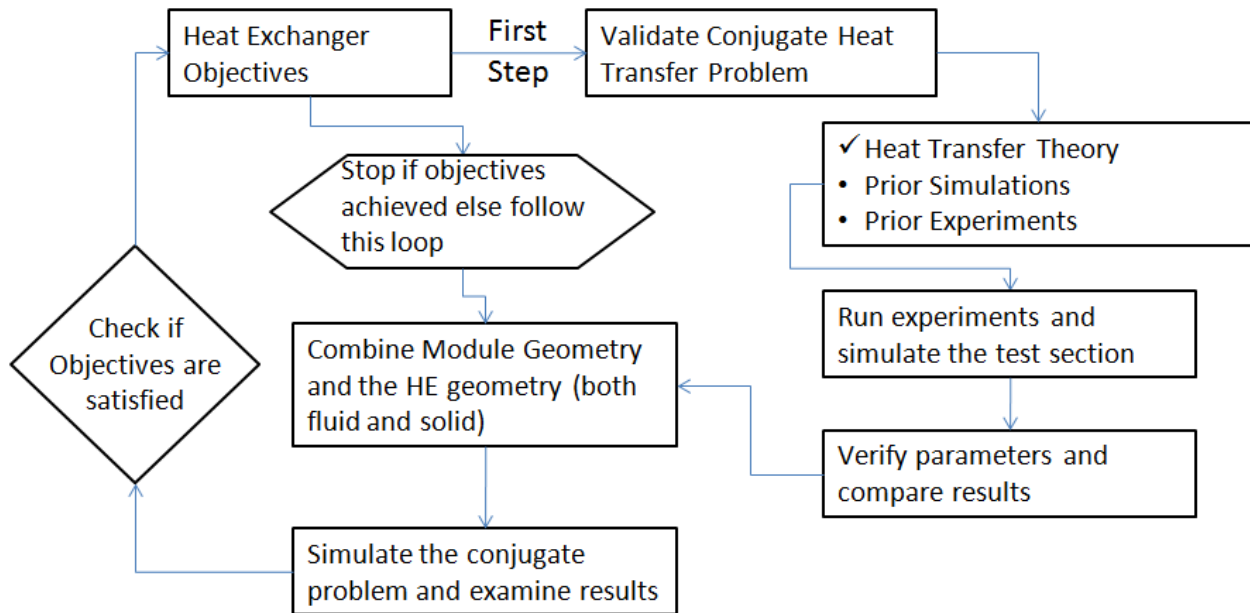


Figure 5.26. Flow chart summarizing the present simulation strategy.

The conjugate model was validated against analytical results and then it was compared against the data available in literature. For validation against theory, flow through a long thick-walled tube was simulated for constant outer wall temperature and for constant heat flux at the outer wall. Nusselt number predictions in the fully developed region were mostly within 3% error. Next step in validation was to validate against literature for conjugate heat transfer involving jet impingement cooling. The study of Sung and Mudawar [73] was used for this

validation. It was found out that k- ϵ model showed a better agreement as compared to any other model. Once validated, the test section of the thermal test bed was simulated and results compared to check the accuracy. Thermal test bed is the experimental set-up designed for simulating the actual engine running conditions. After this, the whole module with the heat exchanger was simulated to check for the hot-spots and possible failure locations. Based on the results, subsequent design changes are being made to achieve the heat exchanger objectives.

5.4. Model Verification

As a first step in model verification, the conjugate model shown in Figure 5.27 was used to validate against theory. Figure 5.27(a) shows the CFX model and Figure 5.27(b) shows the cross-sectional view of the conjugate model and the applied boundary conditions. Air at 25 °C with an average inlet velocity of 0.01 m/s was considered as the coolant and the outer wall was maintained at 80 °C. The diameter of the tube was taken to be 80 mm while the surrounding wall thickness was taken to be 1 mm. The entire length of the tube was taken to be 1000 mm. A sufficiently low flow rate was considered so that the flow is thermally and hydro-dynamically fully developed.

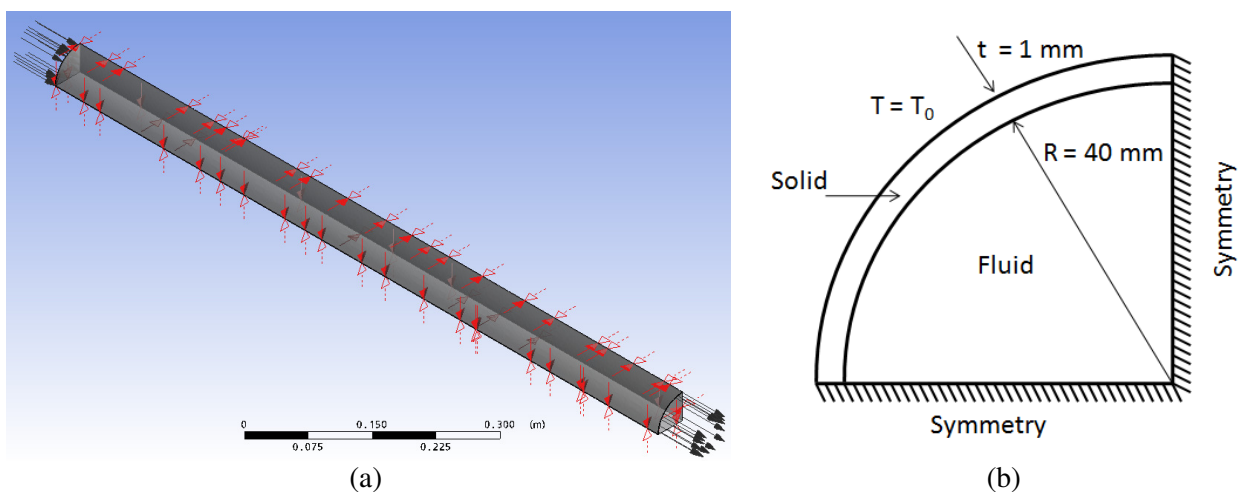


Figure 5.27. Conjugate heat transfer model. (a) ANSYS-CFX model with black arrows showing the in-flow and out-flow directions and red arrows indicating the symmetry boundary conditions. (b) Cross-sectional view of the model.

Figure 5.28 shows the temperature contours and Figure 5.29 represents the velocity contours on the symmetry planes. Clearly, the flow gets thermally and hydro-dynamically fully developed much before the channel exit. Figure 5.30(a) shows the wall adjacent temperature and centerline temperature profile along the length of the tube. Figure 5.30(b) shows the wall heat flux distribution along the length of the tube. Both the figures clearly suggest that the flow is fully developed. For comparison with theory (analytical results), the Nusselt number in the fully developed should be 3.66 for a constant wall temperature. From the simulation, the average Nusselt number in the fully developed region was found out to be 3.6865 (0.73% error) with a maximum value of 3.76 (~3% error) and minimum value of 3.57 (~2.4% error).

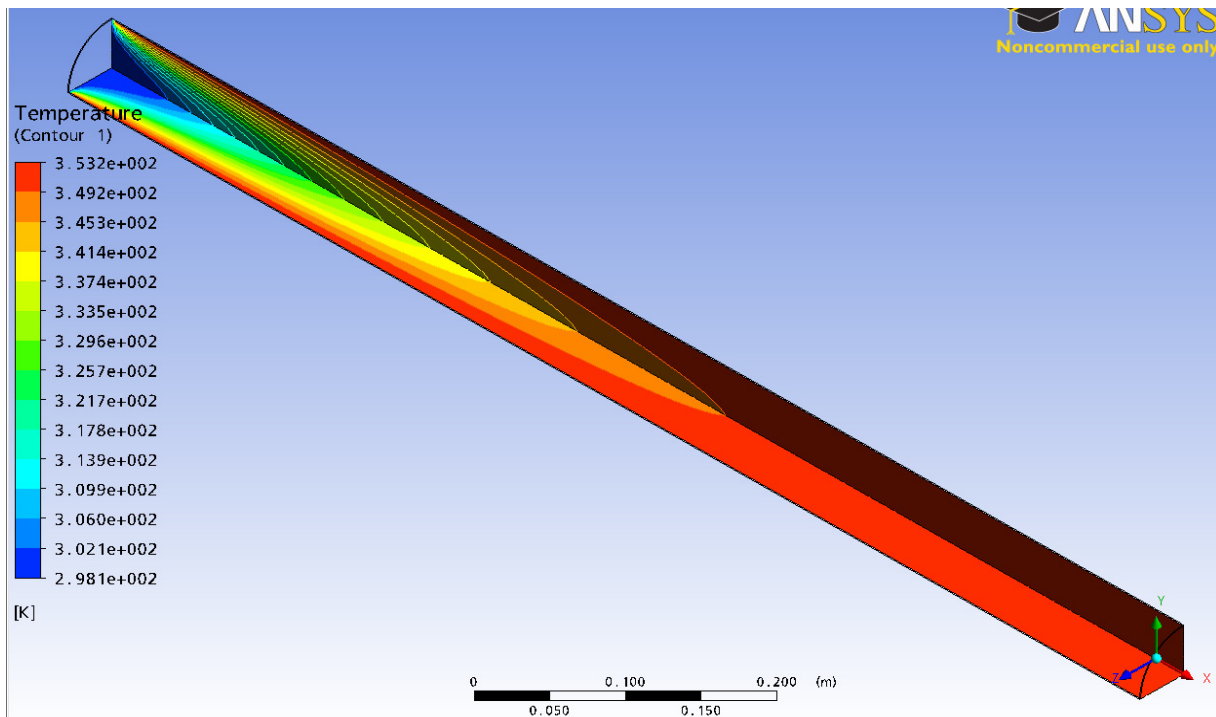


Figure 5.28. Temperature contours on the symmetry planes showing the flow is thermally fully developed much before the outlet.

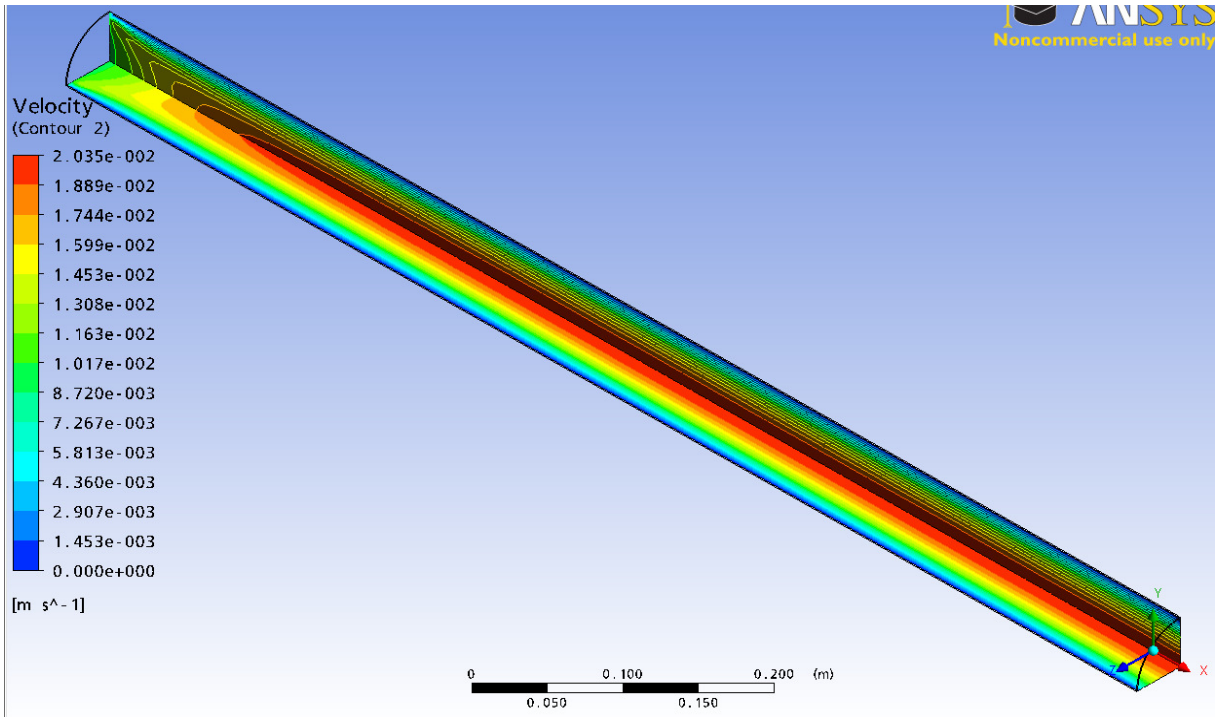


Figure 5.29. Velocity contours on the symmetry planes showing the flow is hydro-dynamically fully developed much before the outlet.

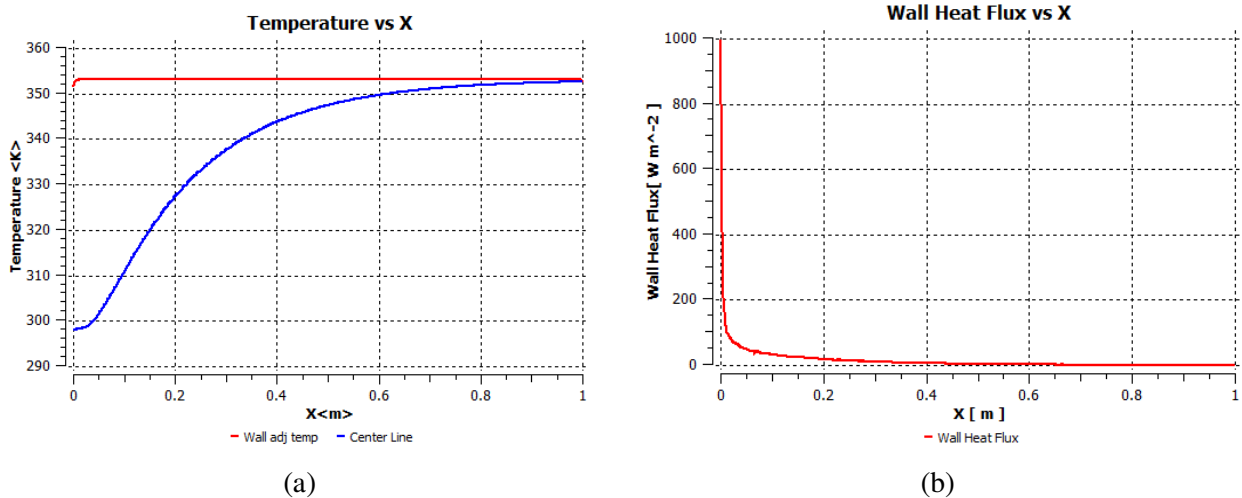


Figure 5.30. (a) Wall adjacent temperature and center line temperature profile (b) Wall heat flux profile for the conjugate heat transfer problem subject to constant temperature boundary condition.

A similar validation was performed to validate for constant wall heat flux for which the theoretical Nusselt number is 4.36. Air at 25 °C with an average inlet velocity of 0.01 m/s was considered as the coolant and a constant heat flux of 100 W/m² was applied (instead of constant

wall temperature) at the outer wall. From the simulation, the average Nusselt number in the fully developed region was found out to be 4.51 (3.4% error) with a maximum value of 4.72 (~8.5% error) and minimum value of 4.24 (~2.8% error).

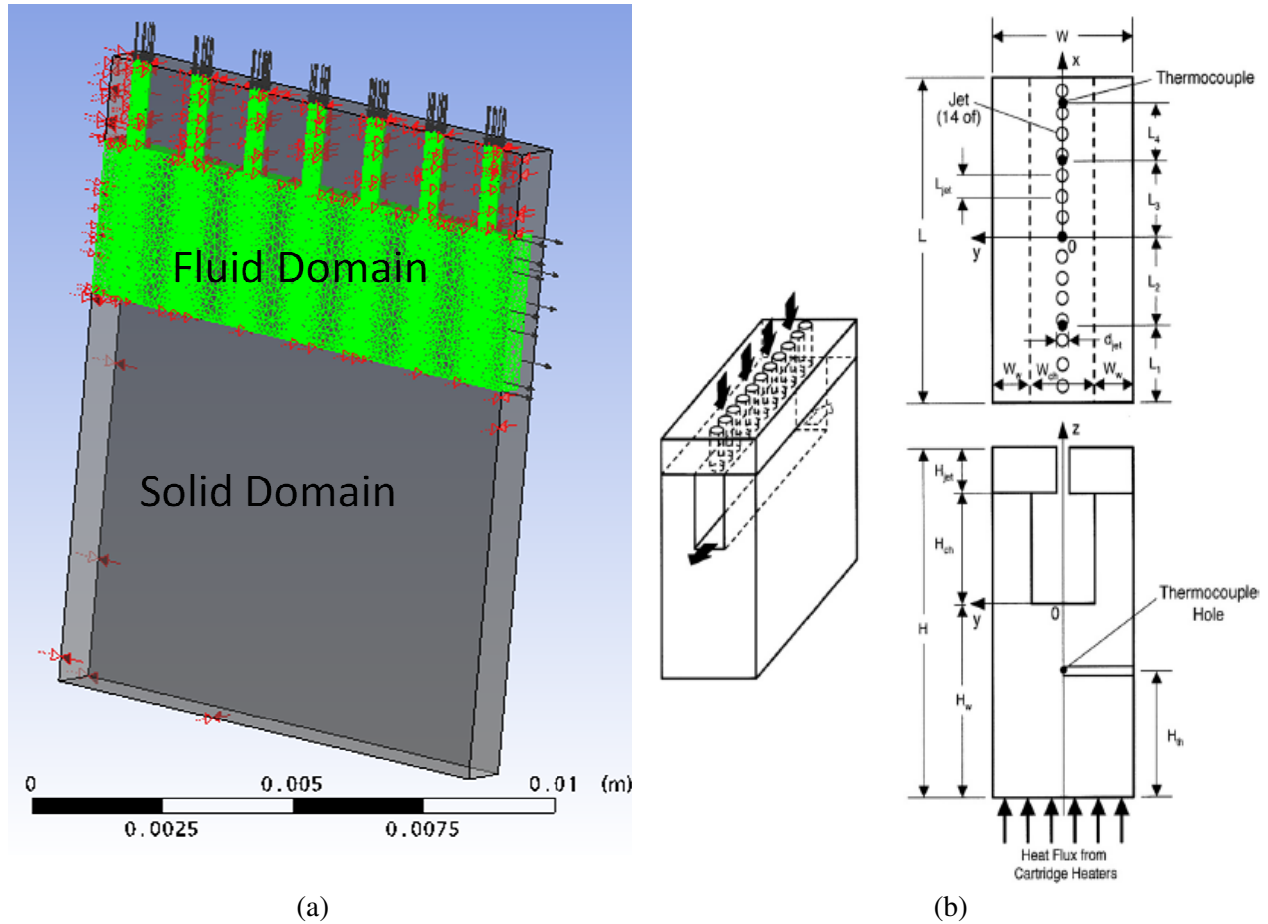


Figure 5.31. (a) Conjugate simulation model for validation against the literature. (b) Conjugate model used in the literature [73]. Black dots show the location of the thermocouples [73].

Table 5.2. Dimensions of the conjugate geometry used Sung and Mudawar [73].

L	L ₁	L ₂	L ₃	L ₄	W	W _{ch}	W _w	H	H _{jet}	H _{ch}	H _w	H _{th}	D _{jet}	L _{jet}
(mm)	(mm)	(mm)	(mm)	(mm)	(mm)	(mm)	(mm)	(mm)	(mm)	(mm)	(mm)	(mm)	(mm)	(mm)
20.00	4.00	6.00	3.00	6.00	1.83	1.00	0.42	14.27	1.65	3.00	7.62	5.08	0.39	1.43

Next step in validation was to validate against literature for conjugate heat transfer involving jet impingement cooling [73]. Figure 5.31 shows the geometry used (along with the complete model dimensions) in the literature as well as the CFX model simulated. The grey

portion is the solid domain while the green portion is the fluid domain. The red arrows show the symmetry boundaries while the black arrows indicate the inlet and outlet boundaries. In order to compare against the experiments, the temperature value on the symmetry plane at 2.54 mm from the fluid-solid interface was used. q''_{eff} is the effective heat flux applied at the bottom solid surface of the domain. The ANSYS-CFX simulation was carried out for the 20 °C inlet coolant temperature. However, for the CFX simulations, a double the amount of effective heat flux was used to obtain a good agreement with the experimental temperature measurements. The comparisons are presented in Figure 5.32. CFX simulations under predicted the temperature values. A similar observation was observed for the 0 °C inlet coolant temperature case. The velocity contours are plotted on the symmetry plane in the fluid domain and the temperature contours are plotted in the solid domain. This shows that the flow and thermal behavior are as expected, however, the numerical values do not match perfectly. The reason for this discrepancy was not clear and at that point, it was difficult to explore the cause as the simulations were validated against the heat exchanger sample 2 experiments.

5.5. Simulation Validation

ANSYS-CFX as well as ANSYS-Fluent, commercial computational fluid dynamics (CFD) codes were used to study the flow and heat transfer behavior in the proposed impingement based heat exchanger models. It was observed that both the commercial codes predicted similar results for all cases. CFX mesh method with appropriate mesh controls was used to mesh the models and it was ensured that the y^+ is always less than 1 for proper estimation of the flow and heat transfer behavior. Also, a fine mesh was used around all the sharp corners and normal to all the boundary surfaces, except the inlet and the outlet faces.

Figure 5.33 shows the cross-sectional view of the meshed domain with fine mesh spacing at all the interfaces.

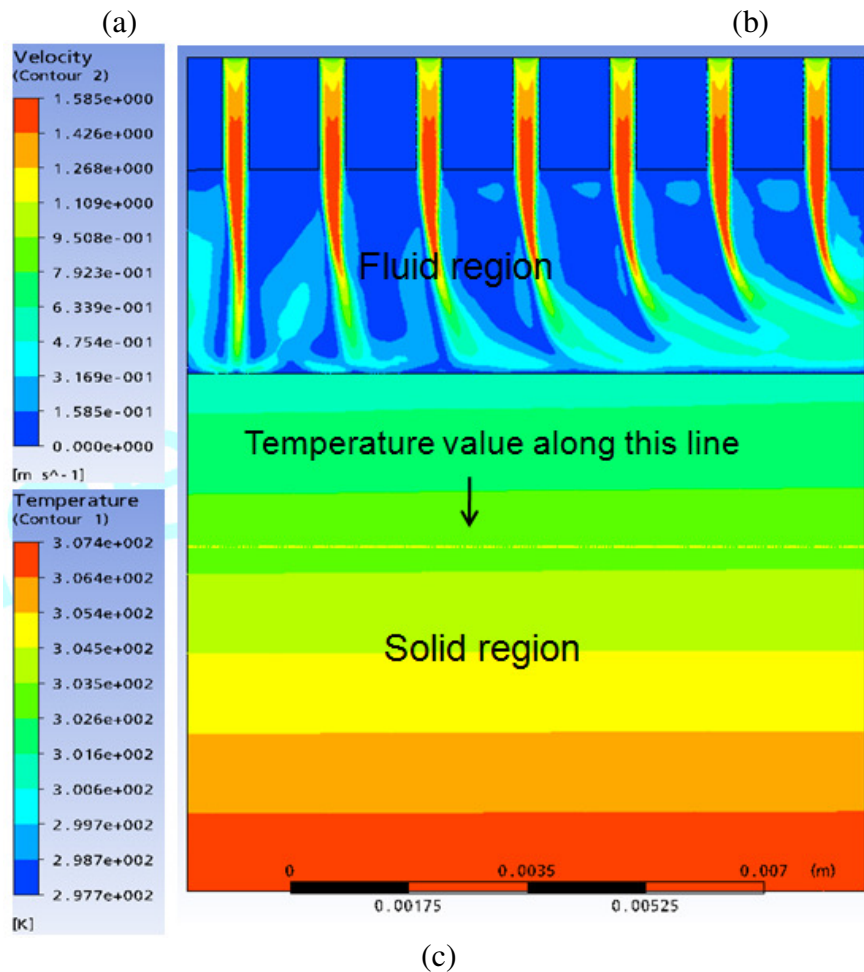
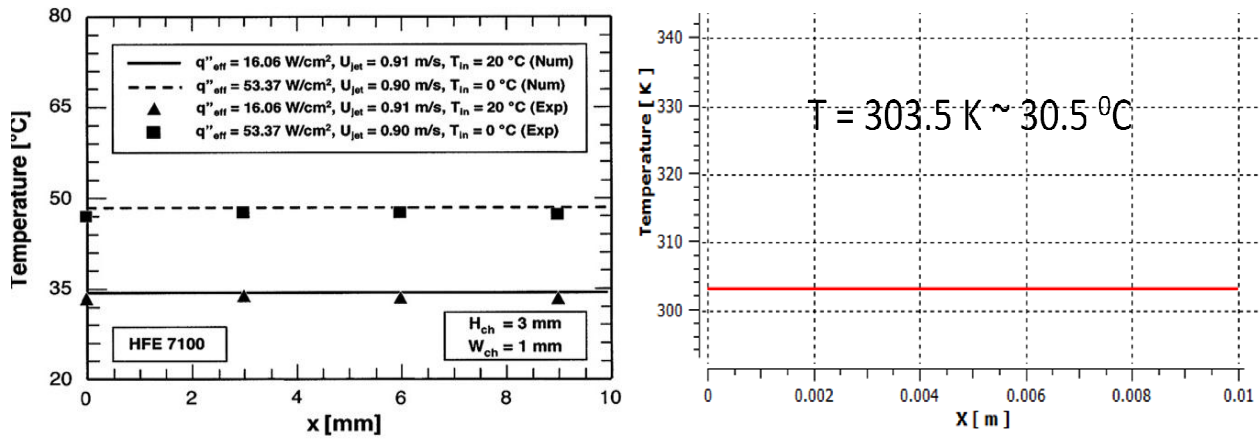


Figure 5.32. Comparison of the simulation data with the data provided in the literature. (a) Experimental and numerical data in the literature [73] (b) ANSYS-CFX simulation data for the inlet temperature of 20 °C. (c). Temperature and velocity contours on the symmetry plane. Velocity contours in the fluid region and temperature contours in the solid region.

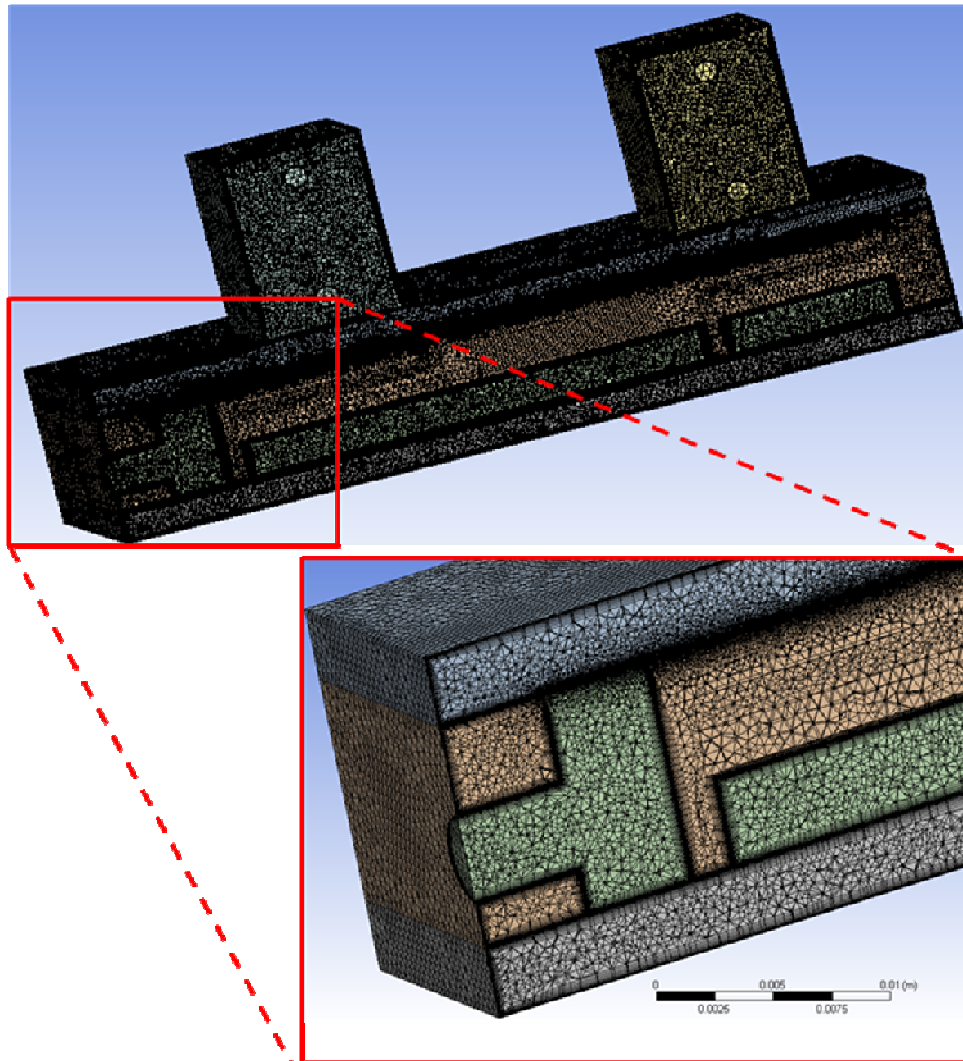


Figure 5.33. Cross-sectional view of the meshed domain with fine meshing at all the interfaces.

A 3-D simulation model shown in Figure 5.34 was simulated using the $k-\epsilon$ model as well as using the SST $k-\omega$ model. Turbulence models were used as the flow was in transition to turbulent region with Reynolds number based on jet diameter of ~ 2000 . The convergence criterion for each case was kept at 10^{-5} . The model shown here is slightly different from the model shown in Figure 5.23 in the sense that the physical orientation of the cooler is inverted. All the yellow cross-hairs represent the temperature and pressure measurement locations corresponding to the experimental set-up. The HP and LP locations were the high pressure and

low pressure probing locations respectively. The difference between these two pressures was compared with the experimental data. In each experiment, the difference between the pressure at HP and the pressure at LP (that is, HP-LP) was recorded as the pressure drop. The locations a, b, c, d, e, f, g, h, i and j are all the temperature probing locations. The temperatures at locations *a* and *b* and *f* and *g* were used to measure the heat flux from Heater leg 2 and Heater leg 1 respectively. This measured flux was then used as a boundary condition for the simulations. Also, for all the simulation models, thermal adhesive layer was not modeled as it was less than 50 microns.

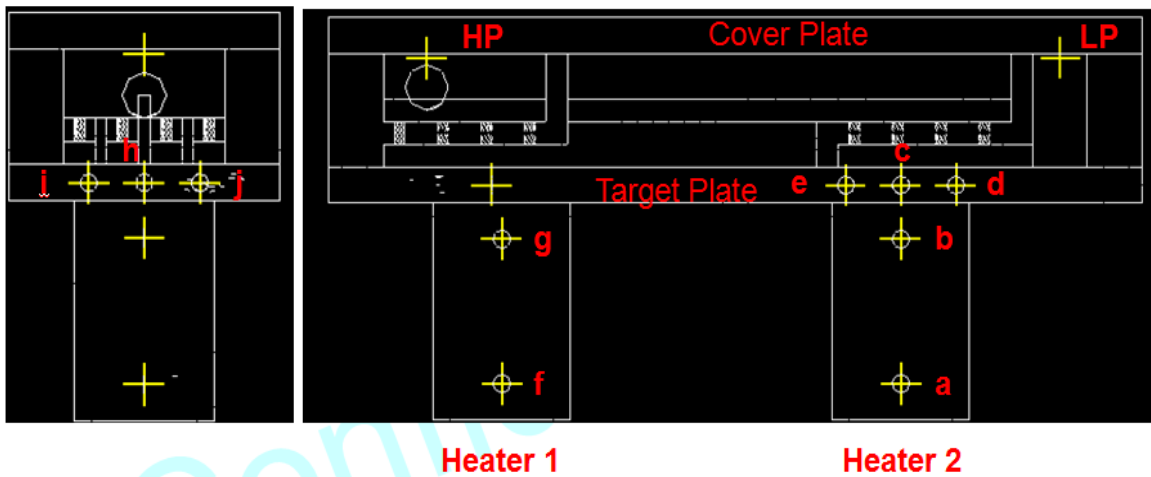


Figure 5.34. Simulation model for comparison with experimental data. Yellow cross-hairs represent the temperature and pressure measurement locations. (HP: High Pressure) (LP: Low Pressure).

For the present test case two sets of experiments were performed - one with low power (111 W, 115.21 V, 0.968 A) and the other one with medium power (337 W, 202.3 V, 1.665 A). In the low power experiments, the flux through Heater leg 1 and Heater leg 2 were recorded to be 28.94 W/cm² and 39.1 W/cm², respectively and, water at 22 °C with an average flow rate of 0.82 L/min (mass flow rate = 13.63 g/s) was used as the coolant. The same heat flux was applied at the top face (face away from the cooler) of the rectangular heater legs. Figure 5.35 compares the temperature at various locations for the low power experiment as well as the temperatures

predicted by simulations for different mesh sizes. The details of these three mesh sizes are presented in Table 5.3. Coarse and Medium mesh had similar meshing in the fluid domain with fine meshing at and around the impingement region. Moreover, medium mesh had slightly denser mesh in all the solid domains.

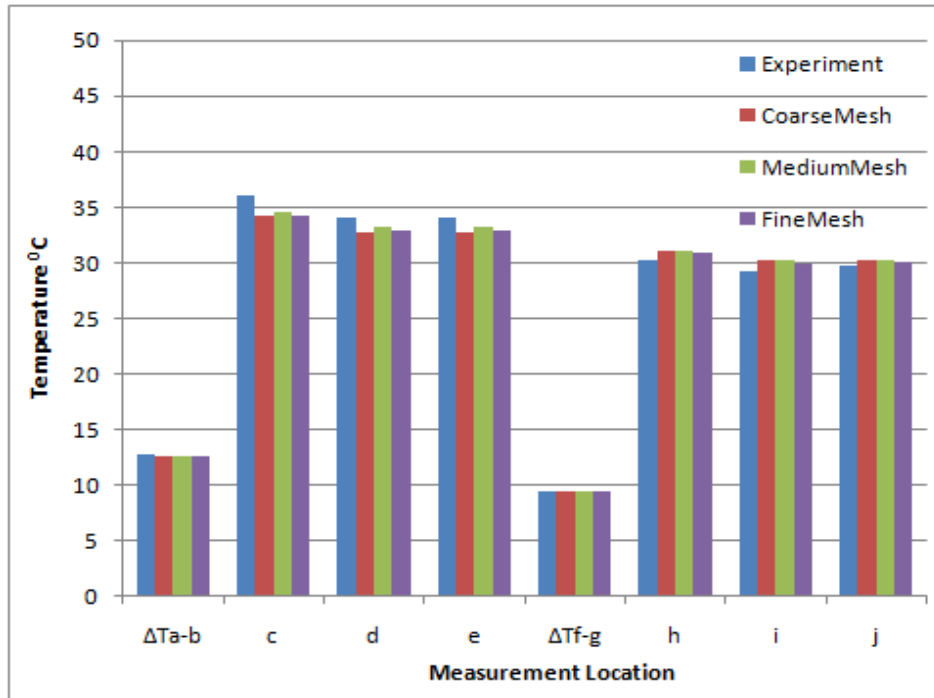


Figure 5.35. Temperature measurement at different measurement locations indicated in Figure 5.34 for low power experiment and its comparison with the simulation predictions (k- ϵ) for different mesh sizes.

Table 5.3. Mesh details for the simulation validation experiments.

Domain	Coarse		Medium		Fine	
	# of Nodes	# of Elements	# of Nodes	# of Elements	# of Nodes	# of Elements
Cover Plate	1899	7618	22316	105996	243564	664401
Fluid	538816	1493909	606418	1740261	5610138	16443819
Cooler	361123	945321	459127	1179800	2356844	6796593
Heater 1	12567	36696	32495	86986	86687	285255
Heater 2	12644	37180	32666	88184	86937	286455
Target Plate	445579	1323707	496617	1518419	6184166	19984623
Total	1372628	3844431	1649639	4719646	14568336	44461146

From Figure 5.35, it can be seen that the target plate temperature predictions by the medium mesh and fine mesh k- ϵ models were mostly within $\pm 5\%$ of the experimental data. Moreover, the temperature predictions at the locations *a*, *b*, *f* and *g* were much lower than that recorded experimentally as the thermal contact resistance between the heater blocks and the heat exchanger were not modeled. Thus, temperature predictions at these locations were dropped for the mesh and turbulence model selection. However, the temperature gradient predictions between locations *a* and *b* (i.e. ΔT_{a-b}) and locations *f* and *g* (i.e. ΔT_{f-g}) were used to check the lateral heat spreading and it was observed that this spreading was $\sim 0.5\%$ of the applied heat flux.

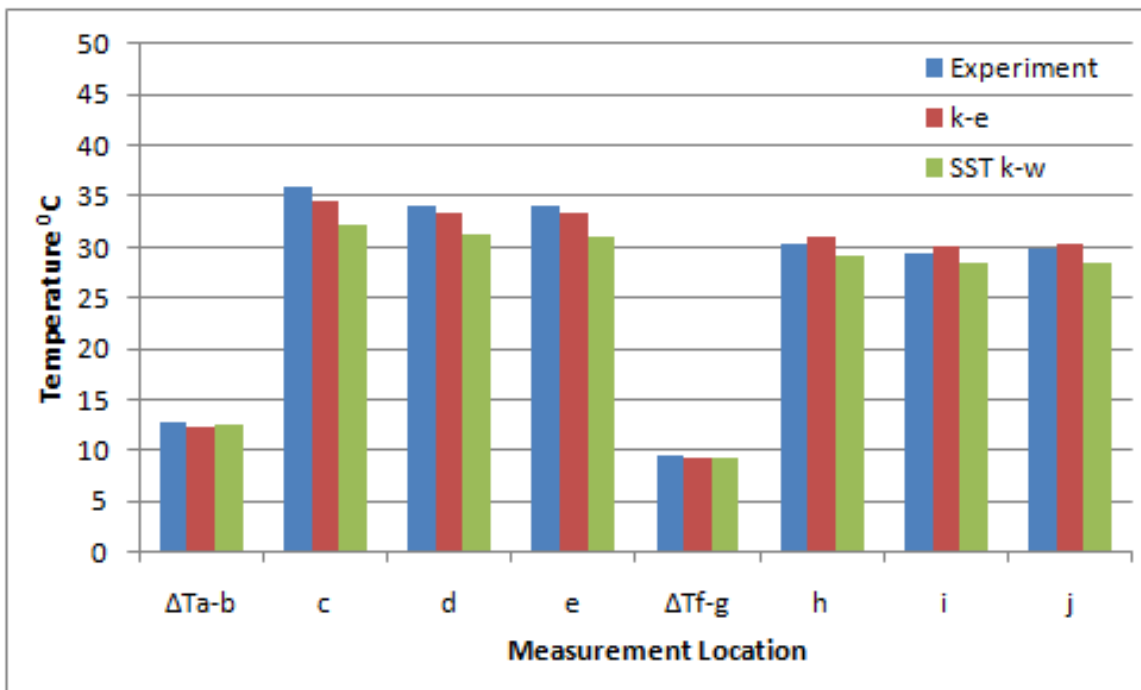


Figure 5.36. Temperature prediction at measurement locations indicated in Figure 5.34 by k- ϵ and SST models and its comparison with the experimental data for low power experiments.

Temperature prediction for low power experiments by the k- ϵ and SST models for the medium mesh are presented in Figure 5.36. It can be clearly seen that the temperature predictions made by SST model are as much as 7 – 8 % lower than that made by k- ϵ model. This could be because k- ϵ model has a more conservative approach as compared to SST model. In accordance

to the study conducted by Sung and Mudawar [73], k- ϵ model was shown to have a better temperature match in the present study. Table 5.4 compares the pressure drop for the low power experiments with the pressure drop predictions made by k- ϵ and SST model for different mesh sizes. Clearly, all the models under-predicted the pressure drop and the prediction by SST model was higher than the k- ϵ model.

Table 5.4. Pressure prediction by k- ϵ and SST k- ω models for different mesh sizes and its comparison with the experimental data for low power experiments.

Pressure	Inlet	Outlet	dP	HP	LP	HP-LP	HP-LP (Exp)	Error %
Coarse	4.4	0.07	4.33	4.49	1.27	3.22	3.6	-10.56
Med	4.33	0.01	4.32	4.38	1.2	3.18	3.6	-11.75
Fine	4.21	0.001	4.21	4.29	1.23	3.06	3.6	-15.03
Med (SST)	4.61	0.008	4.60	4.57	1.23	3.34	3.6	-7.33

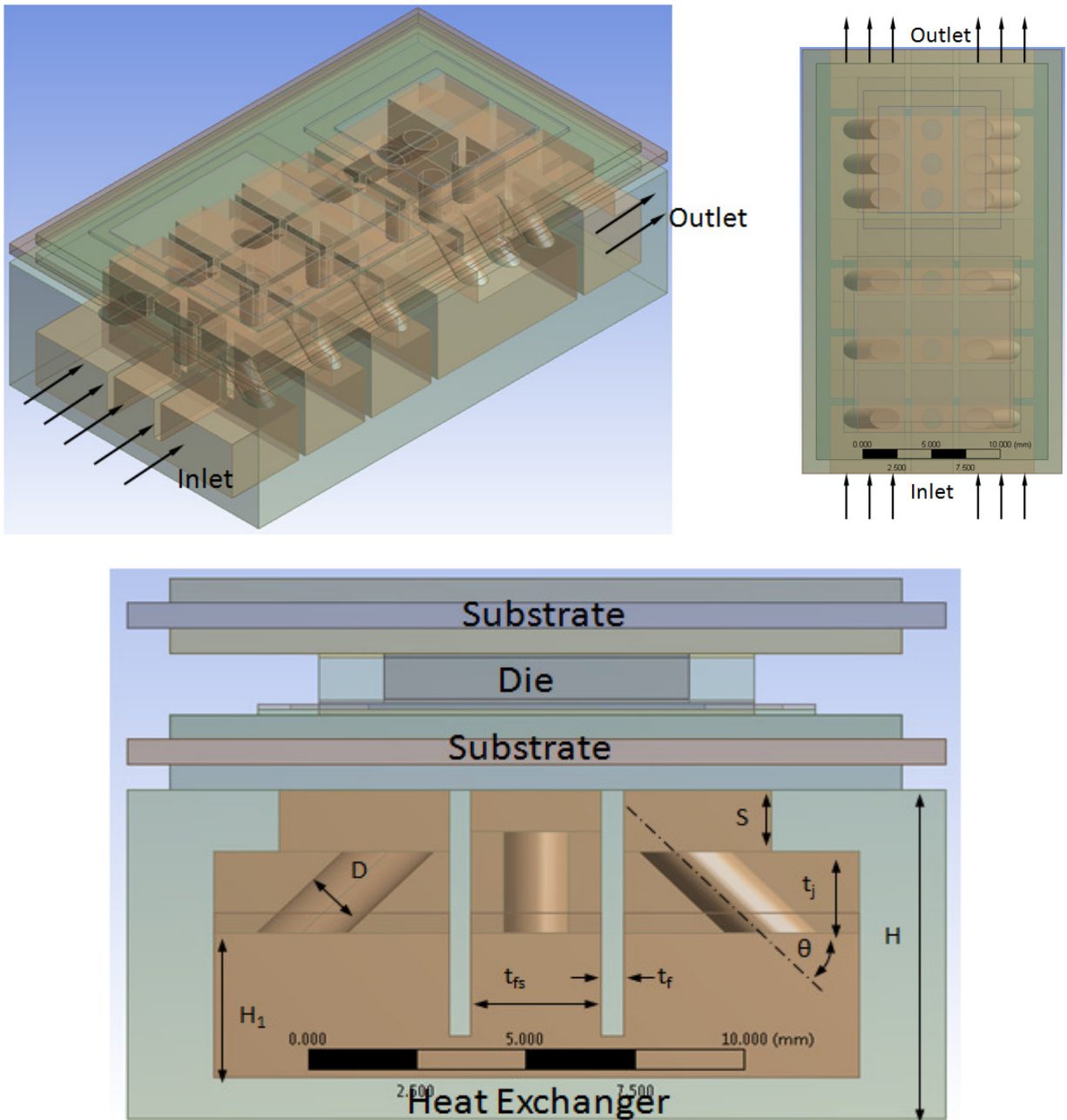
In the medium power experiments, the flux through Heater leg 1 and Heater leg 2 were recorded to be 77.28 W/cm² and 116.07 W/cm² respectively and water at 24.1 °C with an average flow rate of 0.83 L/min (mass flow rate = 13.79 g/s) was used as the coolant. For this case as well the target plate temperature predictions by the medium mesh k- ϵ model were mostly within $\pm 5\%$ of the experimental data. Similar to the low power case, the temperature predictions made by SST model are as much as 8 – 10 % lower than that made by k- ϵ model. Similar to the low power case, all the models under-predicted the pressure drop and as usual the prediction by SST model was higher than the k- ϵ model. Overall, a good prediction of the pressure drop and temperature at key locations was obtained using the k- ϵ model. Also, medium mesh showed promising results with acceptable error percentages and was used a standard mesh scheme for future simulations. After this, a unit structure of the whole power module along with the heat exchanger was simulated to check for the hot-spots and possible failure locations. Based on the results, subsequent design changes were being made to achieve the heat exchanger objectives.

5.6. Partial Module Simulations

A unit structure of the whole power module along with the heat exchanger was simulated. Figure 5.37 shows the different views of a typical partial module model. The model consisted of the heat exchanger, one top and one bottom DBA substrate layers, one copper shim for each IGBT and Diode, and three SAC305 solder layer each for the Silicon IGBT and diode heat sources. Various conjugate heat transfer simulations were performed on such partial module models. Different heat exchanger geometries were considered and for most of the simulations conducted engine coolant and water at the actual operating temperatures were used as the coolant. The allowed pumping power across the partial module section was either 0.0416 W or 0.0694 W or 0.0923 W based on the overall heat exchanger structures. Also, the target temperature difference between the active devices temperature and the fluid inlet temperature was fixed at 55 °C. All the heat exchanger designs studied were modeled so as to meet the pumping power and target temperature difference requirements.

Heat exchanger geometries having various numbers of jets with diameters ranging from 1 mm – 2 mm were placed locally under the IGBT unit and central walls/rectangular fins were extended to increase the contact surface area locally under the diode unit. Variations of other design parameters such as jet-target plate spacing, jet angles, heat exchanger height, heat exchanger width, number of fins on the target wall, spacing between the fins and other such parameters were considered. Volumetric heat dissipation rate were applied at the IGBT and diode respectively. The value of total heat dissipation from each IGBT – Diode pair was set based on the foot-print area of the active unit in the IGBT and diode and also to match the heat flux dissipation of $\sim 220 \text{ W/cm}^2$ from the IGBT and $\sim 65 \text{ W/cm}^2$ from the diode. Simulations were performed mostly for 90° and angled impingement to predict the IGBT and diode temperatures.

Both SST $k-\Omega$ and $k-\epsilon$ were used to predict these temperature. As usual, $k-\epsilon$ model over predicted these temperatures. In all the simulations, the maximum temperature was obtained at the IGBT. Figure 5.37 is also the simulation model of the best impingement design in terms of meeting both the temperature as well as pumping power constraints.



View from the inlet with few of the design parameter.

Figure 5.37. Different views of the conjugate simulation model of a typical partial power module package.

5.7. Summary

A Thermal Test Bed was designed and fabricated to test the performance of heat exchangers developed during the course of this work, under a load from either a powered module or a calibrated heat source. This test bed is also capable of simulating the actual running conditions of a hybrid vehicle cooling system. Monitors were installed to measure the temperature increase of the coolant as well as the pressure drop through the heat exchanger. The system is capable of varying the in-coming fluid temperature, pressure, and flow rate, in order to evaluate the heat exchanger performance over a range of parameters. Details of the apparatus used are also presented. In all 4 different heat exchanger samples were fabricated and tested for thermal performance evaluation and for simulations validation.

ANSYS-CFX as well as ANSYS-Fluent, commercial computational fluid dynamics (CFD) codes were used to study the flow and heat transfer behavior in the proposed heat exchanger models. It was observed that both the commercial codes predicted similar results for all cases. Overall, a good prediction of the pressure drop and temperature at key locations was obtained using the $k-\epsilon$ model. Also, medium mesh showed promising results with acceptable error percentages and was used a standard mesh scheme for future simulations. After this, a unit structure of the whole power module along with the heat exchanger was simulated to check for the hot-spots and possible failure locations. Based on the results, subsequent design changes were being made to achieve the heat exchanger objectives.

CHAPTER 6: IMPINGEMENT BASED DESIGNS

From the earlier verification, validation and comparative study, it was observed that standard k- ϵ model provided a good prediction of the heat transfer coefficient in comparison to experimentally derived values and that high local heat transfer coefficients can be obtained by using angled impingement. As a first step in electronic cooling application, small heat exchanger modules were designed, modeled and simulated. Both convection and conduction heat transfer modes were simulated, that is, conjugate heat transfer simulations were performed so as to study the effect of the center wall/fin and different impingement angles.

6.1. Parametric Study and Optimization

For this study, conjugate models shown in Figure 6.1 were used. The model shown in Figure 6.1(a) consists of 12 jets distributed into 4 parallel rows. There is no wall in between the second and third row. Diameter of the jets was taken to be 0.5 mm owing to the space constraints and the heat flux of 200 W/cm^2 was applied at the top surface which had a foot print area of 1 cm^2 . Water at $25 \text{ }^\circ\text{C}$ with an inlet velocity of 10 m/s was used as the coolant.

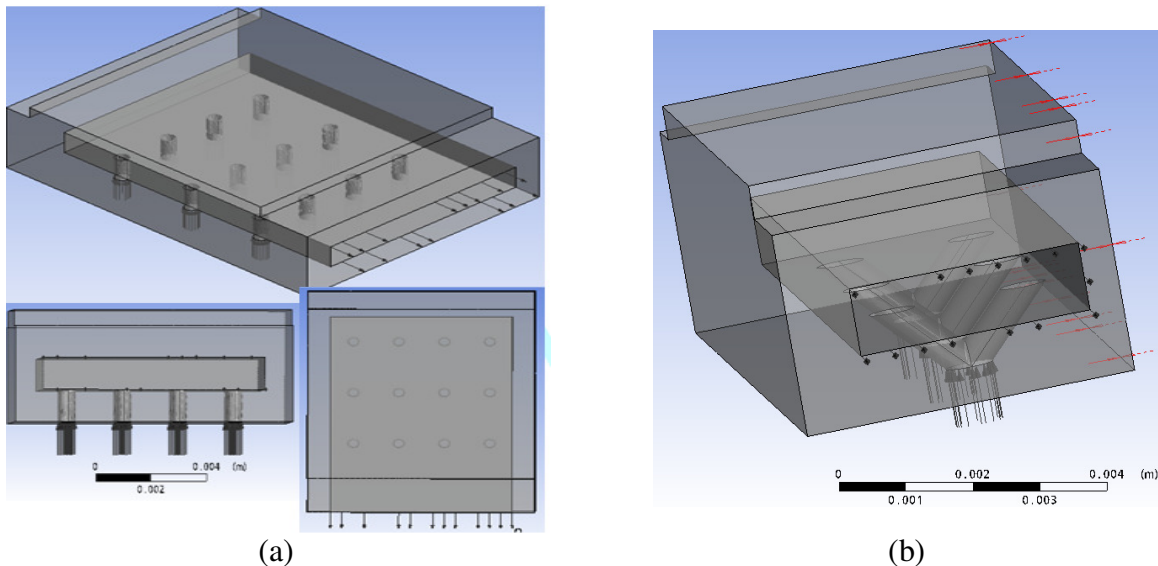


Figure 6.1. Conjugate heat transfer models for the study of wall/fin and impingement angle effects on the effective heat transfer coefficient and solid bulk temperature. (a) Simulation model with no center wall/fin. (b) Simulation model with center wall/fin (half domain).

Model shown in Figure 6.1(b) is a half domain with a wall between the second and third row of jets and consists of 12 jets. But since, only half the domain was simulated, only 6 jets are visible. For both the models, impingement angles of 90° , 70° , 60° and 45° were considered. For the 45° case, the inlet for two rows overlapped and thus an inlet velocity of 20 m/s was applied. The exit locations of each jet were kept constant. Moreover, for the angled jets, the wall was placed in such a way that the first row of jets impinges on the base plate and the second row of jets impinges on the side walls/fins. The velocity streamlines shown in Figure 6.2 emphasize the effect of such model on the flow trend. For the jets impinging on the base plate, the jet breaks down in-to two vortices – one large and one small vortex for the angled jets and two similar vortices for the normally impinging jets. While, for the jets impinging on the side walls, jets form a single huge vortex.

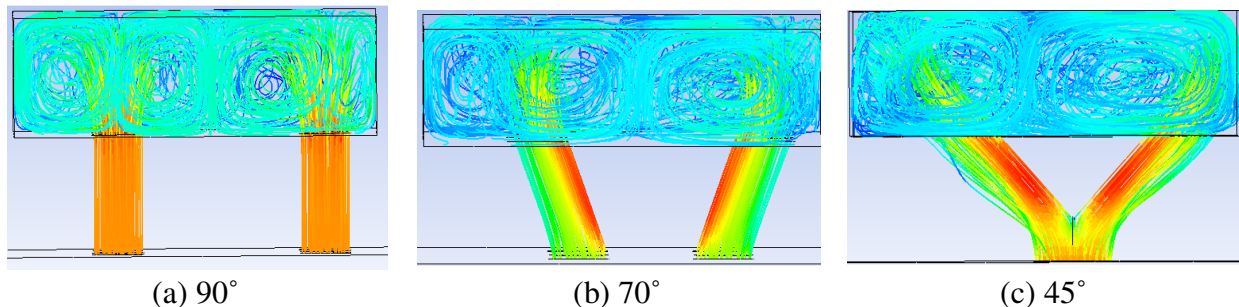


Figure 6.2. Velocity streamlines showing the vortices for different impingement angles and wall locations. (a) 90° (b) 70° , (c) 45° .

The wall heat transfer coefficients and the temperature contours for the 90° impingement cases are presented in Figure 6.3. It can clearly be seen that the peak as well as the local wall heat transfer coefficient does not change with the placement of center wall. Thus, the reduction in the maximum surface temperature (~ 7.1 K) can solely be attributed to enhanced conduction through the center wall. This highlights the fin-conduction effect. The heat transfer coefficient predictions are presented in Table 6.1. ΔT was measured as the temperature difference between the coolant inlet temperature and maximum top surface (where the heat flux was applied)

temperature. Effective heat transfer coefficient (h_{eff}) defined as Eq. (6.1) was used to compare the heat exchanger performance.

$$h_{eff} = \frac{q''_{input}}{T_{Wall,avg} - T_{f,avg}} \quad (6.1)$$

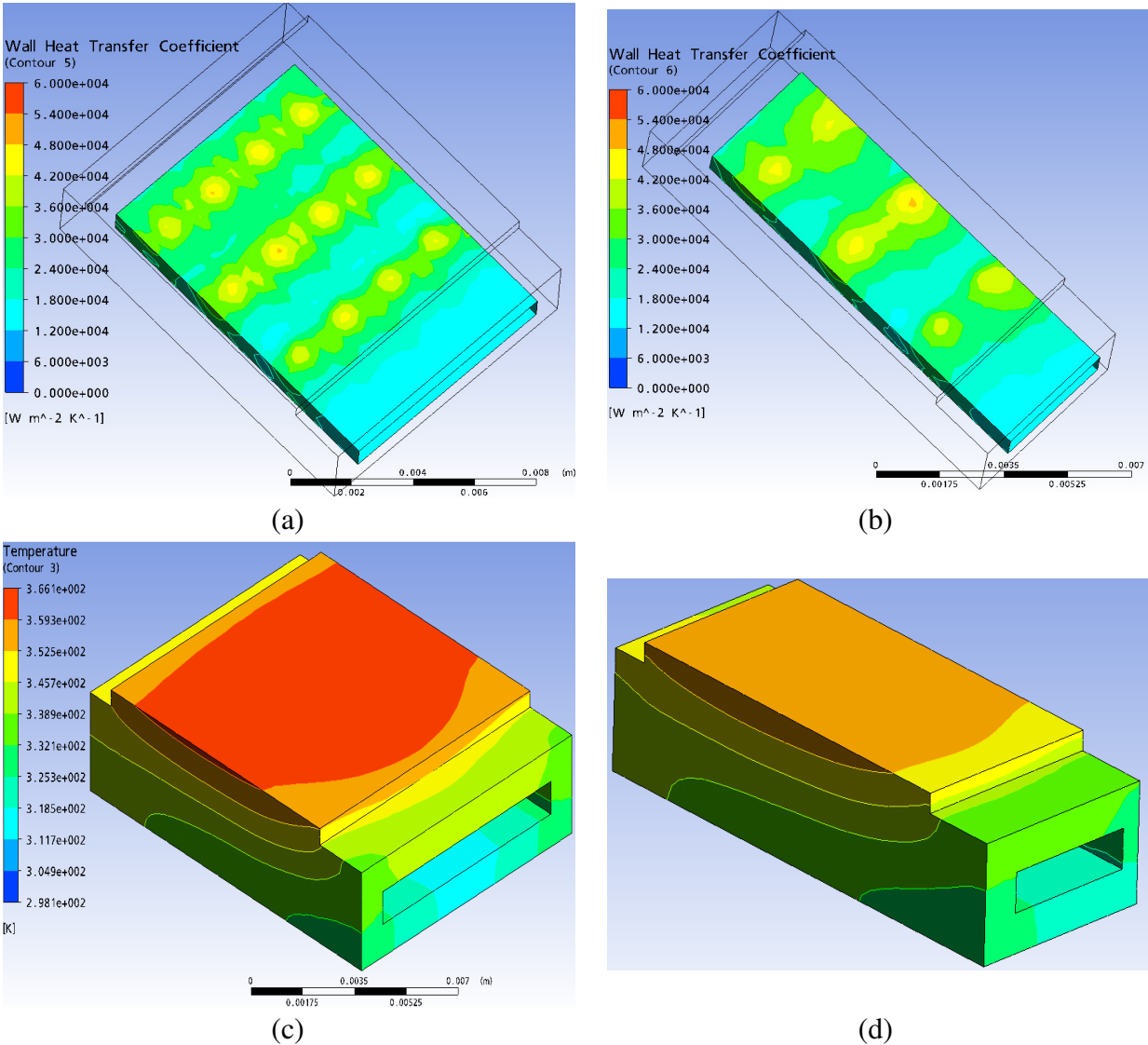


Figure 6.3. Wall heat transfer coefficient and temperature predictions using k- ϵ model for the 90° impinging jets (a), (c) With no center wall/fin (b), (d) with center wall/fin (half domain). No change in wall heat transfer coefficient. 7.1K reduction in maximum surface temperature due to center wall/fin.

Table 6.1. Heat transfer coefficient ($\text{W}/\text{m}^2\text{K}$) predictions for 90° impingement.

Case	Overall average heat transfer coefficient	From CFX-Post	Effective heat transfer coefficient	Reduction in max. surface temperature
No Center Wall/fin	24331	25486	32015	Ref: 366.1 K ($\Delta T=68.1$ K)
Center Wall/fin	25326	26593	36071	7.1 K ($\Delta T = 61$ K)

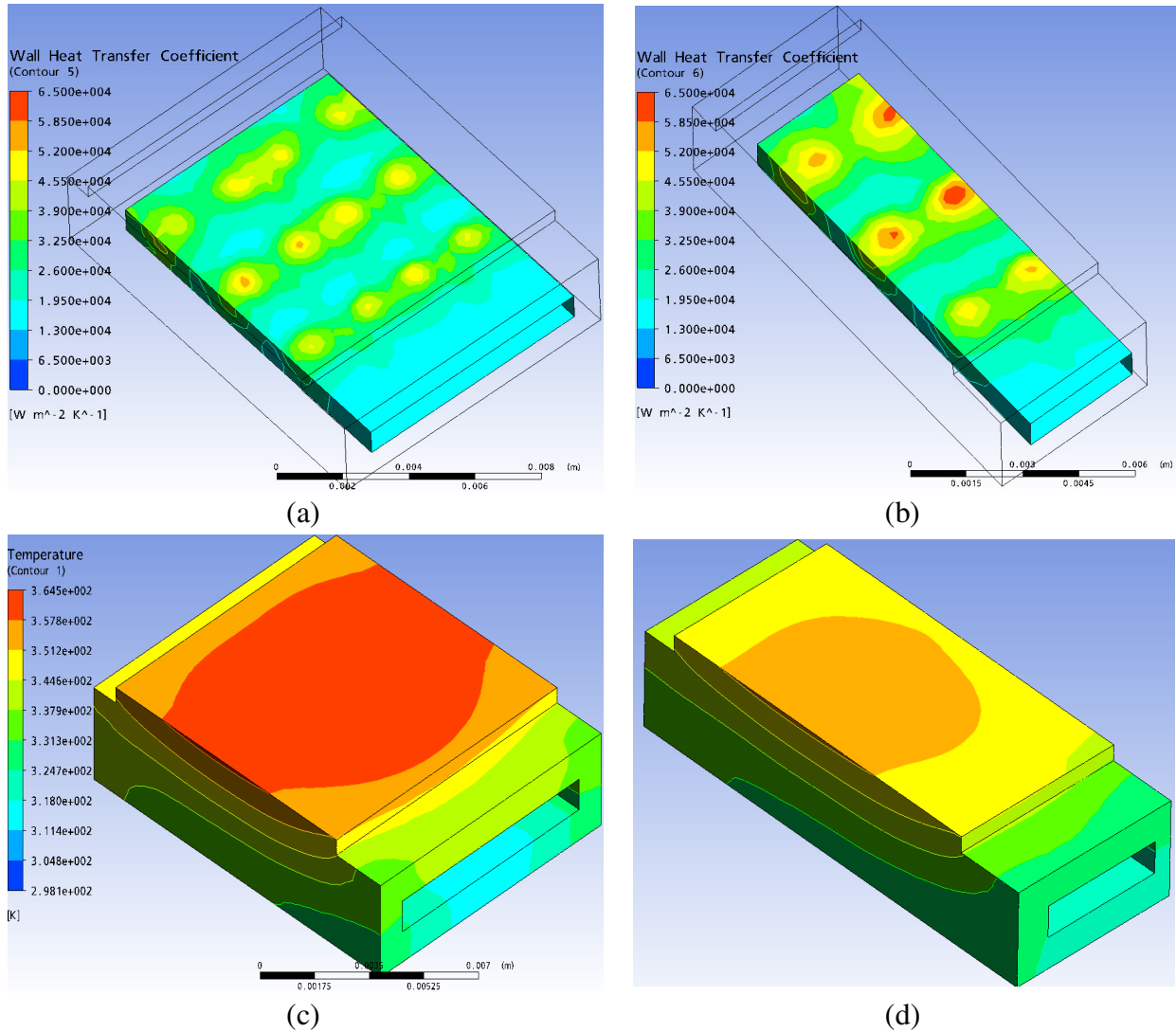


Figure 6.4. Wall heat transfer coefficient and temperature predictions using $k-\epsilon$ model for the 70° impinging jets (a), (c) With no center wall/fin (b), (d) with center wall/fin (half domain). Peak heat transfer coefficient increases with the placement of a wall. 12.8 K reduction in the maximum surface temperature as compared to 90° impinging jets.

The wall heat transfer coefficients and the temperature contours for the 70° impingement cases are presented in Figure 6.4. It can clearly be seen that the peak as well as the local wall heat transfer coefficient change significantly with the placement of center wall/fin. Also, the increase is noticeable when the jets are impinging on the side walls and forming a single huge vortex rather than two vortices (one large and one small). A reduction of about 12.8 K was observed in the maximum surface temperature as compared to the baseline case of 90° impinging jets. Out of this, 1.6 K reduction in the maximum surface temperature could be due to 70° impinging jets. Following the earlier observation, the reduction in the maximum surface temperature (~ 7.1 K) can solely be attributed to enhanced conduction through the center wall and an additional 4.1 K reduction in temperature can be attributed to enhanced swirl effect due to impingement on the center wall/fin. This highlights the enhancement of heat removal rate due to swirl. The heat transfer coefficient predictions are presented in Table 6.2.

Table 6.2. Heat transfer coefficient (W/m²K) predictions for - 70° impingement.

Case	Overall average heat transfer coefficient	From CFX-Post	Effective heat transfer coefficient	Reduction in max. surface temperature
No Center Wall/fin	25596	26724	33190	1.6 K ($\Delta T = 66.5$ K)
Center Wall/fin	29185	30354	41060	12.8 K ($\Delta T = 55.3$ K)

Similar wall heat transfer coefficients and the temperature contours for the 45° impingement cases are presented in Figure 6.5. Here again, it can clearly be seen that the peak as well as the local wall heat transfer coefficient change significantly with the placement of center wall/fin. Also, the increase is noticeable when the jets are impinging on the side walls and forming a single huge vortex rather than two vortices (one large and one small). A reduction of about 23 K was observed in the maximum surface temperature as compared to the baseline case

of 90° impinging jets. Out of this, 11.2 K reduction in the maximum surface temperature could be due to 45° impinging jets.

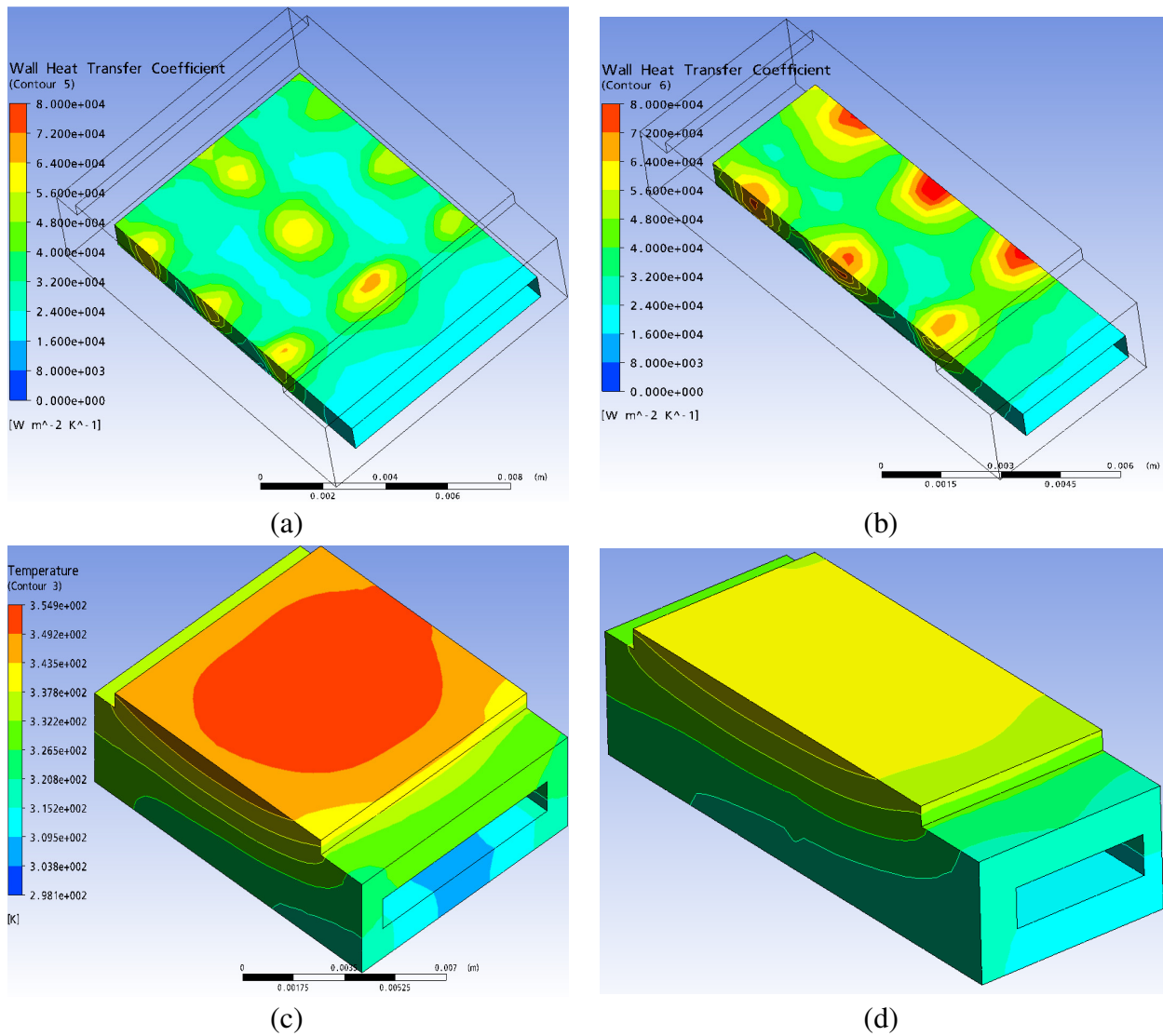


Figure 6.5. Wall heat transfer coefficient and temperature predictions using $k-\epsilon$ model for the 45° impinging jets (a), (c) With no center wall/fin (b), (d) with center wall/fin (half domain). Peak heat transfer coefficient increases with the placement of a wall. 23 K reduction in the maximum surface temperature as compared to 90° impinging jets.

Following the earlier observation, the reduction in the maximum surface temperature (~ 7.1 K) can solely be attributed to enhanced conduction through the center wall and an additional 4.1 K reduction in temperature can be attributed to enhanced swirl effect due to impingement on

the center wall/fin. The remaining 0.6 K reduction in temperature can be attributed to the impingement angle. This highlights the effect of the impingement angle on the heat removal rate. The heat transfer coefficient predictions are presented in Table 6.3. Based on all the above observations, a better swirl after impingement is needed for higher heat transfer rates and 45° impinging jets provide the highest swirl after impingement.

Table 6.3. Heat transfer coefficient (W/m²K) predictions for 45° impingement.

Case	Overall average heat transfer coefficient	From CFX-Post	Effective heat transfer coefficient	Reduction in max. surface temperature
No Center Wall/fin	35331	39254	42046	11.2 K ($\Delta T = 56.9\text{K}$)
Center Wall/fin	42653	46352	55225	23 K ($\Delta T = 45.1\text{K}$)

6.2 Impingement-Based Partial Module Simulation

This optimized configuration was then applied to the partial module model simulations. Various impingement based heat exchanger geometries having various numbers of jets with diameters ranging from 1 – 2 mm were placed locally under the IGBT unit and central walls/rectangular fins were extended to increase the contact surface area locally under the diode unit. Variations of other design parameters such as jet-target plate spacing, jet angles, heat exchanger height, heat exchanger width, number of fins on the target wall, spacing between the fins and other such parameters were considered. For most of the simulations, both SST k- Ω and k- ϵ were used to predict the maximum IGBT and Diode temperatures. As usual, k- ϵ model over predicted these temperatures. In all the simulations, the maximum temperature was obtained at the IGBT. Figure 6.6 shows the variation of the difference between the IGBT device temperature and fluid temperature versus the pumping power for various impingement based heat exchanger geometries studied. None of the numerous high performance jet impingement designs studied were able to meet the target pressure and temperature constraints. However, one of the high

performance models was selected and was fabricated for thermal performance evaluation. Figure 5.37 is also the simulation model of the best impingement design in terms of being close to both the temperature as well as pumping power constraints. Figure 6.7 shows the IGBT and Diode temperature predictions along with velocity streamlines for LLC at 0.00925 kg/s and 65 °C as the coolant.

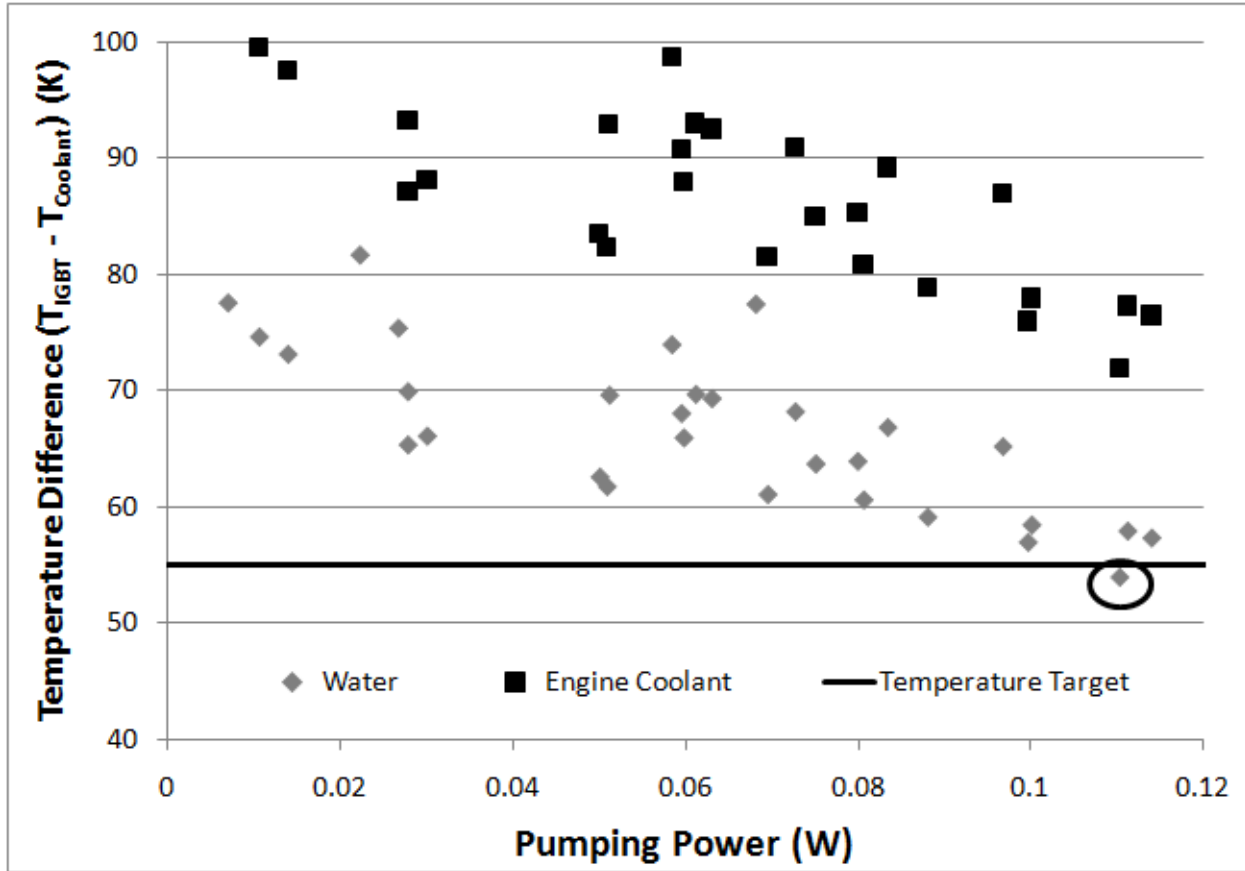


Figure 6.6. Variation of the maximum IGBT temperature with respect to the coolant inlet temperature with pumping power for water as well as ethylene glycol as the coolant.

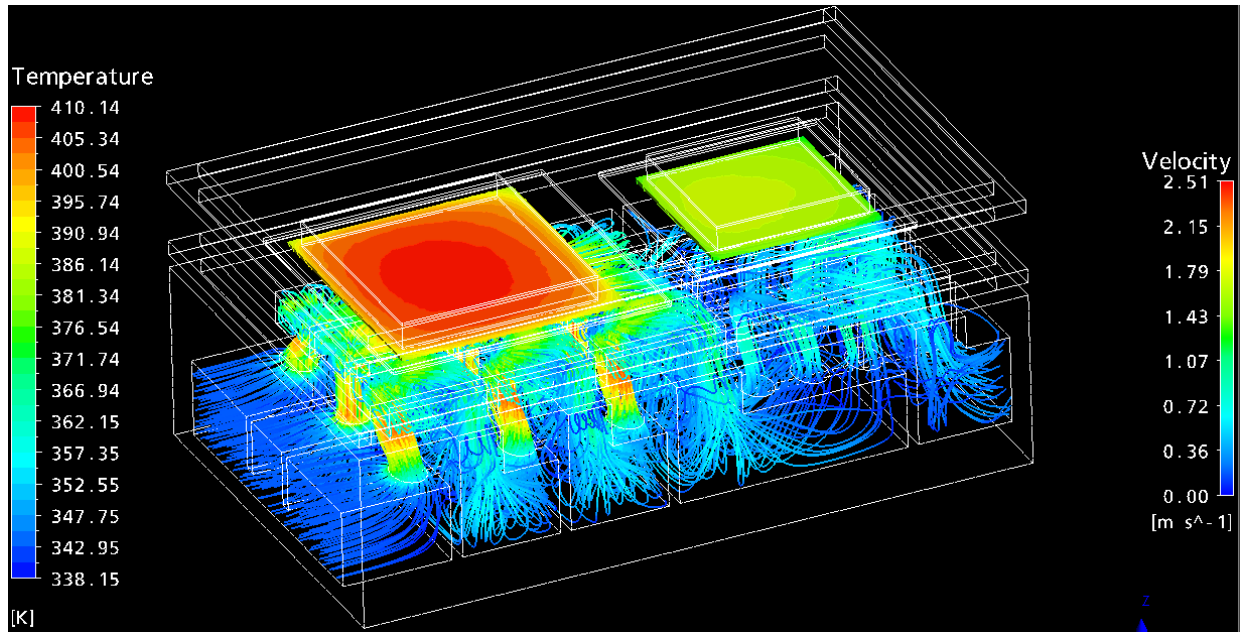


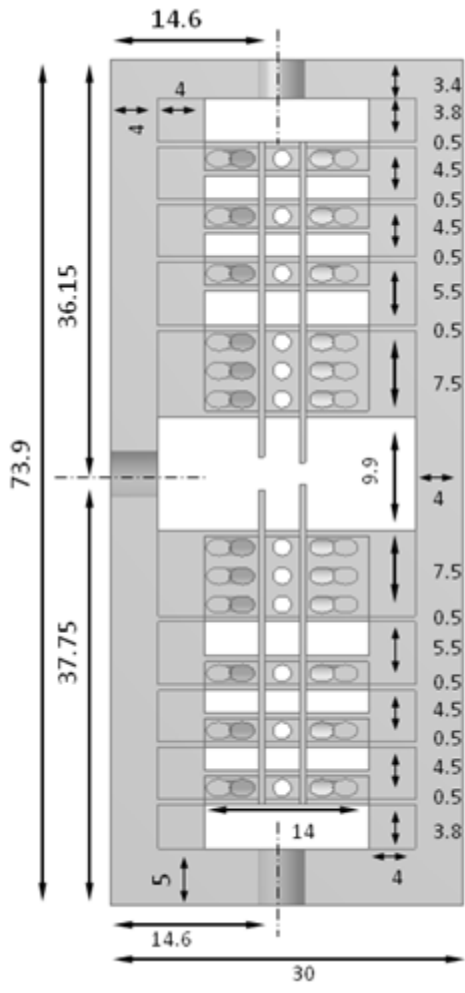
Figure 6.7. IGBT and Diode temperature prediction and velocity streamlines for the partial module shown in Figure 5.37.

6.3. Cooling Performance:

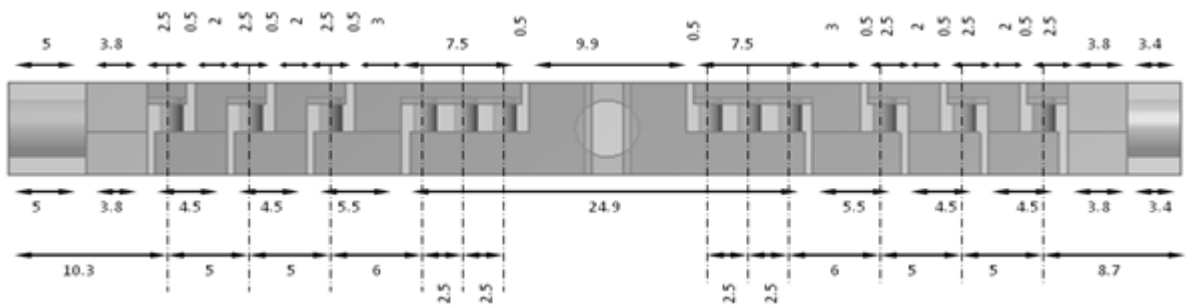
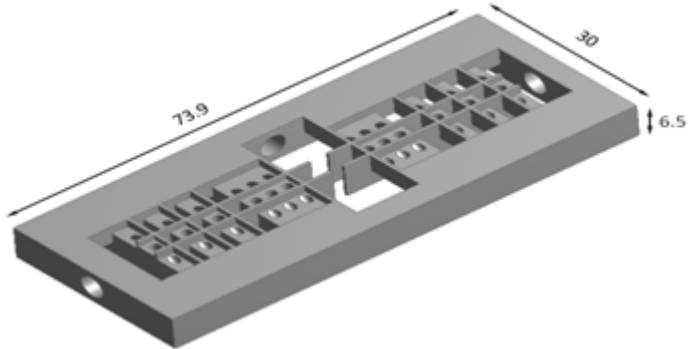
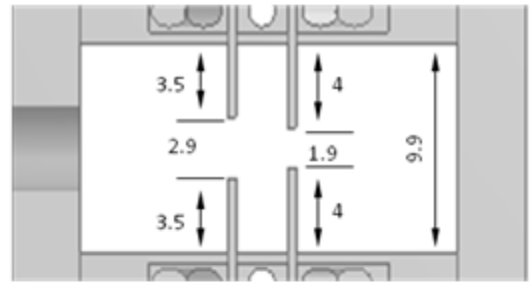
The best performing cooler from the previous section was then modeled to work with a single-sided multi-chip power module. The power module section was modeled first so as to have the correct device locations and then the cooler geometry was modeled to have the jets aligned directly under the active devices. Figure 6.8 shows the different views and dimensions of the cooler designed for the testing of single-sided single channel multi-chip power module. This model consisted of a single inlet and two outlets. Once fabricated, this piece was soldered directly to the back side of the single-sided power module and to a bottom cover-plate on the other side. Once assembled, the single-sided single channel multi-chip power module package was tested using the thermal test bed. Figure 6.9 shows the assembled power module package with the active device and inlet and outlet locations. Figure 6.10 shows the thermal test bed set-up for cooler performance evaluation. Figure 6.10(a) shows the overall set-up with the power supply sources. Figure 6.10(b) shows a zoomed-in image of the test section. It is to be noted here

that the overall package thickness was less than 10 mm whereas the overall package thickness of a conventional package is usually greater than 25 mm.

A regulated power was supplied to the heat sources (2 IGBTs and 2 Diodes) to simulate the real thermal loads. Moreover, IGBTs and Diodes junction temperature were measured using a sense diode. The experiments were conducted at a various total thermal loads ranging from 250 W to 650 W and for each set the heat dissipated by Diodes was about one quarter of that dissipated by the IGBTs. Water at 29 °C with an overall flow rate of 1 l/min was used as the coolant, that is, about 0.5 l/min to cool each IGBT and Diode pair. Figure 6.11 shows the experimentally recorded thermal resistance values for both the IGBTs for different power dissipation levels. The cooler performance was as expected and the average thermal resistances for IGBT1 and IGBT2 were reported to be 0.275 K/W and 0.28 K/W respectively. The differences in the maximum IGBT temperatures was due to the fact that for one pair, Diode was closer to the IGBT than the other pair and thus, resulted in higher temperature due to thermal coupling effect. This single-sided multi-chip power module configuration was also modeled and the experimental conditions were simulated in ANSYS-CFX.



3 Big through holes: ϕ 4 mm
 36 Small through holes: ϕ 1.5 mm
 All thin wall/fin thickness: 0.5 mm



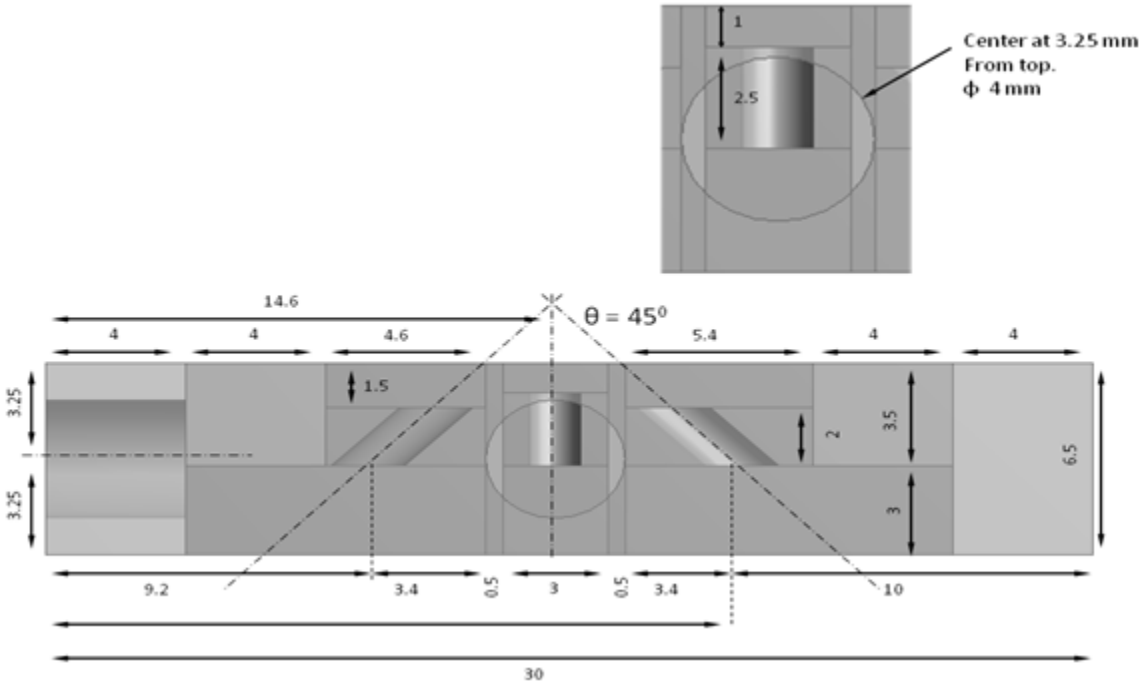


Figure 6.8. Different views and dimensions of the cooler designed for single-sided single channel multi chip power module.

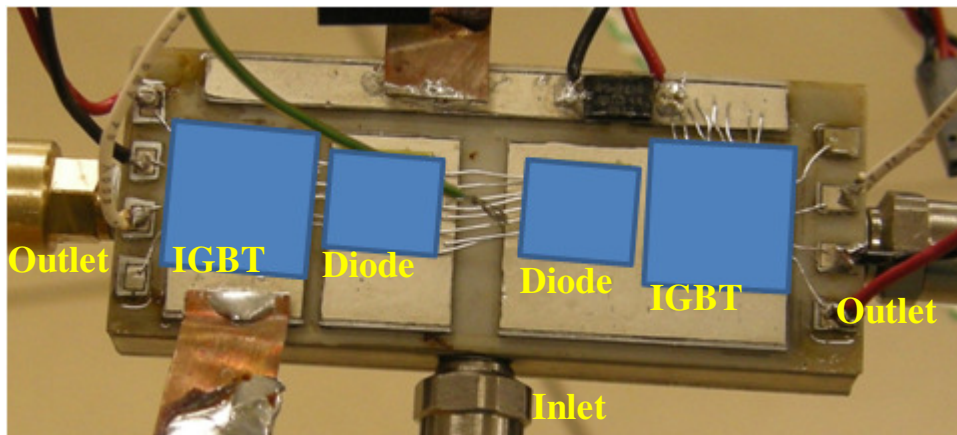
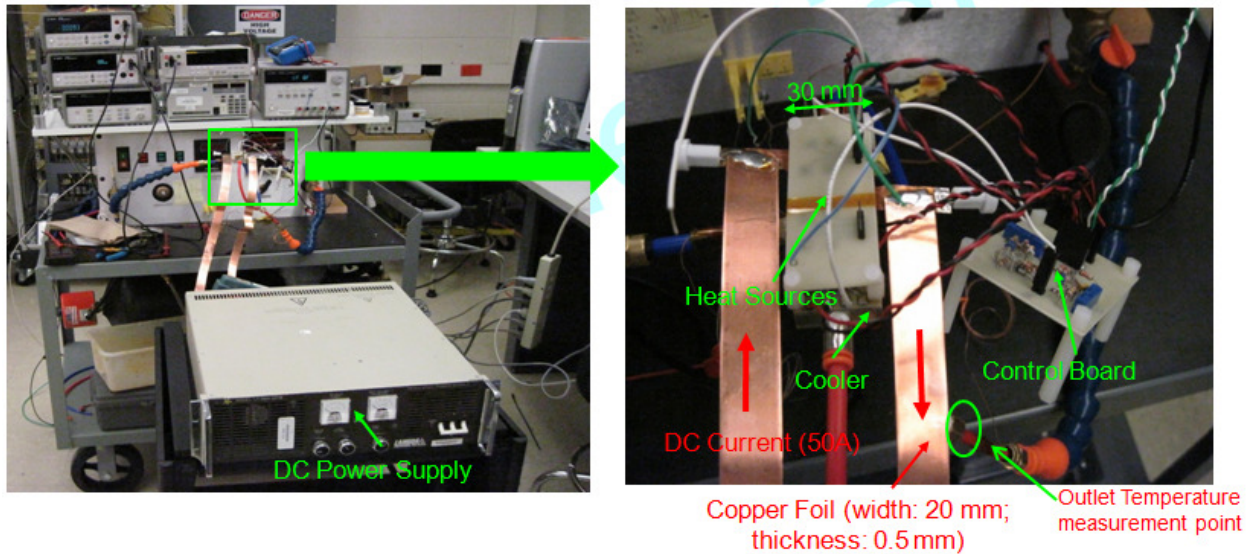


Figure 6.9. Assembled power module package with the active devices as heat sources and inlet and outlet locations.

Figure 6.12 shows the simulation model for the packaged power module configuration. In this model, solder layer between the power module and the cooler as well as the solder layer between the cooler and the bottom cover plate were not modeled. The k- ϵ turbulence model was used for the fluid flow simulation. Moreover the meshing scheme used was kept similar to the

medium meshing scheme used for the best angled impingement model. Table 6.4 summarizes the simulation predictions and compares it with the experimental data. It can clearly be seen that the *simulations were able to closely predict the experimental conditions and thus, validated most of the earlier conjugate packaging module simulations as well.*



(a) Overall set-up for cooler evaluation. (b) Zoomed-in image of the test section.
 Figure 6.10. Thermal Test Bed set-up for cooler performance evaluation. (a) Overall set-up for cooler evaluation. (b) Zoomed-in image of the test section.

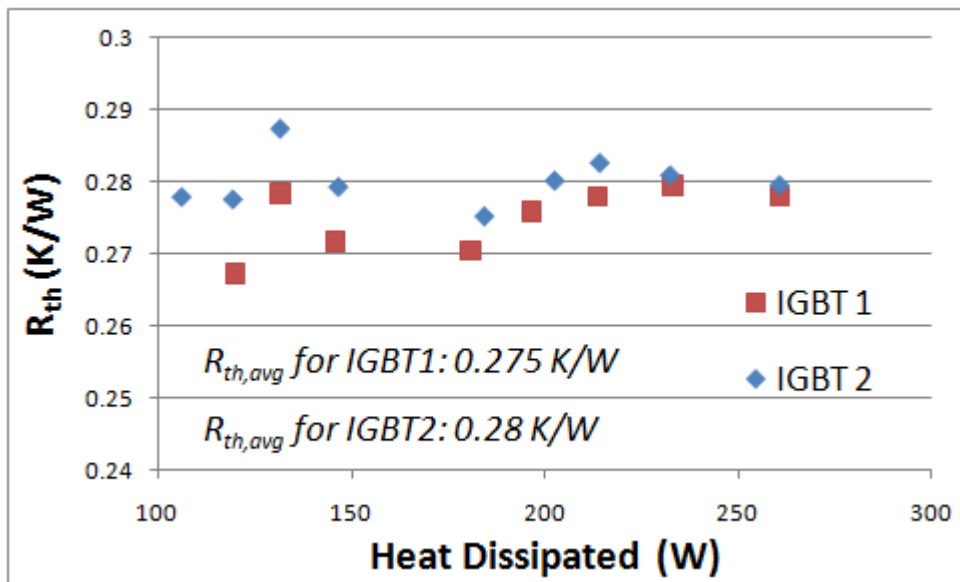
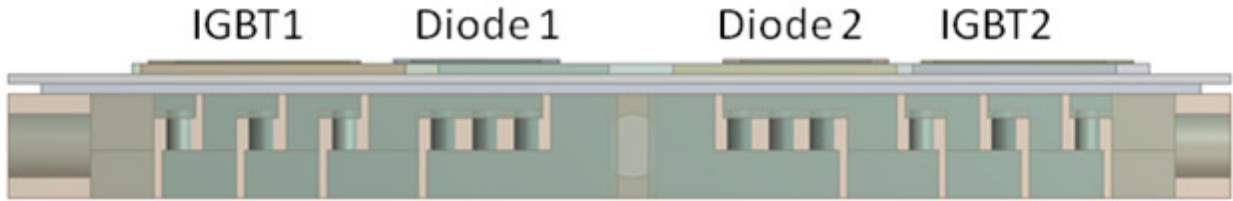


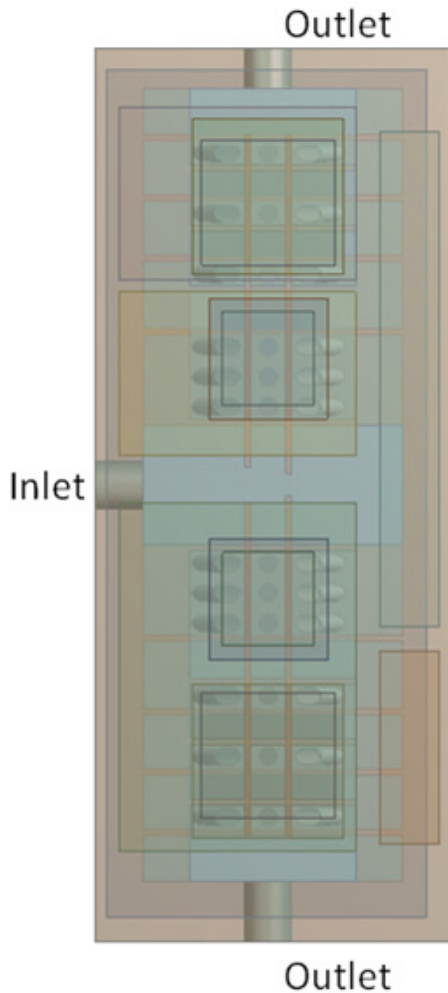
Figure 6.11. Thermal resistances corresponding to the IGBTs for various heat dissipation rates through each device.

Table 6.4. Comparison of the thermal resistances predicted by simulations with those obtained experimentally.

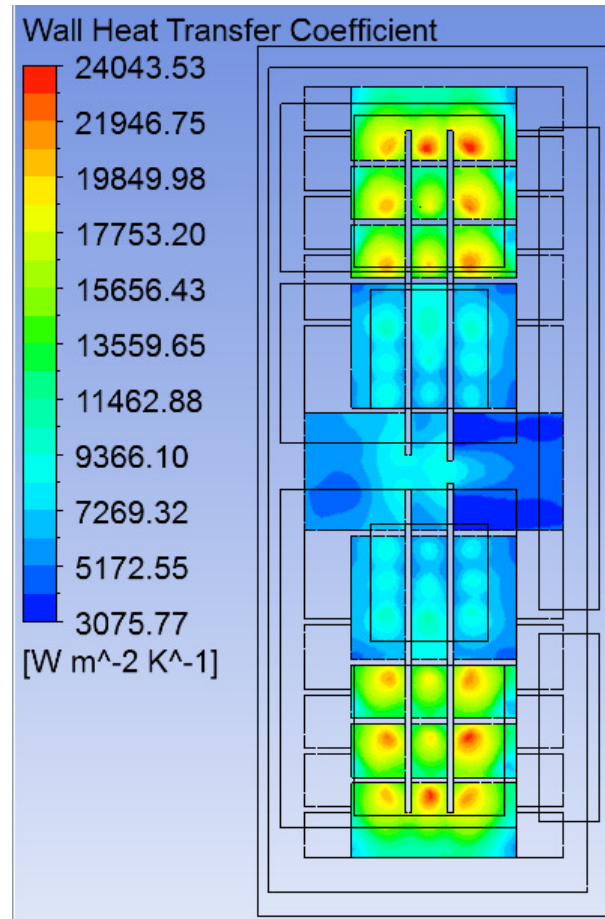
Case	R_{th} for IGBT1 (K/W)	R_{th} for IGBT2 (K/W)
Experiment	0.275	0.28
Simulation	0.277	0.2814



(a)



(b)



(c)

Figure 6.12. Simulation model for the packaged single-sided power module configuration that was fabricated and tested. (a) Side View (b) Top View (c) Wall heat transfer coefficient at the bottom surface of the DBA substrate emphasizing the even coolant distribution inside the cooler.

It is clearly evident that the flow inside the cooler bifurcates in to 2 similar paths and then the flow has to merge in to one single channel outside the cooler. Simulations showed that the flow inside the cooler was symmetric (Figure 23(c)). So in order to maintain even flow distribution inside the cooler and to help the flow from both the outlets to merge together, 2 tubes of similar length and a brass T-fitting were used. The outlet temperature was measured inside this T-fitting where the flows merged. Moreover, the physical distance of this T-fitting from the cooler outlets was about 15 cm due to which there could be a slightly different flow path causing a slight uneven coolant distribution in the cooler which in-turn could have also affected the two IGBT junction temperatures.

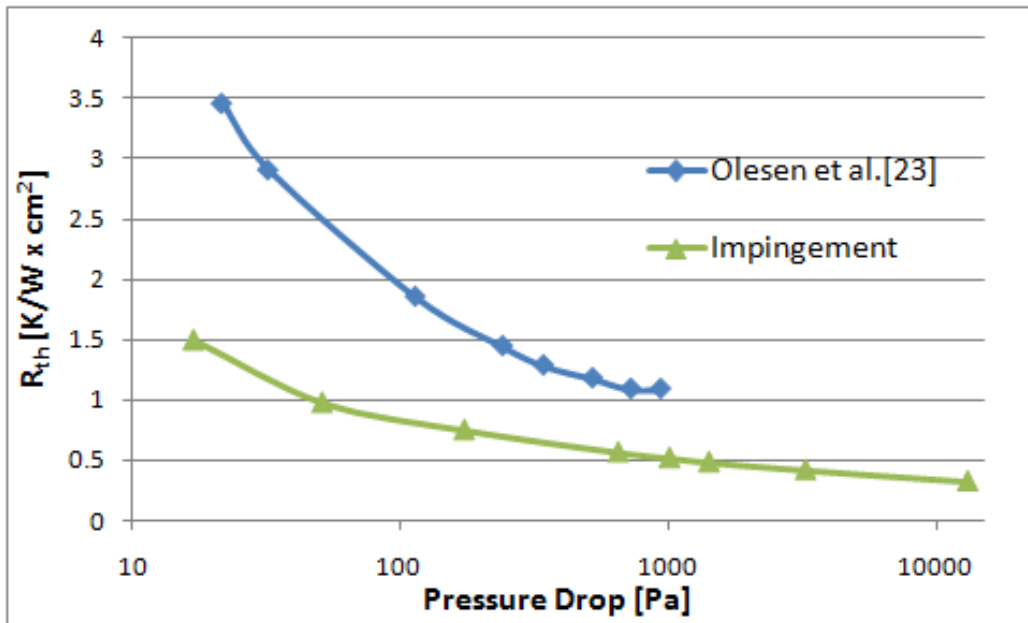


Figure 6.13. Variation of the thermal resistance with pressure drop for the present impingement based configuration and its comparison with existing high performance technology.

The performance of this cooler was also compared to the ones already existing in the market. Figure 24 shows a comparison of the present high performance heat exchanger with one of the high performance heat exchangers presented by Olesen *et al.* [38]. It can be clearly seen

that it performs much better than the existing technology, especially in the automotive power converter cooling system's operating pressure drop region (10 – 1000 Pa).

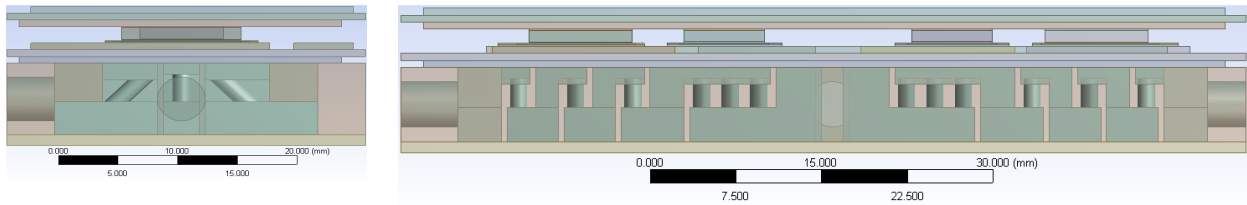


Figure 6.14. Double-sided single channel multi chip power module configuration.

Based on the single-sided power module configuration, a double-sided power module configuration was also generated as shown in Figure 6.14. The heat dissipated by each device was kept the same as that for single sided configuration. For these simulations, LLC as well as water with a flow rate of 1 lpm was used as the coolant. For this configuration, R_{th} value was predicted to be 0.246 K/W when water was used as the coolant and 0.288 K/W when LLC was used as the coolant. Although the performance of the present cooler was much better than the existing configurations, it was not sufficient enough to meet the constraints.

6.4. Summary

Various impingement based configurations were generated for the present high performance hybrid electric vehicle application. Simulations validated with theory and experiments were used to study such heat exchanger designs and to perform parametric and optimization study on the selected designs. Parametric study was also performed to analyze the effect of geometric parameters such as center wall and jet impingement angles. It was found out that the presence of a centre wall can greatly increase the heat removal rate due to conduction heat transfer effects. It was also found out that the centre wall can also help attain a better swirl after impingement and thus, can greatly enhance the convective heat transfer rates. Moreover, it was required to have the impingement on side walls to take the advantage of angled impingement as well as conduction through the center walls. The optimized configuration was

then applied to generate specific heat exchanger designs for cooling of automotive power converters and simulated to meet the required temperature and pumping power constraints. The high performance design was then fabricated and tested under conditions similar to the actual running environment. The experimental data and simulation predictions had a very close match.

For the planar power module configuration, R_{th} value was predicted to be 0.246 K/W when water was used as the coolant and 0.288 K/W when LLC was used as the coolant. Although the cooling performance of the high performance impingement cooler was as-expected and significantly higher than its competing counterparts, it was not sufficient to meet all the design constraints.

CHAPTER 7: MINI-CHANNEL, RIBBED MINI-CHANNEL AND DOUBLE SIDED COOLING BASED DESIGNS

Experimental results presented in the previous chapter showed that the best cooler model based on impinging jets performed as predicted by simulations. The expected performance was however, much lower than the target performance. Therefore, it was worth exploring other cooling options. For this conjugate heat transfer simulations were performed on a double-sided (planar) single channel power module model as shown in Figure 7.1. The module consisted of 2 DBA layers and 3 SAC305 solder layers and 1 copper block each for the Silicon IGBT and diode heat sources. LLC at 65 °C with different mass flow rates was used as the coolant. All the simulations were performed using the k- ϵ turbulence model. In all the simulations, the maximum temperature was obtained at IGBT 2 (device closer to the outlet).

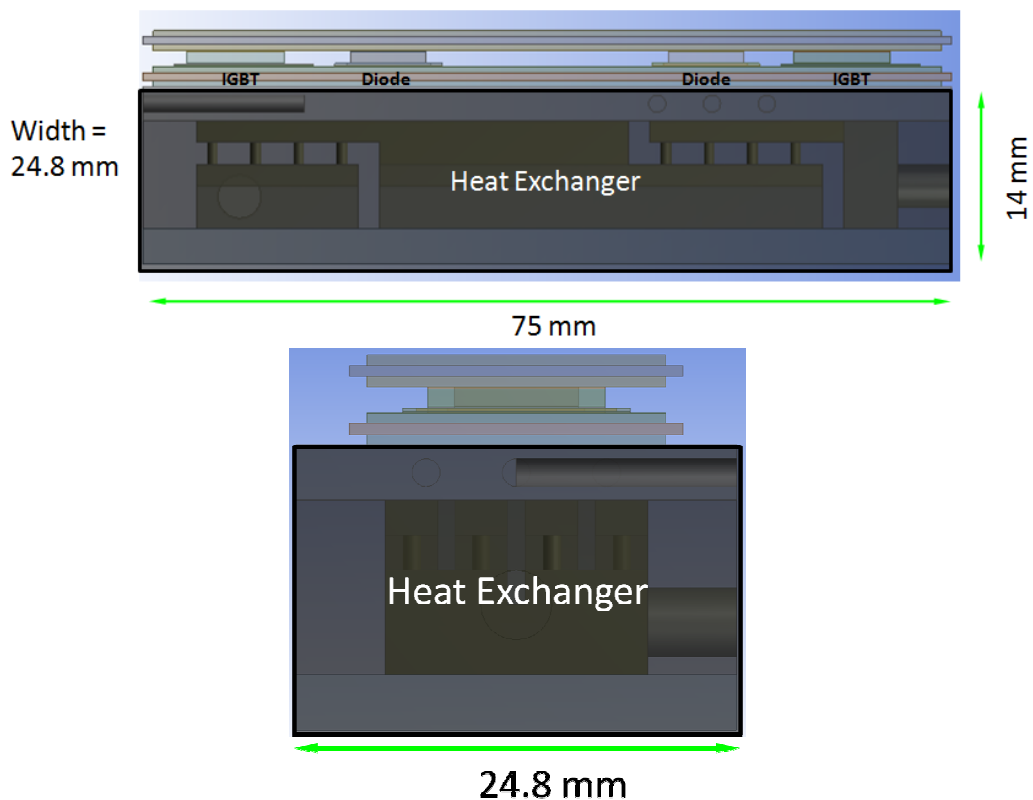


Figure 7.1. Different views of the conjugate heat transfer simulation model for double-sided single channel multi chip power module.

Alternate options such as tapered jets, phase change material based cooling, mini-channels, combined impingement and mini-channels and ribbed mini-channels were incorporated into the double-sided (planar) single-channel multi-chip power module (Figure 7.1). Significant improvements in terms on pressure drop and maximum IGBT temperature reduction were observed. Development of heat exchanger schemes based on mini-channel and ribbed mini-channel cooling schemes are discussed in detail in this chapter. Other alternate cooling schemes are discussed in Chapter 8.

7.1 Mini-channels Based Cooler

Simulation models above were also modified to allow for mini-channel based configurations. Figure 7.2 shows a preliminary mini-channel (~1 mm) based cooler with 11 parallel channels distributed into 5 pass. This design was based on increasing the fluid-solid contact surface area so as to improve the heat removal rate. This model was simulated for LLC at a mass flow rate of 0.0185 kg/s at 65 °C.

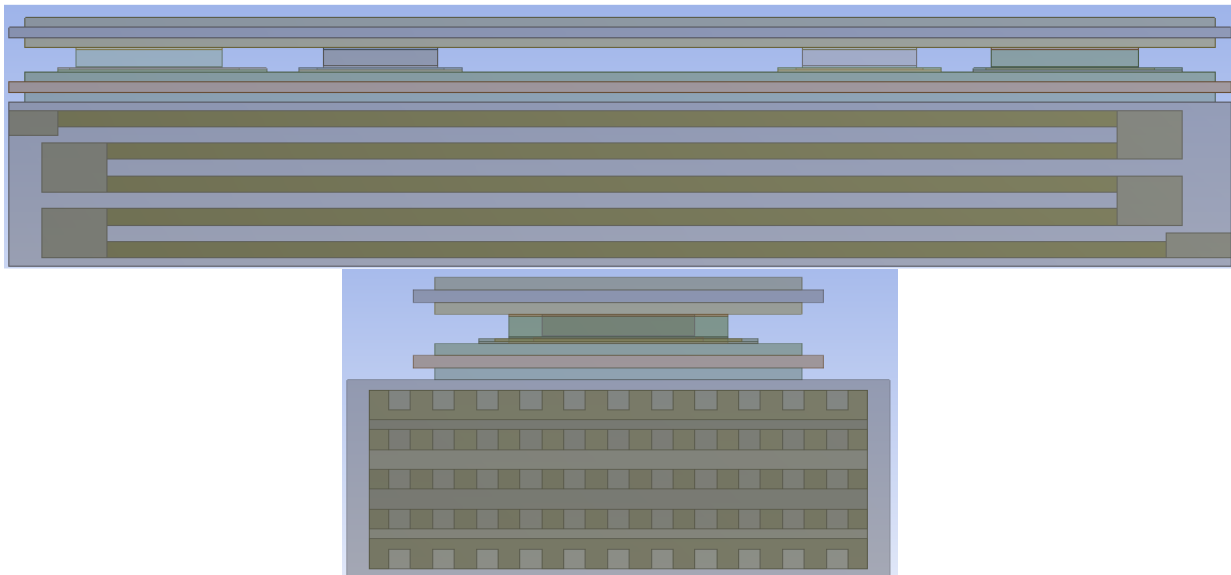


Figure 7.2. Preliminary mini-channel single channel power module packaging design.

Figure 7.3 shows the temperature contours at the central plate. Significantly lower maximum IGBT 1 temperatures were observed at the expense of an increased pressure drop (~33

kPa). It was also observed that the cooler bulk temperatures near the beyond the third pass were more or less similar. In other words, the third fourth and fifth passes did not make a significant contribution towards increasing the heat transfer rates. Moreover, they contributed significantly towards increasing the pressure drop. The pressure drop across each of the five passes was similar as well as the entrance pressure losses. However, different number of passes was required to increase the fluid-solid contact surface area. This design was slightly modified to increase the spacing between the power module and coolant. Figure 7.4 shows the temperature contours at the central plane for this modified design. It can be seen that the maximum IGBT 1 and IGBT 2 temperature increases as the coolant moves away from the power module. In other words, the effective heat transfer rates in the first pass itself were high enough to not require a heat spreader.

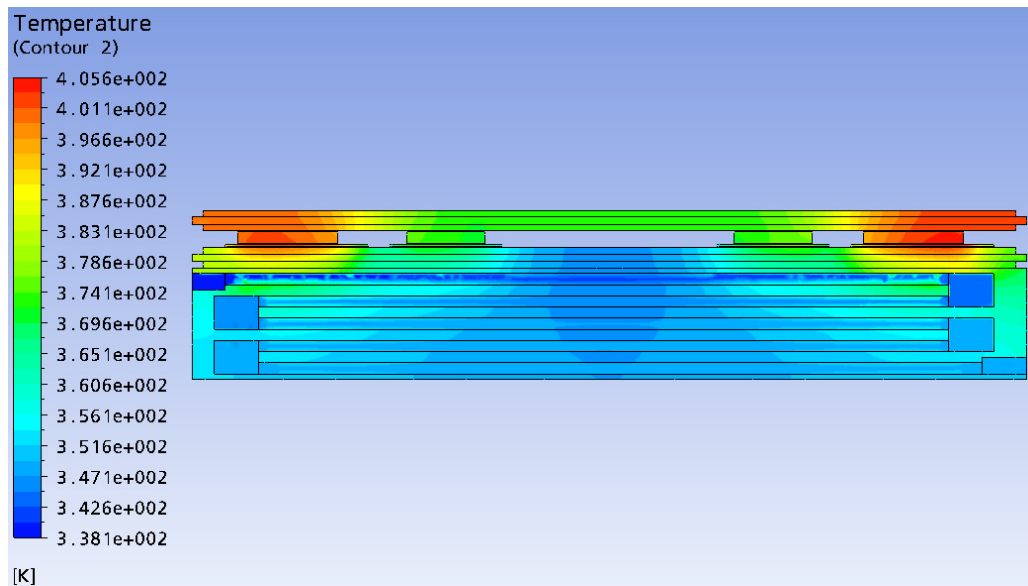


Figure 7.3. Temperature contours at the central plane for the preliminary mini-channel based design.

Using the above observations, the concept of mini-channel based cooler was modified further to reduce the pressure drop and maintain similar heat transfer performance. Figure 7.5 shows the modified design. It consists of 4 pass mini-channel configuration. In the first pass, the

flow is distributed into 9 parallel channels while in the second, third and fourth pass the flow is distributed into 18 parallel channels. This reduces the effective flow through each channel in each pass to half of that in the first pass and thereby, significantly reduces the pressure drop across the channels as well as the entrance pressure losses for the second, third and fourth passes. The predictions for this design along with the predictions for few other mini-channel designs are summarized in Table 7.1.

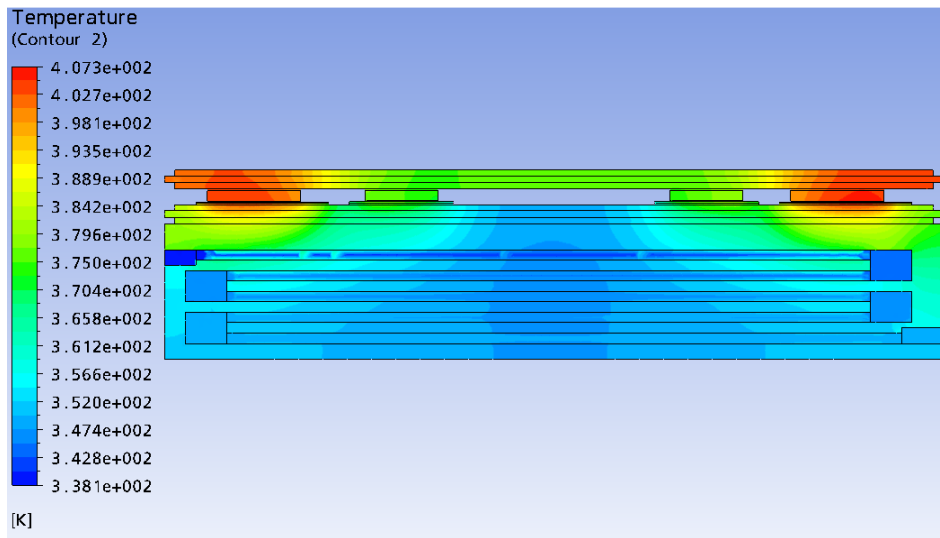


Figure 7.4. Temperature contours at the central plane for the mini-channel based design having a slightly larger coolant to power module separation.

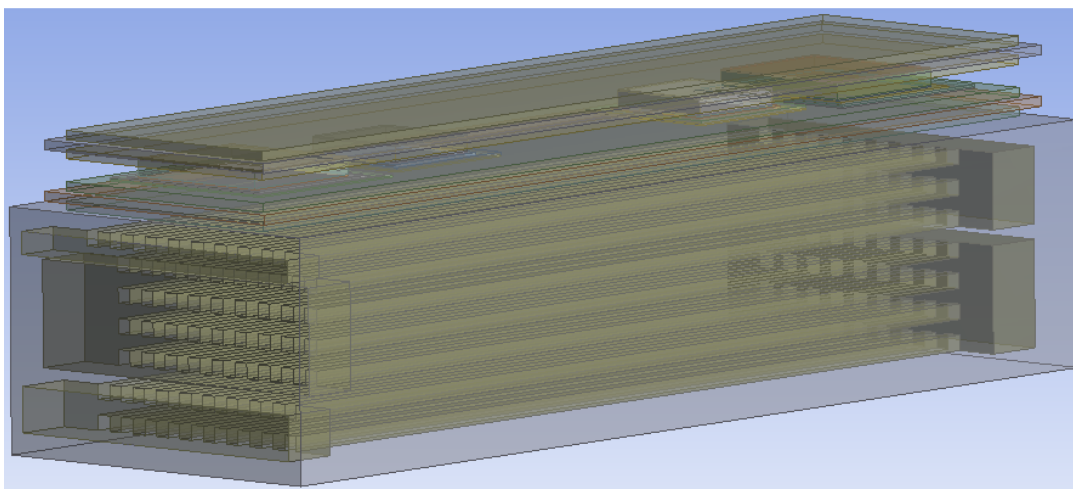


Figure 7.5. Modified mini-channel based configuration.

Table 7.1. Pressure drop and temperature predictions for various mini-channel based configurations.

Case	Mass Flow Rate	Maximum IGBT 1 Temperature	Maximum IGBT 2 Temperature	Pressure Drop
5 pass, 11 parallel 1 mm channels, target wall: 0.5 mm	18.5 g/s LLC @ 65 °C	403.8 K (130.7 °C)	405.6 K (132.5 °C)	33 kPa
5 pass, 11 parallel 1 mm channels, target wall: 1.5 mm	18.5 g/s LLC @ 65 °C	406.4 K (133.3 °C)	407.3 K (134.2 °C)	33 kPa
4 pass, 9 parallel 1 mm channels in first pass, 18 parallel 1 mm channels in other 3 passes, target wall: 0.5 mm	18.5 g/s LLC @ 65 °C	404.6 K (131.5 °C)	405.8 K (132.7 °C)	13 kPa
4 pass, 7 parallel 1 mm channels in first pass, 14 parallel 1 mm channels in other 3 passes, target wall: 1.5 mm	18.5 g/s LLC @ 65 °C	402.4 K (129.3 °C)	403.6 K (130.5 °C)	22 kPa

It was also observed that the bulk of the pressure drop in these mini-channel coolers was at the entrance of the mini-channels. Figure 7.6 shows the cross-section of a 4 pass mini-channel based cooler. The pressure at the inlet was 22.45 kPa and the pressure at location 1 was 16.6 kPa giving a total of 5.84 kPa of entrance losses whereas the pressure loss across the channel (between locations 1 & 2) was about 7.33 kPa. Efforts were made to reduce such entrance pressure losses and at the same time attain a high heat transfer rate. One way to reduce such losses was to use bigger cross-section channels with carefully placed turbulators or bumps in the channels so as to attain a higher heat transfer rates. Another way was to use curved entrances, tapered entrances and other such modifications.

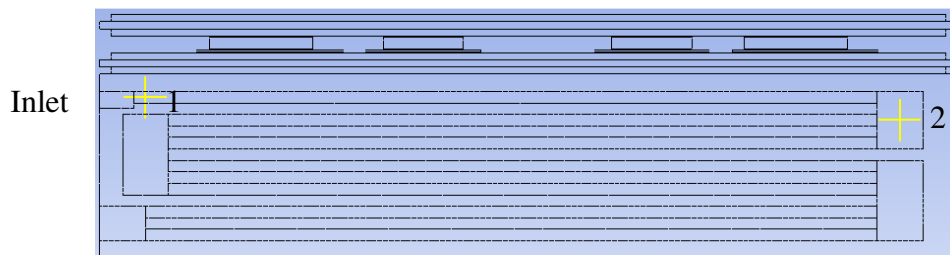


Figure 7.6. Cross-section of a 4-pass mini-channels based cooler with different pressure measurement locations.

7.2 Ribbed Mini-channels

From the above observations, it was concluded that mini-channel provided the required performance. The thermal performance enhances further when it is combined with impingement cooling scheme however, at the expense of increased pressure drop (see Chapter 8). So in order to improve the thermal performance of mini-channels without significantly improving the pressure drop, ribs or trips can be placed inside the channels so as to attain higher average convective heat transfer coefficient at the surfaces close to the power module. Ribs in a channel act as flow turbulators and keep the flow in the channel turbulent. Moreover, ribs can act as surface extensions to enhance the local heat transfer rates. In order to characterize the effect of ribs on heat transfer rate and pressure drop, flow and heat transfer behavior in ribbed mini-channels were compared with that in a straight channel. Figure 7.7(a) shows the flow domain in a straight channel, Figure 7.7(b) shows the flow domain in a 90° ribbed channel and Figure 7.7(c) shows the flow domain in a 45° ribbed channel.

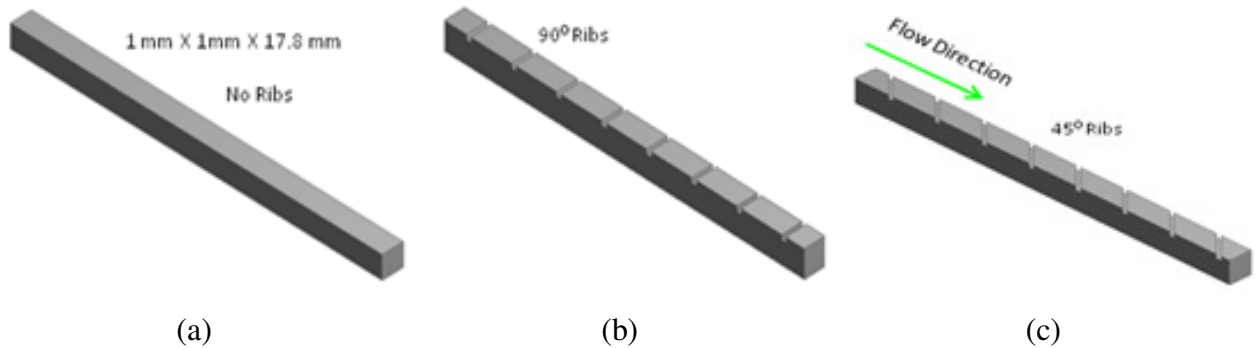


Figure 7.7. Flow domain in a (a) straight channel, (b) 90° ribbed channel and (c) 45° ribbed channel.

For a better heat transfer rate comparison, all the four faces were named as shown in Figure 7.8. Various different ribbed channel configurations were studied. In all these configurations, only one wall/face was ribbed (Face B) and the angle of the ribs was calculated with respect to the flow direction.

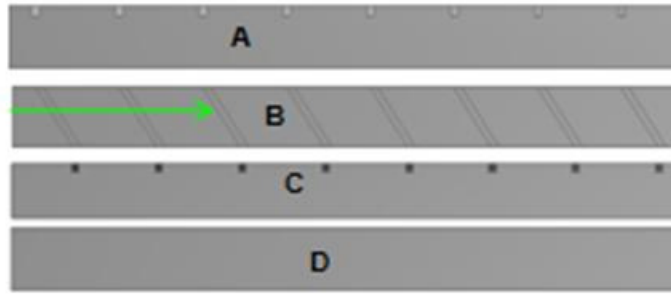


Figure 7.8. Four different faces of a ribbed channel.

Table 7.2. Channel and rib dimensions with associated thermal performance and pressure drop.

Model #	Channel Cross-section (mmXmm)	Rib Height (mm)	Rib Thickness (mm)	Rib Angle	Rib Spacing (mm)	Channel Avg h (W/m ² -K)	Avg h on Face A (W/m ² -K)	Avg h on Face B (W/m ² -K)	Avg h on Face C (W/m ² -K)	Avg h on Face D (W/m ² -K)	Pressure Drop (kPa)
1	1 X 1	-	-	-	-	7870	7870	7869	7872	7872.4	2.5
2	1 X 1	0.2	0.2	90°	2.225	11862	11817	13807	11811	9680	8.6
3	1 X 1	0.2	0.2	45°	2.225	11174	9810	13671	11581	9172	11.4
4	1 X 1.3	0.2	0.2	90°	2.225	10640	10573	12518	10602	8561	6.65
5	1 X 1.3	0.2	0.2	45°	2.225	10265	8955	12901	10633	8170	8.81
6	1 X 1.5	0.3	0.2	90°	2.225	10205	10398	11260	10416	8269	6.28
7	1 X 1.5	0.1	0.2	90°	1.1125	7993	7585	10741	7527	6046	3
8	1 X 1.5	0.1	0.2	45°	2.225	6842	5960	9577	6734	5239	2.55
9	1 X 1.5	0.1	0.1	26.5°	2.225	6340	5555	8490	6341	4931	2.2
10	1 X 1.5	0.2	0.2	90°	1.1125	9350	9169	11408	9196	7043	4.82
11	1 X 1.5	-	-	-	-	4951	4952	4947	4952	4951	0.9
12	1 X 1.5	0.1	0.2	90°	2.225	7200	6863	9469	6850	5752	2.5
13	1 X 1.5	0.2	0.2	90°	2.225	8908	8826	10844	8782	6930	4.2

Table 7.2 summarizes the channel and ribs dimensions and their associated thermal performance and pressure drop. For all the simulations, LLC at 65 °C with a mass flow rate of 3.08 g/s was used as the coolant. In all the simulations, it can be seen that a high average heat transfer rate was obtained at the ribbed surface. It can also be seen that for Model 7 the average heat transfer coefficient on face B was much higher than that for Model 1 and the pressure drop across the ribbed channel was similar to that of Model 1. Thus, by using ribbed mini-channels similar to Model 7 in mini-channel based heat exchangers, we can attain a better thermal

performance. Moreover, the cross-sectional area was also 50% higher resulting in much lower entrance losses. Figure 7.9 shows the temperature contours at the central plane of the power module-cooler package based on ribbed mini-channel configuration as well as at a cross-sectional plane passing through the center of one of the IGBT. Few other ribbed mini-channel configurations, such as those based on models 10 and 13 above, were also modeled and simulated. Table 7.3 summarizes the key predictions.

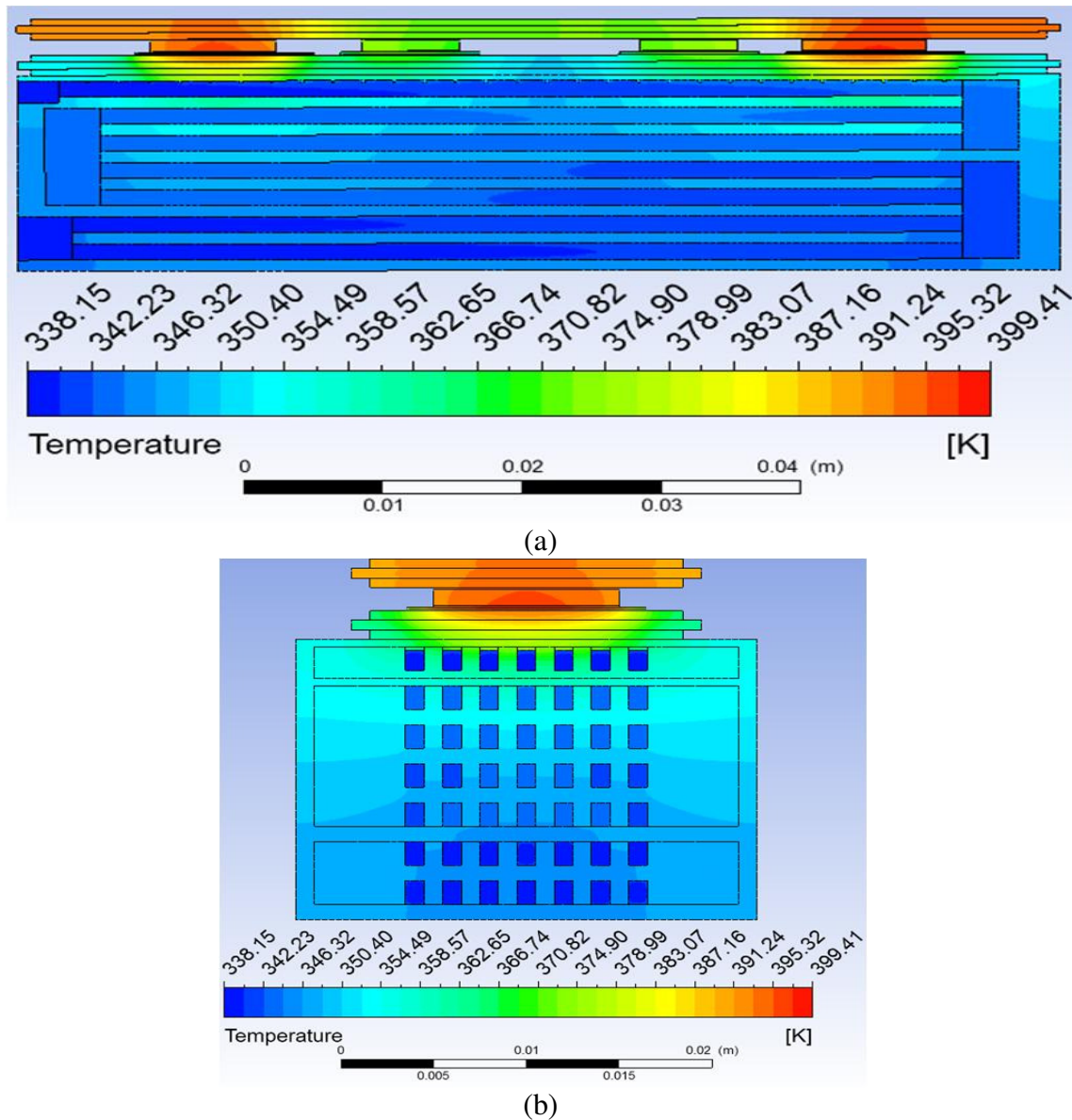
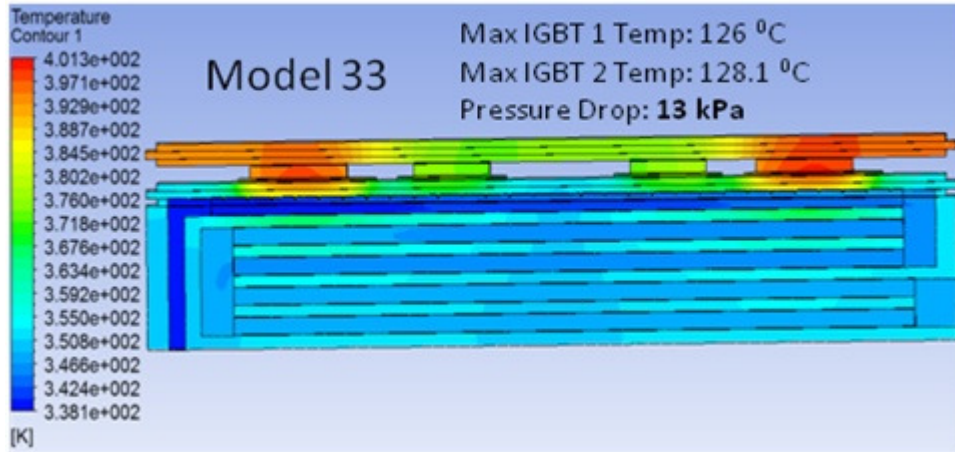


Figure 7.9. Temperature contours at the (a) packaging central plane and at the (b) cross-sectional plane at the IGBT 1 center for a cooler based on ribbed mini-channel configuration.

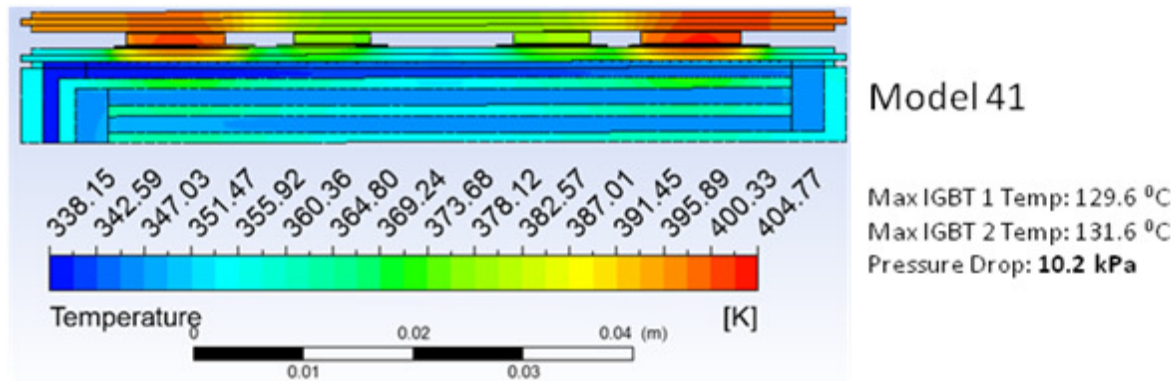
Table 7.3. Pressure drop and temperature predictions for ribbed mini-channels based configurations.

Case	Mass Flow Rate	Maximum IGBT 1 Temperature	Maximum IGBT 2 Temperature	Pressure Drop
4 pass, 7 parallel 1.5 mm 90° ribbed channels in the first pass, 14 parallel 1.5 mm channels in the rest. target wall: 0.5 mm	18.5 g/s LLC @ 65 °C	397.7 K (124.6 °C)	399.4 K (126.3 °C)	16 kPa
3 pass, 7 parallel 1.5 mm 90° ribbed channels in the first pass, 0.2mm X 0.2mm ribs; 2.2 mm pitch, one face ribbed, 14 parallel 1.5 mm channels in the rest. No target wall. (<i>Model 33</i>)	18.5 g/s LLC @ 65 °C	399.2 K (126.1 °C)	401.3 K (128.2 °C)	13 kPa
2 pass, 7 parallel 1.5 mm 90° ribbed channels in the first pass, 0.1mm X 0.1mm ribs; 0.9 mm pitch, one face ribbed, 14 parallel 1.5 mm channels in the next. No target wall. (<i>Model 41</i>)	18.5 g/s LLC @ 65 °C	402.7 K (129.6 °C)	404.7 K (131.6 °C)	10.2 kPa
1 pass, 12 parallel 1.2mm X 1.5mm 90° ribbed channels in the first pass, 0.1mm X 0.2mm ribs; 1.1 mm pitch, all four faces ribbed. Target wall: 1 mm. (<i>Model 42</i>)	18.5 g/s LLC @ 65 °C	401.2 K (128.1 °C)	406 K (133 °C)	12.9 kPa

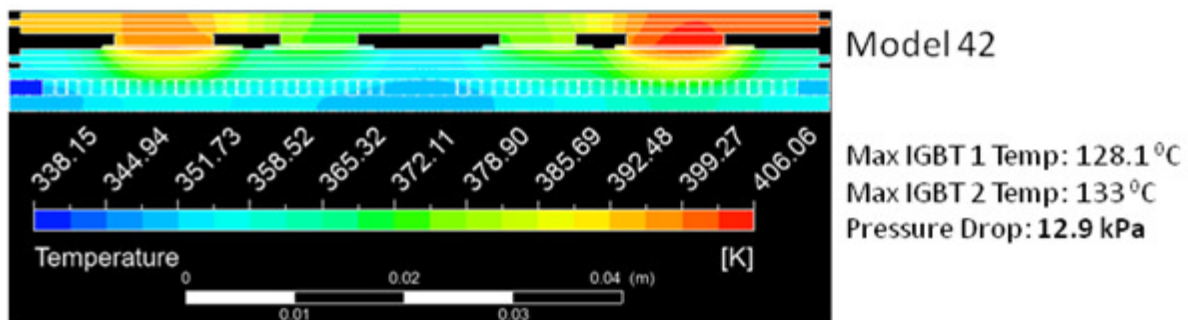
Figure 7.10 shows the temperature contours at the central plane of the power module-cooler package for the other ribbed mini-channels based models summarized in Table 7.3. It can be seen that by incorporating ribs into the mini-channels much higher heat transfer rates can be attained at much reduced pressure drops. Moreover, subsequent passes with non-ribbed channels can be utilized to increase the fluid-solid contact surface area to take the advantage of conduction through the cooler bulk. From Figure 7.10(c), it can be clearly seen that for one pass, the cooler bulk is not quite at the coolant exit temperature. Thus, the effective heat transfer rate of this cooler can be increased further by incorporating another layer of mini-channels.



(a) Model 33



(b) Model 41



(c) Model 42

Figure 7.10. Temperature contours at the packaging central plane for models based on ribbed mini-channels (a) Model 33, (b) Model 41 and (c) Model 42.

7.3. Parametric Study & Optimization

As a first step towards ribbed mini-channel based cooler optimization, preliminary parametric study was performed. For this study, fluid model of a single ribbed channel as shown

in Figure 7.11 was used. Rib height, rib angle and rib spacing were used as the input parameters. Pressure drop and channel average heat transfer coefficient were used as the output parameters. The effect of a range of these input parameters on the two output parameters was studied. The rib angle, calculated with respect to the flow direction, was varied from 30° to 90° , rib height was varied from 0.05 mm to 0.3 mm and the rib spacing was varied from 1 mm to 3 mm. The effect of these parameters on the output parameters are summarized in Figure 7.12. It can be observed that pressure drop and channel average heat transfer coefficients increased linearly with rib height.

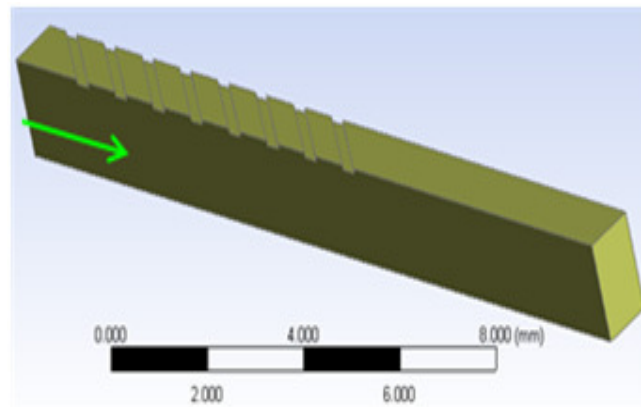
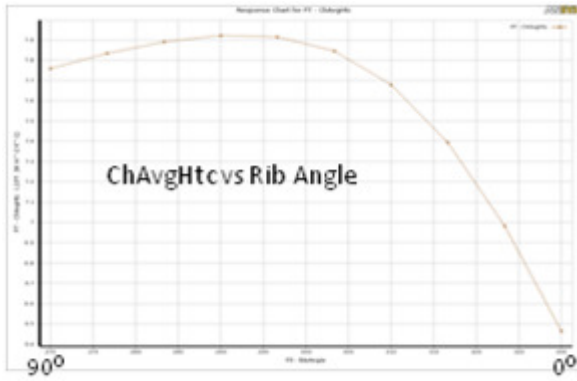


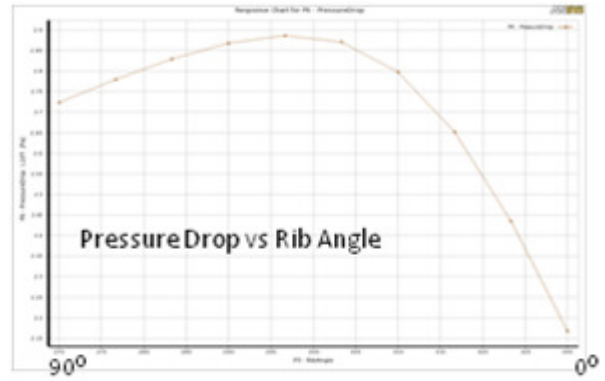
Figure 7.11. Fluid model for rib based parametric study.

The variation of pressure drop and channel average heat transfer coefficient with rib angle and rib spacing was non-linear and showed to have a maximum value. Rib spacing of 2 mm (i.e. 10 times the rib width) allowed for a high heat transfer rate and low pressure drop. Similarly, for 90° ribs, the pressure drop was low as well as the heat transfer rate was acceptably high. Based on these curves, a sensitivity of the output parameters to the input parameters was generated (Figure 7.13). This in turn enabled us to identify key input parameters as well as what parameters need larger variation for say better heat transfer rates at a lower pressure drop. From this study, it was observed that $70^\circ - 75^\circ$ angled ribs showed higher heat transfer rates, however, the pressure drop was also higher. It was also observed that 90° ribs showed a better heat transfer

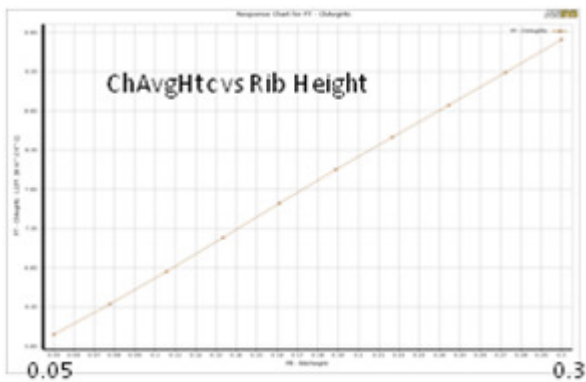
rate at much reduced pressure drop. Moreover, manufacturing 90° ribs is simpler than angled ribs. Thus, for future ribbed mini-channel optimization study, rib angle was fixed at 90° .



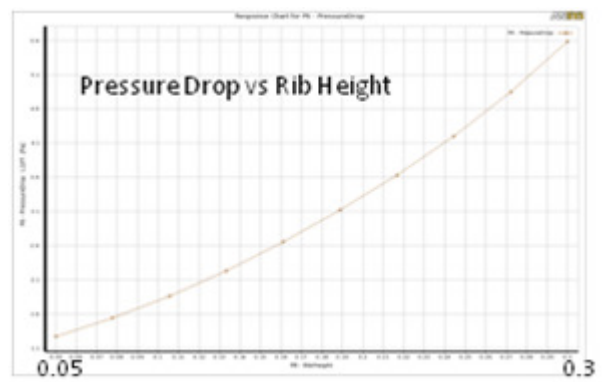
(a)



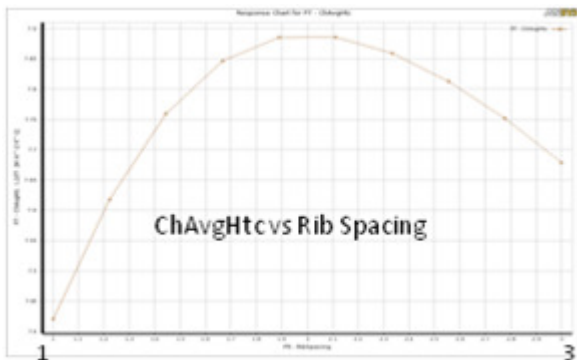
(b)



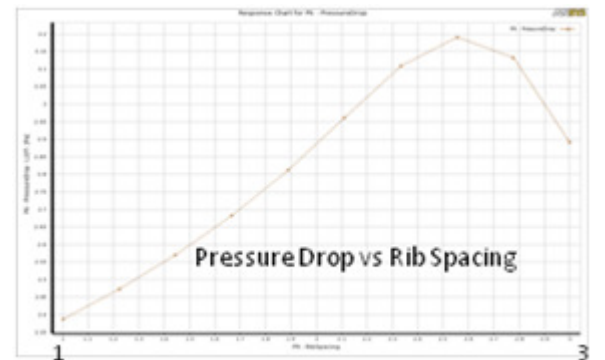
(c)



(d)



(e)



(f)

Figure 7.12. Variation of Output parameters (channel average HTC and pressure drop) with input parameters (rib angle, rib height and rib spacing).

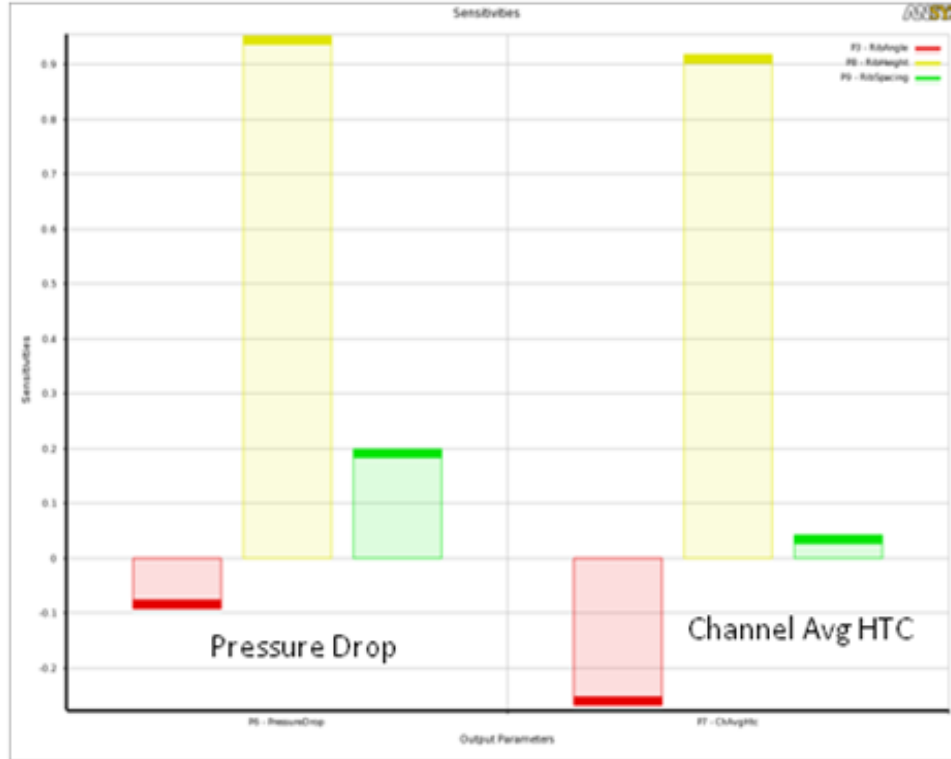


Figure 7.13. Sensitivity of the output parameters to the input parameters.

7.4 Conjugate Analysis for Ribbed Mini-Channels Based Cooler Optimization

As shown in the previous sections, ribbed mini-channels based cooler showed some promising results. However, full conjugate model simulations of ribbed mini-channels based packaging module took a huge amount of time from the order of few days to couple of months. So in order to minimize the simulation time, it was necessary to model and simulate smaller conjugate models. Then, these smaller models were characterized with respect to the full single channel cooler models followed by optimization of the ribbed mini-channels based coolers using the smaller conjugate models. Figure 7.14 shows the smaller conjugate model based on ribbed mini-channels. Many different ribbed mini-channel models were generated by varying the number of ribbed faces, number of ribs, rib spacing, rib width and rib height and were simulated for performance comparison. A uniform heat flux value was applied at the top solid surface (surface closest to Face B). A symmetry boundary condition was applied at the side solid

surfaces (surfaces closest to Face A and Face C). At the bottom solid surface, adiabatic boundary condition was applied. The dimensions of these models and simulation predictions are summarized in Table 7.4.

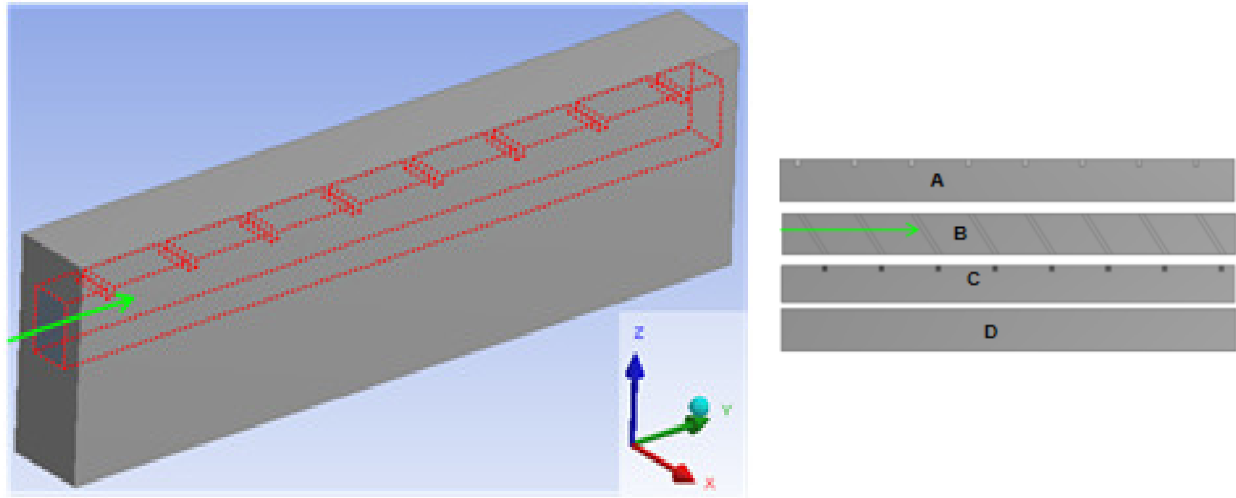


Figure 7.14. Smaller conjugate model for ribbed mini-channel based cooler optimization.

In order to characterize the simulation with the single channel packaging model, smaller models of Model 33 (Conj model 15), Model 41 (Conj Model 16) and Model 42 (Conj model 13) above were used as the baseline. It is to be noted here that the overall flow rate for the entire cooler was constant and thus, the mass flow rate through each channel varied depending upon the number of channels in each pass. Also, the section of the power module-cooler package that was simulated had certain flow rate and pressure drop target based on the overall heat exchanger structure (discussed in Chapter 3). For this configuration of partial module-cooler package, the allowed mass flow rate was 18.5 g/s and the allowed pressure drop was 10 kPa. Since the conjugate ribbed mini-channel models discussed here was about a quarter of the total channel length, the target pressure drop was roughly about 2.5 kPa. This target value was flexible and models showing pressure drops closer to 4 kPa were also considered. This is because, the rib dimensions and rib spacing under the diode section and in the region between the two diodes can

be augmented to operate at lower pressure drops and lower heat transfer rates. Moreover, for the Model 42 (Figure 7.10(c)) the pressure drop was about 12.9 kPa and that for the small conjugate model (Conj Model 13) corresponding to Model 42 was about 4 kPa (roughly one third of the total pressure loss).

The aim of the study was to come-up with certain ribbed mini-channel configuration which will provide enhanced heat transfer rate with a reduced or similar pressure drop than the base line cases. Figure 7.15 graphically represents the thermal performance of the base-line case and some new improved high performing geometries. From this study, it was found out that *having ribs on 3 faces can significantly enhance the heat transfer coefficient at a much reduced pressure drop*. Moreover, the cross-section of the mini-channels has to be slightly bigger (~1.2mm X 1.5mm as compared to 1mm X 1.5mm) in order to accommodate the ribs on three faces and reduce pressure drop as well as meet the minimum channel dimensions of 1 mm.

Table 7.4. Dimensions and thermal performance of few of the conjugate ribbed mini-channel models.

Conj Model #	Solid Block Size(mm)			Fluid Domain (mm)			Ribs (mm)				Heat Flux (W/m ²)	Mass Flow Rate (g/s)	Avg Wall Temp (K)	Avg Fluid Temp (K)	Effective h (W/m ² -K)	Pressure Drop
	L(y)	B(x)	H(z)	L (y)	B (x)	H (z)	Rib height	Rib Width h	Pitch	Ribbed Walls						
1	17.8	2	5	17.8	1	1.2	-	-	-	-	530000	3.08	381.441	339.029	12496.46	1.58
2	17.8	2	5	17.8	1	1.2	0.1	0.2	1.1125	B	530000	3.08	365.728	339.288	20045.39	5.246
2	17.8	2	5	17.8	1	1.2	0.1	0.2	1.1125	B	1060°00	3.08	393.31	340.424	20043.11	5.246
3	17.8	2	5	17.8	1	1	-	-	-	-	1060°00	3.08	415.733	339.901	13978.27	2.53
4	17.8	2	5	17.8	1.2	1	0.1	0.2	1.1125	A,B	1060°00	3.08	380.301	340.54	26659.29	11.67
5	17.8	2	5	17.8	1.2	1	0.1	0.2	1.1125	A, B, C	1060°00	3.08	372.993	340.435	32557.28	21.36
6	17.8	2	5	17.8	1.2	1.5	0.1	0.2	1.1125	A, B, C, D	1060°00	1.54	389.64	342.36	22419.63	4
6	17.8	2	5	17.8	1.2	1.5	0.1	0.2	1.1125	A, B, C, D	1060°00	3.08	373.456	340.395	32061.95	12.75
7	17.8	2	5	17.8	1.2	1.5	0.1	0.2	1.1125	A, B, C	1060°00	1.54	395.732	342.419	19882.58	2.7
7	17.8	2	5	17.8	1.2	1.5	0.1	0.2	1.1125	A, B, C	1060°00	3.08	377.434	340.442	28654.84	8.58
8	17.8	2	5	17.8	1.2	1.5	0.1	0.2	1.1125	A,B	1060°00	1.54	413.217	342.753	15043.14	1.34
8	17.8	2	5	17.8	1.2	1.5	0.1	0.2	1.1125	A,B	1060°00	3.08	387.982	340.623	22382.23	4.27
9	17.8	2	5	17.8	1.2	1.5	0.1	0.2	1.1125	B	1060°00	1.54	443.064	342.726	10564.29	0.6
9	17.8	2	5	17.8	1.2	1.5	0.1	0.2	1.1125	B	1060°00	3.08	404.004	340.531	1670°01	1.9
10	17.8	2	5	17.8	1.2	1.5	0.1	0.2	1.1125	-	1060°00	1.54	566.965	341.544	4702.313	0.13
10	17.8	2	5	17.8	1.2	1.5	0.1	0.2	1.1125	-	1060°00	3.08	448.987	339.88	9715.234	0.55
11	17.8	2	5	17.8	1.2	1.5	0.1	0.2	1.1125	B, D	1060°00	1.54	411.248	342.342	15383.28	1.2
11	17.8	2	5	17.8	1.2	1.5	0.1	0.2	1.1125	B, D	1060°00	3.08	388.163	340.44	22211.51	3.6
12	17.8	2	5	17.8	1.2	1.5	0.1	0.2	1.1125	A, C	1060°00	1.54	408.862	342.097	15876.58	1.5
12	17.8	2	5	17.8	1.2	1.5	0.1	0.2	1.1125	A, C	1060°00	3.08	386.905	340.31	22749.22	4.6
13	17.8	1.5	5	17.8	1.2	1.5	0.1	0.2	1.1125	A, B, C, D	1060°00	1.54	382.399	341.313	25799.54	4
13	17.8	1.5	5	17.8	1.2	1.5	0.1	0.2	1.1125	A, B, C, D	1060°00	3.08	369.821	339.838	35353.37	12.76
14	17.8	1.5	5	17.8	1.2	1.5	0.1	0.2	1.1125	A, B, C	1060°00	1.54	387.029	341.403	23232.37	2.7
14	17.8	1.5	5	17.8	1.2	1.5	0.1	0.2	1.1125	A, B, C	1060°00	3.08	372.911	339.91	32120.24	8.58
14	17.8	1.5	5	17.8	1.2	1.5	0.1	0.2	1.1125	A, B, C	1060°00	2.64	375.621	340.168	29898.74	6.58
14	17.8	1.5	5	17.8	1.2	1.5	0.1	0.2	1.1125	A, B, C	1060°00	1.85	382.775	340.912	25320.69	3.632
15	17.8	2	5	17.8	1	1.5	0.2	0.2	2.225	B	1060°00	2.64	405.236	340.976	16495.49	2.674
16	17.8	2	5	17.8	1	1.5	0.1	0.1	0.9	B	1060°00	2.64	405.059	340.957	16536.15	2.254

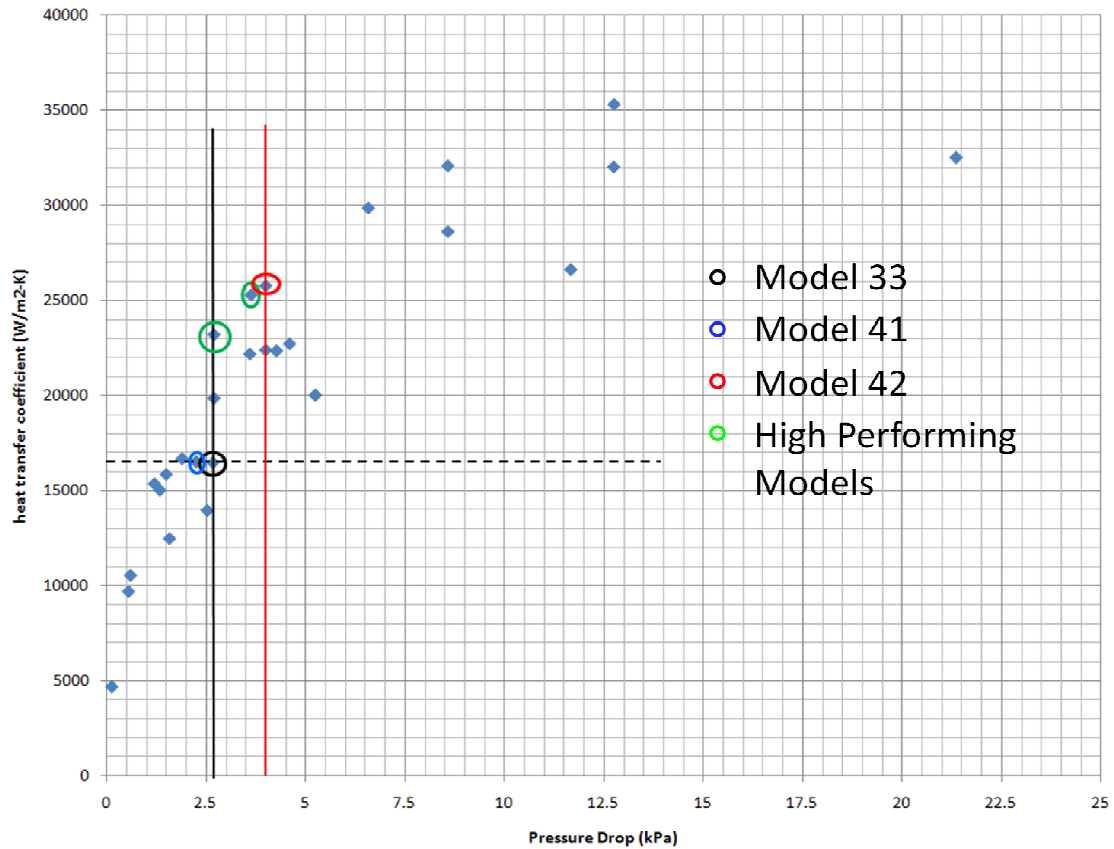


Figure 7.15. Comparison between the various ribbed mini-channels models.

Next step in the ribbed mini-channel parametric and optimization study was to perform a detailed conjugate analysis. The study was performed to study the effect and optimum value of the following parameters:

- i. Vertical Offset
- ii. Horizontal Offset
- iii. Number of Passes/Layers in Inline arrangement
- iv. Number of Passes/Layers in Staggered arrangement
- v. Rib Angle
- vi. Rib Height

- vii. Rib Width
- viii. Rib Spacing
- ix. Mass flow Rate

For a better comparative study, baseline model was defined as a conjugate mini-channel model as shown in Figure 7.16. The solid block was considered to be of Al 6063 and the coolant was taken to be LLC 50% @ 65 °C. At the top surface, a heat flux of 53 W/cm² was applied while at the side surfaces, symmetry boundary condition was applied. As the minimum channel dimension (1 mm X 1 mm) was fixed, it was kept constant and the following parameters – vertical offset, horizontal offset and inlet mass flow rate were varied. The effect of these parameters on the effective heat transfer coefficient at the target surface and on the pressure drop was studied. It was observed that the heat transfer coefficient increased more or less linearly with mass flow rate while the pressure drop showed a quadratic response. It was also observed that for the same channel dimensions, the effective heat transfer coefficient increased as the horizontal offset was reduced, that is, the smaller the horizontal offset, the higher the effective heat transfer coefficient. However, the minimum horizontal offset was limited at a value of 0.25 mm due to easy of fabrication and solderability. In the case of vertical offset, a maximum was obtained for effective heat transfer coefficient at vertical offset of 0.25 mm. This study was used to define the baseline model as:

- Channel dimensions: 1 mm X 1 mm X 20 mm.
- Inlet: 2g/s LLC @ 65 °C.
- Solid Block: Al 6063

- Horizontal Offset: 0.25 mm
- Vertical Offset: 0.5 mm
- Input heat flux: 53 W/cm^2 , symmetry BC at the side walls.
- Effective Heat Transfer Coefficient: $12245 \text{ W/m}^2\text{-K}$ (for a mass flow rate of 2 g/s).
- Effective Heat Transfer Coefficient: $60^\circ 0 \text{ W/m}^2\text{-K}$ (for a mass flow rate of 1 g/s).
- Pressure Drop (2 g/s): 1.216 kPa or 60.8 Pa/mm (pressure drop per unit length).

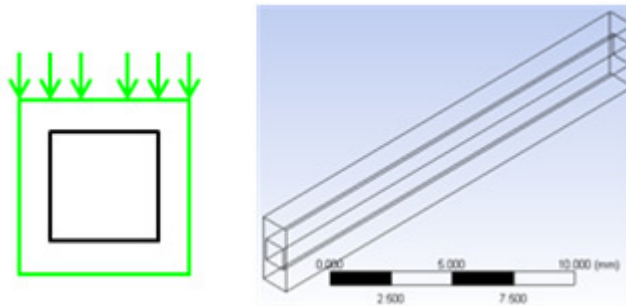


Figure 7.16. Conjugate mini-channel model.

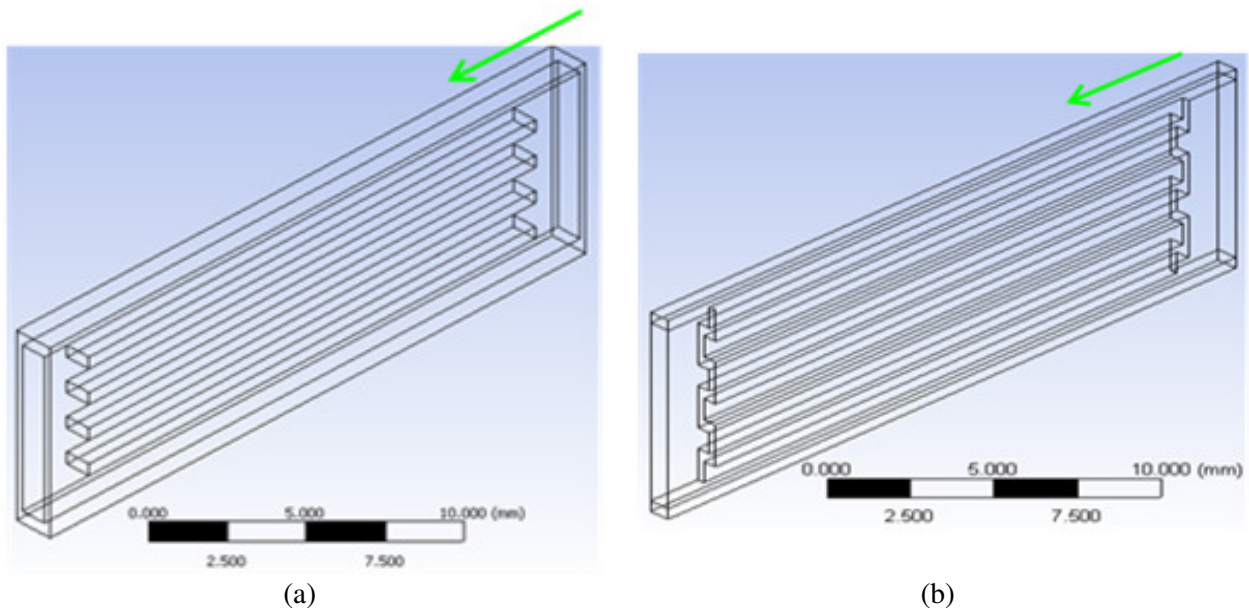


Figure 7.17. (a) Inline multi-layer mini-channel arrangement with green arrow indicating the flow direction. (b) Staggered multi-layer mini-channel arrangement with green arrow indicating the flow direction.

Once the reference was set, the optimum number of passes/layers was investigated. For this, two different configurations – inline and staggered, were studied. Figure 7.17(a) shows the inline arrangement with 5 layers while Figure 7.17(b) shows staggered arrangement with 6 layers. For both the configurations the number of layers was varied from 2 to 5 and 6 respectively and the vertical offset and separation between the layers was taken to be 0.5 mm. For the case of 1 layer, the model was same as the baseline case. In this study, a same amount of flow (2g/s) was distributed among different layers, that is, the total flow through the simulated section remained same. For the staggered case, only half the channels in each layer were simulated, thus the total flow through the simulated section was taken to be half of that taken for inline case.

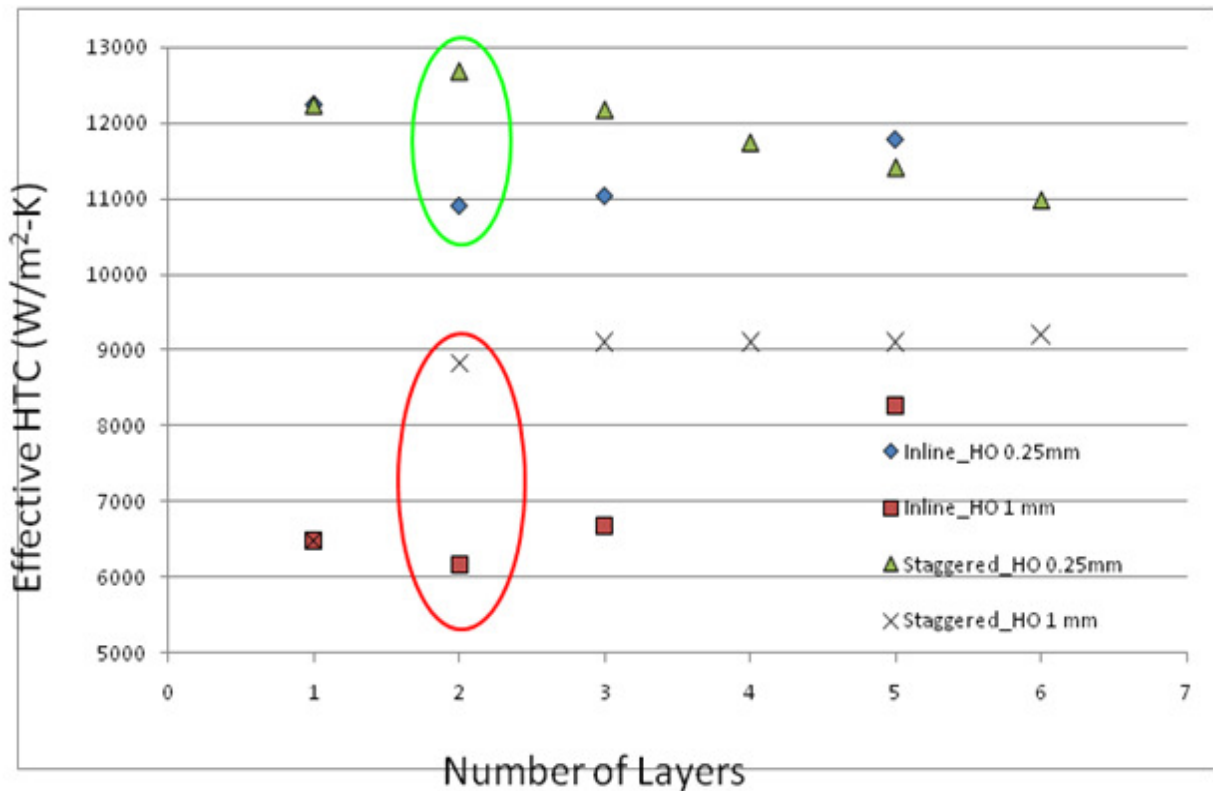


Figure 7.18. Effect of number of layers on the effective heat transfer coefficient for inline and staggered arrangement for two different horizontal offsets (0.25 mm and 1 mm).

It was observed that for a smaller horizontal offset (0.25 mm), more than 6 layers are required to show some improvement in effective heat transfer coefficient as compared to the base line case. Moreover, a minimum effective heat transfer coefficient was observed for 2 layer inline arrangement. For the same horizontal offset (0.25 mm), the staggered arrangement showed a maximum effective heat transfer coefficient at 2 layers. Thus, staggered arrangement was found out to be much better from both size and fabrication point of view. Figure 7.18 summaries the effect of number of layers on the effective heat transfer coefficient for both the configurations. Additionally, it was observed that the pressure drop is also reduced by at least 35% as go from 1 layer to 2 layers. For inline case, this pressure reduction is almost 50%. Thus, *2 layer staggered arrangement was taken as the optimum mini-channel configuration.*

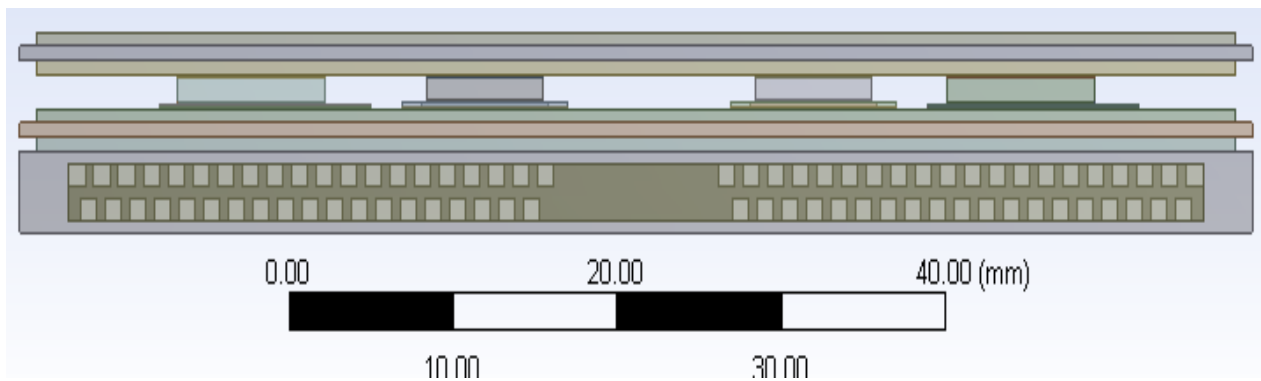


Figure 7.19. Double-sided single channel multi-chip power module packaging model based on optimum 2 layers mini-channel configuration. Flow direction based on overall structure 6.

This optimum 2 layer staggered mini-channel configuration was then applied to a double sided (planar) single channel multi chip power module-cooler package model (Figure 7.19) and simulated. The flow distribution and allowed pressure drop was based on overall heat exchanger structure 6. Due to the large number of channels, the flow rate through each channel was 1 g/s. The model shown in Figure 7.19 has 78 1 ribbed wall mini-channels arranged in a 2 layers staggered configuration with 40 parallel channels in the first layer and 38 parallel channels in the second. Separation between the channels in the same layer as well as between the layers was

taken to be 0.5 mm. The effective heat transfer coefficient at the bottom surface of the bottom DBA was computed to be 16500 W/m²-K and the pressure drop was estimated to be 1.45 kPa. The maximum IGBT1 and IGBT2 temperatures were 142 °C and 143 °C. As there was not much cooling in the region between the two diodes, the effective heat transfer coefficient was lower than that locally under the IGBTs and Diodes. So based on the IGBT temperatures, the effective heat transfer coefficient under the IGBTs was estimated to be equivalent to 190°0 W/m²-K. Figure 7.20 shows the variation of IGBT temperatures as a function on effective heat transfer coefficient under the IGBTs. This graph was used as the reference to find out the equivalent heat transfer coefficient under the IGBTs and Diodes.

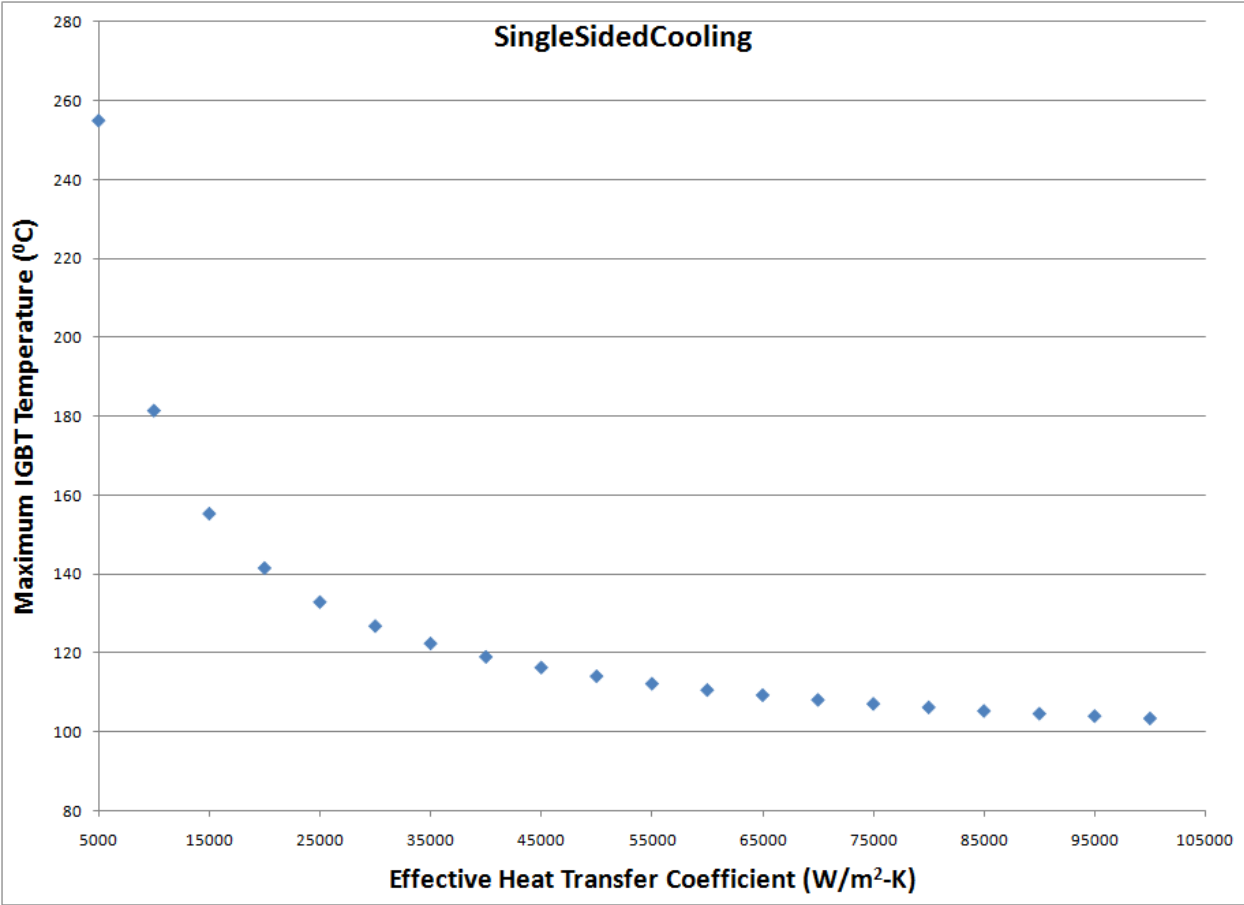


Figure 7.20. Variation of IGBT temperature as a function of effective heat transfer coefficient under the IGBTs.

Next step in parametric and optimization study was to study the case of ribbed mini-channels. Four different cases – ribs on 1 wall, ribs on 2 walls, ribs on 3 walls and ribs on all 4 walls, were studied. For each case, a conjugate model was used and the horizontal and vertical offsets were kept at 0.25 mm and 0.5 mm respectively. Other conditions were taken to be similar to the baseline case. Figure 7.21 shows the conjugate mini-channel model with one ribbed wall. For the case of 1 ribbed wall, rib angle, rib height, rib width and rib width were simultaneously varied to find the best possible combination. Similar to the earlier study, it was found out that 90° ribs performed well in terms of high heat transfer rates at reduced pressure drop. So for all further simulations, 90° ribs were considered as the optimum rib angle. This angle was computed with respect to the flow direction inside the channel. The optimum rib width, rib height and rib spacing were found out to be 0.1 mm, 0.3 mm and 3 mm (10 times the rib height) respectively. However, a rib width of 0.3 mm was used for future simulation as it was considered to be more robust and showed a slightly lower heat transfer coefficient ($\sim 2\%$) as well as slightly lower pressure drop ($\sim 3\%$).

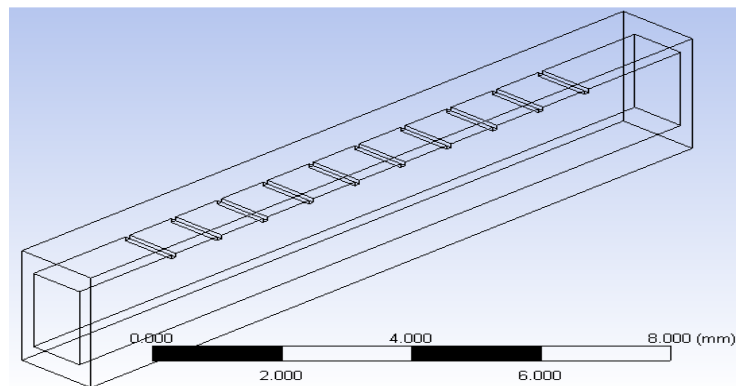


Figure 7.21. Conjugate mini-channel model with one ribbed wall.

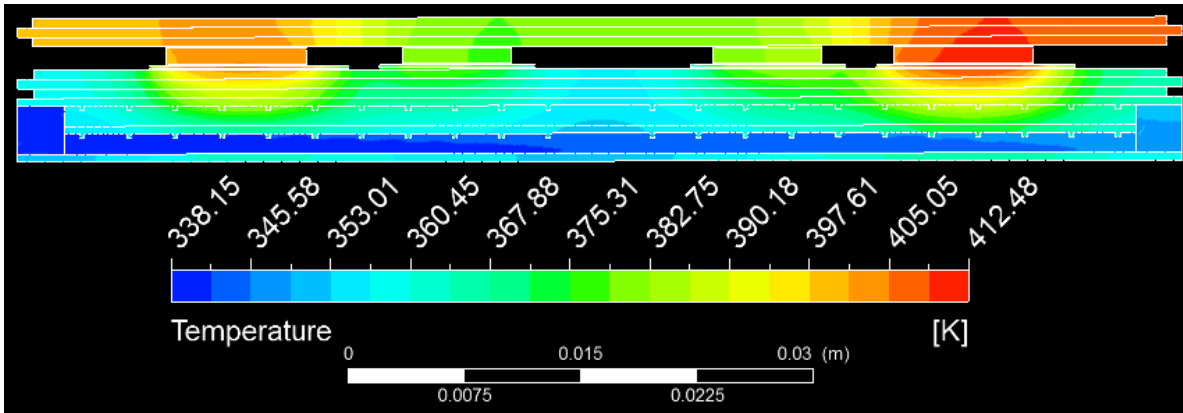


Figure 7.22. Double-sided single channel multi-chip power module packaging model based on optimum 2 layers 1 ribbed wall mini-channel configuration. Flow direction based on overall structure 3.

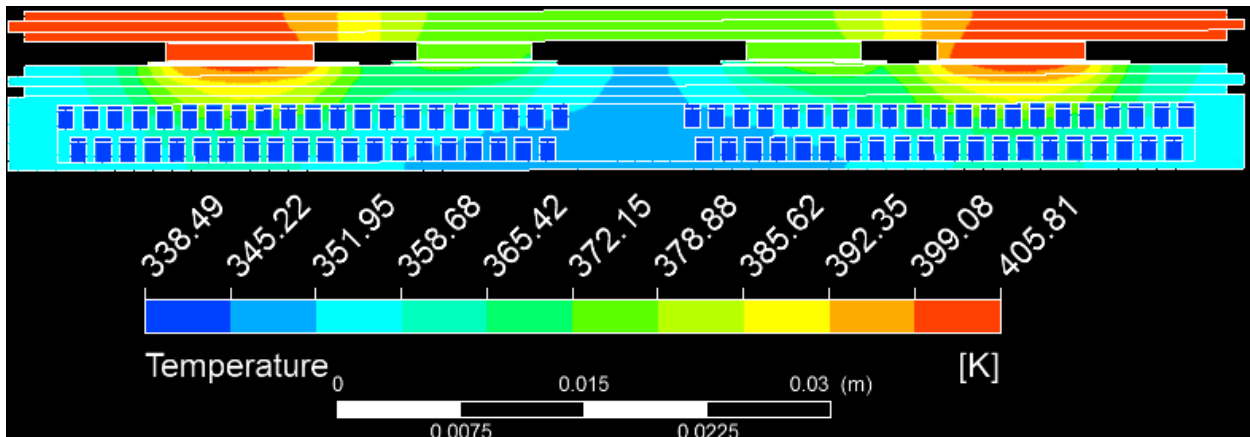


Figure 7.23. Double-sided single channel multi-chip power module packaging model based on optimum 2 layers 1 ribbed wall mini-channel configuration. Flow direction based on overall structure 6.

This optimum model was applied to the double sided single channel multi-chip power module-cooler package model (Figure 7.22 and Figure 7.23) and simulated. The flow distribution and the allowed pressure drop were based on overall heat exchanger structures 3 and 6. Due to the large number of channels, the flow rate through each channel was ~ 1 g/s. The model, shown in Figure 7.22, had 19 1 ribbed wall mini-channels arranged in a 2 layers staggered configuration with 10 parallel channels in the first layer and 9 parallel channels in the second. Separation between the channels in the same layer as well as between the layers was taken to be 0.5 mm. For the model shown in Figure 7.22, the effective heat transfer coefficient at

the bottom surface of the bottom DBA was computed to be $20500 \text{ W/m}^2\text{-K}$ and the pressure drop was estimated to be 4.1 kPa (allowed pressure drop: 10 kPa). The maximum IGBT1 and IGBT2 temperatures were $133.3 \text{ }^\circ\text{C}$ and $139.3 \text{ }^\circ\text{C}$. As there was not much cooling in the region between the two diodes, the effective heat transfer coefficient was lower than that locally under the IGBTs and Diodes. So based on the IGBT temperatures, the effective heat transfer coefficient under the IGBTs was estimated to be equivalent to $24500 \text{ W/m}^2\text{-K}$.

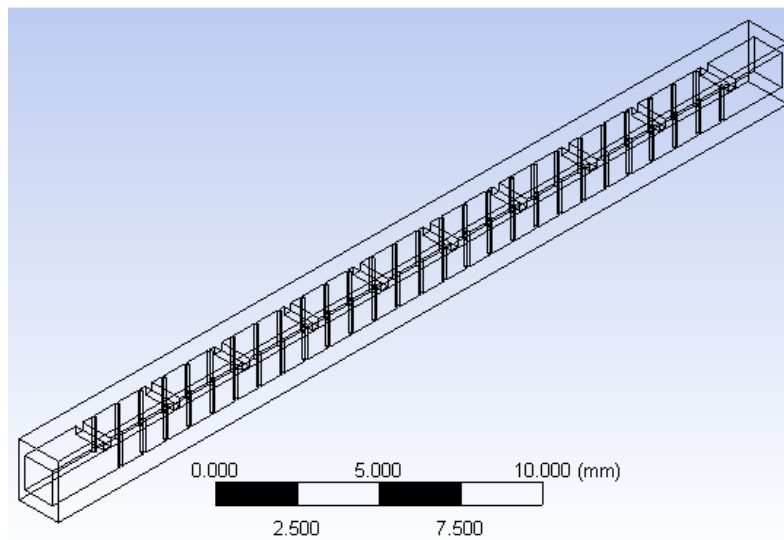


Figure 7.24. Conjugate mini-channel model with 3 ribbed walls.

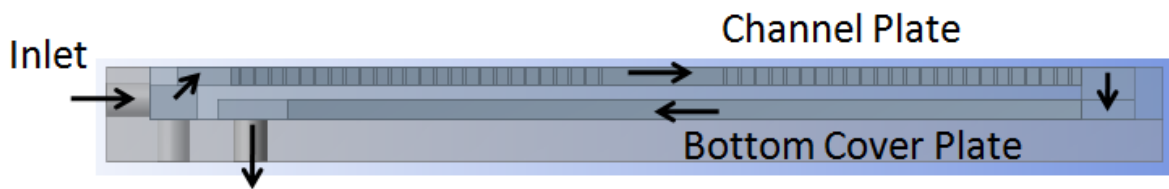
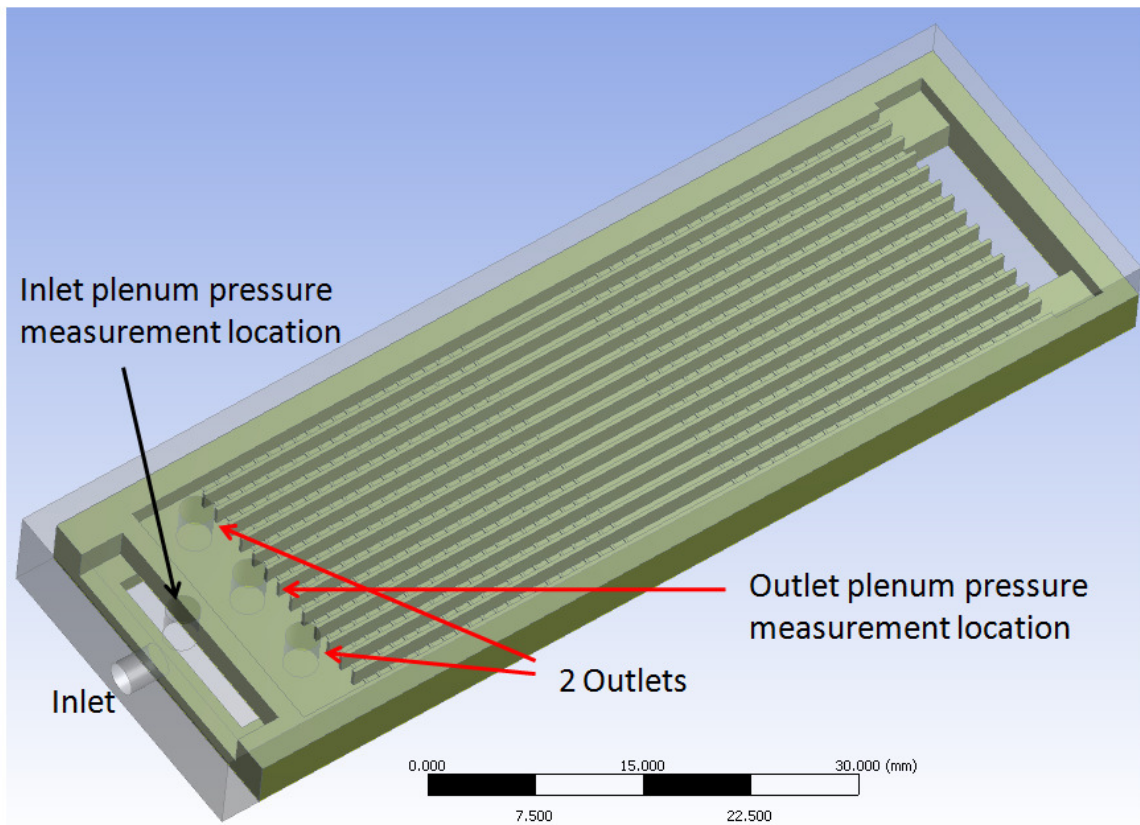
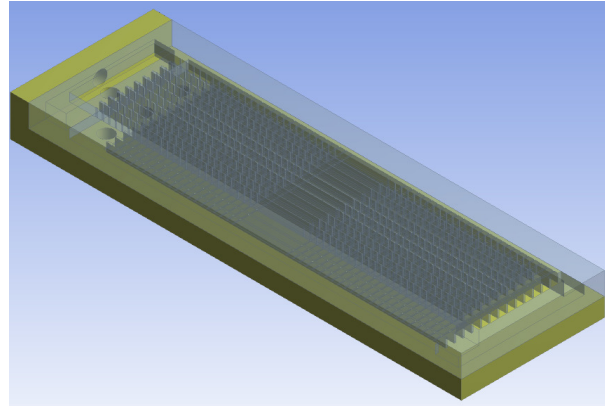
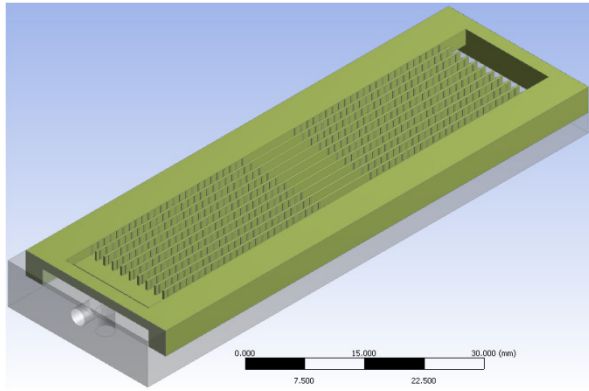
The model, shown in Figure 7.23, had 82 1 ribbed wall mini-channels arranged in a 2 layers staggered configuration with 42 parallel channels in the first layer and 40 parallel channels in the second. Separation between the channels in the same layer as well as between the layers was taken to be 0.5 mm . For the model shown in Figure 7.23, the effective heat transfer coefficient at the bottom surface of the bottom DBA was computed to be $22000 \text{ W/m}^2\text{-K}$ and the pressure drop was estimated to be 1 kPa (allowed pressure drop: 2 kPa). The maximum IGBT1 and IGBT2 temperatures were $131.7 \text{ }^\circ\text{C}$ and $132.7 \text{ }^\circ\text{C}$. Based on the IGBT temperatures, the effective heat transfer coefficient under the IGBTs was estimated to be equivalent to $25500 \text{ W/m}^2\text{-K}$. The channel dimension was $1 \text{ mm} \times 1.5 \text{ mm}$ with 0.3 mm rib height, 0.3 mm rib width

and 3 mm rib spacing. When the channel dimensions was reduced to 1 mm X 1.3 mm, the heat transfer coefficient improved by 12.5% and the pressure drop increased by 65%. But the pressure drop value was still less than the allowed pressure drop.

Similar study was performed for ribs on 2, 3 and 4 walls. It was found out that rib on the bottom surface does not improve the thermal performance and also they significantly increase the pressure drop. It was also found out that rib on 3 walls performed better than ribs on 2 walls. Thus, further optimization was performed on 3 ribbed walls case. *The optimum configuration was found out to have a channel dimension of 1.2 mm X 1.3 mm with 0.3 mm X 0.3 mm ribs (rib spacing 3 mm) on the top surface and 0.1 mm X 0.1 mm ribs (rib spacing 1 mm) on both the side walls and an offset of 0.5 mm between the top surface ribs and side surface ribs.* This configuration provided for a 50% improvement in the heat transfer coefficient with respect to the 1 ribbed-wall case at twice the pressure drop. Figure 7.24 shows a conjugate model of this optimum 3 ribbed wall mini-channel configuration. A double sided single channel power module packaging model was modeled and simulated. An effective heat transfer coefficient of 35000 W/m²-K with pressure drop under allowable limits was achieved using this configuration.

7.5. Ribbed Mini-Channels Based Cooler Prototype

Ribbed mini-channels based coolers showed promising results and a ribbed mini-channel based cooler was fabricated and tested. The cooler model shown in Figure 7.25 was modeled and fabricated. The model consisted of three parts – etched bottom Cu of the bottom DBC, the cooler bulk and a bottom cover plate. Figure 7.26 schematically represents the ribs on the bottom copper of the ribbed DBC. Initially, DBA was supposed to be used. However, due to the unavailability of proper etching solution/solution chamber for Aluminum and reasons presented in the next section, DBC was used instead.



1 Inlet plenum pressure measurement location 2 Outlets and 1 Outlet plenum pressure measurement location

Figure 7.25. Schematic showing the cooler bulk and the bottom cover plate with the arrow heads showing the flow direction.

The active devices were soldered to the top Copper of the DBC and on the other side, ribs were etched. For enhanced heat transfer rates, it was beneficial to have the ribs etched on the bottom Cu of the bottom DBC. The cooler part was fabricated in two parts – ribbed mini-channels part and a bottom cover plate. The ribbed mini-channels part was fabricated from a single Al 6063 block by machining the channels from either faces (top and bottom). This block was then soldered to the bottom cover plate and the etched DBC. The bottom cover plate had five through holes – one for flow inlet, one for inlet plenum pressure, two for flow outlet and one for outlet plenum pressure. The cover plate was soldered to the cooler bulk and then the power module was attached to the cooler part.

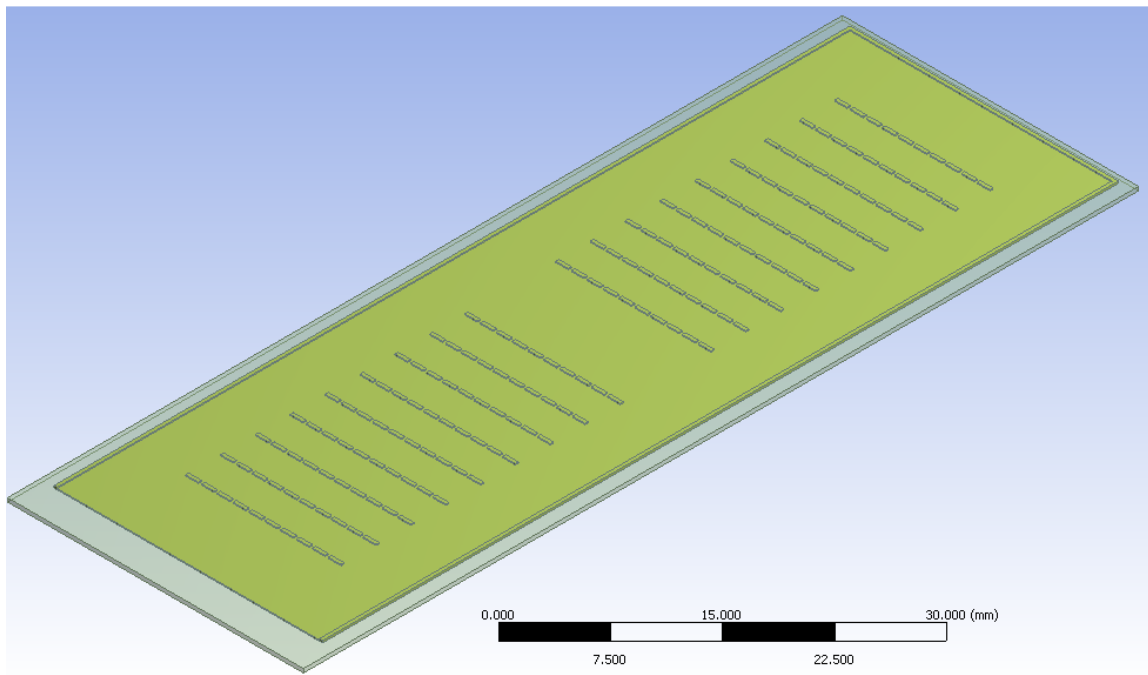
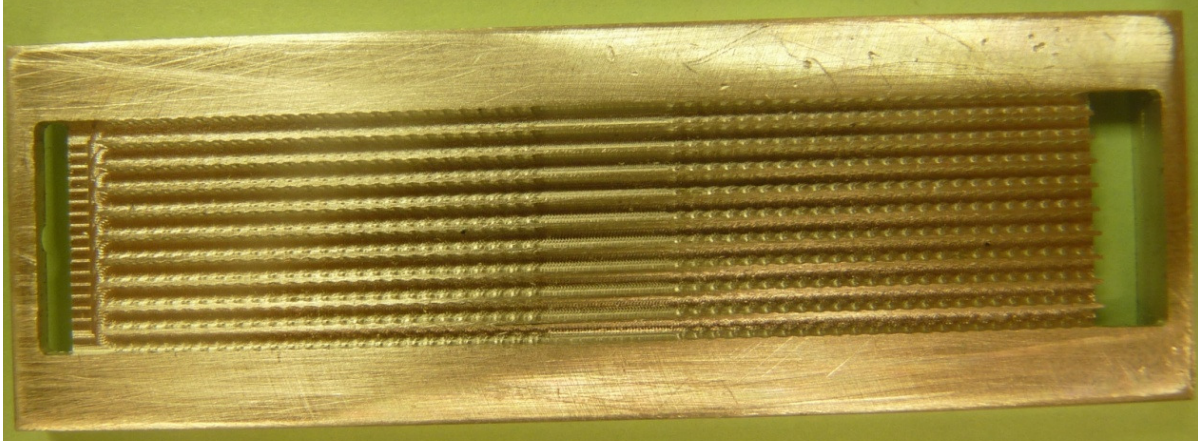
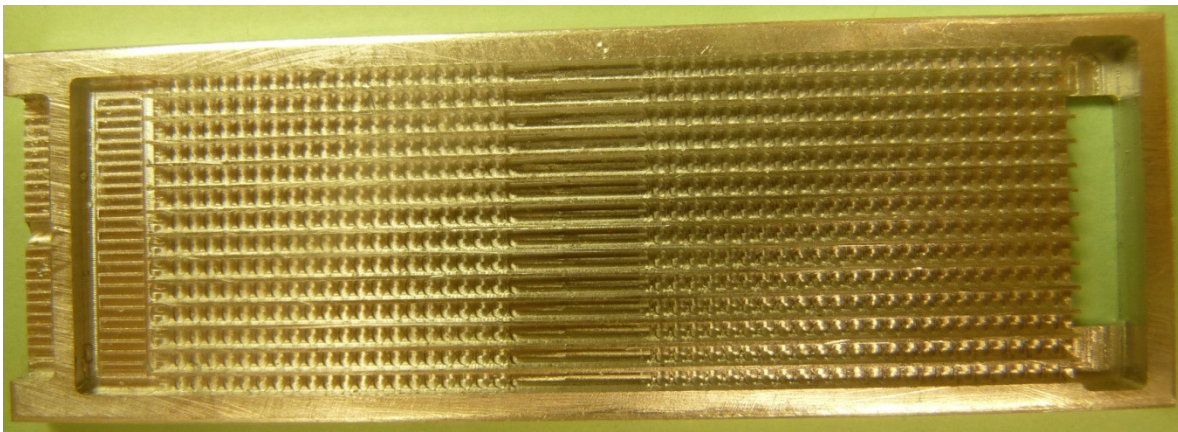


Figure 7.26. Schematic representation of the etched ribs on the bottom copper of the DBC substrate.

Figure 7.27 shows the different views of the cooler bulk and the bottom cover plate that were fabricated. The overall size of the cooler bulk was about 75 mm X 24.8 mm X 4.9 mm. It was a 2 pass ribbed mini-channel based cooler having 10 parallel ribbed mini-channels in the first pass and 14 parallel ribbed mini-channels in the second pass.



(a) Top view of the cooler bulk



(b) Bottom view of the cooler bulk



(c) Bottom cover plate

Figure 7.27. Different views of the cooler bulk and the bottom cover plate.

The first pass had ribs on three faces while in the second pass only one face had the ribs. Also in the first pass, one face of the channels was formed by the etched DBC. So the

corresponding channels machined on the cooler bulk had ribs on the walls separating each adjacent channel. In the first pass, the cross-section of each channel was 1.2 mm X 1.5 mm with 0.1 mm X 0.2 mm ribs having a pitch of 1.1125 mm on the two side faces and 0.1 mm X 0.2 mm ribs on the DBC surface. While in the second pass, the cross-section of each channel was 1.2 mm X 1.5 mm with 0.1 mm X 0.2 mm ribs having a pitch of 1.1125 mm on only one face. This cooler structure was simulated and the effective heat transfer coefficient at the top surface was estimated to be about $2600 \text{ W/m}^2\text{-K}$.

7.6 Etching Ribs/Channels on DBA Substrate and Al 6063 Block

A part of the ribbed mini-channel cooler design required ribs to be etched on the bottom Al/Cu of the DBA/DBC substrate. As an initial step in this regard, two ribbed channels were etched on the DBA substrate. Figure 7.28 summarizes the process flow for etching ribbed channels on the DBA substrate. First the DBA substrate was covered with Kapton-tape and then the ribbed channel pattern was laser-cut on to this Kapton-tape. The final width of the ribs was required to be 0.2 mm, so a margin of 0.2 mm was taken to account for the Kapton burn width due to laser-cut and for etching uncertainty. The Kapton-tape was removed from the regions that were to be etched. The sample was then placed in the pre-heated etching bath for approximately one minute and then removed and cleaned.

Figure 7.29 shows the final etched ribbed channels. The depth of the channels was about 0.1 mm. For the measurement of the rib thickness and groove width measurement, an image digitizing software was used. This software allowed for digitizing the image and helped assign a physical scale to the image. Then key measurement locations can be manually selected/marked and relative distance can be measured by setting a reference location on the image. Figure 7.30 shows the dimensions of the grooves and ribs along 4 different measurement rows. After the

etching process, the average width of the grooves between the ribs was measured to be about 1.2 mm and the average width of the ribs was measured to be about 0.3 mm. Before the laser-cutting and etching process (that is, at the sketching stage), the width of the grooves was taken to be 1.1 mm and that of the ribs to be 0.4 mm.

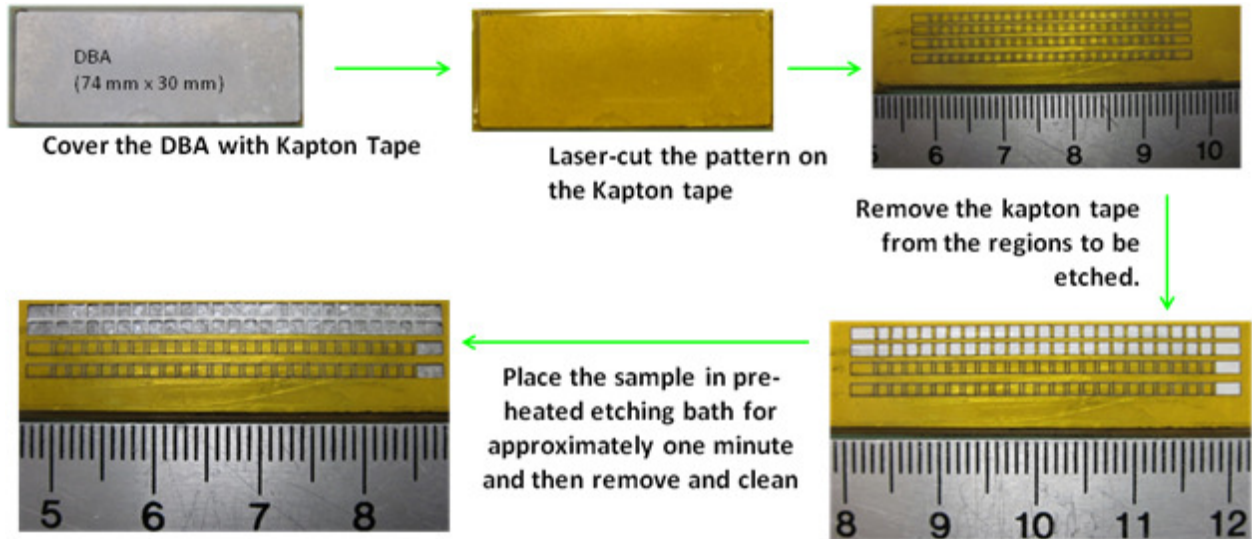


Figure 7.28. Process flow for etching ribbed channels on the DBA substrate.

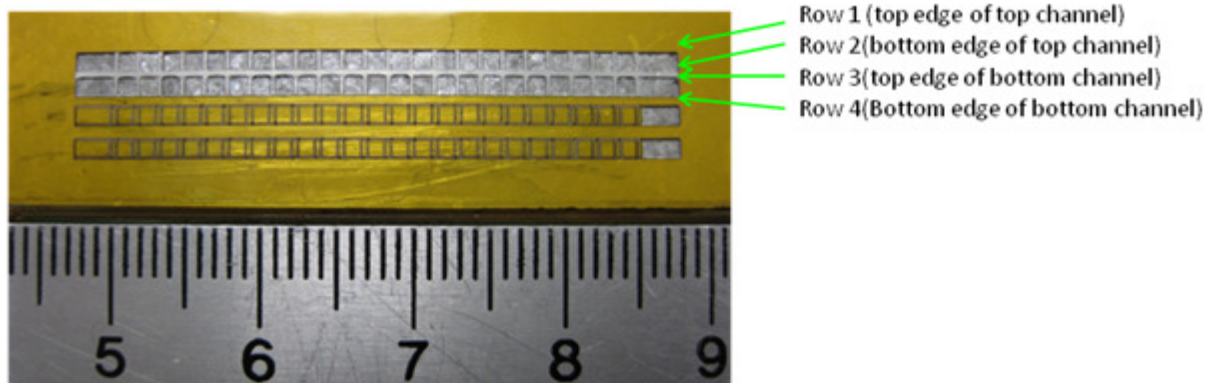


Figure 7.29. Final etched ribbed channels (2) with 4 measurement rows.

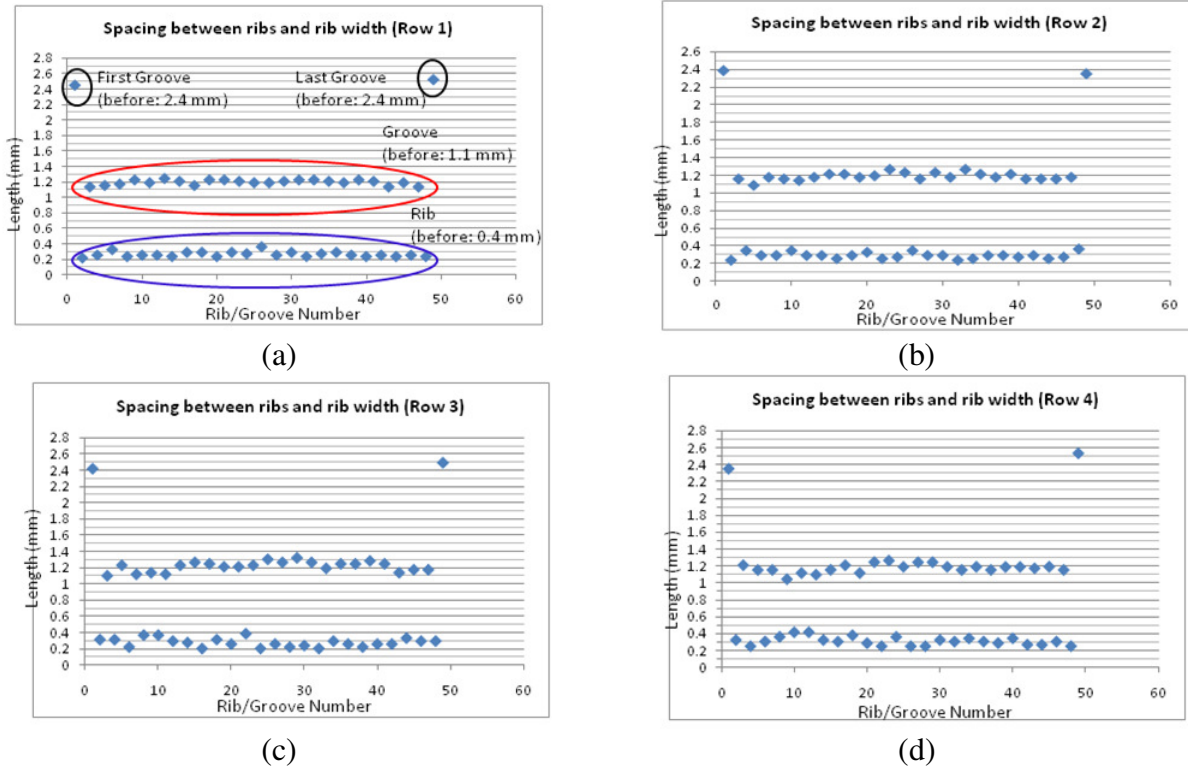


Figure 7.30. Dimensions of the grooves and ribs along four different rows for the two channels after etching.

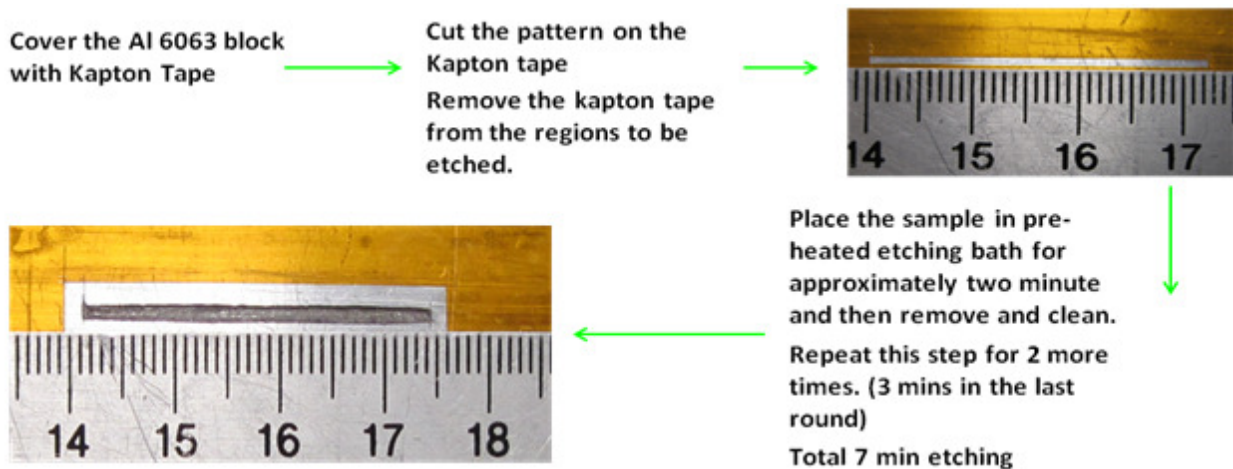


Figure 7.31. Process flow for etching channel on the Al 6063 block.

A similar process was followed for the etching of channel in the Al 6063 block (Figure 7.31). However, the sample was placed for a longer time in the etching bath (~ 7 min) as we required deeper cut. The sample was removed from the bath after every 2 minutes to remove any reaction residue layer. Figure 7.32 shows before etching and after etching view of the channel. A

similar digital image analysis was followed to measure the dimensions of the initial pattern and final etched channel (Figure 7.33).

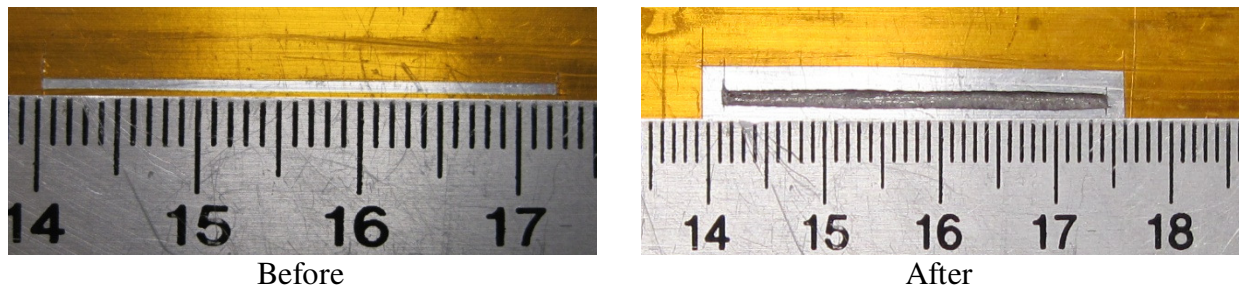


Figure 7.32. Top view of the channel before and after etching.

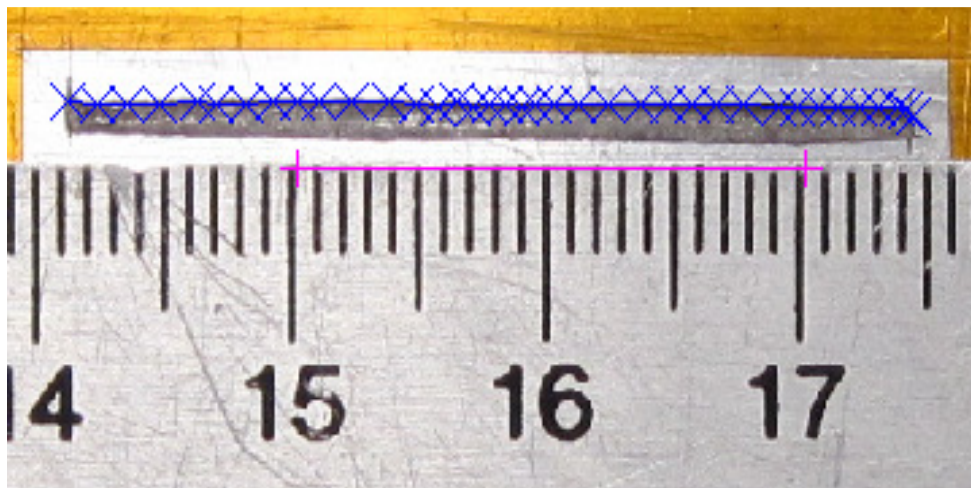


Figure 7.33. Digitized image with pink line showing the digital scale and blue cross-hairs as the curve points used for channel dimension measurement.

The dimensions of the initial pattern and final etched channel are presented in Figure 7.34. For measurement purpose, the bottom-left corner of the channel was considered as the reference location. The average width of the channel before etching was 0.77 mm with a variation of thickness of about 0.15 mm and that after etching was about 1.3 mm with a variation of thickness of about 0.45 mm. From Figure 7.34, it can also be seen that the channel significantly widens from both the edges. Also the length of the channel increases slightly. However, the depth of the channel is about 0.5 mm (~ 40% of the channel width) that is, the channel was shallow. This was caused due to the isotropic nature of the wet etching process. This

process was modified to try and etch deep channels but these attempts were unsuccessful for Aluminum because the etching solution used was more suitable to etching copper than Aluminum. A similar process was followed for etching DBC substrates and copper block.

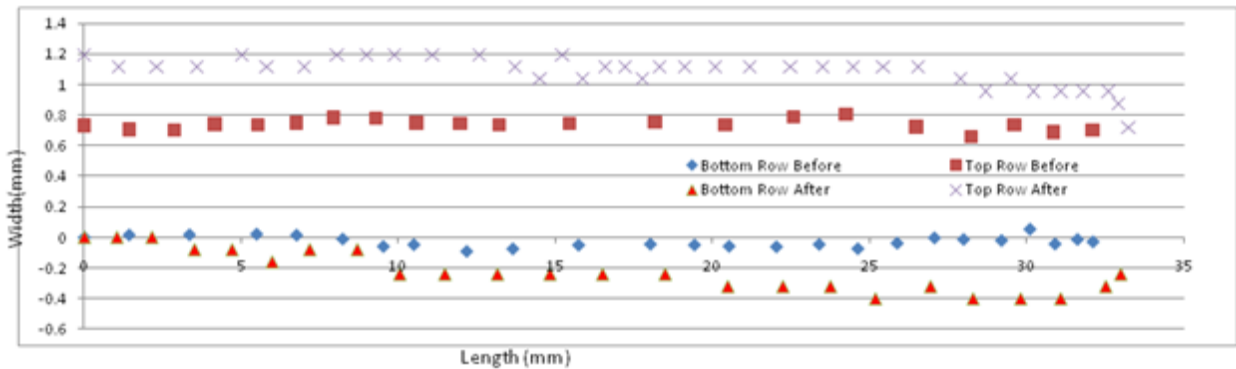


Figure 7.34. Dimensions of the channel before and after etching. The bottom left corner of the channel was used as the reference (0,0).

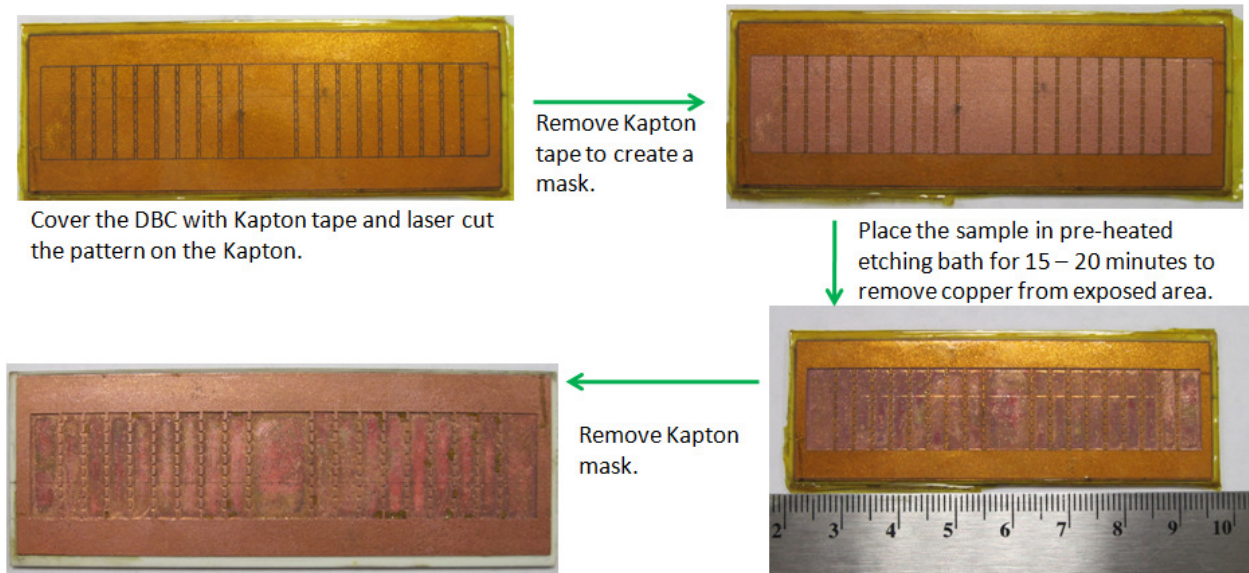


Figure 7.35. Process flow for etching ribbed channels on the DBC substrate.

Figure 7.35 shows the process flow for etching ribbed channels on the DBC substrate. First the DBC substrate was covered with Kapton-tape and then the ribbed channel pattern was laser-cut on to this Kapton-tape. The final width of the ribs was required to be 0.2 mm, so a margin of 0.2 mm was taken to account for the Kapton burn width due to laser-cut and for

etching uncertainty. The Kapton-tape was then removed from the regions that were to be etched. The sample was then placed in the pre-heated etching bath for approximately 15 - 20 minutes and then removed and cleaned. Figure 7.35 also shows the final ribbed back-side of the etched DBC. It can be clearly seen that the etching solution was more compatible to etching copper and that the etched cuts were much sharper than that for Aluminum. Similar process was followed for etching mini-channels with thin walls (~0.2 mm – 0.3 mm) between adjacent channels on copper blocks to generate sample to practice soldering of thin walls to ribbed back-side of DBC/DBA.

7.7. Test Assembly and Cooler Performance

Once sufficient practice of etching ribs was achieved and confidence gained, the back-side of a DBC substrate was etched to form small ribs. On the other side, active devices were soldered and electrical connections were made to form a power module test sample. This was then soldered to the ribbed-mini-channel cooler and cover plate assembly. Figure 7.36 shows the ribbed mini-channel cooler and cover plate assembly. Figure 7.37 shows the assembled power module – cooler package sample that was tested for its thermal performance evaluation. The overall height of this package was found out to be less than 8.5 mm. It is to be noted here that the bottom cover plate used here has a thickness of 3.175 mm. In the actual practice, this cover plate will around 1 mm as in the case of impingement based test sample. Thus, the total package thickness of the cooler will be less than 6.5 mm (~ 25% of conventional package thickness).

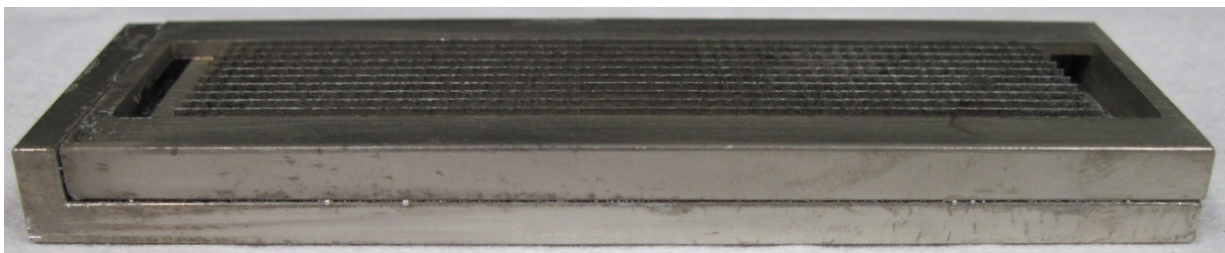


Figure 7.36. Ribbed mini-channel cooler and cover plate assembly.

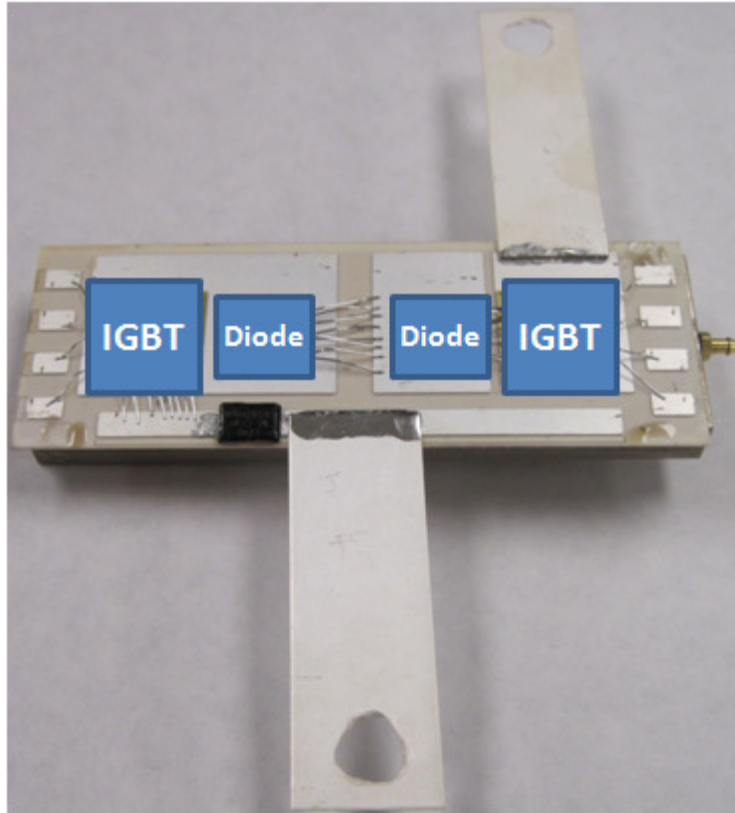
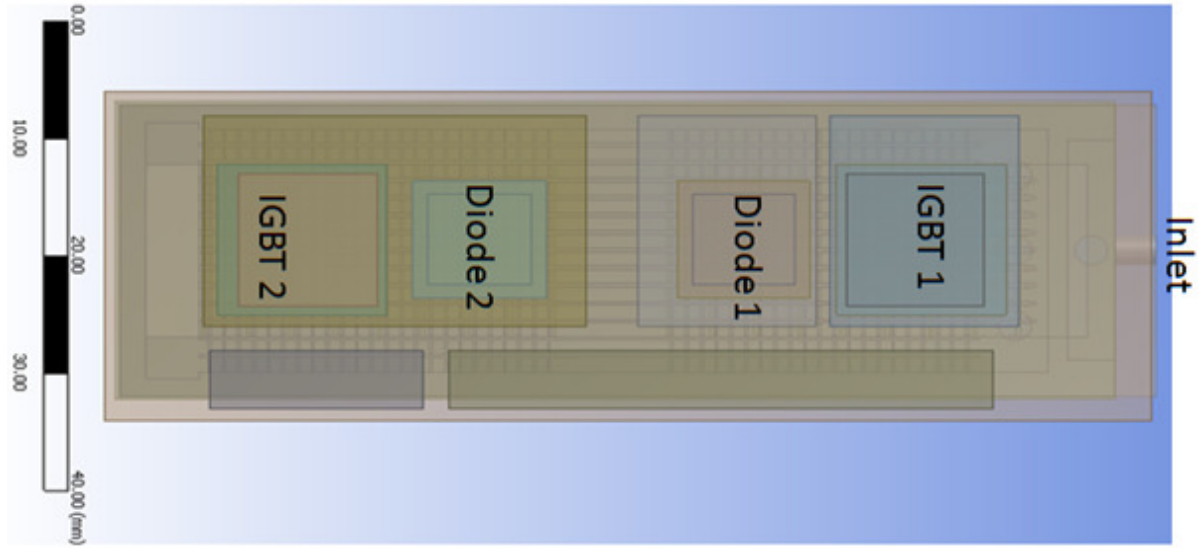
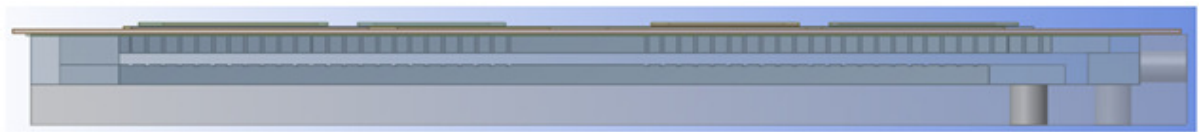


Figure 7.37. Assembled power module – ribbed mini-channel cooler test sample.

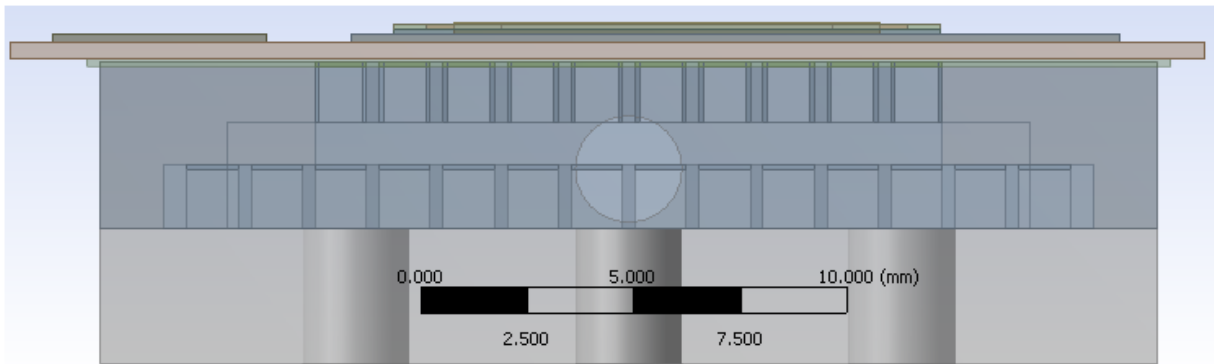
Figure 7.38 shows different views of the simulation model for the packaged power module configuration. In this model, solder layer between the power module and the cooler as well as the solder layer between the cooler and the bottom cover plate were not modeled. The $k-\epsilon$ turbulence model was used for the fluid flow simulation. Moreover, the meshing scheme used was kept similar to the medium meshing scheme used for the best angled impingement model. Table 7.5 summarizes the simulation predictions and compares it with the experimental data. It can clearly be seen that the *simulations were able to closely predict* the experimental conditions and thus, *validated most of the earlier conjugate packaging module simulations as well.*



(a) Top view



(b) Side view



(c) View from the inlet

Figure 7.38. Different view of the simulation model corresponding to the ribbed mini-channel based heat exchanger test sample.

Table 7.5. Comparison of the thermal resistances predicted by simulations with those obtained experimentally.

Case	R_{th} for IGBT1 (K/W)	R_{th} for IGBT2 (K/W)
Experiment	0.474	0.5
Simulation	0.48	0.514

For the thermal testing of this cooler sample, experiments were performed at about half the allowed flow rate (~ 9 g/s) and at about one third of the full (~ 270 W). Water at 23 °C was used as the coolant. Moreover, the substrate used was DBC with Alumina as the ceramic.

Alumina has a thermal conductivity of 24 W/m-K which is about a fifth of that for AlN present in DBA. The presence on Alumina significantly increases the thermal resistance of the substrate in comparison to DBA. This increase is usually of the order of 0.1 – 0.2 K/W depending upon the ceramic layer thickness. For the present case sample, this increase was about 0.11 K/W owing to the ~0.35 mm thick ceramic layer.

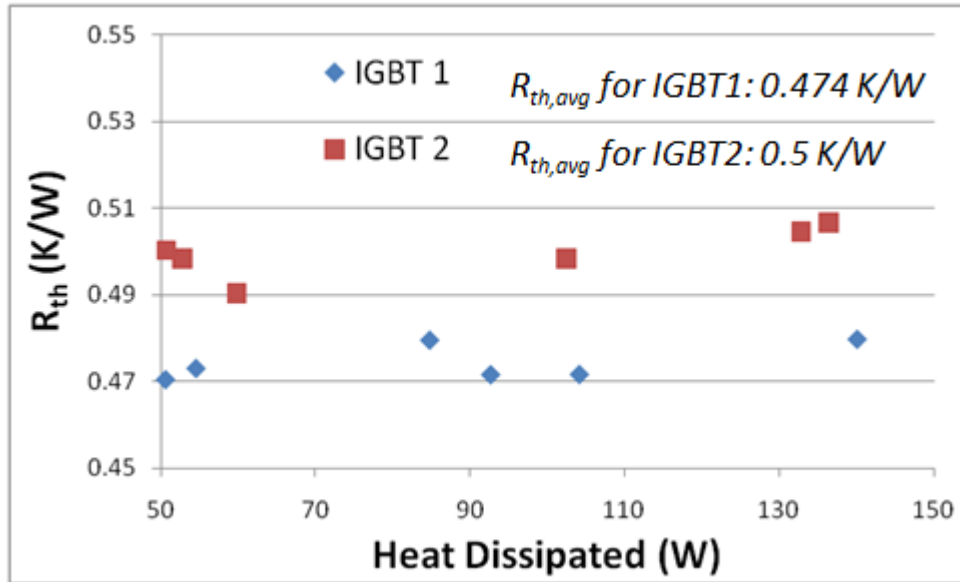


Figure 7.39. Thermal resistances corresponding to the IGBTs for various heat dissipation rates through each device.

The experiments were conducted at a various total thermal loads ranging from 100 W to 380 W and for each set the heat dissipated by Diodes was kept around one quarter of that dissipated by the IGBTs. Figure 7.39 shows the experimentally recorded thermal resistance values for both the IGBTs for different power dissipation levels. The cooler performance was as expected and the average thermal resistances for IGBT1 and IGBT2 were reported to be 0.474 K/W and 0.514 K/W respectively. The differences in the maximum IGBT temperatures was due to the fact that the active devices were cooled in a sequential manner and that for one pair, Diode was closer to the IGBT than the other pair and thus, resulted in higher temperature due to thermal coupling effect.

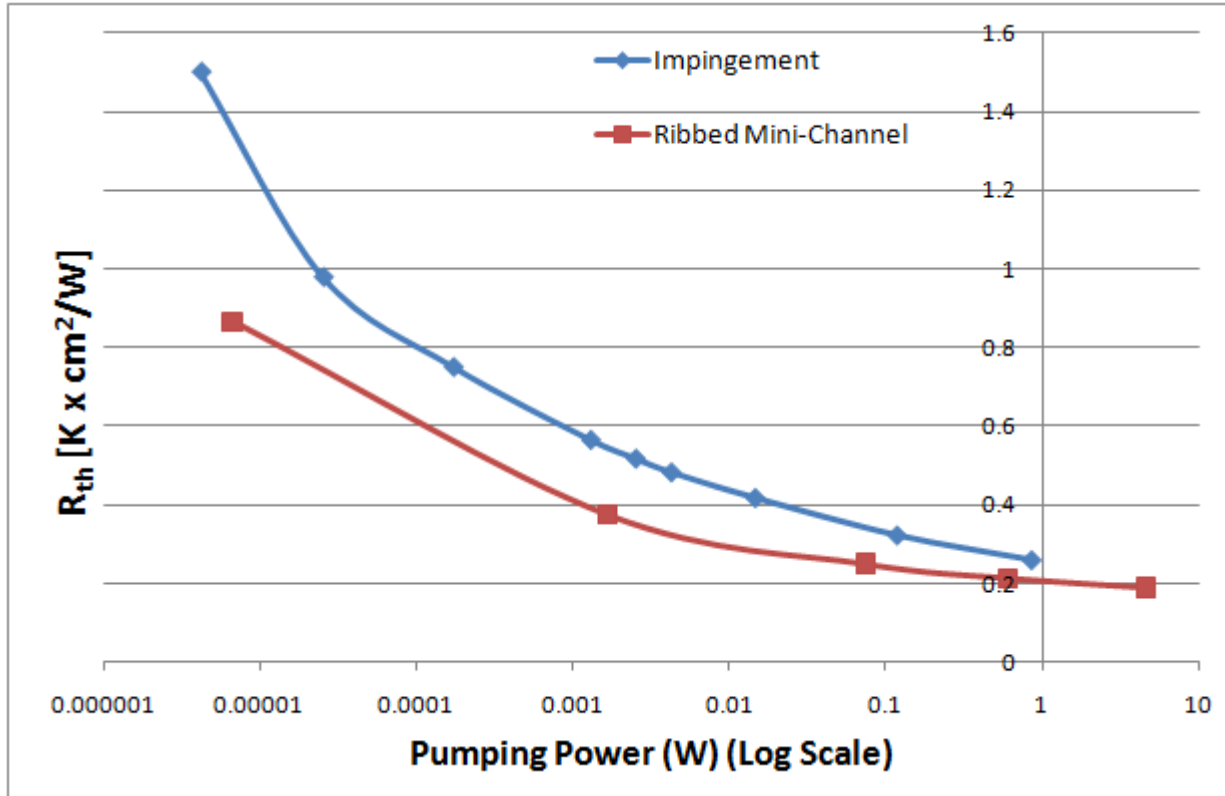


Figure 7.40. Variation of the thermal resistance with pumping power for the present ribbed mini-channel based configuration with that of the impingement based configuration studied earlier.

The performance of this cooler was also compared to the impingement based heat exchanger sample tested earlier. Figure 7.40 shows a comparison of the thermal performance of the ribbed mini-channel cooler with that of the impingement based cooler. It can be clearly seen that it performs much better than the impingement based cooler in the allowed pumping power region (~ 0.1 W).

7.8. Double Sided Cooling

Previous sections of this chapter show that ribbed mini-channel based coolers perform much better than the impingement based designs studied earlier and with the optimized ribbed mini-channel cooler simulations predict a maximum IGBT 1 temperature of about $122^\circ C$ (that is, an effective heat transfer coefficient of ~ 35000 W/m^2-K). Although, the performance of this optimized ribbed mini-channel cooler might be good enough to barely meet the design

constraints, it really does not give any margin or factor of safety. In the event of such stiff targets, using both the sides of each die (that is, top and bottom) to improve the cooling performance becomes an obvious solution. This requires some changes in the electrical connections of the devices, as wire-bonding of devices becomes infeasible, but it doubles the effective area of the heat dissipation path, theoretically allowing for a two-fold reduction in thermal resistance.

Figure 7.41 shows a comparison of the maximum IGBT temperatures for single-sided cooling configuration with that for double-sided cooling configuration for similar effective heat transfers coefficients at the exposed faces. Although it requires double the pumping power to obtain similar heat transfer coefficients on either faces as compared to that required for a single face, the effective single-sided heat transfer coefficient could be much more than double. For example, 25000 W/m²-K of heat transfer coefficient on either side of the power module is comparable to having 95000 W/m²-K on one side of the power module.

Based on this observation, a double-sided (planar) power module with double-sided cooling configuration shown in Figure 7.42 was modeled and simulated. It was observed that for such configuration the effective heat transfer coefficient of 190°0 W/m²-K can be easily maintained on either side using simple mini-channel configuration. This situation is equivalent to having 65000 W/m²-K on one side (see Figure 7.41). Moreover, few of the ribbed mini-channel based configurations (such as Figure 7.22 and Figure 7.23) can be easily extended to double-sided cooling to attain nearly 95000 W/m²-K of equivalent single sided cooling. Also, if properly optimized, equivalent single-sided heat transfer coefficient of 140000 W/m²-K (~30000 W/m²-K) can also be attained using the current limitations.

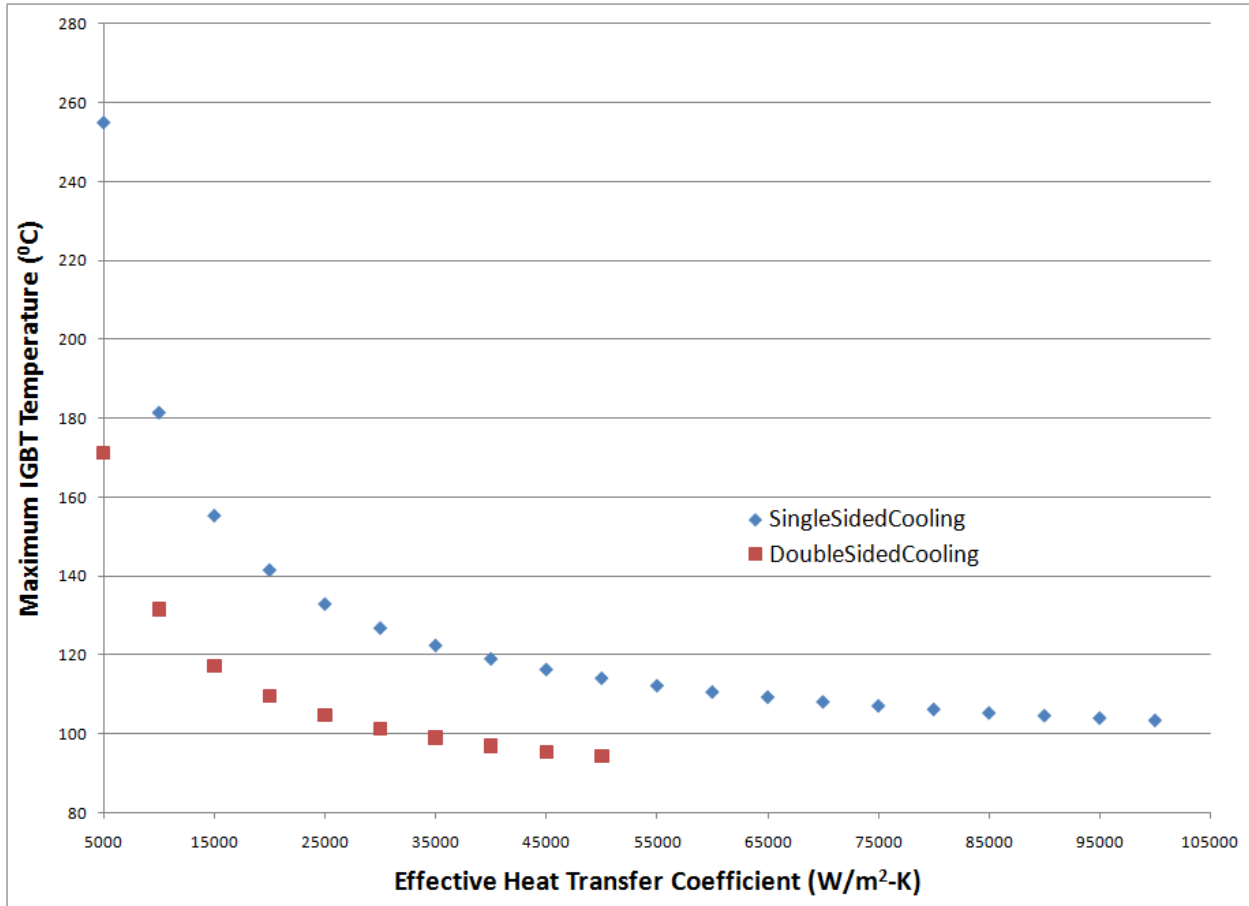


Figure 7.41. Variation of IGBT temperature as a function of effective heat transfer coefficient under the IGBTs for single-sided and double-sided cooling configurations.

Pressure Drop = 1.45 kPa
 Inlet: 170 g/s LLC @ 65 C

IGBT1 Temp: 108.7 C
 IGBT2 Temp: 109.6 C

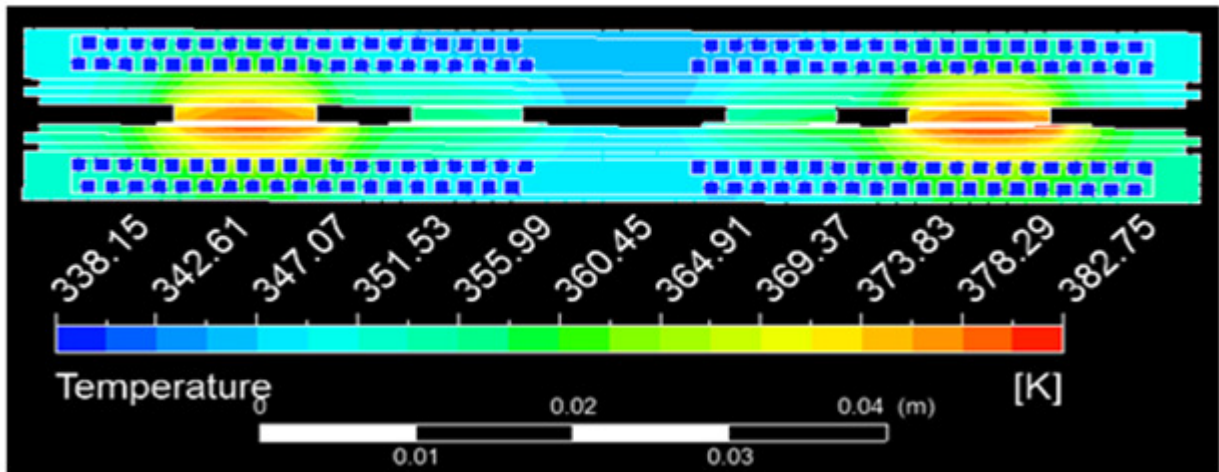


Figure 7.42. Mini-channel based double-sided cooler configuration.

7.9. Summary

Although the cooling performance of the high performance impingement cooler was as expected and significantly higher than its competing counterparts, it was not sufficient to meet all the design constraints. An alternative to this was to use mini-channel based coolers which are based on using convection as well as conduction heat transfer. By conduction, meaning the heat spreading through the cooler body and by convection, meaning the high average wall heat transfer rates. The average heat transfer coefficient was much higher than that for impingement cooling. However, the peak values were much less than that for impingement. But because of the conduction effect (heat spreading) a high effective heat transfer coefficient at a lower pressure drop was observed for mini-channels configuration.

In light of these trends, configurations based on combined impingement and mini-channel configurations were studied. In addition to the high effective heat transfer rate obtained for coolers based on such configurations, a high pressure drop (~80 kPa) was also obtained. Efforts were made to reduce this pressure drop. The pressure drop was successfully reduced to ~53 kPa with a similar heat transfer performance. Any further reduction in pressure drop caused a significant reduction in heat transfer performance.

As an alternative to these concepts, ribbed mini-channels configurations were studied. Promising results were obtained for these configurations. It was observed that a very high average heat transfer coefficient can be maintained at the target surface at much reduced pressure drop. This scheme was further optimized. *The best performing single-side cooler configuration was in fact based on ribbed mini-channel configuration.* This model showed to have an effective heat transfer coefficient of 35000 W/m²-K.

In addition to single-sided cooling configurations, double-sided cooling configurations were also studied. It was found out that having X amount of heat transfer coefficient on either side of the double-sided (planar) power module resulted in much lower maximum IGBT temperatures than that with $2X$ amount of heat transfer coefficient on one side of the double-sided (planar) power module.

CHAPTER 8: PHASE CHANGE MATERIAL (PCM) BASED AND ALTERNATE DESIGNS

In addition to the impingement cooling configurations presented in the earlier chapters, options such as tapered jets, phase change material based cooling and combined impingement and mini-channels were also explored as possible cooling schemes for the warranted application. This chapter gives a detailed description of these alternate cooling configurations.

8.1. Phase Change Materials (PCM) as Heat Spreader Option

In addition to the impingement based conjugate heat transfer simulations, phase change materials were also explored as possible heat spreading options. Phase change materials (PCMs), also referred to as latent heat storage units are materials that are capable of storing as well as dissipating large amount of energy by changing their phase from solid to liquid or liquid to solid, respectively. When the material is undergoing change of phase, it can store-up a lot of energy while maintaining its temperature. This property of phase change at constant temperature was believed to be effective for our present case. For that reason, the heat exchanger sample 2 (Figure 5.23) was modified to incorporate the PCM testing as well. Figure 8.1 shows a schematic of the test section that was fabricated and tested for simulation validation and also tested for its performance under concentrated heat sources [74, 75]. The flow enters the impingement based cooler from one side and impinges onto the foot print of one of the heat sources and is then collected into a plenum and then re-impinges on the PCM plate under the second heat source. The PCM is held between the PCM plate and the target plate. The heat is conducted to the target plate from the heaters and accounts for some spreading. The heat is transmitted into the PCM and is then dissipated by the impinging jets cooling the PCM plate. Figure 8.2 shows a detailed schematic of the PCM plate that was used. Readily available paraffin wax having a melting point

of 130 F (~55 °C) was used as the PCM and was placed inside the cavity in the PCM plate. The target plate, the cover plate, the PCM plate and the jet plate were attached in the desired orientation by means of a thermal adhesive (thermal conductivity: 1.8 W/m-K).

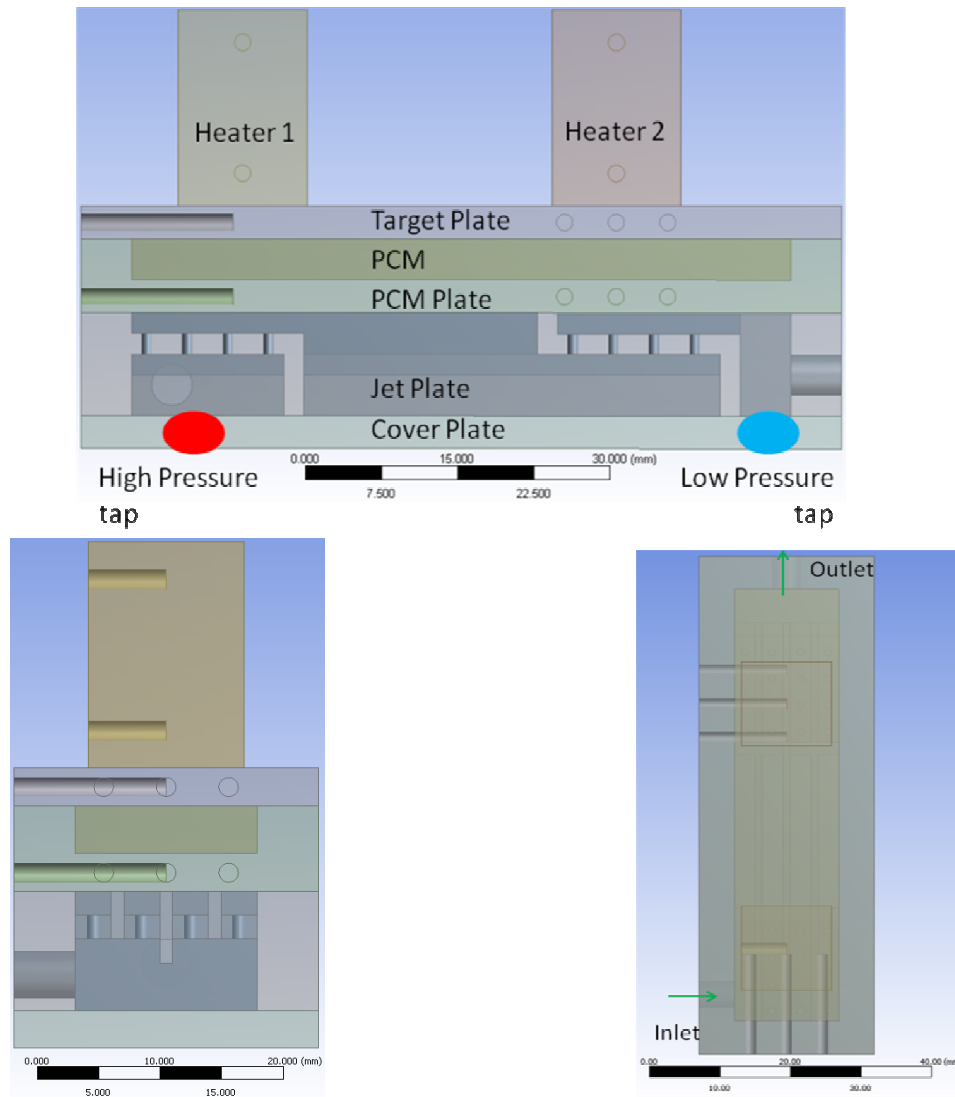


Figure 8.1. Different views of the simulation model corresponding to the test section of the thermal test bed. Red and Blue dots represent the location of high and low pressure taps respectively

Two pressure taps were drilled on the cover plate for pressure drop measurements and six cylindrical holes were drilled into the target plate as well as on the PCM plate for temperature measurements. The cover plate and the target plate were fabricated from Al 6061 while the jet plate and the PCM plate were fabricated from Al 6063. Two different sets of experiments were

performed – one with no PCM as well as no PCM plate and the other one with paraffin wax as the PCM. The case with no PCM, presented in Chapter 5, was used as a baseline case and was also used for simulation validation.

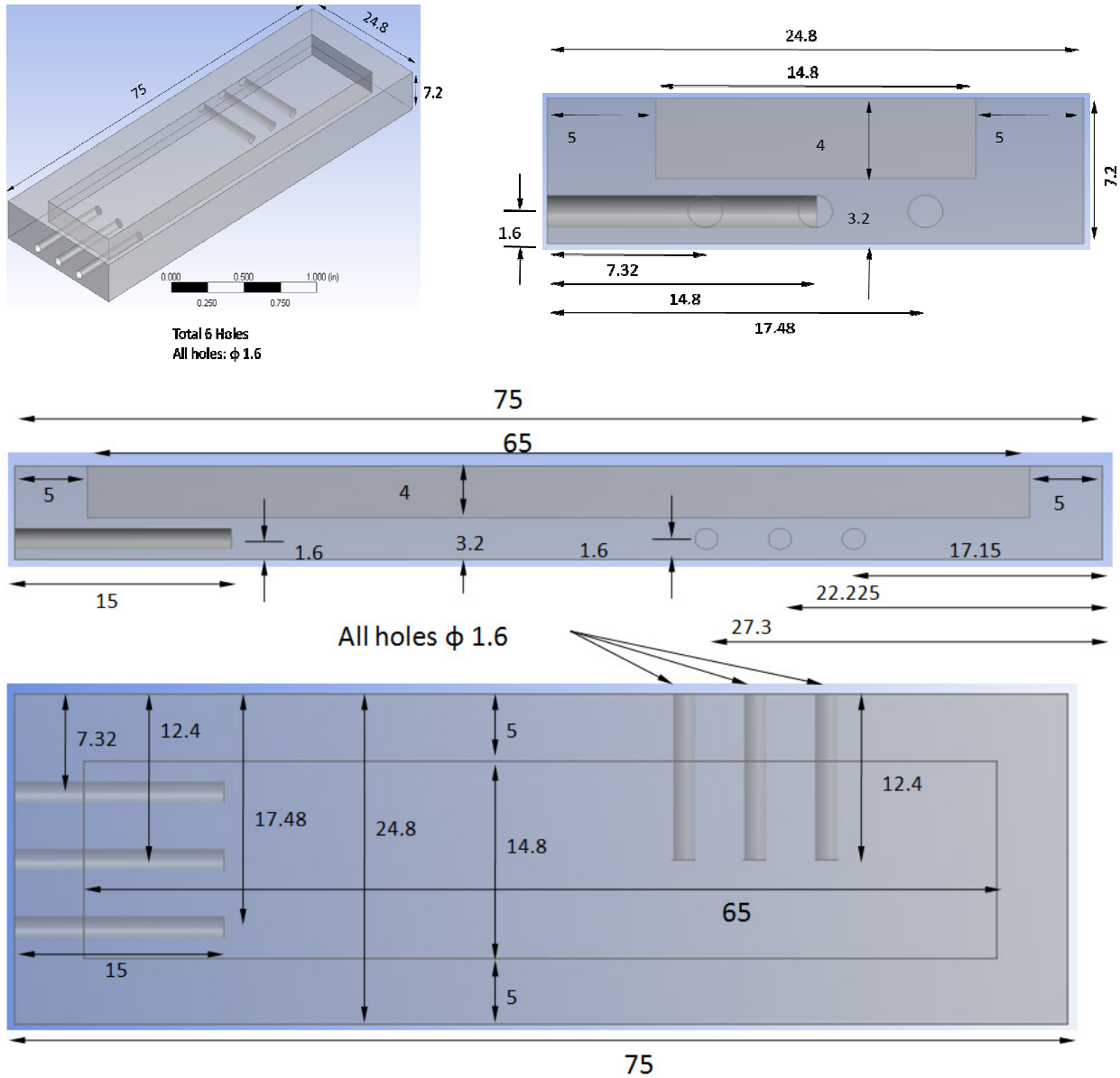


Figure 8.2. Different views of the PCM plate. The rectangular cavity will be filled with paraffin wax having a melting point of 130 F. The cylindrical holes are for temperature measurements. All Dimensions in mm.

ANSYS-CFX as well as ANSYS-Fluent, commercial computational fluid dynamics (CFD) codes were used to study the flow and heat transfer behavior in the proposed

impingement-PCM based heat exchanger models. It was observed that both the commercial codes predicted similar results for no PCM case. However, for the PCM case, only Fluent was used and CFX was not used as it was much easier in Fluent to set-up the problem. As presented in Chapter 5, CFX mesh method with appropriate mesh controls was used to mesh the models and it was ensured that the y^+ is always less than 1 for proper estimation of the flow and heat transfer behavior. Also, a fine mesh was used around all the sharp corners and normal to all the boundary surfaces, except the inlet and the outlet faces.

The baseline case of *No-PCM* has been discussed in detail in Chapter 5. It was observed that a good prediction of the pressure drop and temperature at key locations was obtained using the $k-\epsilon$ model. Also, medium mesh showed promising results with acceptable error percentages and was used a standard mesh scheme for future simulations.

A. *Low Power with PCM*

For the PCM case as well two sets of experiments were performed - one with low power (111 W, 115.21 V, 0.968 A) and the other one with slightly higher power (195 W, 153.5 V, 1.268 A). In the low power experiments, the flux through Heater leg 1 and Heater leg 2 were recorded to be 31.83 W/cm^2 and 30.92 W/cm^2 respectively and water at $21 \text{ }^\circ\text{C}$ with an average flow rate of 0.83 L/min (mass flow rate = 13.79 g/s) was used as the coolant. Simulations for the low power case with PCM were performed using these conditions.

Figure 8.3 shows the simulation model used. All the yellow cross-hairs represent the temperature and pressure measurement locations corresponding to the experimental set-up. The HP and LP locations were the high pressure and low pressure probing locations respectively. The difference between these two pressures was compared with the experimental data. In each experiment, the difference between the pressure at HP and the pressure at LP (that is, HP-LP)

was recorded as the pressure drop. The locations $a - p$ are all the temperature probing locations. The temperatures at locations $a-b$ and $f-g$ were used to measure the heat flux from Heater leg 2 and Heater leg 1, respectively. This measured flux was then used as a boundary condition for the simulations. Also, for all the simulation models, thermal adhesive layer was not modeled as it was ~ 50 microns.

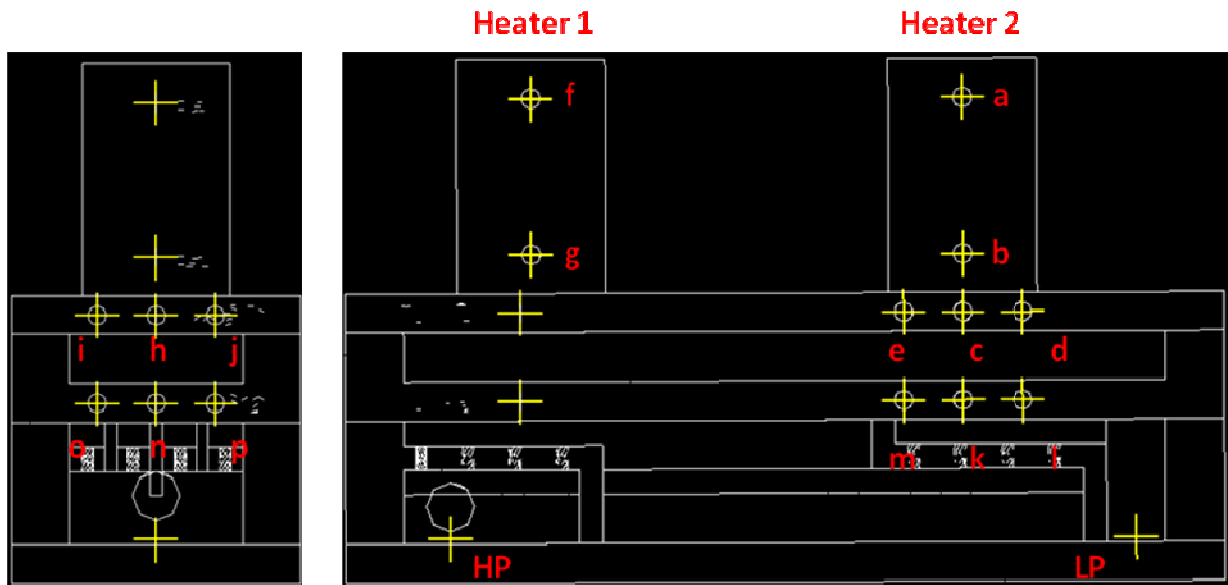


Figure 8.3. Simulation model of PCM based heat exchanger for comparison with experimental data. Yellow cross-hairs represent the temperature and pressure measurement locations. (HP: High Pressure) (LP: Low Pressure).

For these simulations, $k-\epsilon$ model with medium mesh characterized in the earlier section was used. Since the mass flow rate was maintained at the same value, the pressure drop predictions were more or less consistent with the earlier case of no PCM. However, due to additional thermal resistance from the PCM and PCM plate, the heat sources and target plate temperatures were higher than the no PCM case. Figure 8.4 compares the temperature at various locations for the low power experiment. From Figure 8.4, it can be see that the PCM plate temperature predictions by the medium mesh $k-\epsilon$ models were within 8% of the experimental data. However, the target plate temperature predictions were mostly above 10% of the

experimental data. This can be due to insufficient modeling knowledge at the PCM-solid wall interface or it could be due to lack of proper contact between the PCM and the walls of the target plate.

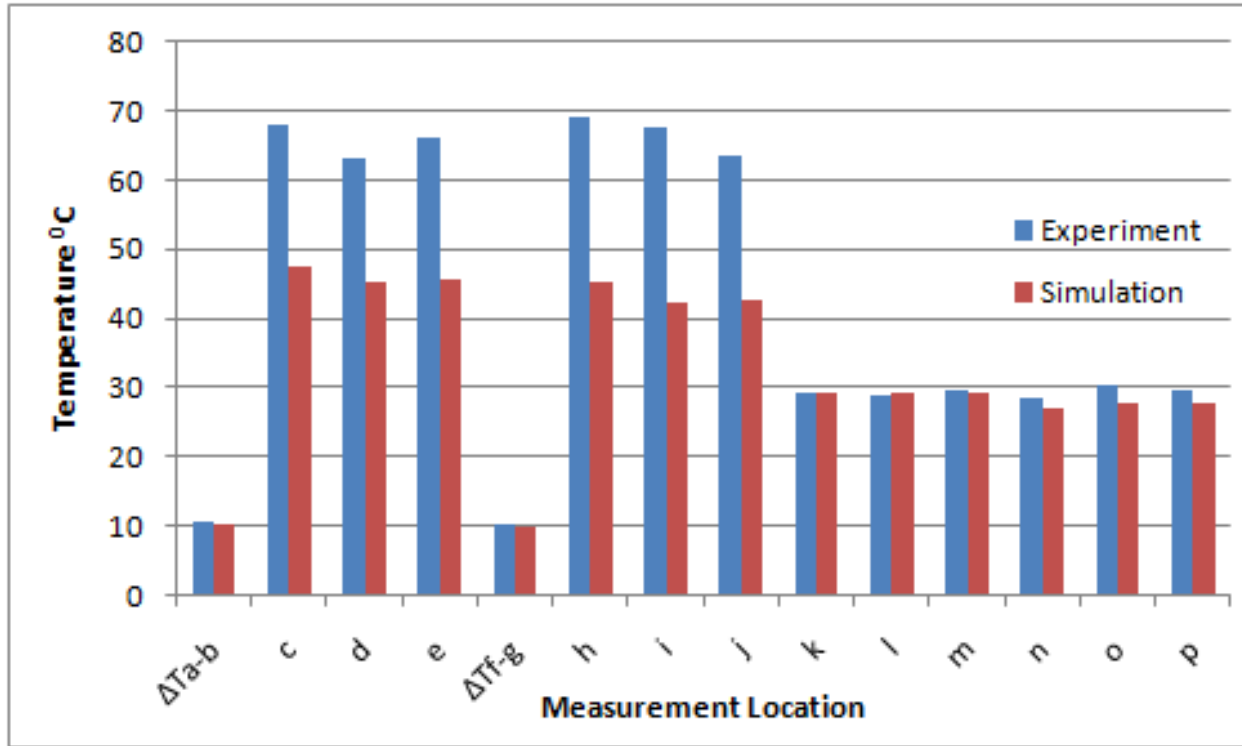


Figure 8.4. Temperature measurement at different measurement locations indicated by Figure 8.3 for low power experiment with PCM and its comparison with the simulation predictions (k- ϵ).

B. Medium Power with PCM

In the medium power experiments, the flux through Heater leg 1 and Heater leg 2 were recorded to be 51.54 W/cm^2 and 51.54 W/cm^2 respectively and water at $21 \text{ }^\circ\text{C}$ with an average flow rate of 0.82 L/min (mass flow rate = 13.63 g/s) was used as the coolant. Simulations for the medium power case with PCM were performed using these conditions. For these simulations as well, k- ϵ model with medium mesh characterized in the earlier section was used. Since the mass flow rate was maintained at the same value, the pressure drop predictions were more or less consistent with the earlier case of no PCM. However, due to additional thermal resistance from the PCM and PCM plate, the heat sources and target plate temperatures were higher than the no

PCM case. Figure 11 compares the temperature at various locations for the low power experiment. From Figure 11, it can be seen that the PCM plate temperature predictions by the medium mesh $k-\epsilon$ models were again mostly within 10% of the experimental data. However, the target plate temperature predictions were much higher than the experimental data. Clearly, a much better modeling is required at the PCM-solid wall interface to capture the thermal contact resistance at the interface. Moreover, a cause of this discrepancy could be lack of proper contact between the PCM and the walls surrounding the PCM.

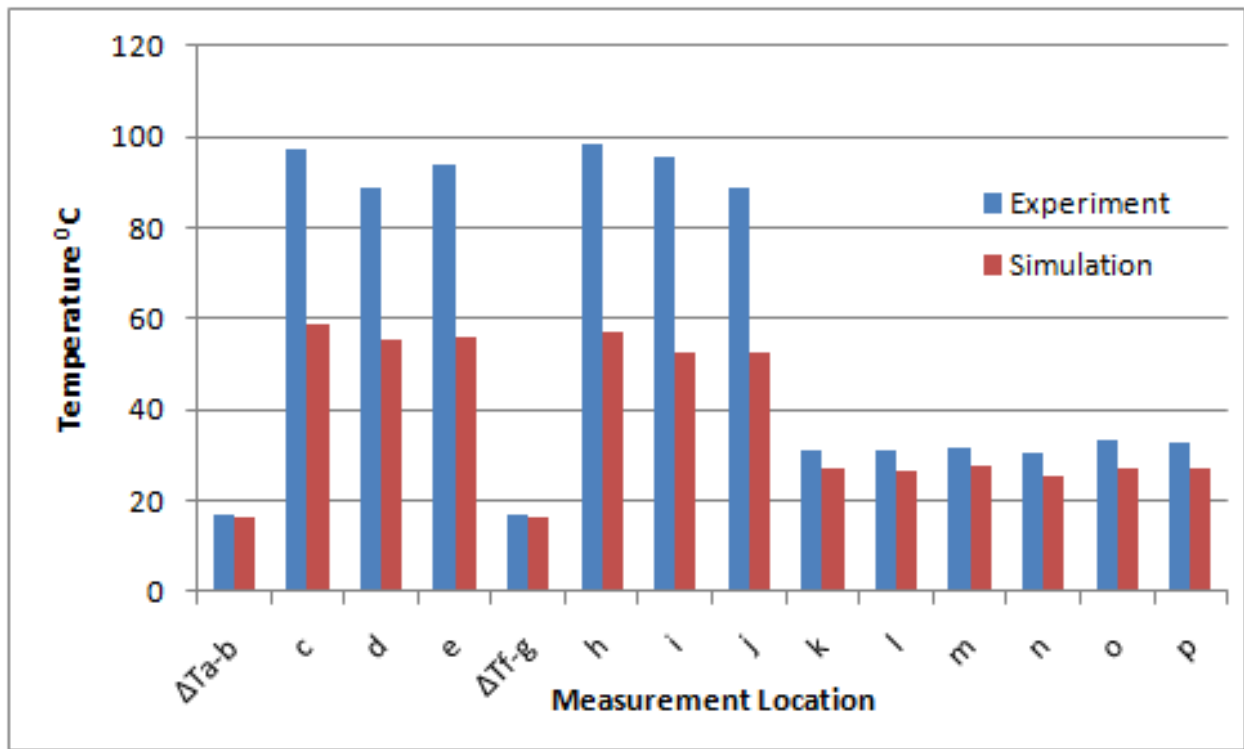


Figure 8.5. Temperature measurement at different locations indicated by Figure 8.3 for Medium power experiment with PCM and its comparison with the simulation predictions ($k-\epsilon$).

C. Transient Test Comparison

Transient temperatures profiles for the low power and medium power cases were also recorded. For a better evaluation of the transient performance of PCM based cooler, the transient temperature profile of the heater source (heater leg, location a) has been compared in Figure 12. It can clearly be seen that when the heat flux is not sufficiently high enough to melt the PCM, the

presence of PCM does not appreciably delay the time required to reach steady state and also the heat source temperature at steady state is much higher than that for a no PCM case. However, when the applied heat flux is sufficiently high enough to partially melt the PCM, the heat source temperature stays at a lower value for a much longer time than that for no PCM case. Physically, at steady state the heat source temperature for PCM case would be higher than that for no PCM case. But the time required to reach that steady state for PCM case is much large as compared to no PCM case. In other words, PCM works better in situation where the heat flux is high enough to partially melt the PCM and the cooler is effective enough to remove the heat at a faster rate.

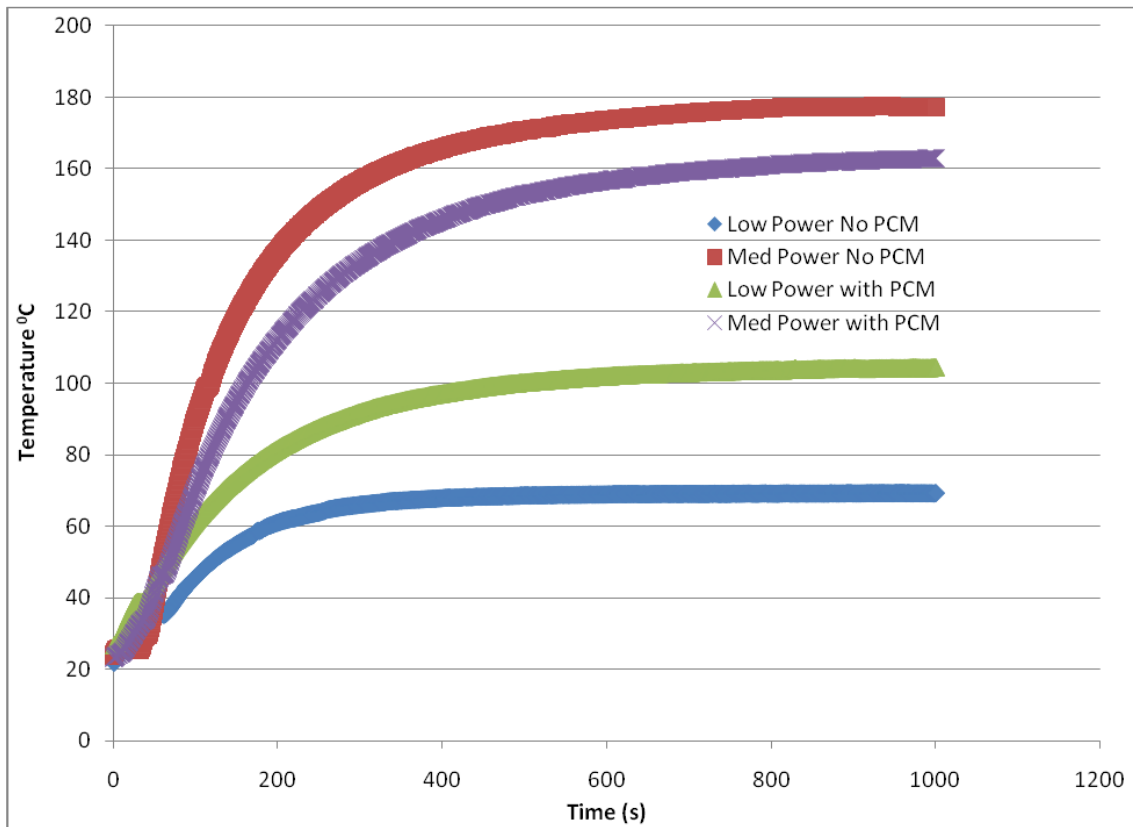


Figure 8.6. Transient temperature profile for different experimental cases of with and without PCM.

Experimental and numerical investigation of normally impinging jets based and PCM-normally impinging jets combination based heat exchangers were performed. A very good agreement between the simulation prediction and experimental data were recorded for the no

PCM case. For the PCM based case, acceptable agreement was found out between the simulation predictions and experimental data. It was also found out that when the heat flux is not sufficiently high enough to melt the PCM, the presence of PCM does not appreciably delay the time required to reach steady state and also the heat source temperature at steady state is much higher than that for a no PCM case. However, when the applied heat flux is sufficiently high enough to partially melt the PCM, the heat source temperature stays at a lower value for a much longer time than that for no PCM case. However physically, at steady state, the heat sources temperature are significantly higher than that for no PCM case as PCM and PCM plate act as additional thermal resistance between the coolant and heat sources. To be specific, it is very important to design the PCM layer to be activated for the required operating temperature and heat flux. The device performance will be greatly benefited in the range of the PCM operating temperature. However, it is very important to note that PCM will not be beneficial if the device operating temperature is extremely variable.

In summary, it was found out that PCM significantly increases the time required for reaching the steady state and at steady state it increases the thermal resistance due to its low thermal conductivity. *Therefore, on the whole, PCM did not help spread the heat and was not a viable option for the warranted application.*

8.2. Tapered Jets

The conjugate power module-heat sink simulation designs were also modified to allow for tapered jets with the same jet exit diameters. It was observed that with tapered jets, for the same mass flow rate a higher local heat transfer coefficient can be observed at a lower pressure drop. Figure 8.7 compares the wall heat transfer coefficients for the case of cylindrical jets with tapered jets. The peak heat transfer coefficient value can be increased by about 2000 W/m²-K

causing a 2.5 °C reduction in the maximum IGBT 1 temperature at a lower pressure drop by using tapered jets. Table 8.1 summarizes the key predictions. Although the higher heat transfer coefficient can be attributed to the higher jet velocity, the required pressure drop for that increased heat transfer coefficient is lower than that for cylindrical jets. In other words, by using tapered jets we can recover pressure drop and at the same time reduce the maximum active devices temperature.

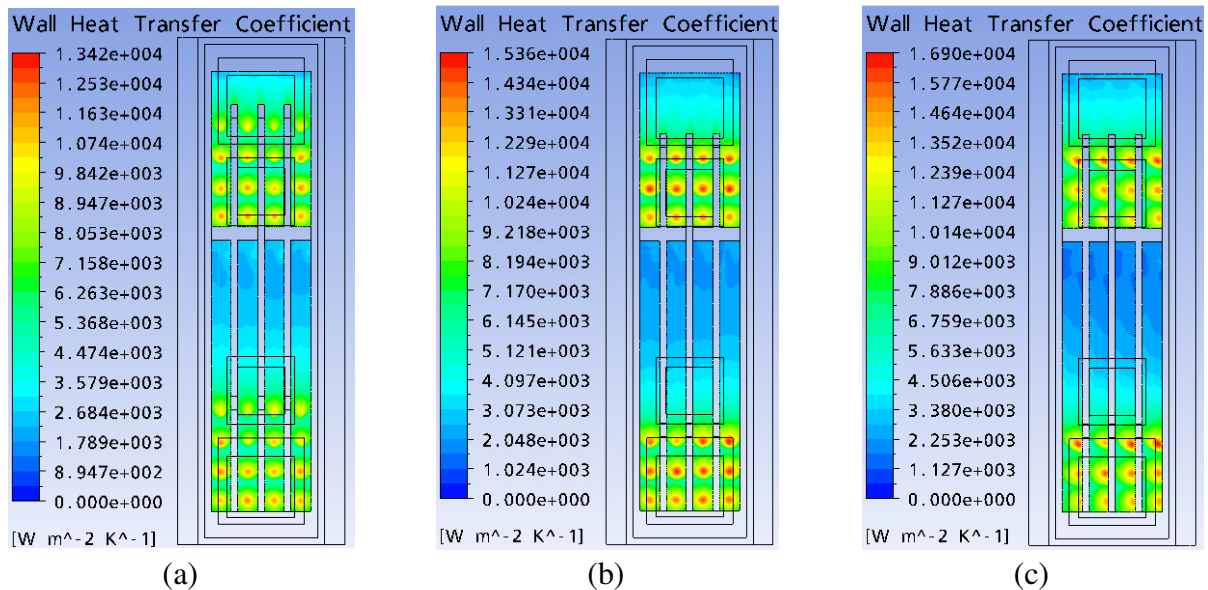


Figure 8.7. Wall heat transfer predictions at the fluid-solid interface on the back side of the power module for (a) cylindrical jets, (b) tapered jets and, (c) 60° angled tapered jets with the same exit diameter as the cylindrical jets.

Table 8.1. Pressure drop and temperature predictions for single channel power module packaging using k-ε model for different cases of tapered jets.

Case	Mass Flow Rate	Maximum IGBT 1 Temperature	Maximum IGBT 2 Temperature	Pressure Drop
Cylindrical Jets	18.5 g/s LLC @ 65 °C:	421.45 K (148.3 °C)	436.23 K (163.1 °C)	7.5 kPa
Tapered Jets	18.5 g/s LLC @ 65 °C:	418.95 K (145.8 °C)	448.95 K (175.8 °C)	6.8 kPa
60° Angled Tapered Jets	18.5 g/s LLC @ 65 °C:	416.4 K (143.3 °C)	446.75 K (173.6 °C)	7.8 kPa

It can also be observed that the maximum IGBT 2 temperature increases because the jets are further away from the IGBT 2 and can be reduced by placing the jets under the IGBT 2.

8.3. Combined Impingement and Mini-Channel Based Coolers

Many heat exchanger designs were modeled and simulated. Most of these designs were based on impingement cooling which aimed at attaining a very high local heat transfer coefficient. However as we go away from the impingement region, the heat transfer coefficient is relatively low and hence, a low averaged heat transfer coefficient. It becomes essential to remove the heat from these low heat transfer coefficient regions by employing conduction effect through the cooler body (that is, by using fins, center walls, etc.). Moreover, by using angled impingement a higher local heat transfer coefficient can be obtained as well as the high heat transfer regions can be extended. But under the flow rate and pressure drop limitations, attaining the target heat transfer coefficient just by convective heat transfer coefficient seemed a bit unrealistic. So it was needed to incorporate conduction effects as well which caused a reduction in the coolant volume inside the cooler which in turn increased the pressure drop significantly.

An alternative to this was to use mini-channel based coolers which are based on using convection as well as conduction heat transfer. By conduction, we mean the heat spreading through the cooler body and by convection we mean the high average wall heat transfer rates. The average heat transfer coefficient was much higher than that for impingement cooling. However, the peak values were much less than that for impingement. But because of the conduction effect (heat spreading) a high effective heat transfer coefficient at a lower pressure drop was observed for mini-channels configuration.

In light of these trends, it was worth a try to combine impingement and mini-channel concept. It was observed that lower maximum IGBT temperatures can be obtained at a given mass flow rate at the expense of increased pressure drop. Figure 8.8 shows the temperature contours for a cooler based on combined slot impingement and mini-channels configuration.

Figure 8.9 shows another cooler based on combined tapered angled impingement and mini-channel configuration. The wall heat transfer coefficient at the target surface for this cooler is shown in Figure 8.10. Table 8.2 summarizes the key predictions for a few coolers based on combined cooling schemes. In addition to the high effective heat transfer rate obtained for coolers based on such configurations, a high pressure drop (~ 80 kPa) was also obtained. Efforts were made to reduce this pressure drop. The pressure drop was successfully reduced to ~ 53 kPa with a similar heat transfer performance. However, any further reduction in pressure drop caused a significant reduction in heat transfer performance.

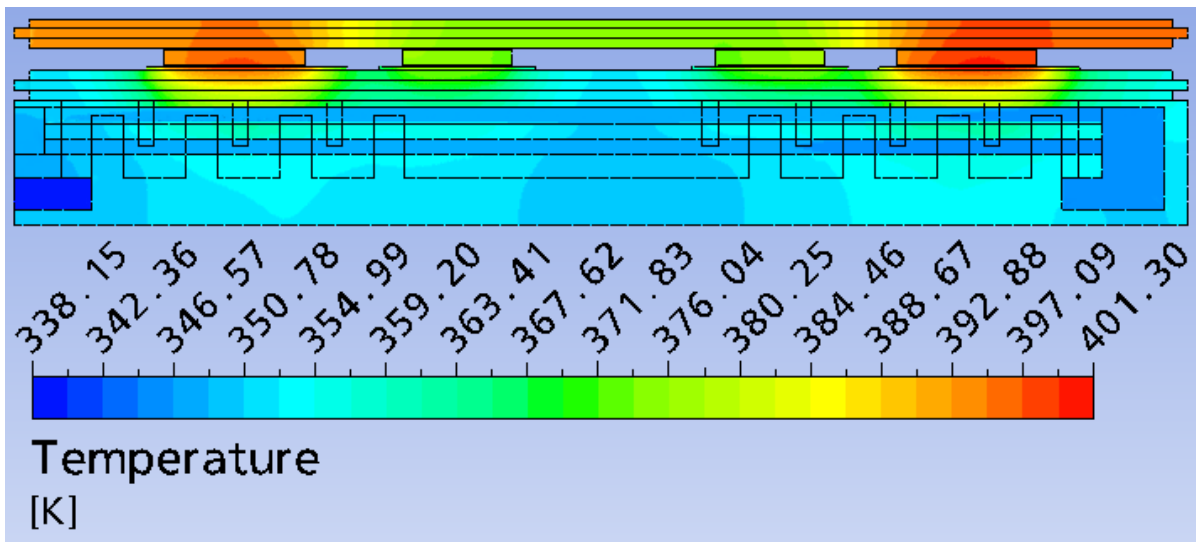


Figure 8.8. Temperature contours on the central plane for a combined slot impingement and mini-channels based cooler.

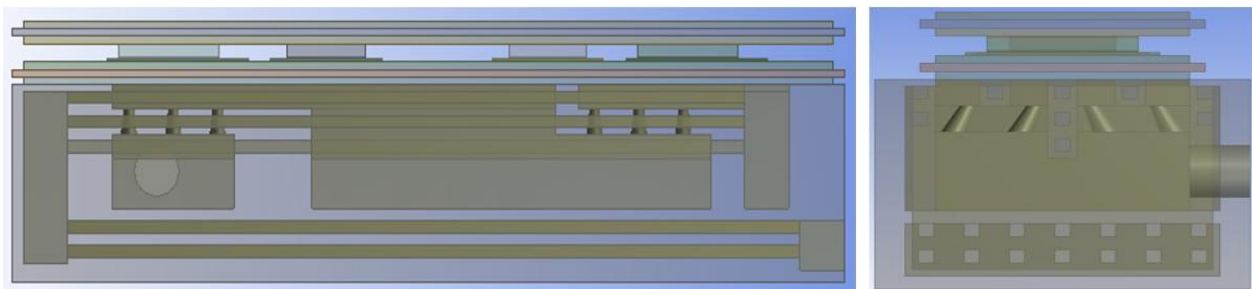


Figure 8.9. Combined tapered angled impingement and mini-channel configuration.

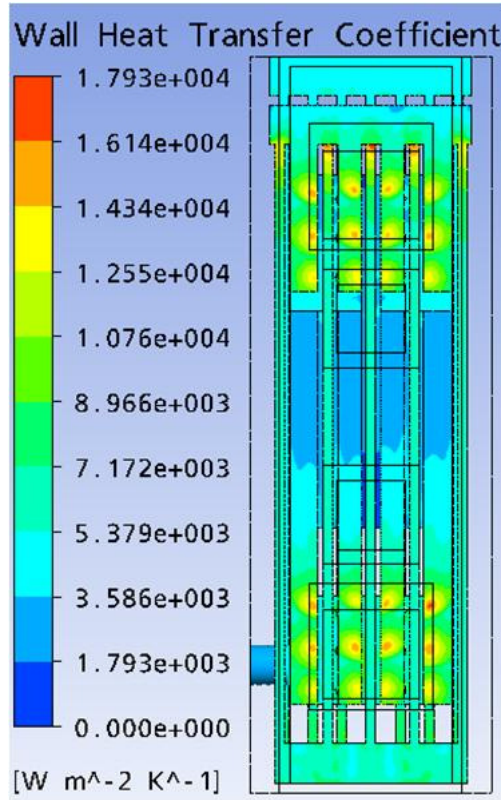


Figure 8.10. Wall heat transfer coefficient on the target surface for the design shown in Figure 8.9.

Table 8.2. Pressure drop and temperature predictions for combined impingement and mini-channel based configurations.

Case	Mass Flow Rate	Maximum IGBT 1 Temperature	Maximum IGBT 2 Temperature	Pressure Drop
Slot impingement (44 Slots) and 1 pass, 14 parallel channels, no target wall for impingement. Channels 0.5 mm away from DBA back side.	18.5 g/s LLC @ 65 °C	397.8 K (124.7 °C)	400.8 K (127.7 °C)	80 kPa
Slot impingement (32 Slots) and 1 pass, 10 parallel channels, no target wall for impingement. Channels 0.5 mm away from DBA back side.	18.5 g/s LLC @ 65 °C	399 K (126 °C)	401.3 K (128.2 °C)	53 kPa
60° angled impingement and 2 pass, 9 & 14 parallel channels, no target wall for impingement. Channels 0.5 mm away from DBA back side.	18.5 g/s LLC @ 65 °C	409.7 K (136.6 °C)	413.8 K (140.7 °C)	17.8 kPa

8.4. Summary

Although, the alternate cooling schemes presented in this chapter were high performance schemes, they were found out to be not much useful for the problem at hand. Each of the schemes presented here had certain drawbacks which made them inapplicable. For example, PCM based cooling scheme was not suitable for this application as the low thermal conductivity of the PCM increased the thermal resistance between the active devices and the coolant. On the other hand, the combined impingement and mini-channel schemes performed much better and offered much lower thermal resistances between the active devices and the coolant. However, they incurred high pressure drop. The tapered jets scheme was one of the promising scheme which offered higher heat transfer rates at a reduced pressure drop. However, the complexity involved with the manufacturing of tapered jets restricted they application for the warranted application.

CHAPTER 9: BEYOND ELECTRONIC COOLING

Over the years, various efforts have been made to maximize the heat transfer coefficients for turbine blade internal cooling while minimizing the coolant flow rate. Leading and trailing edges are such regions on the turbine blade that require a high heat transfer rate. It is well known that such higher cooling effectiveness is required to design for higher turbine inlet temperatures which can result in higher engine efficiency. However, the size and strength constraints at the trailing edge of turbine vanes and blades significantly reduce cooling options. Furthermore, the small wall thickness in the trailing edge region limits the magnitude of the conduction heat transfer to internal cooling passages as well as limits the size of the passage itself. Additionally, coolant ejection through the vanes and blades are associated with aerodynamic losses. Balancing of such trade-offs results in well-known “gill slot”, “covered” and “letter-box” trailing edge geometries [76-78] as shown in Figure 9.1.

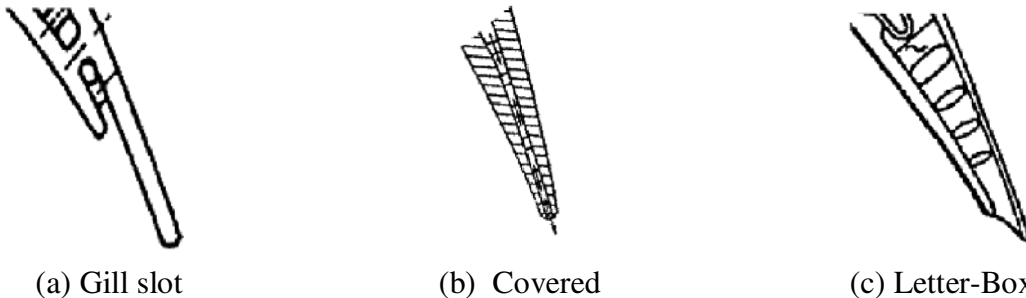


Figure 9.1. Typical first stage stator trailing edge ejection configuration [76-78]. (a) Gill slot (b) Covered (c) Letter-box.

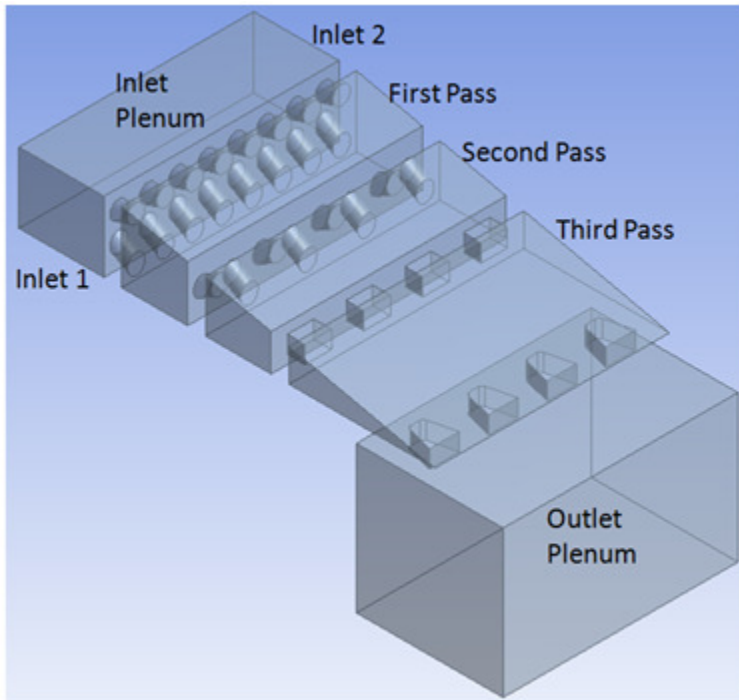
Most of the trailing edge cooling research till date has essentially been focused on inline and staggered arrangement of pin-fins having varied cross-sections such as circular, diamond and elliptical [79-81]. It is believed that pin-fins at the trailing edge provide for rigidity and act as turbulence promoters to enhance heat transfer. However, impingement cooling at the trailing edge has never been explored as a viable trailing edge cooling option. It is well known that the impinging jets have a highly turbulent nature and results in concentrated high heat transfer rates

which make them a strong viable candidate for high heat flux removal applications such as annealing of metals, drying of textiles, electronic cooling, internal cooling of turbine vanes and blades, cooling of combustor walls and cooling of rotor disks [82]. Thus, current demands for higher engine efficiency make it a viable trailing edge cooling option.

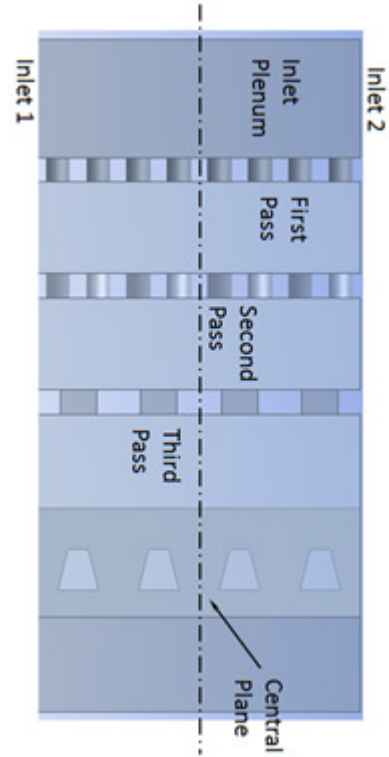
In the chapter, a conceptual three pass impingement based trailing edge cooling scheme has been proposed and examined for heat transfer enhancement. This geometry was based on the experimental observations and numerical analysis presented in Chapter 4. Moreover, this geometry was selected such that the jet plates improve the rigidity of the trailing edge as well as provide for enhanced conduction heat transfer in the trailing edge region. Coolant ejection path similar to “Gill slot” configuration was considered. The objective of this investigation was to understand the governing flow structures and to determine the local and averaged heat transfer distributions on all passage walls. In other words, only the fluid domain was studied. Flow and heat transfer pattern analysis was conducted using ANSYS-CFX, commercial Computational Fluid Dynamics (CFD) software.

9.1. Geometry and Simulation Model

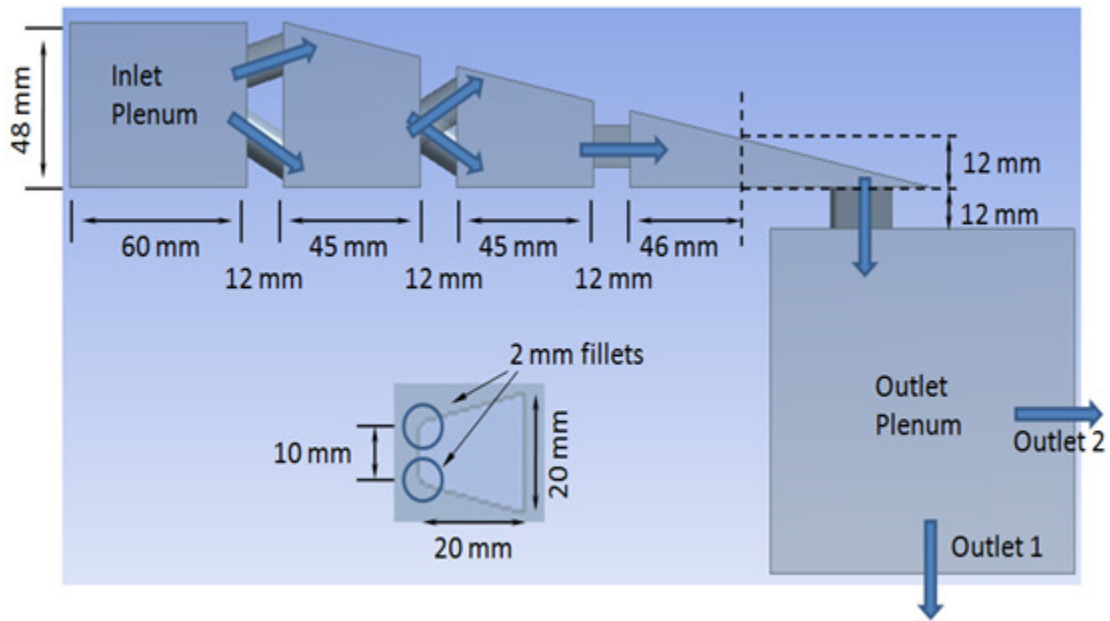
In general, three basic structures of the trailing edge region (Figure 9.1) have been widely tested [76-78]. Out of these, the Gill slot structure was selected for the present work and modified to incorporate impingement based cooling scheme. Moreover, the external geometry of the trailing edge considered is somewhat similar to that considered by Hwang *et al.* [83] and Chen *et al.* [84]. Figure 9.2 shows different views of the model of the flow domain in the trailing edge with the inlet and outlet plenums. It is a scaled-up three pass impingement based model having either one inlet or two inlets. One-inlet models were simulated to check for non-uniform distribution while two-inlet models were simulated to check for uniform distribution.



(a) Orthographic view



(b) Top view



(c) Side view with cross section of the third pass exit.

Figure 9.2. Different views of the model of the flow domain in the trailing edge with the inlet and outlet plenums. (a) Orthographic view. (b) Top view. (c) Side view.

Three models, tabulated in Table 9.1, each having a similar configuration were studied. For each model, first pass consisted of 16 inline jets distributed in two rows, second pass consisted of 8 staggered jets distributed in two rows and the third pass consisted of 4 slot jets arranged in a single row. In the first pass, the jets were inclined so as to have an angle of 30° with the side walls. In the second pass, all the jets were inclined at 30° with the horizontal. The thickness of all the jet plates was 12 mm. A trapezoidal cross-section as shown in Figure 9.2(b) was considered for the trailing edge exit passage. A large outlet plenum was selected so as to minimize the effects of flow recirculation near the trailing edge exit.

Table 9.1. Geometrical parameters of the jets in the three trailing edge models.

Model	Channel	Slot Width (m)	Slot Height (m)	Aspect Ratio	Jet Diameter or D_h (m)
1	First Pass	-	-	-	0.012
	Second Pass	-	-	-	0.012
	Third Pass	0.018	0.012	1.5	0.0144
2	First Pass	-	-	-	0.012
	Second Pass	-	-	-	0.012
	Third Pass	0.022	0.01	2.2	0.01375
3	First Pass	-	-	-	0.006
	Second Pass	-	-	-	0.012
	Third Pass	0.025	0.0125	2.0	0.0167

Same inlet plenum, outlet plenum and trailing edge exit passage geometry was considered for the three models. Similar second pass geometry, that is, same second pass jets inlet and exit locations was considered for all the three models. Moreover, same locations for each cylindrical jets and slot jets center were considered. Model 1 and Model 2 differed from each other only on the basis of third pass slot jet cross-section. Model 2 had flatter slots to allow for more spreading and even flow distribution. However, the total cross-sectional area of the slot jets for Model 1 and Model 2 were nearly the same. Moreover, the cross-sectional area of the

trailing edge exit considered was slightly larger than that of the slot jets of Models 1 and 2. Model 3 on the other hand, differed from the other two models on the basis of first pass and third pass jets. Model 3 had smaller first pass jets and bigger third pass slots to have a high heat transfer coefficient in the first pass and also to have a consistent Reynolds number across the trailing edge. As a result, the cross-sectional area of the trailing edge exit was slightly smaller than that of the slot jets of Model 3.

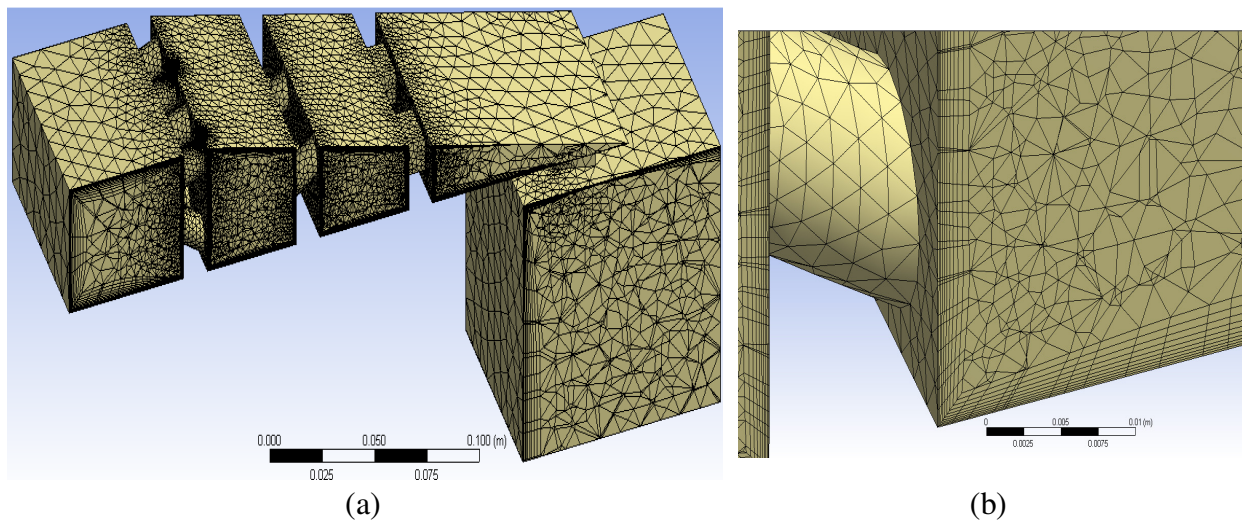


Figure 9.3. (a) Sectional view of the typical meshed geometry. (b) Zoomed-in image of the mesh.

ANSYS-CFX, commercial computational fluid dynamics (CFD) software was used to study the flow and heat transfer behavior in the proposed impingement based trailing edge geometries. CFX mesh method with appropriate mesh controls was used to mesh the geometries and it was ensured that the y^+ is always less than 1 for proper estimation of the flow and heat transfer behavior. Also, a fine mesh was used around all the sharp corners and normal to all the boundary surfaces, except the inlet and the outlet faces. Figure 9.3(a) shows the sectional view of a typical meshed geometry. Figure 9.3(b) shows a zoomed-in image of the mesh. Typical mesh for all the models consisted of 4.6 million elements with nearly 1.05 million nodes. This mesh size was considered after performing a grid independency study.

9.2. Data Reduction

The Reynolds number corresponding to the coolant flow through the trailing edge channels was based on the hydraulic diameter of the jets at each pass and can be expressed as:

$$\text{Re} = \frac{GD_h}{\mu} \quad (9.1)$$

where, G is the total mass flux through the jets at each pass, D_h is the equivalent hydraulic diameter of the corresponding jets and μ is the dynamic viscosity of air. Owing to the differences in the hydraulic diameters at each pass, the Reynolds numbers for each pass were computed separately. However, for the average Nusselt number comparison for different models, Reynolds number of the first pass was used.

Figure 9.4 shows a side view of the proposed trailing edge geometry with the regions of interest as named faces. For example, the faces A , B , C and D form region of interest in the first pass. These faces were used essentially for the heat transfer and pressure measurements. The pressure drop (Δp) across each pass was evaluated by considering the pressures at the jet inlets of each pass. For example, pressure drop for the first pass was evaluated between the faces L and D . It was then expressed in the dimensionless form as:

$$K_L = \frac{2\Delta p}{G^2/\rho} \quad (9.2)$$

The average and local heat transfer coefficients were evaluated and presented in terms of the Nusselt number. Similar to the Reynolds number definition, the Nusselt number was computed based on the hydraulic diameters of the jet and is defined as:

$$\text{Nu} = \frac{hD_h}{k} \quad (9.3)$$

where, h is the heat transfer coefficient and k is the thermal conductivity of air. Local and average Nusselt numbers for different passes were thus computed separately.

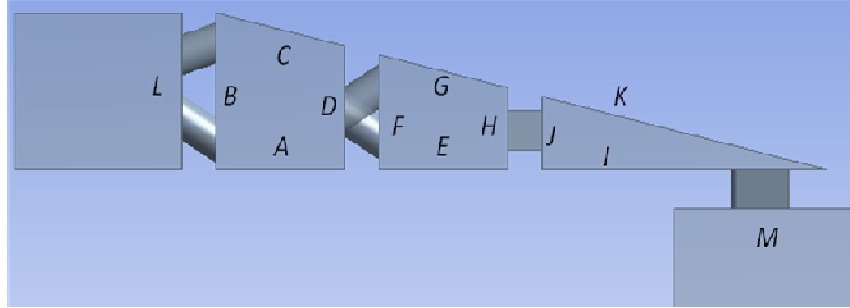


Figure 9.4. Side view of the impingement based trailing edge geometry with regions of interest as named faces. Faces *A*, *B*, *C* and *D* are the regions of interest in first passage. Faces *E*, *F*, *G* and *H* are the regions of interest in second passage. Faces *I*, *J* and *K* are the regions of interest in third passage. The outlet pressure was measured at face *M*.

9.3. Boundary Conditions

Flow and heat transfer simulations were performed using the incompressible $k-\varepsilon$ turbulence model in ANSYS-CFX (v12). This model was selected as being a reasonably accurate cost and time effective turbulence model option. Air at 25 °C was used as the working fluid and the outlet was maintained at zero relative pressure. No-slip boundary condition and a similar uniform heat flux (100 W/m²) were applied at all the boundary surfaces for all simulations. Simulations were performed for three different total mass flow rates – 0.01 kg/s, 0.01884 kg/s and 0.03768 kg/s.

9.4. Results and Discussion

For each total mass flow rate, both one inlet and two inlets cases were simulated to check for any non-uniform distribution. Figure 9.5 shows the streamlines in the third model for the cases of one-inlet and two-inlets at an inlet Reynolds number (based on first pass hydraulic diameter) of 7240. It can clearly be seen that the flow distribution throughout the trailing edge is more or less uniform for both the cases. Similar trend was observed for the other cases as well.

Figure 9.6 shows the variation of overall pressure drop across the trailing edge in terms of the loss coefficient, K_L . This pressure drop was measured between the faces *L* and *M* and thus, pressure losses due to the entrance effects have not been included. Owing to the variation in the

jet hydraulic diameters for the three impingement passages, the Reynolds number in those passages varied greatly for the same total mass flow rate. To avoid any ambiguity and misinterpretation, two different definitions of the loss coefficient were used.

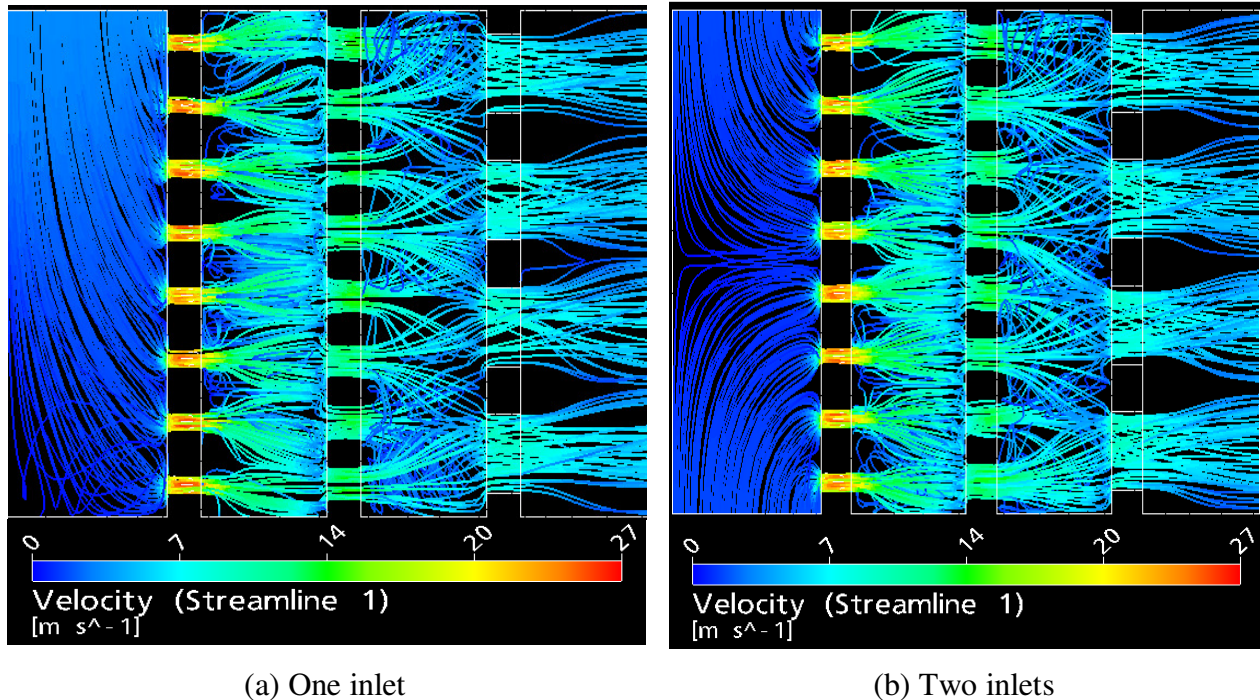


Figure 9.5. Streamlines in the third model for the cases of one inlet and two inlets at an inlet Reynolds number of 7240.

The data set represented by the filled symbols (curves Model 1, Model 2 and Model 3) were evaluated based on the jet hydraulic diameter of the first passage while those represented by the outlined symbols (curves Model 1*, Model 2* and Model 3*) were evaluated based on the maximum Reynolds number and its corresponding hydraulic diameter. Table 9.2 summarizes the variation in the Reynolds number across the trailing edge for the three models at a given total mass flow rate. For models 1 and 2, the inlet Reynolds number was the smallest and thus, the loss coefficient was highly over-predicted and should be *avoided*. While for the model 3, the Reynolds number in all the three passages was consistent and thus, a more realistic loss coefficient was obtained. Moreover, the curves Model 3 and Model 3* predict almost the same

loss coefficients. Similarly, the curves Model 1* and Model 2* show a more realistic loss coefficients prediction and it can be understood more clearly by looking at the channel wise loss coefficient prediction.

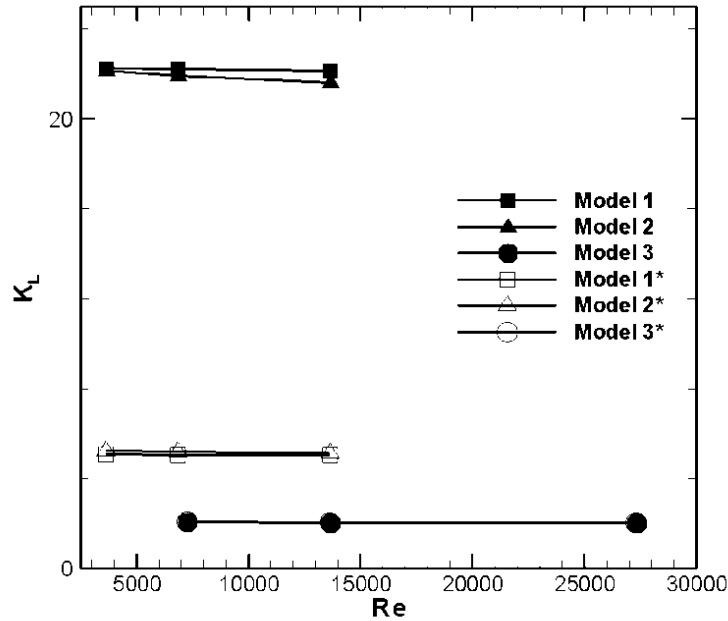


Figure 9.6. Variation of overall pressure drop across the trailing edge with Reynolds number.

Table 9.2. Variation in Reynolds number across the trailing edge for three models at a given total mass flow rate.

Model	Channel	Mass Flow rate (kg/s)	Jet Hydraulic Diameter (m)	Mass Flux (kg/m ² s)	Reynolds number
1	First Pass	0.01	0.012	5.53	3620
	Second Pass	0.01	0.012	11.1	7240
	Third Pass	0.01	0.0144	11.6	9100
2	First Pass	0.01	0.012	5.53	3620
	Second Pass	0.01	0.012	11.1	7240
	Third Pass	0.01	0.01375	11.4	8530
3	First Pass	0.01	0.006	22.1	7240
	Second Pass	0.01	0.012	11.1	7240
	Third Pass	0.01	0.0167	8	7280

Figure 9.7 shows the channel-wise loss coefficient predictions as well as the entrance losses for the three models. The entrance losses for all the cases were evaluated based on the jet

hydraulic diameter of the first passage. Clearly, higher entrance losses were obtained for the model 3 and can be attributed to the fact that the first passage jet diameters of model 3 are 50% smaller than that for other two models. The first passage losses were observed to be higher for models 1 and 2 due to 50% contraction in the flow cross-sectional area at the second pass inlet with respect to the first pass inlet. On the other hand, for model 3 it was lower due to doubling of the flow cross-sectional area at the second pass inlet with respect to first pass inlet. Pressure losses across the second and third channels were similar for Model 1 and Model 2. This due to fact that for both the models the cross-sectional areas of the second pass jets and third pass slots jets were almost the same. However, for Model 3 the cross-sectional area of the third pass slots were bigger than that of Models 1 and 2 which resulted in smaller flow contraction and thus, slightly lower loss coefficient across the second passage. This smaller loss coefficient in Model 3 was compensated for by a much higher the loss coefficient across the third passage. This was due to the fact that the trailing edge exit holes had a smaller cross-section as compared to the cross-sectional area of the third passage inlet and the flow had to contract before flowing out to the ambient. This loss can greatly be reduced by modifying the exit/cutback holes.

Figure 9.8 shows the typical heat transfer coefficient distribution obtained at the internal faces of the trailing edge for a first passage Reynolds number of 1360°. Figure 9.8(a) shows the heat transfer distribution at the faces *A*, *E* and *I* while Figure 9.8(b) shows the heat transfer distribution at the faces *C*, *G* and *K*. These heat transfer distribution contours were obtained for Model 3. The first channel of this model consisted of smaller jets (6 mm) and hence high localized heat transfer regions can be observed on faces *A* and *C* of the first passage. Both the faces (*A* and *C*) showed similar heat transfer rates. A more uniform spreading was also observed. However, the heat transfer coefficient distribution on the face *B* (not shown in Figure 9.8) was

relatively much lower causing the average heat transfer rate inside the first channel to be lower than the second channel. In the second passage, less number of jets was present and thus, heat transfer distribution was not uniform at the *E* and *G* faces. In the third passage, larger slot jets were present which allowed for more uniform distribution on both *K* and *I* faces.

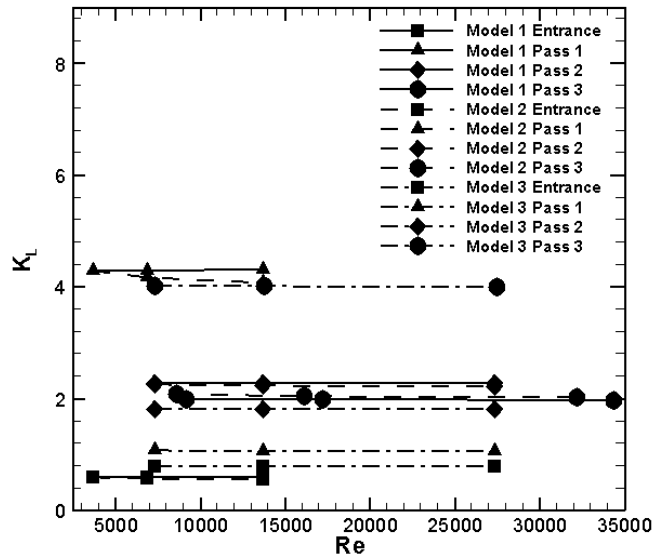


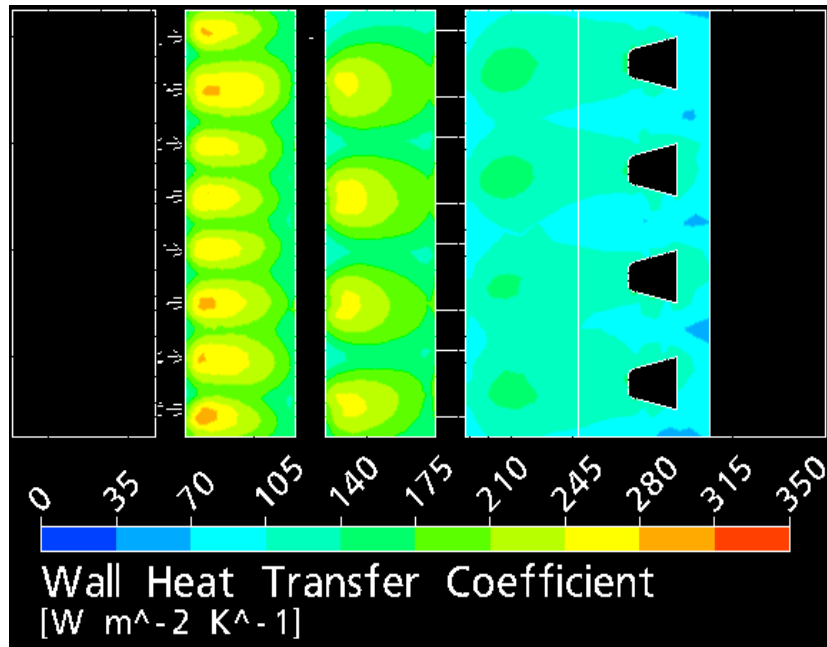
Figure 9.7. Variation of channel wise loss coefficient as well as entrance losses with Reynolds number.

Figure 9.9 shows the variation of area averaged Nusselt number with the first passage inlet Reynolds number. Six faces namely, *A*, *C*, *E*, *G*, *I* and *K* representing the internal surfaces of the trailing edge were considered. Similar to the pressure loss distribution, the Nusselt number variation with Reynolds number for the models 1 and 3 showed an unusual trend. In other words, the slope of the curves Model 1 and Model 2 in Figure 9.9 was too high to be realistic. It was again due to the fact that the Reynolds number at the first passage inlet was the smallest for models 1 and 2. A more common Nusselt number trend was observed for model 3 and it was because the Reynolds number was consistent across the trailing edge. For the curve Model 3*, hydraulic diameter was matched with that of models 1 and 2 and a similar trend of higher slope was observed. Thus, for such cases of varying Reynolds number it is best either to consider the

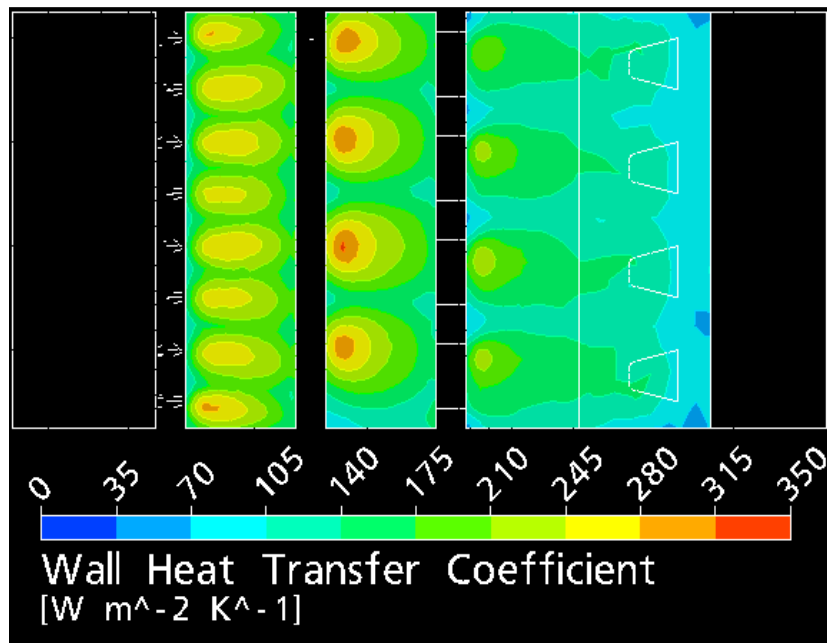
channel-wise Reynolds number or to consider the total mass flow rate through the geometry. It can also be observed that for curve Model 3* at a given total mass flow rate, the corresponding Nusselt number was higher than that for Model 1 and Model 2. In Figure 9.9, it can also be observed that the Nusselt number curves for Model 1 and Model 2 are over-lapping. This shows that a flatter slot with a cross-sectional area similar to that of a squarer slot at the third passage does not make a significant difference to the overall heat transfer rate.

Figure 9.10 shows the channel-wise averaged Nusselt number variation with Reynolds number for the three models. For the first pass, faces *A*, *B*, *C* and *D* were considered, for the second pass, faces *E*, *F*, *G* and *H* were considered and for the third pass, faces *I*, *J* and *K* were considered. Similar to the pressure loss distributions, more realistic Nusselt number distributions were observed. Acceptably high Nusselt numbers were observed for all the cases and regions except for the first passage of model 3. First passage of Model 3 had smaller jets which produced localized high heat transfer regions. Although there was a sufficient spreading of the impinging jets on the *A* and *C* faces (see Figure 9.5 and Figure 9.8) the channel averaged heat transfer coefficient in the first passage was observed to be lower as compared to Model 1 and 2 due to very low heat transfer rates on face *B*. The heat transfer rate in the first passage of Model 3 can be improved upon by proper arrangement of the jets.

It can also be observed in Figure 9.10 that for the second channel all the three models showed same average heat transfer rate and that the heat transfer rates in the second channel was also the highest among the three channels for each model. This trend could be attributed to the fact that the second passage had relatively high speed jets and also more uniform distribution with significant recirculation. Moreover, the overall size of the second channel size was smaller than that of the first channel.



(a)



(b)

Figure 9.8. Typical heat transfer coefficient distribution obtained at the internal faces of the trailing edge for a first passage Reynolds number of 1360°. (a) faces A, E and I (left to right) (b) faces C, G and K.

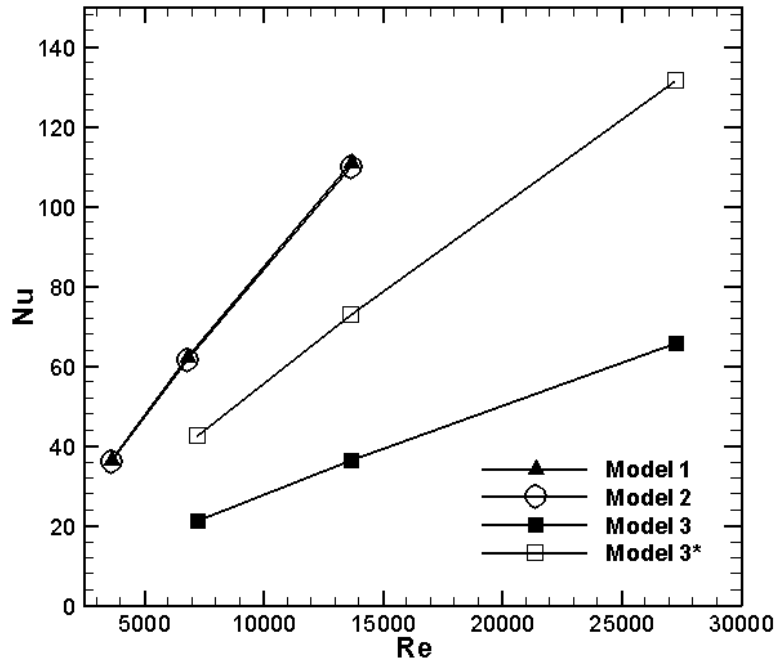


Figure 9.9. Variation of area averaged Nusselt number with first passage inlet Reynolds number.

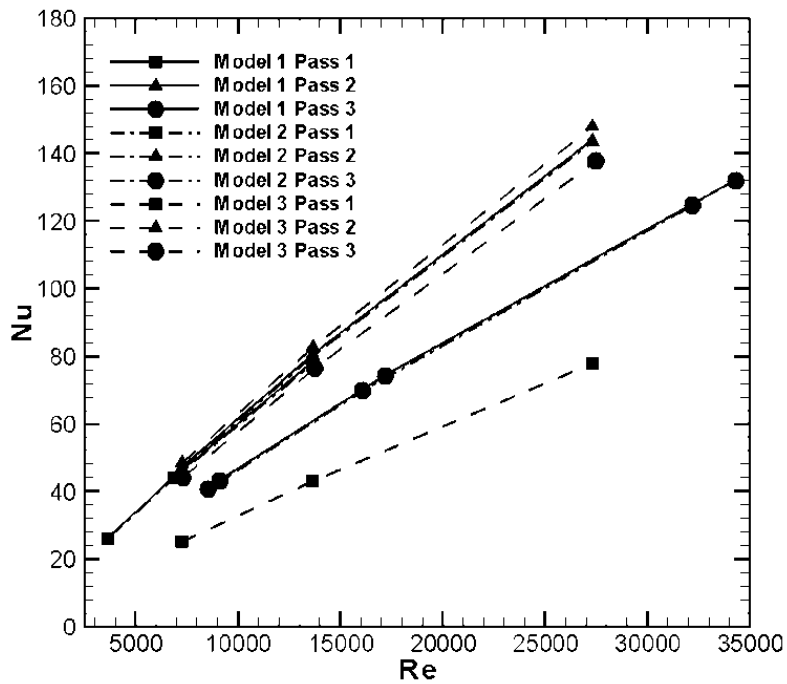


Figure 9.10. Variation of channel wise averaged Nusselt number with channel specific Reynolds number.

In the third channel for Model 1 and Model 2, relatively lower heat transfer rates were observed due to insufficient jet spreading and also due to lower heat transfer rates on the face *I*. This is because the jets impinge mostly on the face *K* and exit through the trapezoidal opening without recirculation and thus there is not much impingement effect on the face *I*. However, that is not the case for Model 3 where the recirculation is observed in the third channel owing to the smaller exit cross-sectional area as compared to the slot jets cross-sectional area. Moreover, the jets impinge on both the faces (*K* and *I*).

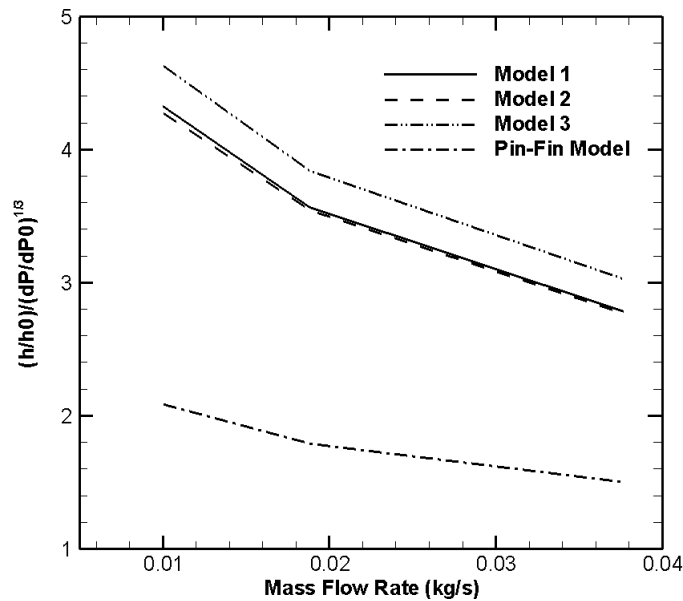


Figure 9.11. Variation of ratio of overall averaged heat transfer coefficient to overall pressure drop with the total mass flow rate.

Channel-wise representation of the heat transfer rates helps understand the flow and thermal behavior as well as allows for better comparison of the different models. However, in absence of sufficient experimental data, a norm is required to justify the performance of each model. For this purpose, a baseline case having no internal features was also simulated. For each total mass flow rate, average baseline heat transfer rate (represented as $h0$) and baseline pressure drop (represented as $dP0$) were evaluated. These baseline values were then used to define the performance index as:

$$\frac{(h/h_0)}{(dP/dP_0)^{1/3}} \quad (9.4)$$

where, h is the average trailing edge heat transfer coefficient and the dP is the overall pressure drop across the trailing edge. Figure 9.11 shows the variation of this performance index with total mass flow rate. It can clearly be seen that Model 3 performs the best out of the three. Moreover, Model 1 and Model 2 having similar geometries were observed to have a similar performance as well.

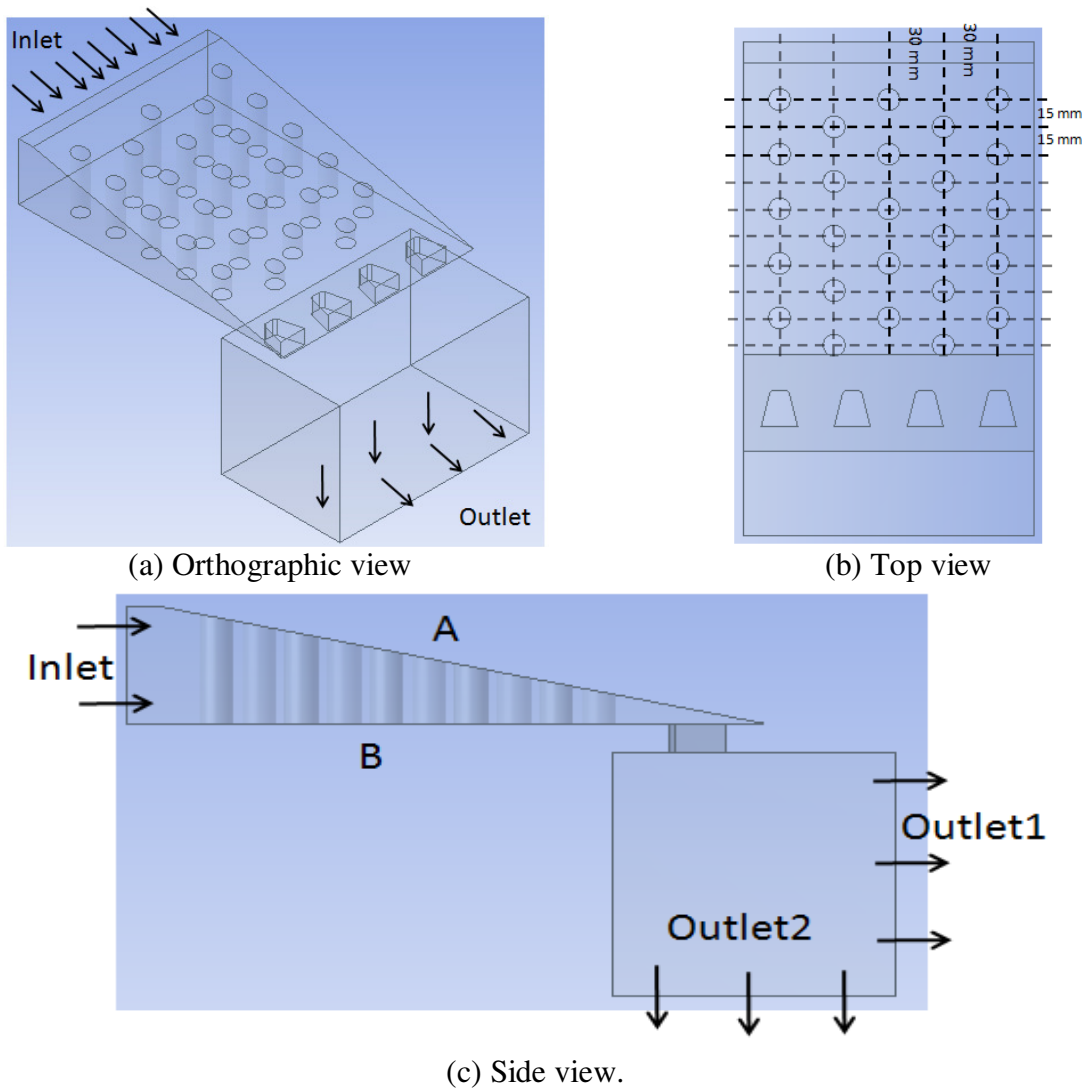


Figure 9.12. Different views of the model of the flow domain in the trailing edge for a pin-fin based scheme with the inlet and outlet plenums. (a) Orthographic view. (b) Top view. (c) Side view.

Figure 9.11 also shows the comparison of the thermal performance of the above three models with that of a pin-fin based trailing edge geometry (Figure 9.12). For the pin-fin based geometry, 25 12 mm diameter cylindrical fins arranged in a staggered manner were considered. The center to center spacing between the fins is also indicated in Figure 9.12. It can be clearly observed that for the same amount of mass flow rate, the proposed impingement scheme performed much better than the conventional pin-fin scheme.

9.5. Conclusion and Future Work

Three different three-pass impingement-based trailing edge geometries each having either one-inlet or two-inlets were modeled. Flow and thermal behavior in these geometries were studied using ANSYS-CFX. Flow field was checked for uniformity and it was found out that the flow field was more or less uniform for both one inlet and two inlet cases. Due to varied jet hydraulic diameters at the inlet of each channel different Reynolds numbers were computed for each channel. The loss coefficient across each channel was evaluated for different Reynolds number and compared for all the three geometries. Overall averaged as well as channel-wise averaged heat transfer rates were also compared for the three models. It was found out that larger jets worked better in both the first pass as well as in the third pass as they allowed for more spreading. Baseline geometry with no internal features was used to define a performance index and to compare all the three models. Model 3 was observed to perform the best for the conditions studied in this project.

Being a preliminary study, only a few cases have been studied in this work and design optimization along with experimental validation remains a futuristic goal. Additionally, conjugate heat transfer analysis will be conducted to evaluate the effective heat transfer rates at the internal as well as external surfaces of the trailing edge.

CHAPTER 10: CONCLUSION AND RECOMMENDATIONS

Various cooling options based on jet impingement, mini-channel, ribbed mini-channel, phase change material and double sided cooling configurations were considered for application in hybrid electric vehicle and other similar consumer products and perform parametric and optimization study on selected designs. Detailed experimental and computational analysis was performed on different cooling designs to evaluate overall performance. Severe constraints such as choice of coolant, coolant flow-rate, pressure drop, minimum geometrical size and operating temperature were required for the overall design.

- Owing to the localized nature of the active heat sources and high local heat transfer rates offered by impingement, impinging jets based cooling schemes were preferred. These configurations were based on having an inclined impingement on finned surfaces and were shown to have a better thermal performance as compared to their conventional counterparts.
- Liquid crystal- and infrared thermography-based experiments and ANSYS-CFX and Fluent simulations showed that inclined/angled impingement having a configuration similar to Figure 3.2(b) and Figure 3.2(d), showed a higher local heat transfer coefficient resulting in lower devices temperature.
- Configurations similar to Figure 3.2(e) were not found out to be useful as the local as well as the average wall heat transfer coefficients were lower than the convention jet impingement scheme for a fixed jet-target-plate spacing.
- It was observed, if properly oriented, wall-integrated inclined impingement can help attain much higher local as well as overall heat transfer rates than the normal impingement case. Thus, the present swirl-impingement-fin (SIF) configuration was

selected as a viable candidate for high heat density applications such as thermal management of power converters. This SIF geometry was then optimized and applied to generate specific heat exchanger designs for cooling of automotive power converters and simulated to meet the required temperature and pumping power constraints. The high performance design was then fabricated and tested under conditions similar to the actual running environment. The experimental data and simulation predictions had a very close match.

- For the planar power module cooled by a high performance impingement based cooler configuration, thermal resistance value was found out to be 0.246 K/W when water was used as the coolant and 0.288 K/W when LLC was used as the coolant. Although this cooling performance was as-expected and significantly higher than its competing counterparts, it was not sufficient to meet all the design constraints.
- Alternate cooler design structures such as PCM-based cooler, tapered/nozzle-shaped jets, mini-channel and ribbed mini-channel based coolers and combined impingement and mini-channel based coolers were also studied. Tapered/nozzle-shaped jets showed promising results (~40% reduction in overall pressure drop) but were not enough to meet the temperature requirements either. PCM based cooling scheme was also not suitable for this application as the low thermal conductivity of the PCM increased the thermal resistance between the active devices and the coolant.
- Mini-channel based coolers provided much higher average heat transfer coefficient than that for impingement cooling. However, the peak values were lower than that for impingement. But the conduction effect (heat spreading) helped improve and provide a high effective heat transfer coefficient at a lower pressure drop.

- Combined impingement and mini-channel schemes, on the other hand, performed much better and offered lower thermal resistances between the active devices and the coolant. However, these configurations needed high pressure drop to obtain significantly higher heat transfer rates.
- As an alternative to these concepts, ribbed mini-channels configurations were studied. It was observed that a very high average heat transfer coefficient can be maintained at the target surface at much reduced pressure drop compared to all other techniques. This scheme was further optimized. *The best performing single-side cooler configuration was in fact based on ribbed mini-channel configuration.* This model showed to have an effective heat transfer coefficient of $35000 \text{ W/m}^2\text{-K}$.
- In addition to single-sided cooling configurations, double-sided cooling configurations were also studied. It was found out that having X amount of heat transfer coefficient on either side of the double-sided (planar) power module resulted in much lower maximum IGBT temperatures than that with $2X$ amount of heat transfer coefficient on one side of the double-sided (planar) power module.
- Additionally, one of the impingement based configuration (Swirl-Impingement-Fin) developed during the course of this work was applied to the internal cooling of a turbine blade trailing edge and was shown to enhance the thermal performance by at least a factor of 2 in comparison to the existing pin-fin technology for the conditions studied in this work.

Figure 10.1 summarizes the observations for various high performance heat exchanger configurations that were investigated during the course of the present study. Based on these observations, it can be concluded that *with single-sided cooling schemes not meeting the target*

heat transfer coefficient, double-sided cooling seems to be an ideal approach from thermal management point of view.

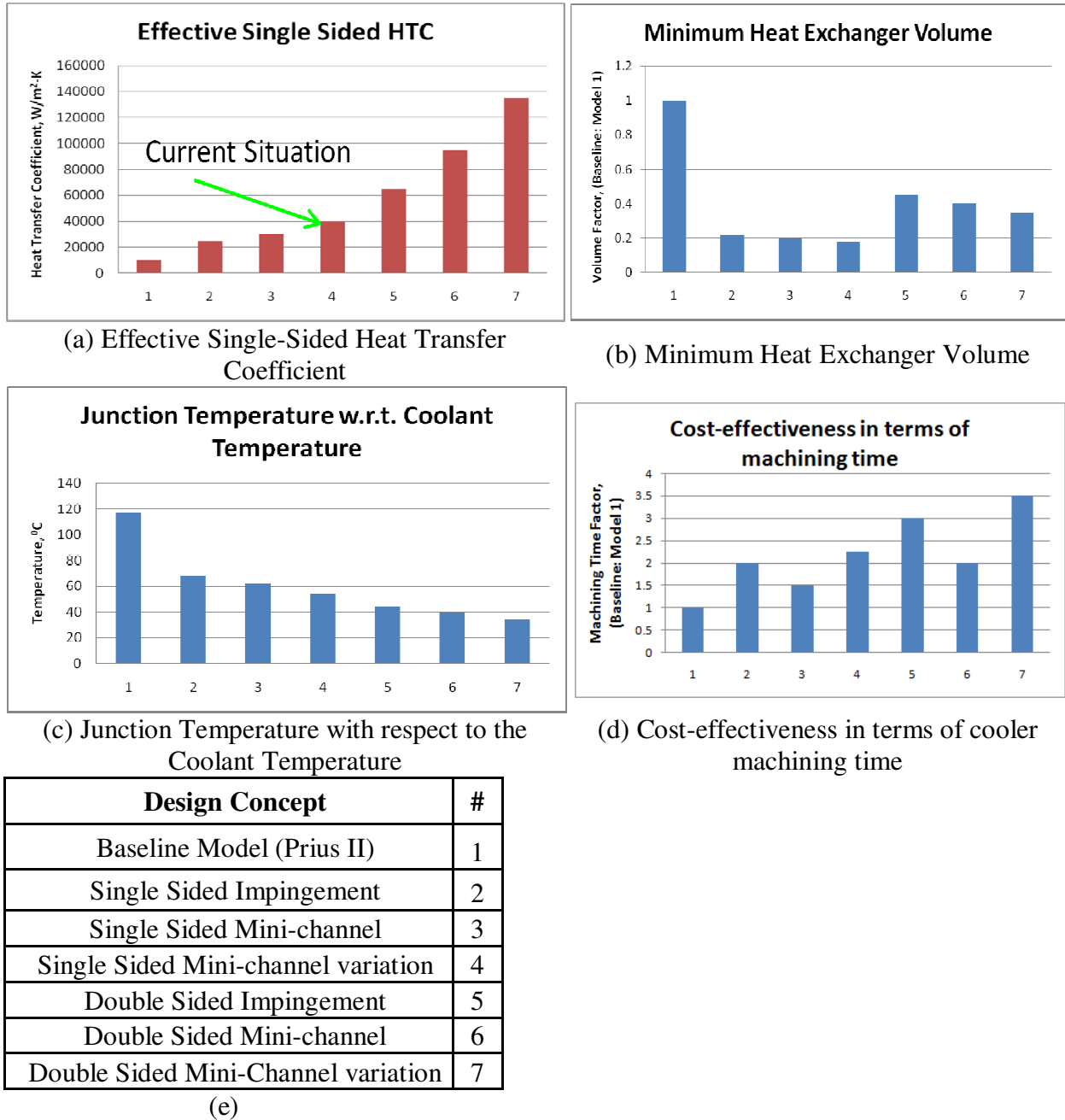


Figure 10.1. Comparison among various cooler configurations for the same pumping power.

During the course of the present study, it was observed that the heat transfer coefficient is essentially a non-linear monotonically increasing function of the flow rate and the effective fluid-solid contact surface area. In other words, if for the same configuration the flow rate is

doubled, the effective heat transfer coefficient will increase by a fraction (that is, less than 100%). Similarly, when the effective fluid-solid contact surface area is increased (say, by using double sided cooling), the effective heat transfer coefficient increases significantly. The applicable geometry, on the other hand, is a function of allowed pressure drop and in more general terms, a function of pumping power (product of volumetric flow rate and pressure drop).

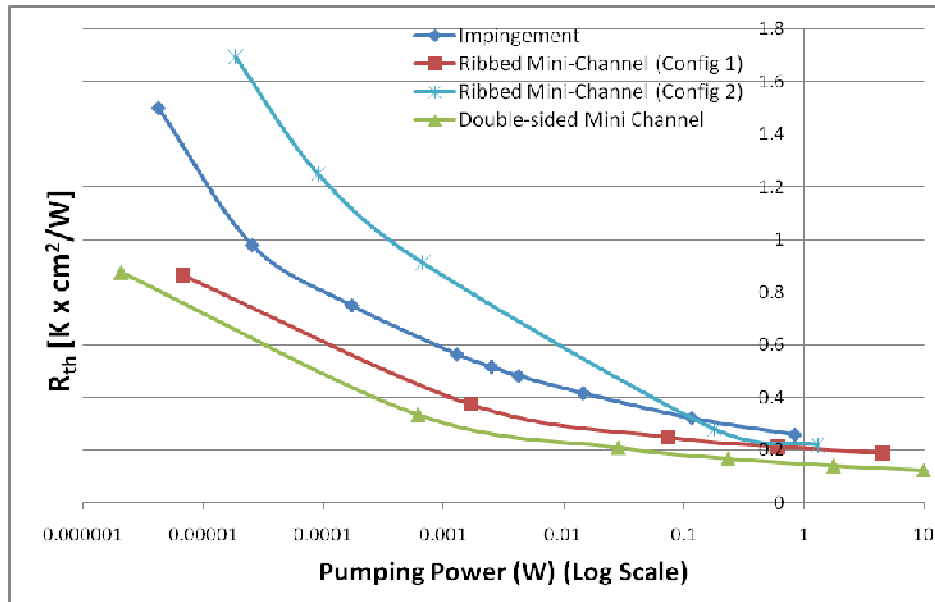


Figure 10.2. Comparison of the variation of R_{th} (thermal resistance) values with pumping power for few of the cooler configurations studied.

Figure 10.2 shows the variation of thermal resistance as a function of pumping power for few of the cooler configurations studied. It can be seen that at low pumping powers, one of the ribbed mini-channel configuration performs worse than the impingement configuration and at relatively high pumping powers; the same configuration performs better than the impingement configuration. In such cases, it becomes really important to identify the operating pumping power to make a geometry/configuration selection. Moreover, the pressure drop across a particular cooler configuration is more or less proportional to the square of the flow rate (that is, $\Delta p \propto Q^2$). So when the flow rate is doubled for a particular configuration, the pressure-drop across the cooler increases by about four times.

REFERENCES

1. Aldhous, P., “China’s burning ambition”, Nature 435, 1152, June 30, 2005.
2. <http://www.eetimes.com/news/latest/showArticle.jhtml?articleID=188101955>.
3. Agostini, B., Fabbri, M., Park, J. E., Wojtan, L., Thome, J. R. and Michel, B., “State of the Art of High Heat Flux Cooling Technologies”, Heat Transfer Engineering, Vol. 28(4), pp. 258–281, 2007.
4. Tuckerman, D. B., and Pease, R. F. W., “High performance heat sinking for VLSI”, IEEE Electron Device Letters, Vol. 2, No. 5, pp. 126-129, 1981.
5. <http://www2.toyota.co.jp/en/tech/environment/th2/system.html>.
6. Rogers, S. A., “Annual Progress Report for the Advanced Power Electronics and Electric Machinery Program”, 2007 Annual Progress Report, Vehicle Technologies Program, US DOE, December 2007.
7. Bennion, K., and Kelly, K., “Rapid Modeling of Power Electronics Thermal Management Technologies”, Vehicle Power and Propulsion Conference, 2009, pp. 622-629, 7-10 Sept 2009.
8. Hanreich G, Nicolics J, Musiejovsky L., “High resolution thermal simulation of electronic components” Microelectron Reliability, Vol. 40, pp. 2069–2076, 2000.
9. Janicki M, Napieralski M., “Modeling electronic circuit radiation cooling using analytical thermal model” Microelectron J, Vol. 31, pp. 781–785, 2000.
10. Yin H, Gao X, Ding J and Zhang Z., “Experimental research on heat transfer mechanism of heat sink with composite phase change materials” Energy Conversion and Management, Vol. 49, pp. 1740-1746, 2008.
11. Thebaud, J.-M.; Woirgard, E.; Zardini, C.; Sommer, K.-H., “Thermal fatigue resistance evaluation of solder joints in IGBT power modules for traction applications”, Power Electronics Specialists Conference, 2000. PESC 00, Volume 3, pp. 1285 – 1290, 18-23 June 2000.
12. Calata, J.N.; Bai, J.G.; Xingsheng Liu; SihuaWen; Guo-Quan Lu, “Three-Dimensional Packaging for Power Semiconductor Devices and Modules”, IEEE Transactions on Advanced Packaging, Volume 28, Issue 3, pp. 404 – 412, Aug. 2005.

13. Amon, C. H., Murthy, J., Yao, S. C., Narumanchi, S., Wu, C. F. and Hsieh, C. C., "MEMS-Enabled Thermal Management of High Heat Flux Devices EDIFICE: Embedded Droplet Impingement for Integrated Cooling of Electronics", *Experimental Thermal and Fluid Science*, Vol. 25, pp. 231-242, 2001.
14. Mudawar, I., Bharathan, D., Kelly, K., and Narumanchi, S., "Two-Phase Spray Cooling of Hybrid Vehicle Electronics", 11th Intersociety Conference on Thermal and Thermomechanical Phenomena in Electronic Systems, IThERM 2008, pp. 1210-1221, 28-31 May 2008.
15. Ivanova, M., Avenas, Y., Schaeffer, C., Dezord, J. B. and Schulz-Harder, J., "Heat Pipe Integrated in Direct Bonded Copper (DBC) Technology for the Cooling of Power Electronics Packaging", *IEEE 36th Conference on Power Electronics Specialists*, pp. 1750 – 1755, 2005.
16. Garimella, S. V., "Advances in Mesoscale Thermal Management Technologies for Microelectronics", *Microelectronics Journal*, Vol. 37, pp. 1165-1185, 2006.
17. Bhunia, A., Chandrasekaran, S. and Chen, C. L., "Performance Improvement of a Power Conversion Module by Liquid Micro-Jet Impingement Cooling", *IEEE Transactions on Components and Packaging Technologies*, Vol. 30, No. 2, June 2007.
18. Chu, R. C., "The Challenges of Electronic Cooling: Past, Current and Future", *Journal of Electronic Packaging*, Vol. 126, pp. 491-500, 2004.
19. Wiles, R. H., "Direct-Cooled Power Electronic Substrate", May 21, 2009. http://www1.eere.energy.gov/vehiclesandfuels/pdfs/merit_review_2008/adv_power_electronics/merit08_olszewski_1.pdf.
20. Narumanchi, S. V. J., Amon, C. H., Murthy, J. Y., "Influence of Pulsating Submerged Liquid Jets on Chip-Level Thermal Phenomena", *Transactions of the ASME*, Vol. 125, pp. 354-361, 2003.
21. Wang, E. N., Zhang, L., Jiang, L., Koo, J. M., Goodson, K. E., Kenny, T. W., Maveety, J. G., Sanchez, E. A., "Micromachined Jet Arrays for Liquid Impingement Cooling of VLSI Chips", *Solid-State Sensor, Actuator and Microsystems Workshop*, Hilton Head Island, South Carolina, June 2-6, 2002.

22. Fabbri, M., Jiang, S., Dhir, V. K., "Experimental Investigation of Single-Phase Micro Jets Impingement Cooling for Electronic Applications", Proc. of the HT2003 ASME Summer Heat Transfer Conference, Las Vegas, Nevada, USA, July 21-23, 2003.
23. Cheng, Y., Tay, A. A. O., Hong, X., "An Experimental Study of Liquid Jet Impingement Cooling of Electronic Components With and Without Boiling", Int. Symp. on Electronic Materials and Packaging, IEEE, pp. 369-375 2001.
24. Kercher, D. S, Lee, J.-B., Brand, O., Allen, M. G., Glezer, A, "Microjet Cooling Devices for Thermal Management of Electronics", IEEE Transactions on Components and Packaging Technologies, Vol. 26, No. 2, pp. 359-366, 2003.
25. Hollworth, B. R., Durbin, M., "Impingement Cooling of Electronics", Journal of Heat Transfer, ASME, Vol. 114, pp. 607-613, 1992.
26. Womac, D. J., Aharoni, G., Ramadhyani, S., Incropera, F. P., "Single Phase Liquid Jet Impingement Cooling of Small Heat Sources", Proceedings of the International Heat Transfer Conference, pp. 149-154, 1990.
27. Womac, D. J., Ramadhyani, S., Incropera, F. P., "Correlating Equations for Impingement Cooling of Small Heat Sources with Single Circular Liquid Jets", Transactions of the ASME, Vol. 115, pp 106-115, 1993.
28. Fitzgerald, J. A., Garimella, S. V., "Flow Field Effects on Heat Transfer in Confined Jet Impingement", Transactions of the ASME, Vol. 119, pp. 630-632, 1997.
29. Fitzgerald, J. A., Garimella, S. V., "A Study of the Flow Field of a Confined and Submerged Impinging Jet", International Journal of Heat and Mass Transfer, Vol. 41, Nos 8-9, pp. 1025- 1034, 1998.
30. Huang, C. L., Shieh, Y. R., Hung, Y. H., "Local Thermal Characteristics of a Confined Round Jet Impinging onto a Heated Disk", Electronic Packaging Technology Conference, IEEE, pp. 108-114, 1997.
31. Martin, H., "Heat and mass transfer between impinging gas jets and solid surfaces", Adv. Heat Transfer 13 (1977) 1-60.
32. Chou, Y.J., Hung, Y.H., "Impingement cooling of an isothermally heated surface with a confined slot jet", ASME, J. Heat Transfer 116 (1994) pp. 479-482.

33. Chou, Y.J., Hung, Y.H., “Fluid flow and heat transfer of an extended slot jet impingement”, *J. Thermophys. Heat Transfer* 8 (1994) pp.538–545.
34. Jiji, L. M. and Dagan, Z., “Experimental Investigation of Single-Phase Multi-Jet Impingement Cooling of an Array of Microelectronic Heat Sources,” *Proc. Int. Symp. Cool. Technol. Electron. Equip.*, Honolulu, HI, 1987, pp. 333–351.
35. Womac, D. J., Incropera, F. P. and Ramadhyani, S., “Correlating Equations for Impingement Cooling of Small Heat Sources with Multiple Circular Liquid Jets”, *ASME J. Heat Transf.*, vol. 116, pp. 482–486, 1994.
36. Oliphant, K., Webb, B. W. and McQuay, M. Q., “An Experimental Comparison of Liquid Jet Array and Spray Impingement Cooling in the Non-Boiling Regime”, *Exp. Thermal Fluid Sci.*, Vol. 18, pp. 1–10, 1998.
37. Bhunia, A., Cai, Q. and Chen, C. L., “Liquid Impingement and Phase Change for High Power Density Electronic Cooling”, *Proc. 41st AIAA Aerosp. Sci. Meeting Exhibit*, Reno, NV, Jan. 2003.
38. Bhunia, A., Chandrasekaran, S. and Chen, C. L., “Performance Improvement of a Power Conversion Module by Liquid Micro-Jet Impingement Cooling”, *IEEE Transactions on Components and Packaging Technologies*, Vol. 30, No. 2, June 2007.
39. Olesen, K., Bredtmann, R. and Eisele, R., “Shower Power: New Cooling Concept for Automotive Applications”, *Automotive Power Electronics Conference*, Paris, 21-22 June 2006.
40. Perry, K., “Heat transfer by convection from a hot gas jet to a plane surface”, *Proc. Mech. Inst.*, Vol. 168, pp. 775–784, 1954.
41. Sparrow, E., and Lovell, B., “Heat transfer characteristics of an obliquely impinging circular jet”, *Journal of Heat Transfer*, Vol. 102, pp. 202–209, 1980.
42. Yan, X., and Saniei, N., “Heat transfer from an obliquely impinging circular air jet to a flat plate”, *Int. J. Heat and Fluid Flow*, 18, pp. 591–599, 1997.
43. Goldstein, R. J., and Franchett, M. E., “Heat transfer from a flat surface to an oblique impinging jet”, *Journal of Heat Transfer*, Vol. 110, February, pp. 84–90, 1988.

44. Humphries W. R. and Griggs E. L., “A Design Handbook of Phase Change Thermal Control and Energy Storage Devices”, Greenbelt, MD: NASA, 1974.
45. Hasnain S. M., “Review of sustainable thermal storage technologies, part I: heat storage materials and techniques”, *Energy Conv. Manag.*, vol. 39, pp. 1127–1138, 1998.
46. Krishnan S, and Garimella S, “Analysis of a Phase Change Energy Storage System for Pulsed Power Dissipation”, *IEEE Transactions on Components and Packaging Technologies*, Vol. 27, No. 1, 2004.
47. Ishizuka M. and Fukuoka Y., “Development of a new high density package cooling technique using low melting point alloys”, *Proc. ASME/JSME Joint Thermal Engineering Conference*, vol. 2, pp.375–380, 1991.
48. Baker K. W., Jang J. H., and Yu J. S., “Thermal control of phase change package with periodic pulse heating—a case study”, in *Proc. ASME/JSME Joint Thermal Engineering Conference*, vol. 4, pp. 463–469, 1995.
49. Pal D. and Joshi Y., “Application of phase change materials for passive thermal control of plastic quad packages: a computational study”, *Numerical Heat Transfer A*, vol. 30, pp. 19–34, 1996.
50. Pal D. and Joshi Y., “Application of phase change materials to thermal control of electronic modules: a computational study”, *J. Electron. Packag.*, vol. 119, pp. 40–50, 1997.
51. Alawadhi E. M. and Amon C. H., “Performance analysis of an enhanced PCM thermal control unit”, *Proc. ITherm’00*, pp. 283–289, 2000.
52. Jing C., Martin V., and Setterwall F., “The study of PCM thermal management solution for portable computer”, *Proc. 2ndWorkshop IEA ECESIA Annex 17, Advanced Thermal Energy Storage Techniques*, Apr. 3–5, 2002.
53. Leoni N. and Amon C. H., “Thermal design for transient operation of the TIA wearable portable computer”, *Adv. Electron. Packag.*, pp. 2151–2161, 1997.
54. Alawadhi E. M. and Amon C. H., “Thermal analyses of a PCM thermal control unit for portable electronic devices: Experimental and numerical studies”, *IEEE Compon. Packag. Manufact. Technol.*, vol. 26, no. 1, pp. 116–125, Mar. 2003.

55. Hodes M., Weinstein R. D., Pence S. J., Piccini J. M., Mouziane L., and Chen C., "Transient thermal management of a handset using phase change material (PCM)", *ASME J. Electron. Packag.*, vol. 124, pp. 419–426, 2002.
56. Evans A. G., He M. Y., Hutchinson J. W., and Shaw M., "Temperature distribution in advanced power electronics systems and the effect of phase change materials on temperature suppression during power pulses", *ASME J. Electron. Packag.*, vol. 123, pp. 211–217, 2001.
57. Leland J. and Recktenwald G., "Optimization of a phase change heat sink for extreme environments", *Proc SEMITHERM'03*, pp. 351– 356, 2003.
58. Shatikian V., Dubovsky V., Ziskind G., and Letan R., "Simulation of PCM melting and solidification in a partitioned storage unit", *Proc. ASME Summer Heat Transfer Conf*, pp. 347–353, 2003.
59. Krishnan S., Murthy J. Y., and Garimella S. V., "A two temperature model for the analysis of passive thermal control systems for electronics", *ASME J. Heat Transfer*, vol. 126, pp. 628–637, 2004.
60. Krishnan S., Murthy J. Y., and Garimella S. V., "A two-temperature model for solid/liquid phase change in metal foams", *Proc. ASME Nat. Heat Transfer Conf.*, Charlotte, NC, pp. 609–619, 2004.
61. Chen, Y. P., and Cheng, P., "An Experimental Investigation on the Thermal Efficiency of Fractal Tree-Like Microchannel Nets", *International Communications in Heat and Mass Transfer*, Vol. 32, pp. 931–938, 2005.
62. Chen, Y. P. and Cheng, P., "Heat Transfer and Pressure Drop in Fractal Tree-Like Microchannel Nets", *International Journal of Heat and Mass Transfer*, Vol. 45, Issue 13, pp. 2643-2648, 2002.
63. Pence, D. V., "Reduced Pumping Power and Wall Temperature in Microchannel Heat Sinks with Fractal-Like Branching Channel Networks", *Microscale Thermophysical Engineering*, Vol. 6, Issue 4, pp. 319-330, 2002.
64. Lei, N., Skandakumaran, P. and Ortega, A., "Experiments and Modeling of Multilayer Copper Minichannel Heat Sinks in Single-Phase Flow", *Thermal and Thermomechanical Phenomena in Electronics Systems*, ITherm '06, pp. 9-18, May 30-June 2, 2006.

65. Parida, P. R., Ekkad, S. V. and Ngo, K. D. T., “Experimental and Numerical Investigation of Confined Oblique Impingement Configurations for High Heat Flux Applications”, *International Journal of Thermal Science* (submitted 2010).
66. Parida, P. R., Ekkad, S. V. and Ngo, K. D. T., “Impingement-Based High Performance Cooling Configurations for Automotive Power Converters”, *International Journal of Heat and Mass Transfer* (submitted 2010).
67. Parida, Mei, Jiang, Meng and Ekkad, “Experimental Investigation of Cooling Performance of Metal-Based Microchannels”, *Heat Transfer Engineering*, special edition, Vol. 31 (6), May 2010.
68. Esposito, E, “Jet Impingement Cooling Configurations for Gas Turbine Combustion”, M.S. Thesis, Louisiana State University, etd-07122006-141237, 2006.
69. Lander, R. D., Fish, R. W. and Suo, M., “External Heat-Transfer Distribution on Film Cooled Turbine Vane”, *J. Aircraft*, Vol. 9, No. 10, pp. 707-714, 1972.
70. Moffat, R. J., “Describing the uncertainties in experimental results”, *Experimental Thermal and Fluid Science*, 1, pp. 3–17, 1988.
71. Kaminski, D. A. and Jensen, M. K., *Introduction to thermal and fluids engineering*, Wiley, Hoboken, New Jersey, 2005.
72. Glynn, C., O’Donovan, T. and Murray, D. B., “Jet impingement cooling”, Centre for Telecommunications Value-Chain-Driven Research, Dublin, www.ctvr.ie/docs/PHO_Pubs/UKHeatTransfer%20Sept2005.pdf.
73. Sung, M.K. and Mudawar, I., “Single-Phase Hybrid Micro-Channel/Micro-Jet Impingement Cooling”, *International Journal of Heat and Mass Transfer*, Vol. 51, pp. 4342-4352, 2008.
74. Parida, P. R., Ekkad, S. V. and Ngo, K. D. T., “Experimental and Numerical Investigation of PCM-Jet Impingement Based Cooling Scheme for High Density Transient Heat Loads”, *International Journal of Thermal Science* (to be submitted 2010).
75. Pritish R. Parida, Srinath Ekkad and Khai Ngo, “Novel PCM and Jet Impingement Based Cooling Scheme for High Density Transient Heat Loads”, 14th International Heat Transfer Conference, Washington DC, USA, August 8 – 13, 2010.

76. Hunecke, K., *Jet Engines: Fundamentals of Theory, Design and Operation*, Motorbooks International Publishers, Osceola, WI, p. 146, 1997.
77. Lakshminarayana, B., *Fluid Dynamics and Heat Transfer of Turbomachinery*, John Wiley and Sons, New York, p. 697, 1996.
78. Treager, E., *Aircraft Gas Turbine Engine Technology*, 3rd ed., McGraw-Hill, New York, NY, pp. 550–560, 1996.
79. Takeishi, K., Nakae, T., Watanabe, K., and Hirayama, M., “Heat Transfer Characteristics of a Flow Passage With Long Pin Fins and Improving Heat Transfer Coefficient by Turbulence Promoters on a Endwall”, *Proceedings of ASME Turbo EXPO 2001*, June 4-7, New Orleans, LA, USA, 2001.
80. Uzol, O., and Camci, C., “Elliptical Pin Fins as an Alternate to Circular Pin Fins for Gas Turbine Blade Cooling Applications, Part 1: Endwall Heat Transfer and Total Pressure Loss Characteristics”, *Proceedings of ASME Turbo EXPO 2001*, June 4-7, New Orleans, LA, USA, 2001.
81. Hwang, J. J., and Lu, C. C., “Lateral Flow Effect on Endwall Heat Transfer and Pressure Drop in a Pin-Fin Trapezoidal Duct of Various Pin Shapes”, *Proceedings of ASME Turbo EXPO 2000*, May 8-11, Munich, Germany, 2000.
82. Martin, H., “Heat and mass transfer between impinging gas jets and solid surfaces”. *Advances in heat transfer*, Academic Press: New York, San Francisco, London, 13, pp. 1–60, 1977.
83. Hwang, J. J., Lai, D. Y., and Tsia, Y. P., “Heat Transfer and Pressure Drop in Pin Fin Trapezoidal Ducts”, *Transactions of the ASME*, Vol. 121, April, p. 264, 1999.
84. Chen, S. P., Li, P. W., and Chyu, M. K., “Heat Transfer in an Airfoil Trailing Edge Configuration With Shaped Pedestals Mounted Internal cooling Channel and Pressure Side Cutback”, *Proceedings of ASME Turbo EXPO 2006*, June 6-9, Spain, 2006.

APPENDIX A

The thermal testing of and simulation predictions for heat exchanger sample 1 are presented in this appendix. Figure 5.20 presents the overall view of the heat exchanger sample 1 and Figure 5.21 presents the exploded view of the various components of this sample.

Two sets of experiments were performed on this sample. For the first set, a thermal adhesive was used as a sealant between the target plate and the jet plate. This ensured a proper thermal contact between the target and jet plate. However, repeated experiments showed that there were non-uniform distribution of the sealant on the interface and thus, caused a very small leakage. As an alternative, a gasket was used as the sealant. Though it stopped any leakage, it created a thermal isolation at the target plate – jet plate interface. The following formula was used to calculate the overall heat transfer coefficient (h) of the heat exchanger:

$$h = \frac{\dot{m}c_p (T_{out} - T_{in})}{A_{total} (T_{avg,wall} - T_{avg,coolant})} \quad (A.1)$$

where, \dot{m} is the mass flow rate, T is the temperature, C_p is the specific heat capacity of the coolant and A_{total} is the total surface area of the fluid-solid interface inside the heat exchanger. For the first set, the overall heat transfer coefficient from the experiments was calculated to be 1408 W/m²-K. Experimental data is presented in Table A.1. Experimental data for the second set is presented in Table A.2. Owing to the thermal isolation at the interface in the second set, the cooler bulk and the target plate were at different temperatures and thus, it was difficult to quantify the data. However, the different temperature and the pressure drop measurements were used for the simulation validation. The experiments were performed with an overall DC input power of 200 W through the cartridge heaters and 1.4 lpm of water at about 21 °C was used as the coolant. The flow rate through the heat exchanger was measured to be about

1.4 L/min and the pressure drop across it was about 1.6 kPa. The average target plate temperature was measured to be 34 °C.

Table A.1. Experimental data from the first set of experiments (without the gasket).

Voltage	151.35 V	Mass flow rate	0.0233 kg/s
Current	1.313 A	Specific heat	4178 J/kg-K
Power	198.72 W	Inlet temperature	21 °C
Area	115 cm ²	Outlet temperature	23 °C
Flow rate	1.4 l/min	Average coolant temperature	22 °C
Density	997 kg/m ³	Average wall temperature	34 °C

Table A.2. Experimental data from the second set of experiments (with the gasket).

Voltage	151.65 V	Mass flow rate	0.021 kg/s
Current	1.275 A	Specific heat	4178 J/kg-K
Power	193.354 W	Inlet temperature	21.4 °C
Area	115 cm ²	Outlet temperature	22.6 °C
Flow rate	1.26 l/min	Average coolant temperature	22 °C
Density	997 kg/m ³	Average wall temperature	33 °C

A.1 Measurements from the Experiment

The following measurements from the experiments were helpful in validating the simulation predictions:

1. The coolant temperature at the heat exchanger inlet as well as at the heat exchanger outlet was measured. From this coolant bulk temperature was obtained by using linear interpolation.
2. Average heat exchanger wall temperature. To measure this temperature, various thermocouples were placed at different locations on the target plate of the heat exchanger.
3. Temperature at different locations on the heater surface was also measured.
4. Volumetric flow rate (L/min) of the coolant was measured

5. The total energy flowing into the heat exchanger was computed from the energy dissipated by the cartridge heaters. Thus, for a known applied voltage and current, the rate of dissipation was estimated.
6. Pressure drop measurements were made very close to the heat exchanger.

Using these experimental measurements, the overall heat transfer coefficient was easily estimated. Moreover, the temperature measurements at different locations were used to closely validate the conjugate heat transfer simulations.

A.2. Simulation Predictions

The validated simulation model presented in chapter 5 was used to simulate this heat exchanger sample and compare against the experimental results. The test section shown in Figure 5.20 was modeled in ANSYS as shown in Figure A.1. Figure A.1(a) shows the model without the gasket at the jet plate – target plate interface while Figure A.1(b) shows the model with gasket at the same interface. Figure 5.22 shows the thermocouple locations on the target plate. For this simulation, the target plate and the jet plate were considered as one single piece. Also, no interface material was considered between the heater copper block and the target plate. The inlet mass flow rate and temperature were matched with that for the experiments. The overall average heat transfer coefficient was calculated to be $4844 \text{ W/m}^2\text{-K}$ using Equation (A.1). Also, when the temperature estimated by the simulations at the thermocouple locations were used, the overall heat transfer coefficient was found out to be $1200 \text{ W/m}^2\text{-K}$. Figure A.2 shows the heat transfer coefficient, based on the average coolant temperature, and the temperature at the fluid-solid interface. Simulations showed that the local heat transfer coefficient based on the mean coolant temperature at the target surface had a maximum value of $22000 \text{ W/m}^2\text{-K}$. The overall heat transfer coefficient was closer to the target value; however, the local heat transfer

coefficient was much lower than the target value. Simulations were also performed for the gasket case as well. The jet-to-target plate spacing increased due to the gasket and also it created an alternate path for the fluid. Figure A.3 indicates this alternate fluid path. Thus, a much lower overall as well as local heat transfer coefficient was obtained.

For the above simulation, SST k- Ω turbulence model was used. This model was also simulated using the k- ϵ model. A significant trend was observed. The SST k- Ω model over predicted the heat transfer coefficient and thus under predicted the temperature inside the solid. The k- ϵ model on the other hand under predicted the heat transfer coefficient and thus over predicted the temperature inside the solid. Moreover, modeling the actual test section with the interface contact resistances perfectly is very difficult and this can sometimes lead to significantly higher temperatures inside the solid domain. For such situations, this temperature over prediction is good for simulations. Thus, SST k- Ω model might be predicting the values correctly for the given boundary conditions but the boundary conditions might not be perfect to simulate the test section. In any case, the maximum heat transfer coefficient was much lower than the target value. Hence, further significant design improvements such as reduction of jet numbers and localized impingement are therefore required to improve the local heat transfer coefficient.

A.3. Conclusion

Being a preliminary test, temperature data recording was not efficient and had high error percentages and thus, improvements in data recording were required for future experiments. Also, due to the large contact surface of the cooper heat source block, the heat flux value was much lower ($\sim 1-2 \text{ W/cm}^2$) than that required for the warranted application. Thus, the large heat source was replaced with localized heat sources.

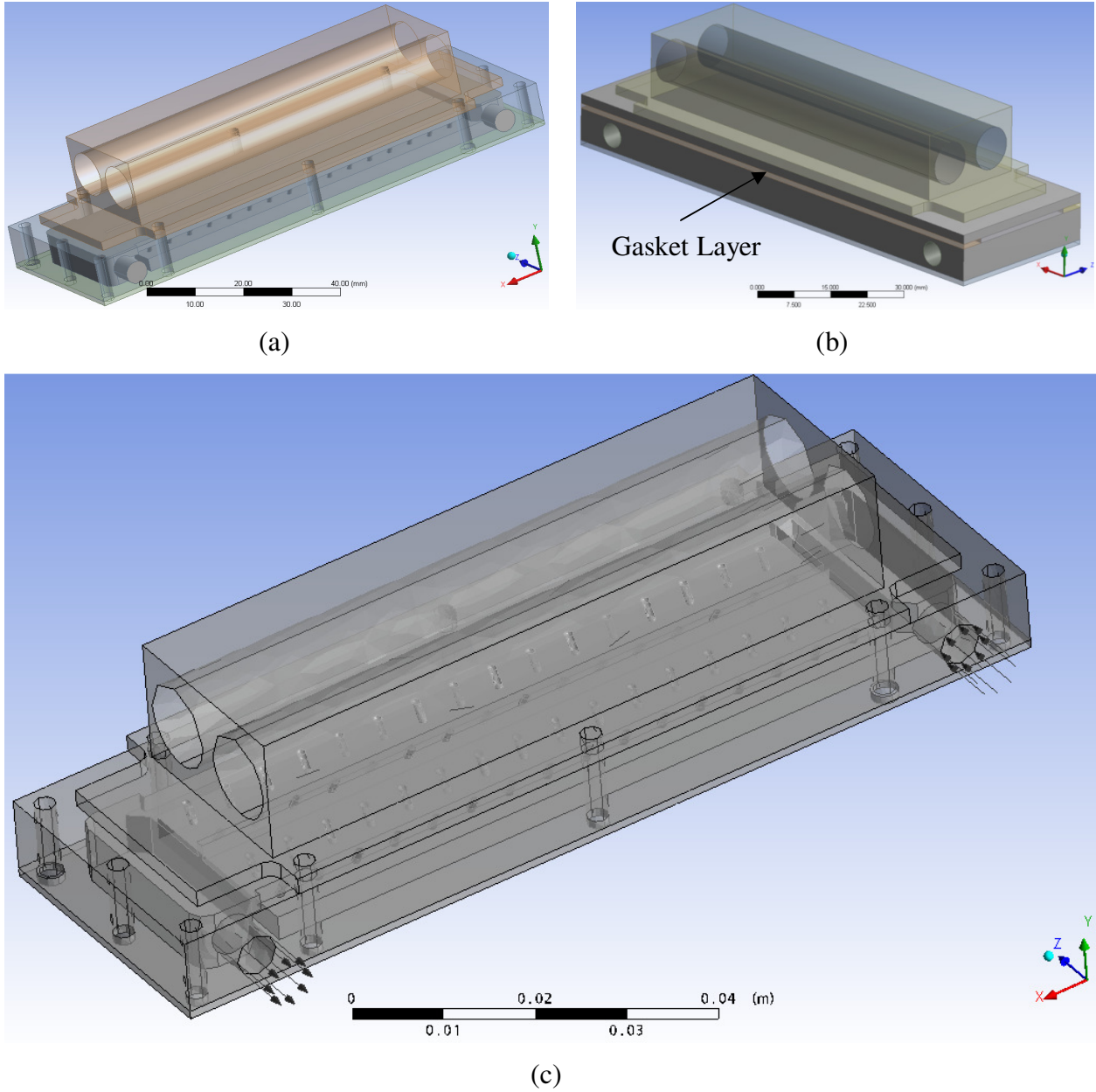
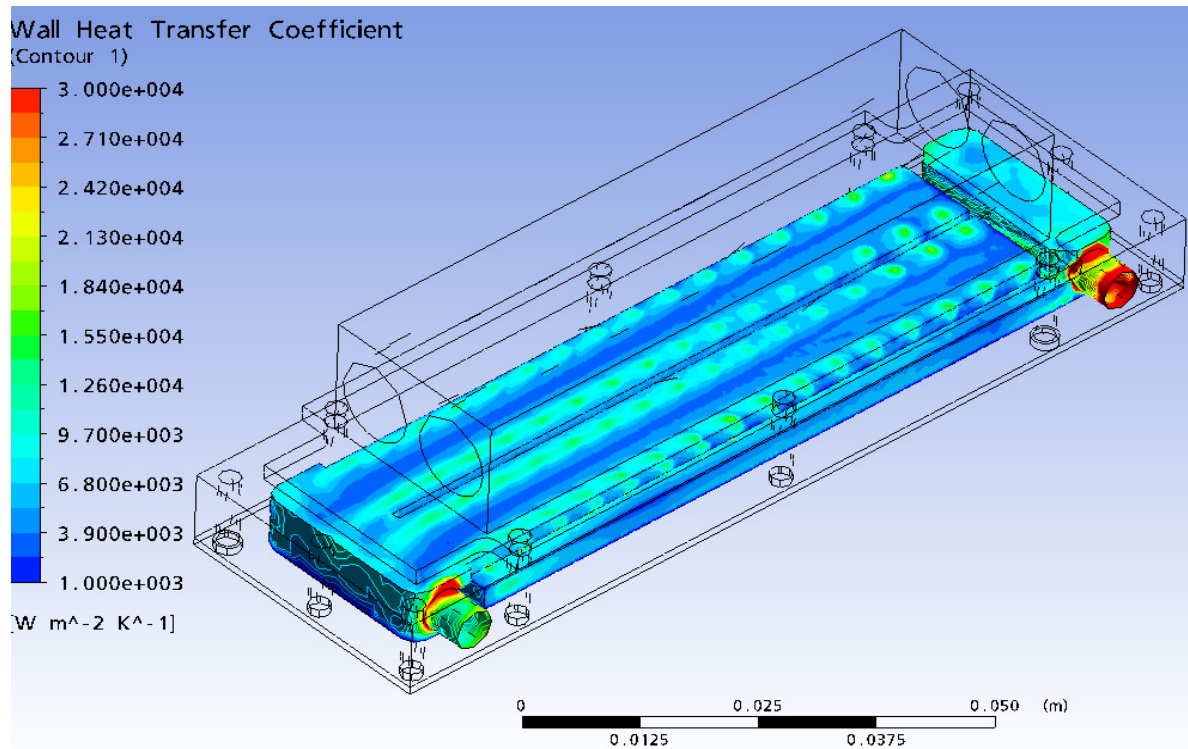
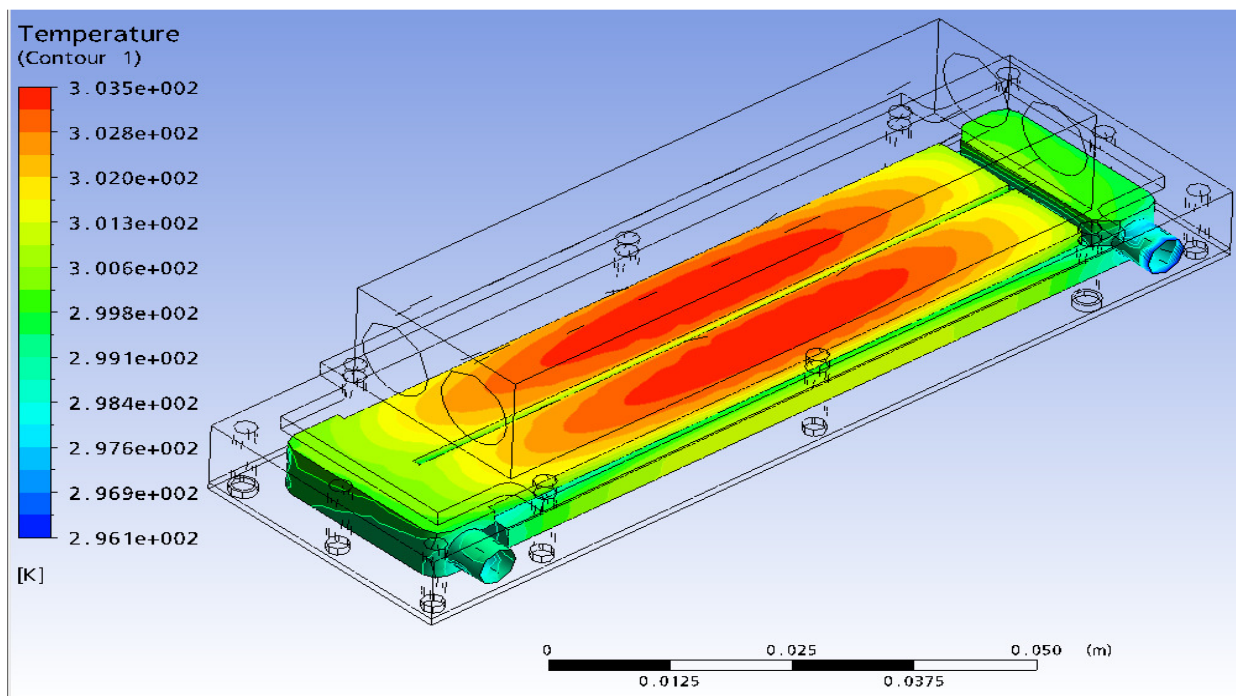


Figure A.1. Overall geometry and the CFX model for the conjugate heat transfer simulations of test section of the thermal test bed. (a) overall geometry without the gasket (b) overall geometry with the rubber gasket. (c) CFX model for the geometry without the gasket.



(a)



(b)

Figure A.2. (a) Local wall heat transfer coefficient on the fluid-solid interface computed based on the average coolant temperature. (b) Temperature at the fluid-solid interface.

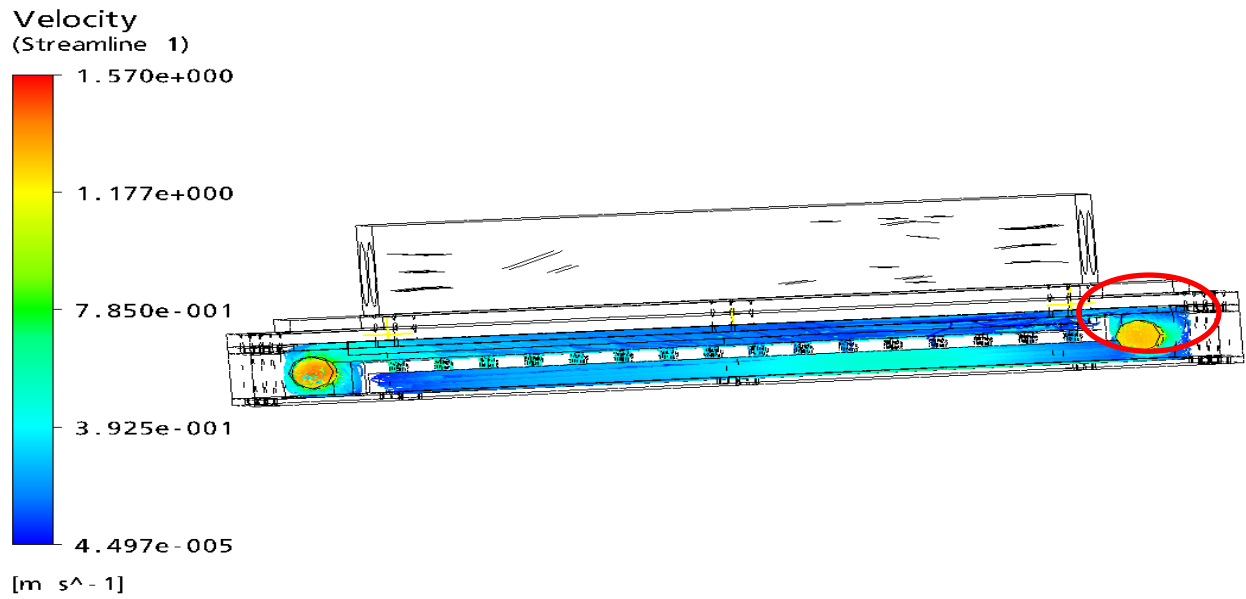


Figure A.3. Velocity streamlines showing the alternate fluid path (red circle) generated due to the placement of a gasket.

APPENDIX B: PUBLICATIONS

A. Journal Papers

1. Parida, P. R., Ekkad, S. V. and Ngo, K. D. T., “Experimental and Numerical Investigation of Confined Oblique Impingement Configurations for High Heat Flux Applications”, *International Journal of Thermal Science* (submitted 2010).
2. Parida, P. R., Ekkad, S. V. and Ngo, K. D. T., “Impingement-Based High Performance Cooling Configurations for Automotive Power Converters”, *International Journal of Heat and Mass Transfer* (submitted 2010).
3. Parida, P. R., Ekkad, S. V. and Ngo, K. D. T., “Multi-Layer Mini-Channel and Ribbed Mini-Channel Based High Performance Cooling Configurations for Automotive Inverters”, *IEEE Transactions on Components and Packaging Technologies* (to be submitted 2010).
4. Parida, P. R., Ekkad, S. V. and Ngo, K. D. T., “Double-Sided High Performance Cooling Configurations for High Heat Flux Applications”, *IEEE Transactions on Components and Packaging Technologies* (to be submitted 2010).
5. Parida, P. R., Ekkad, S. V. and Ngo, K. D. T., “Experimental and Numerical Investigation of PCM-Jet Impingement Based Cooling Scheme for High Density Transient Heat Loads”, *Journal of Heat Transfer Engineering* (submitted 2010).
6. Parida, P. R., Panchal, K. and Ekkad, S. V., “Investigation of Heat Transfer and Flow Characteristics of Jet Impingement Based Trailing Edge Cooling”, *International Journal of Heat and Fluid Flow* (to be submitted 2010).
7. Panchal, K., Parida, P. R. and Ekkad, S. V., “Comparison of Impingement and Pin-Fin Based Trailing Edge Cooling Methods”, *International Journal of Heat and Fluid Flow* (to be submitted 2010).
8. Parida, Mei, Jiang, Meng and Ekkad, “Experimental Investigation of Cooling Performance of Metal-Based Microchannels”, *Heat Transfer Engineering*, special edition, Vol. 31 (6), May 2010.

B. Conference Papers

1. Pritish R. Parida, Srinath Ekkad and Khai Ngo, “Novel PCM and Jet Impingement Based Cooling Scheme for High Density Transient Heat Loads”, 14th International Heat Transfer Conference, Washington DC, USA, August 8 – 13, 2010.
2. Pritish R. Parida, Srinath Ekkad and Khai Ngo, “Innovative Liquid Cooling Configurations for High Heat Flux Applications”, 12th ITherm Conference, Las Vegas, NV, USA, June 2 - 5, 2010.
3. Pritish R. Parida, Kapil Panchal and Srinath Ekkad, “Three-tier Impingement Cooling Scheme for Heat Transfer Enhancement at the Trailing Edge of a Turbine Blade”, 20th National & 9th ISHMT-ASME Heat and Mass Transfer Conference, Mumbai, INDIA, January 4 - 6, 2010.
4. Kapil Panchal, Pritish R. Parida and Srinath Ekkad, “ Evaluation of Pin Fin Cooling Geometries for Turbine Blade Trailing Edge”, 20th National & 9th ISHMT-ASME Heat and Mass Transfer Conference, Mumbai, INDIA, January 4 - 6, 2010.
5. Pritish R. Parida and Srinath Ekkad, “Numerical Prediction of Flow and Heat Transfer Rates in Metal-Based Micro-Channels Using Lattice Boltzmann Method”, ASME Summer Heat Transfer Conference, 10 – 14 August 2008, Jacksonville, FL.
6. Pritish R. Parida, Daniel Huff, Srinath Ekkad, Khai D.T. Ngo, “Impingement Cooling for Power Electronics”, CPES Annual Conference 5 -7 April, 2009, Virginia Tech, Blacksburg, VA.